NANOPLASMONICS AND SILICON NANOPHOTONICS DEVICES FOR SENSING APPLICATIONS

BY

MANAS RANJAN GARTIA

DISSERTATION

Submitted in partial fulfillment of the requirements
for the degree of Doctor of Philosophy in Nuclear, Plasma and Radiological Engineering
in the Graduate College of the
University of Illinois at Urbana-Champaign, 2013

Urbana, Illinois

Doctoral Committee:

Assistant Professor Gang Logan Liu, Chair
Professor Rizwan Uddin
Professor James F. Stubbins
Professor David N. Ruzic

ABSTRACT

Nanophotonics deals with the interaction of light with matter in nanometer scale. One of the subsets of nanophotonics is nanoplasmonics, which deals with manipulation of light using the unique optical properties of metal nanostructures. Manipulation of light in nanoscale using properties of surface plasmon will make it possible to accomplish a myriad of applications ranging from global security to healthcare and environmental sensing. This thesis studies silicon-based nanophotonics and noble metal based nanoplasmonics devices, and explores their utilities for energy, sensing, and photonics applications.

Three dimensional (3D) sub-wavelength tapered periodic hole array plasmonic structure has been designed and fabricated. In contrast to the surface plasmon polariton (SPP) mediated extraordinary optical transmission (EOT), the proposed structure relies on the localized surface plasmon (LSP) enhanced optical transmission. The advantage of LSPs is that the enhanced transmission at different wavelengths and with different dispersion properties can be tuned by controlling the size, shape and materials of the 3D holes. The tapered geometry will funnel and adiabatically focus the photons on to the sub-wavelength plasmonic structure at the bottom, leading to a large local electric field and the enhancement of EOT (due to radiative coupling of surface plasmons). The design principle of such devices for surface enhanced Raman spectroscopy (SERS) applications based on the classical electromagnetic simulations (Finite Difference Time Domain, FDTD) and the quantum mechanical density functional theory (DFT) has been performed.

Due to large transmission and reflection resonance wavelength shifts upon binding of molecules on the above flexible, high throughput, large area 3D plasmonic device, the device showed highest ever reported sensitivity of 46,000 nm per refractive-index unit and unprecedented figure of merit of 1,022. The utility of the sensor for highly sensitive refractive-index sensing, DNA hybridization detection, protein-protein interaction and integration to portable microfluidics device for lab on chip applications have been achieved. The thesis discusses how to transform the nanoplasmonic spectroscopy sensing to become colorimetric sensing with requiring only naked eyes or ordinary visible color photography, eliminating the

need for precision spectrometer or fluorescence labeling. The device can also be utilized for preparing beyond diffraction limit DNA/proteomics microarray using plasmonic nanolithography techniques.

The second part of thesis addresses an important scientific question – how to increase long range energy transfer efficiency in nanoscale. Energy transfer between light and matter (e.g. photons-molecule, molecule-molecule) is essential in sustaining life in nature. One of such examples is photosynthesis. In contrast to the efficient energy transfer processes in the living system (e.g. resonance energy transfer efficiency in reaction center of light harvesting complex for photosynthesis process is over 90%), man-made photonics and plasmonics system are impaired with low energy transfer efficiencies. This poses a serious challenge for the realization of efficient plasmonic devices for signal guiding, modulation and active information processing on nanoscale. Although, many near field energy transfer schemes such as Förster Resonance Energy Transfer (FRET), Dexter Energy Transfer (DET), and Plasmon Resonance Energy Transfer (PRET) have been explored, they are mostly short-ranged (< 100 nm) and the energy transfer efficiency decreases drastically with distance. This thesis proposes a new energy transport route through a hybrid plasmonic-photonic system coupling the dipole-photonic-plasmonic resonance energy transfer (DiP-PRET) to achieve over 90% energy transfer efficiency.

ACKNOWLEDGEMENTS

I express my sincere gratitude to my thesis adviser, Prof. Gang Logan Liu, for his continual guidance, support and encouragement throughout the course of my doctoral research. I am very thankful to him for introducing me to the exciting and interesting field of plasmonics. Without Prof. Liu's strategic direction, and mentoring, I would not have got this far.

I am deeply indebted to Prof. Robert Clegg for all his enthusiastic discussions on spectroscopy and microscopy. He really broadens my learning and interest in spectroscopy. I am also grateful to meet Prof. Gary Eden during my later part of dissertation. His contagious enthusiasm, open minded, and thorough discussion on topics, and plenty of time for students greatly helped reshaping some of the conclusions made in this work. I am also greatly thankful to Dr. Tiziana Bond for her continual support and guidance during my research life. I greatly enjoyed writing some of the proposals with her. It was an immense learning experience. It was also a pleasure to work with Dr. Mayandi Sivaguru. I learned a lot on linear and non-linear microscopy from him. He was kind enough to let me use most of his chemicals. I am also thankful to work with Prof. Andrzej Wieckowski. He was kind enough to allow me use his lab for the nitrate sensor project and he also introduced me to his wonderful postdoc Dr. Björn Braunschweig, who was quite helpful and made possible to complete all the experiments on nitrate sensor project.

During my course taking phase, I met some of the great professors, such as Prof. Rizwan Uddin, Prof. James Coleman, Prof. Jean-Pierre Leburton, Prof. Brian Cunningham, and Prof. Roy Axford, to name a few, whose teaching greatly inspired my career in research. I am also thankful to Prof. Gaurav Bahl, and Prof. Meng Lu for valuable comments on my research. I am specially indebted to Meng for his collaboration during later part of my dissertation. I thank my dissertation committee members, Prof. David Ruzic, Prof. James Stubbins, Prof. Rizwan Uddin, and Prof. Shun-Lien Chuang for agreeing to be in my doctoral committee and for their valuable comments.

My colleagues have been a source of immense support during this work. I would specially like to thank Austin Hsiao, Sujin Seo, Anusha Pokhriyal, Te-Wei Chang, Zhida Xu, Yi Chen, Xinhao Wang, Jing Jiang, Jingwei Wang, Gulsim Kulsharova, Daren Whitlock, and

Yemaya Bordain for being part of the teams that helped solve numerous problems during this work. I am especially thankful to Yemaya for her continuous support during my PhD. My thanks are also due to current and past members in Liu Nanobionics group for creating a very friendly environment to work in.

I thank my friends in Urbana-Champaign-Rajneesh Chaudhary, Hitesh Bindra, Prashant Jain, Udit Molakatalla, Aarti Venkat, Rakesh Komuravelli, Jyothi Sadhu, Krishna Vasanth Valavala, Varun Madhavan, Snehita, Elbakhshham Mohamed, Weiying Chen, and Rabie Abu Saleem for making the stay enjoyable for the entire PhD phase.

I would like to acknowledge the staff of the Micro and Nanotechnology Laboratory, Materials Research Laboratory, the Institute for Genomic Biology, and the Beckman Institute at the University of Illinois at Urbana-Champaign. I would also like to acknowledge financial support from the Department of Energy, Lawrence Livermore National Laboratory and Department of Nuclear, Plasma, and Radiological Engineering. I would like to thank Gail and Becky from NPRE for their encouragement and support during the PhD.

Last, but not least, I would like to thank my wonderful wife Tushara Chakkath for her understanding and love during the past few years and my parents for their continuing support and encouragement throughout my academic endeavors.

TABLE OF CONTENTS

CHAPTER 1

GENERAL INTRODUCTION

The "nano" revolution truly began when Richard Feynman declared "*There's Plenty of Room at the Bottom*." The desire to go small and faster had culminated even before that as it was long understood that miniaturization will speed up processing information and reduce power consumption. Without doubt, we have made tremendous progress in terms of speed of processing information starting from 1900's telegraph to today's supercomputers. However, the new "*Information Age* or *Digital Age*" has added more challenges to measure our progress: faster, smaller and cheaper. In every part of our life, such as communication, data storage, display, medical imaging and medical therapies, technology is striving to make things faster, smaller and cheaper. For example, by making the storage space for data "bits" smaller, we can squeeze more data in the same storage device; by making the size of pixels smaller, we can put more pixels in the display device and hence make the image clear. In addition, miniaturization transforms bulky system into portable one, which improves the convenience in day-to-day life. In this thesis, I will study such miniaturized devices and explore their utility for energy, sensing, and photonics applications. In particular, I will deal with nanophotonics and nanoplasmonics structures as well as their utilization to make sensors, energy harvesting, and light emitting devices.

The thesis has been outlined in the following way. Chapter 1 briefly describes the motivation behind nanophotonics and nanoplasmonics study. Examples of both man-made and natural nanophotonics and nanoplasmonics structure are also provided. Chapter 2 shows the nanophotonics and nanoplasmonics fabrications. Chapter 3 and Chapter 4 are devoted to optical characterization of nanophotonics and nanoplasmonics devices respectively. Chapter 5 deals with the quantum mechanical simulations of metal-molecule interactions. For an example, the charge transfer mechanism of surface enhanced Raman spectroscopy (SERS) has been simulated in Chapter 5. The classical simulation of light-matter interaction relevant to plasmonic devices is presented in Chapter 6. The experimental evidence of plasmon-molecule interaction probed using Fluorescence Lifetime Imaging Microscopy (FLIM) is presented in Chapter 7. Chapter 8 describes an overview of SERS, and the detailed SERS experiment using nanoplasmonic device.

Chapter 9 provides further demonstration of nanoplasmonic device for diverse applications such as biotechnology and environmental contamination sensing. Here, 3D enhanced fluorescence live-cell imaging using the plasmonic sensor is demonstrated. Chapter 10 shows nanohole based plasmonic sensors for colorimetric chemical imaging, DNA sensing, and protein-protein interactions. Chapter 11 deals with integration of fluorescence molecule, dielectric microresonator, and surface plasmon substrate to provide seed-injection amplification. Finally, Chapter 12 provides the future works and perspective on plasmonics.

Introduction to Nanophotonics

Natural nanophotonics structures

Nanophotonics is ubiquitous in nature. Starting from the whiteness of teeth, magnificent color of peacock feathers, wings of butterfly, iridescent of beetles, antireflecting moth eyes, super adhesive gecko feet and to hydrophobicity of lotus leaf, are all because of photonics structure. Most of the structural colors are due to interference, diffraction and scattering. Figure 1.1a shows the scanning electron micrograph (SEM) of the butterfly *Morpho rhetenor*. The bright color is because of the three-dimensional photonic crystals with periodic lattices. Because of photonic band gap in a periodic lattice, light of a particular wavelength is reflected strongly, irrespective of incidence angle [1]. The band gap is further explained in details later in this chapter. Image of a peacock feather and the corresponding SEM image are shown in Fig. 1.1b. The different colors of barbules are because of 2D photonic-crystal structure. Different colors are produced due to variation of the lattice constant and the number of periods in the photonic crystal structure [2]. Figure 1.1c shows a moth eye and the nanostructure of the eye. The inset also shows the ommatidial structures (structural surface units of the eye) and the presence of the corneal nipple arrangement [3]. The anti-reflective property acts as a survival mechanism for the insects to evade predators during night. Figure 1.1d shows the iridescent Manuka beetle and the SEM showing multilayer reflectors in the cuticles. Due to multi layer structures and Bragg

grating on the surface the iridescent colors are produced [4, 5]. The self-cleaning adhesive property of Gecko's feet allow it to climb rapidly even on smooth vertical surfaces. The special high adhesive forces of Gecko's feet is due to the accumulation of van der Waals forces between the nanostructured hairs (spatulae) in the feet (Fig. 1.1e) and the surface molecules of the solid structure [6, 7]. Finally, the hydrophobic nature of the lotus leaf [8] is attributed to the nanostructures on the leaf surface as shown in Fig. 1.1f.

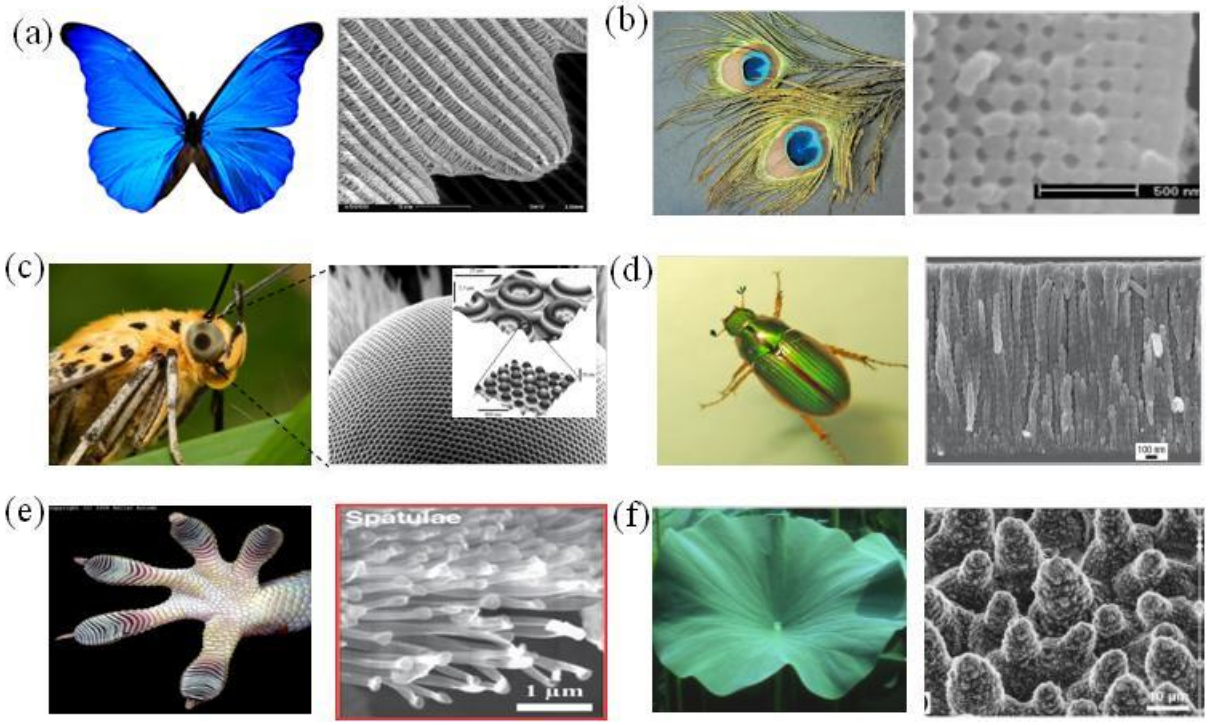

Figure 1.1: (a) *Morpho rhetenor* and SEM showing the nanostructure of the wings [1]. (b) Peacock feathers and SEM images of barbule structures [2]. (c) Image of a Moth and the corresponding SEM showing the photonics structure of the eyes [3]. (d) The Manuka (scarab) beetle and of the chiral reflector in the cuticle of the beetle [4, 5]. (e) Morphology of a Tokay Gecko's toe and SEM image of the *spatulae* [6, 7] (f) Hydrophobic lotus leaf and the nanostructure on top side if the leaf [8].

The origin of photonic band gap is due to periodic variation of refractive index in photonic crystals with lattice period comparable to the wavelength of light. Near the band gap energy certain wavelength of the incident electromagnetic wave is strongly reflected causing bright colors at certain angles. Figure 1.2 plots the photonic band structure for three different multilayer films. The left hand figure is for a system where all the layers have the same dielectric constant (e.g. GaAs bulk system). The middle figure is for the system with alternate dielectric

constant layer of 13 and 12 (e.g. GaAs/ GaAlAs multilayers). The right hand side figure is for system with very high dielectric contrast of 13 and 1 (e.g. GaAs/ Air multilayers) [9]. The frequency is given by [9] $\omega(k) = \frac{ck}{\sqrt{\varepsilon}}$ where c is the speed of light, k is the wave vector and ε is the dielectric constant (or relative permittivity). So, in a multilayer, high frequency modes of light (say, n=2 mode) will be confined in low dielectric constant layers and low frequency modes of light (e.g. n=1 mode) will be confined in high dielectric constant layers. This will create an energy gap or band gap at the edge of the Brillouin zone ($k = \pi/c$) as shown in Fig. 1.2. The band gap increases with the dielectric contrast as shown in Fig. 1.2.

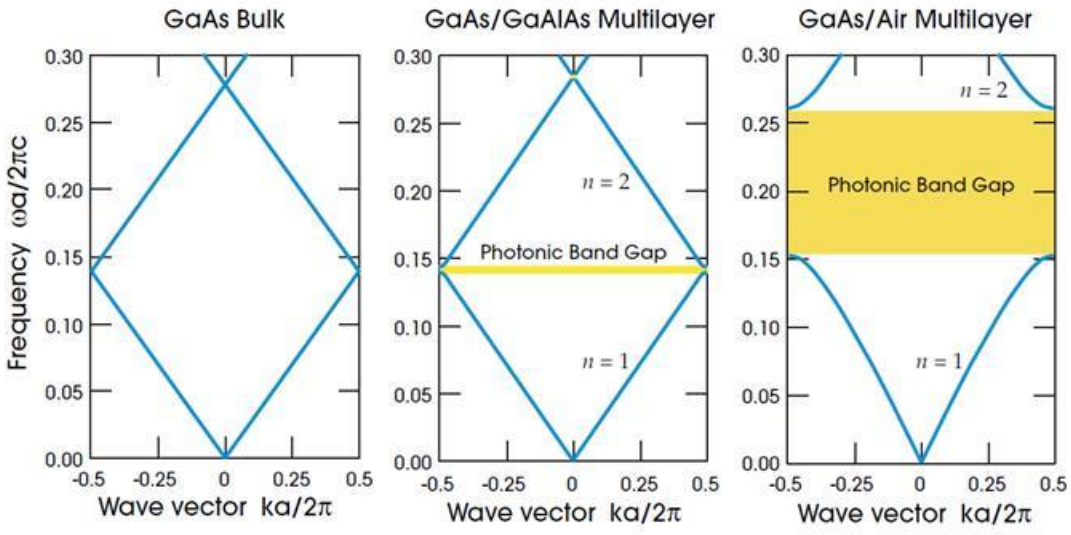

Figure 1.2: Dispersion relation for light traversing a periodic dielectric structure with, (a) zero dielectric contrast, (b) alternate dielectric layer of 13 and 12, (c) alternate dielectric layer of 13 and 1. The figure is taken from [9].

What is diffraction limit?

This section will explain the motivation to built nanophotonics and nanoplasmonics devices. "*Seeing is believing*" - Microscopy has played an important role in advancing the science and technology especially in material science and biology. Much of the advancement is driven by the desire to see live biological cells and bacteria in a non-destructive manner with

sub-wavelength resolution by using low intensity light and without using localized fluoroscent molecules [10]. Although electron microscope can achieve this resolution, it is not suitable for live cell imaging as live cells cannot survive the ultravacuum and the intense electron beam intensity. However, the resolution of optical imaging system is restricted with fundamental "diffraction limit". German physicist Ernst Abbe found that the resolution of an image is dependent on the wavelength of light and the aperture of its optics [11]. The principles of diffraction limit states that two objects located closer than approximately $\lambda/2NA$, where λ is the wavelength of light and NA is the numerical aperture of the imaging lens, could not be resolved by a microscope. Due to this limitation, point sources ~ less than 200 nm apart cannot be distinguished in the visible range and the image of the single-point emitter to appear as a blob because of diffraction [12].

Importance of breaking the diffraction limit

It is useful to discuss the relevance of breaking the diffraction limit for energy, sensing and light emitting applications. Apart from increasing the resolution of existing microscope set-up and imaging systems, breaking the diffraction limit has huge impact on designing new generation of energy harvesting, sensing and light emitting devices. For example, nanophotonics and nanoplasmonic structures, which beat the diffraction limit, strongly interact with light. Hence, these structures have been considered for thin-film photovoltaics to improve the light trapping property, which is currently a problematic issue for the thin-film industry and hence impeding its wider spread growth. Nanophotonics structure has the potential to increase the efficiency of existing solar cells, by providing higher effective absorption area coupled with light trapping property, better carrier transports and reducing the bulk recombination. Nanoplasmonics based sensor will offer better sensitivity and improve the detection limit of analytes. Nanolasers will decrease the power consumptions and reduce the material use. Apart from practical applications nanophotonics and nanoplasmonics offer challenges to understand and study the basic science.

Man-made nanophotonics structure

To date many bio-mimetic structures have been fabricated. Here, mainly nanostructures made on silicon will be introduced and attention will be focused on nanopillar or nanocone structures due to their direct applications to sensing and energy harvesting devices. Four classes of nanomanufacturing techniques to produce nanopillar structures, namely, electrochemical etching, electron beam lithography, nanosphere lithography and growth techniques, will be discussed. Figure 1.3a shows a SEM image of nanopillar silicon produced by electrochemical etching of the silicon wafer. This particular class of structures is also known as porous silicon. Crystalline silicon can be etched in aqueous solution of ethanol and hydrofluoric acid (HF) electrolytes to produce porous silicon. Figure 1.3a, ii shows the porous silicon structure using white-light illumination and the corresponding UV-illuminated fluorescence image is shown in Fig. 1.3a, iii. A 450-nm cutoff filter was used for this purpose so that only the red-orange photoluminescence from porous Si can be observed [13]. Figure 1.3b shows example of different diameter of Si nanowire fabricated using e-beam lithography techniques [14]. As shown in Fig. 1.3b, ii-iii, the spectrum of the color produced by the nanostructured device can be controlled by varying the diameter of the nanowire. Figure 1.3c shows the process of producing nanopillar and nanocone structures using dry gas etching methods by using a dielectric sphere as nanomask [15]. Figure 1.3c, i schematically shows a thin layer (μm) of amorphous Si (a-Si) on Indium Tin Oxide (ITO) coated glass substrate, a self-assembled monolayer of silica nanospheres on top of a-Si thin film, and finally the nanowire and nanocone arrays produced after performing dry etching (ICP-RIE) on the substrate. Figure 1.3c, ii, and iii show the SEM of monolayer of silica nanosphere on the surface and the surface after etching respectively. All of the above structures were produced using top-down manufacturing technique. However, recently a bottom-up manufacturing technique has been introduced to produce micropillar structure [16]. Here, catalytic vapor–liquid–solid (VLS) chemical vapor deposition (CVD) process was used to grow crystalline Si wires for solar cell applications [16]. Figure 1.3d, i shows schematically the fabrication of Si microwire arrays. Figure 1.3d, ii-iii is showing the SEM images of a microwire array.

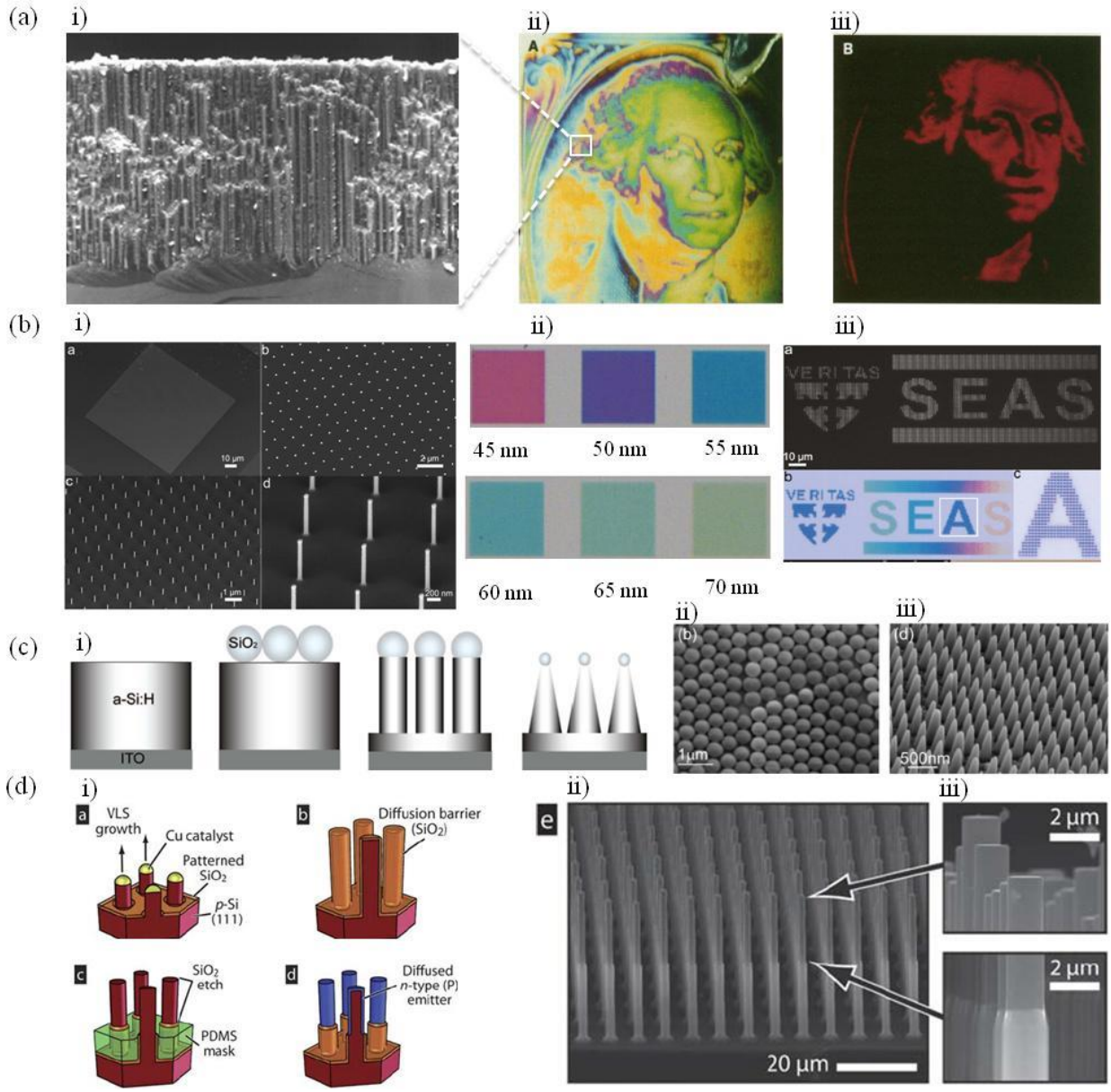

Figure 1.3: Man made nanophotonics silicon structure. (a) Porous silicon [13]. (b) Silicon nanopillar using e-beam lithography [14] (c) Nanostructure using nanosphere lithography [15]. (d) Nanowire produced using VLS-CVD growth techniques [16].

Ancient plasmonics

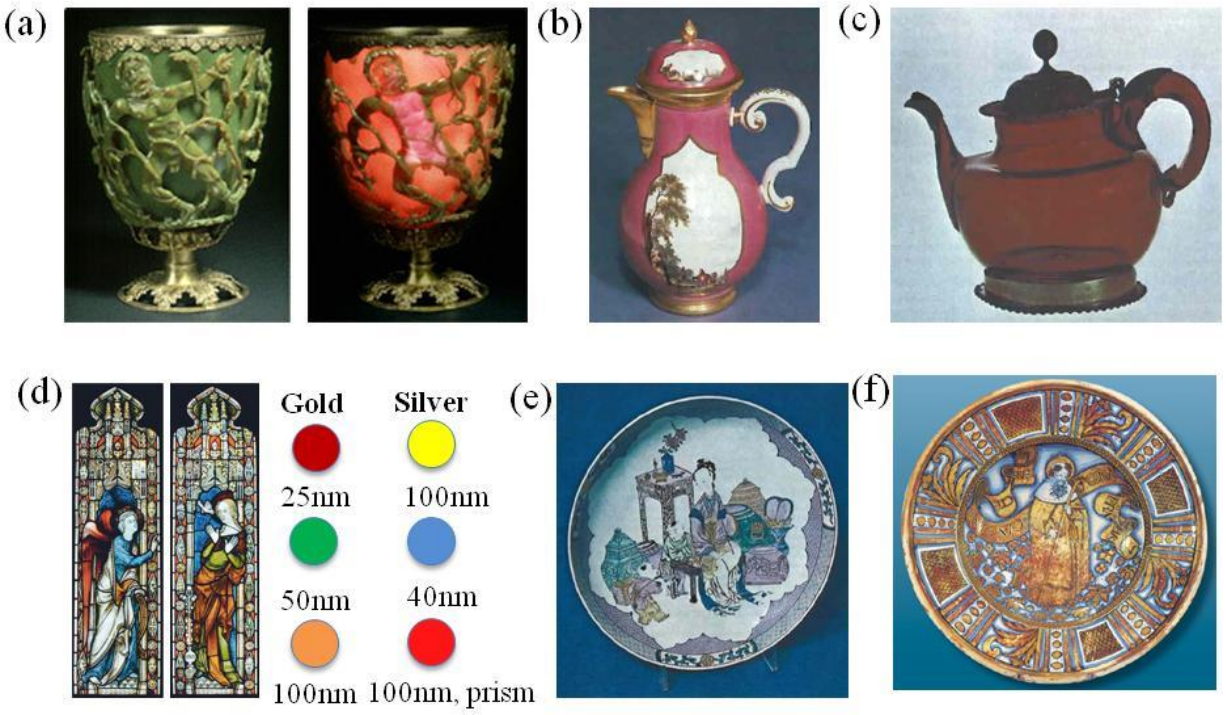

Figure 1.4: (a) Lycurgus Cup in the British Museum [17]. (b) Meissen jug, 1740 [18]. (c) Gold-Based Enamel Colours (1679-1689) [18]. (d) Stained Glass Museum, Britain [19]. (e) Gold-Based Glass and Enamel Colours in China (Famille Rose, 1723) [18]. (f) 15th and 16th centuries, Pottery of Deruta (Umbria, Italy) [18].

Nanoplasmonics, the science behind interaction of light-matter through or around nano scaled structures, is a recent phenomenon. Interestingly, the use of plasmonic structures [17] can be dated back to ancient times. The Lycurgus Cup [17] (Roman pottery – 400 AD), shown in Fig. 1.4a is a perfect example. The cup looks green, when illuminated by a white light source from outside. The cup looks red, when illuminated by the same white light source from inside. The unique feature was due to the fact that the glass contains 70nm particles of silver and gold with a ratio of about 7:3, silver nanoparticle with 70 nm diameter has strong absorption and scattering at ~ 500 nm (green region) and hence the cup looks green when illuminated from outside as it scatters most of the green light. Since, the same particle has strong absorption for green light, the cup appear red in transmission (as once it absorbs shorter wavelength it can transmit only the longer wavelengths). Some of the ancient art work as shown in Fig. 1.4b-f also

contains gold nanoparticles and hence bright red colors [18]. Figure 1.4 (d) also shows the corresponding sizes of nanoparticles to produce different colors on the ancient glass works [19].

Properties of surface plasmon

Plasmon is the density fluctuation of free electrons. When an external electromagnetic field (light wave) is incident on a metallic particle with size smaller than the incident wavelength, the incident electric field will displace the metal's electron with respect to the lattice. Thus, an electromagnetic wave will produce an oscillating electron density known as localized surface plasmon (LSP) (Fig. 1.5a). Incident electric field on a metal-dielectric interface will create a longitudinal surface charge oscillation. This will produce an electric field perpendicular to the interface which decays exponentially with distance, known as propagating surface plasmon (PSP) (Fig. 1.5b). LSP are also known as Mie Plasmon as they have electric field closely related to Mie scattering [20]. PSP are also known as Bragg plasmons and are excited through Bragg scattering off the periodicity of the surface [20]. Bragg plasmons are generally delocalized and highly dependent on the sample orientation. Mie plasmons have generally broader absorption energy spectrum than Bragg plasmons [20] and do not depend on the sample orientation (Fig. 1.5c, d).

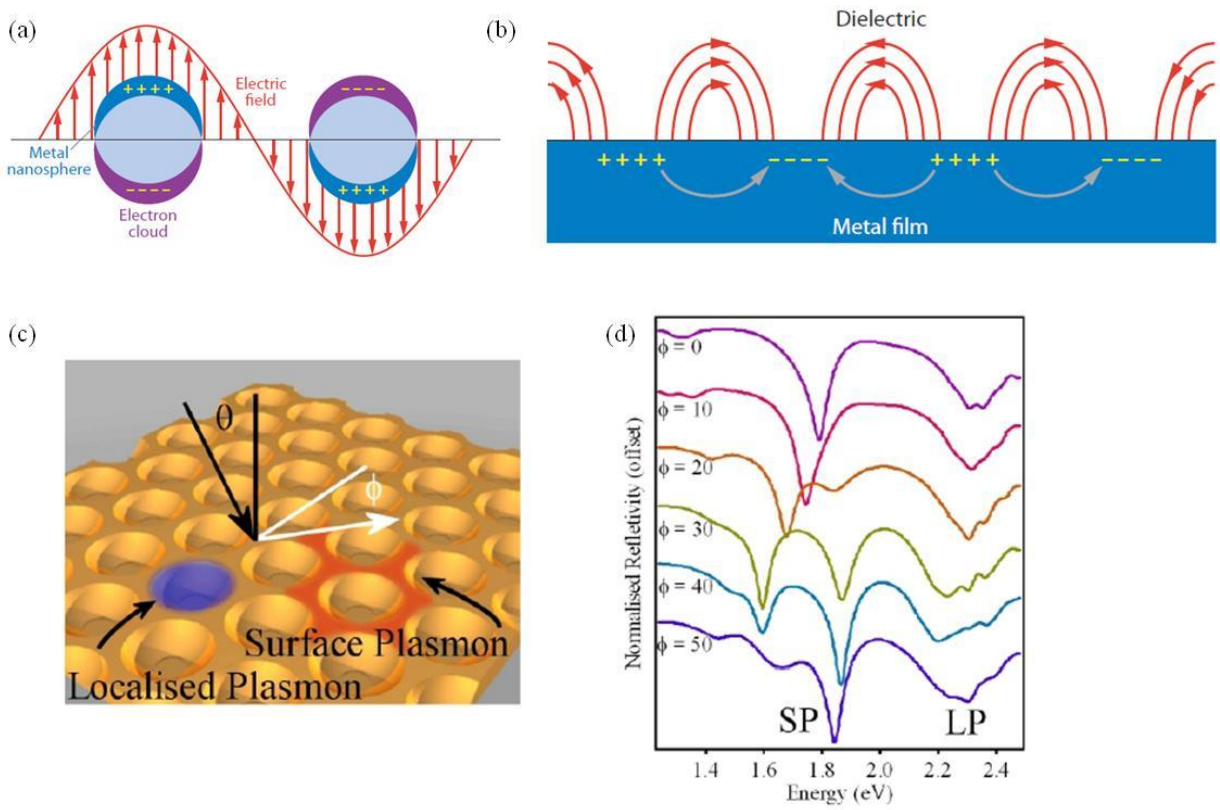

Figure 1.5: Schematic representation of (a) localized surface plasmon resonance (LSPR) (b) propagating surface plasmon (PSP) [21]. (c) Pictorial representation of LSPR and PSPR in the same substrate (nano void) (d) Reflectance data showing the occurrence of LSPR and PSPR [20].

We will now focus on the effect of size and shape of the nanostructure on the resonance spectrum. As the size of particle increases, charge screening effect (damping of electric field between nucleus and free electron) takes place. Hence, the restoring force for the incident field reduces (that is, it is easier to shift the electron clouds) and the resonance shifts to red (longer wavelength). Figure 1.6a-c clearly show that the resonance shifts due to variation of the shape of the nanostructure. Figure 1.6d-f shows the effect of variation of the gap and the direction of polarization on the resonance wavelength. If the two particles (dimer) are in close proximity then there is red shift and for complete overlap of the dimmers there is blue shift of the resonance wavelength. For longitudinal polarization the restoring force reduced by coupling to neighbor and hence resonance shifts to lower frequency (compare d with e and f). On the other hand, for transverse polarization, the restoring force increased by coupling to neighbor (as the incident field has to move more charge clouds) resonance shifts to higher frequency (Fig. 1.6e).

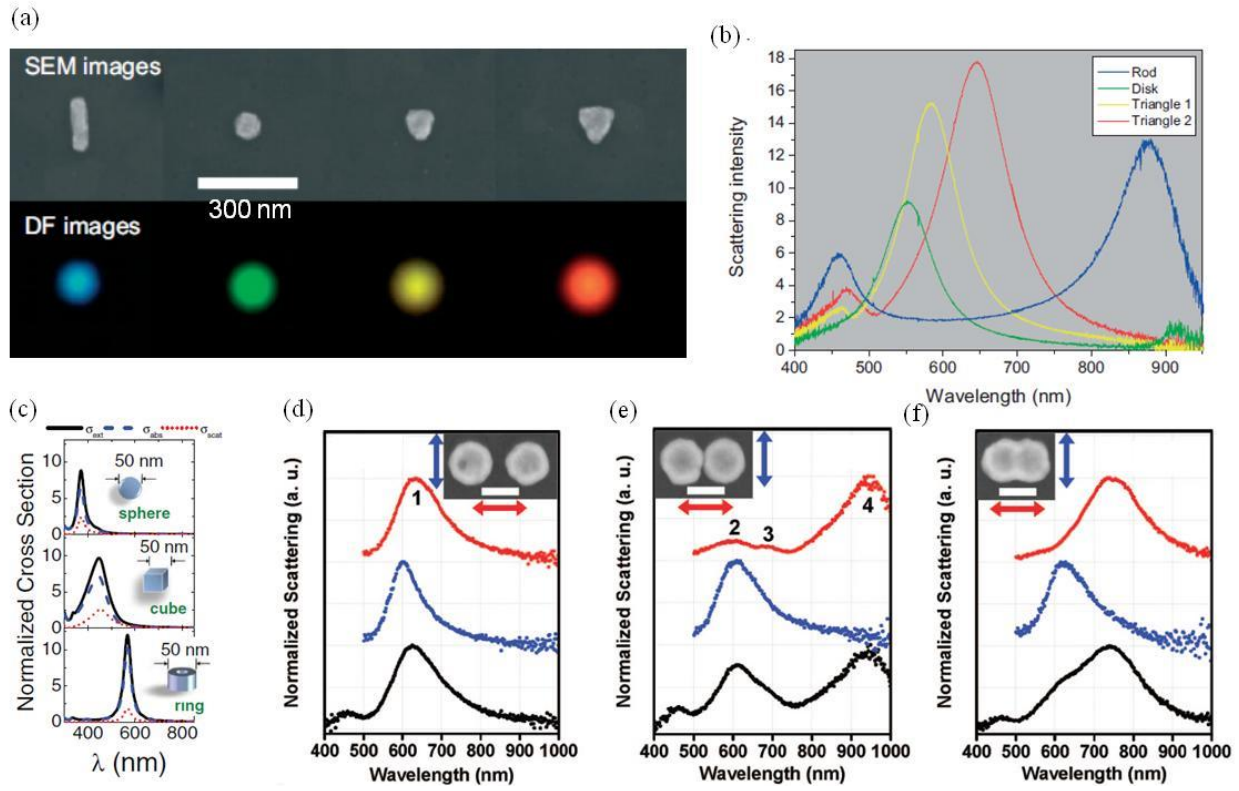

Figure 1.6: (a) SEM (top), dark-field images (bottom) of nanoparticles with different shape. The shapes are a rod, a disc, a small triangle and a big triangle from left to right. The particles were made by e-beam lithography. The thicknesses of these particles were 30 nm and the substrates were silica glass coated with 20 nm of ITO. (b) Corresponding dark-field spectra of particles shown in (a). These figures were taken from [22]. (c) Plot showing normalized extinction, absorption, and scattering cross sections for three different Ag nanoparticles in vacuum. Upper and middle panels are for a 50-nm-diameter sphere and a 50-nm-side cube, respectively. Lower panel shows the cross sections for a 20-nm high ring with inner and outer radii of 15 and 25 nm, respectively [23]. Normalized scattering spectroscopy of nanoshell dimmers (d) slightly close, (e) in close proximity, and (f) overlapped positions [24].

Examples of plasmonic structures

For plasmonic enhancement of incident optical field, various nanostructures have been proposed. Some of the commonly used nanostructures such as nanosphere, nanorods and nanopillar etc. are shown in Fig. 1.7a. The corresponding field enhancements are also shown in the same figure. A planar waveguide structure and the corresponding photoluminescence upconversion spectral map are shown in Fig. 1.7b. This clearly shows plasmons can be used for concentration of the optical energy. Figure 1.7c-f also show metallic bow-tie and grooves used for field enhancement purpose.

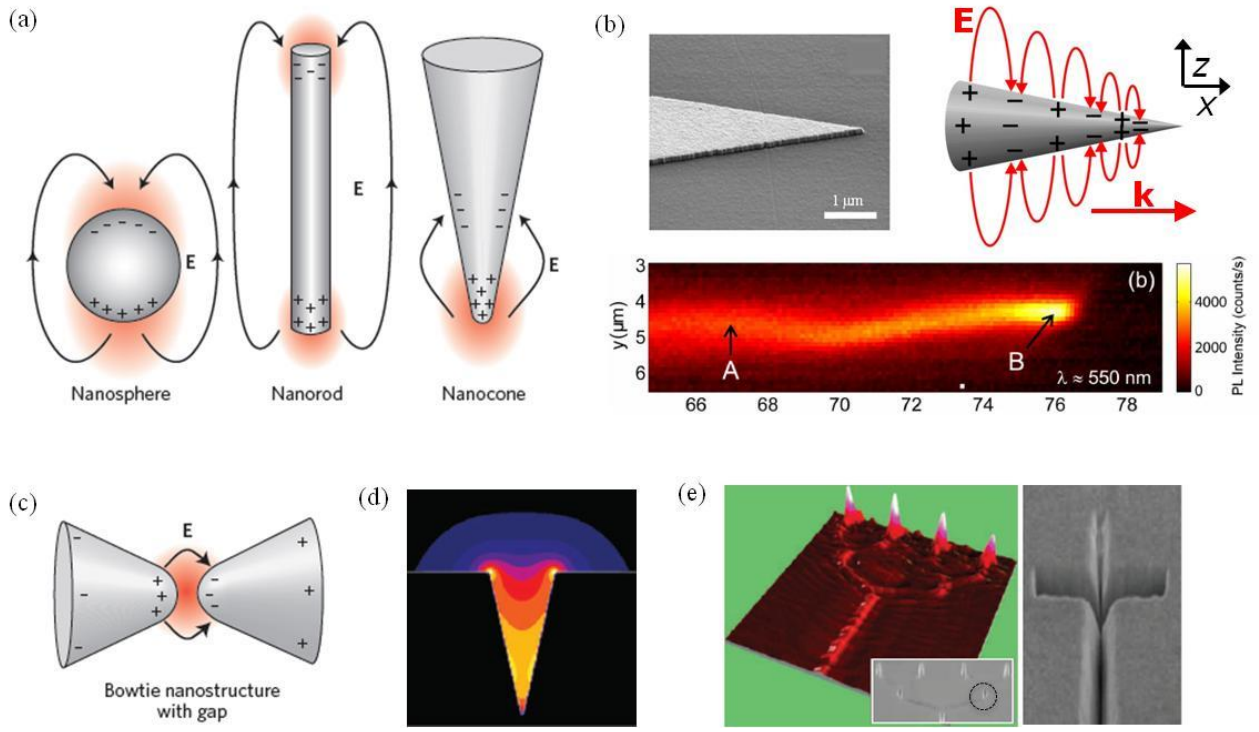

Figure 1.7: (a) Examples of some commonly used nanoplasmonics structures showing field enhancement [25]. (b) SEM image of the tapered Au waveguide on an Er-implanted sapphire substrate. Schematic of the arrangement for field enhancement is shown to the right. Map of the photoluminescence intensity near the tip of the waveguide. The sample is illuminated from the top with an excitation wavelength of 1480 nm. The upconversion due to surface plasmon is detected through the substrate (collection lens situated at the bottom) at 550 nm. The high enhancement of field at the tip is apparent [26]. (c) A commonly used metallic nanostructure, bowtie‑shaped nanoantenna, showing strong field enhancement within the nanogap [25]. Strong field enhancement inside a metallic groove (d) calculated using FDTD (e) experimental results from NSOM measurements [25].

Why nanocone structure?

Due to possibility of fabricating variety of plasmonics structures, it is imperative to discuss about the shape most suitable to us. We want to use the same structure for both nanophotonics and nanoplasmonics applications. Due to manufacturing difficulties, spherical shape is not suitable for nanophotonics applications. Nanocone structure has some advantage over nanopillar structure described as follows. The optical energy concentration at a tapered waveguide is first put forward by Stockman [27]. In a nanocone the excited surface plasmon polaritons (SPP: when surface plasmon couples with a photon, it is known as surface plasmon

polariton) generated at the base and propagating toward the tip of the plasmonic waveguide, undergoes a rapid adiabatic slowing down and asymptotic stopping at the tip due to boundary condition [27]. This phenomenon leads to a giant concentration of energy on the nanoscale. In a sense the SPP's are adiabatically transformed into localized surface plasmons (LSP's) [27]. The scheme is shown in Fig. 1.8a. The local enhancement of electric field intensity, E^2 (normalized to incident electric field intensity E_0^2) is shown in Fig. 1.8b. Enhancement of intensity as high as 1000 times compared to incident field intensity is predicted [28]. Moderate enhancement for micron size pyramid structure (Fig. 1.8c) was also predicted in reference [29]. The idea has already been successfully utilized for Tip-Enhanced Raman Spectroscopy (TERS) where considerable enhancement in Raman scattering was obtained by using a sharp metallic tip like AFM (Atomic Force Microscopy) tip over the analyte. So we can summarize the requirement for obtaining high field enhancement as follows: (i) geometric singularity or discontinuity, (ii) proper polarization and (iii) good conductor. For all of these reasons, we have fabricated nanocone/ nanopillar structures for nanophotonics and nanoplasmonics applications.

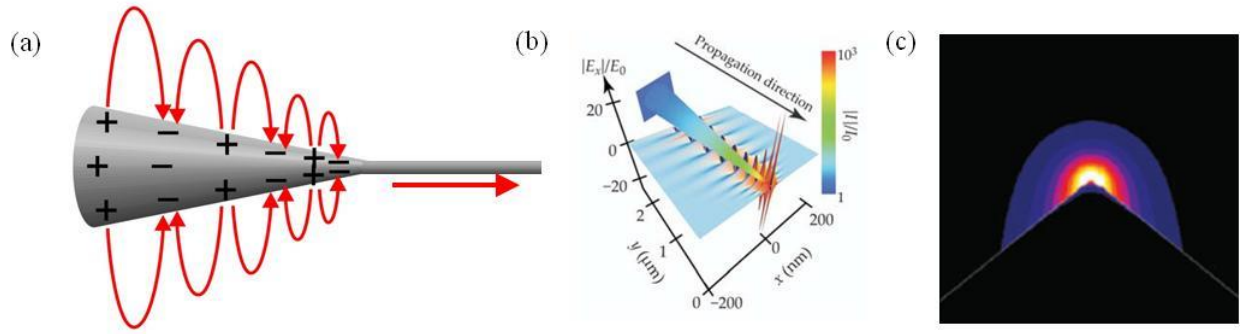

Figure 1.8: (a) Schematic of nanofocusing of optical energy in conical waveguide [27] (b) Optical field enhancement at the tip of a nanocone plasmonic structure [28] (c) Calculated field enhancement for a micron sized tip [29].

Application of nanoplasmonics

Finally, using nanoplasmonic structures we can achieve far enhanced sensitivity in detection by focusing the optical energy in a confined spot [30]. Figure 1.9a, b schematically represents hydrogen sensing using triangular plasmonic structure [30]. Figure 1.9a shows pictorially hydrogen (shown in red) sensing with a single palladium nanoparticle. Due to weak scattering from palladium nanoparticle, the scattering spectrum is damped and broad. Hence, the hydrogen is barely detectable on only palladium nanoparticle [30]. Figure 1.9b depicts hydrogen sensing using a nanoplasmonic antenna. The same palladium nanoparticle is now placed at the focusing distance of the plasmonic antenna, which has a strong scattering. Hence, the change in scattering spectrum can be readily detected due to adsorption of hydrogen atom [30]. As another example, the extraordinary sensitivity of nanoplasmonic structure is demonstrated in Fig. 1.9c-f by directly detecting single monolayer of biomolecules with naked eye [31].

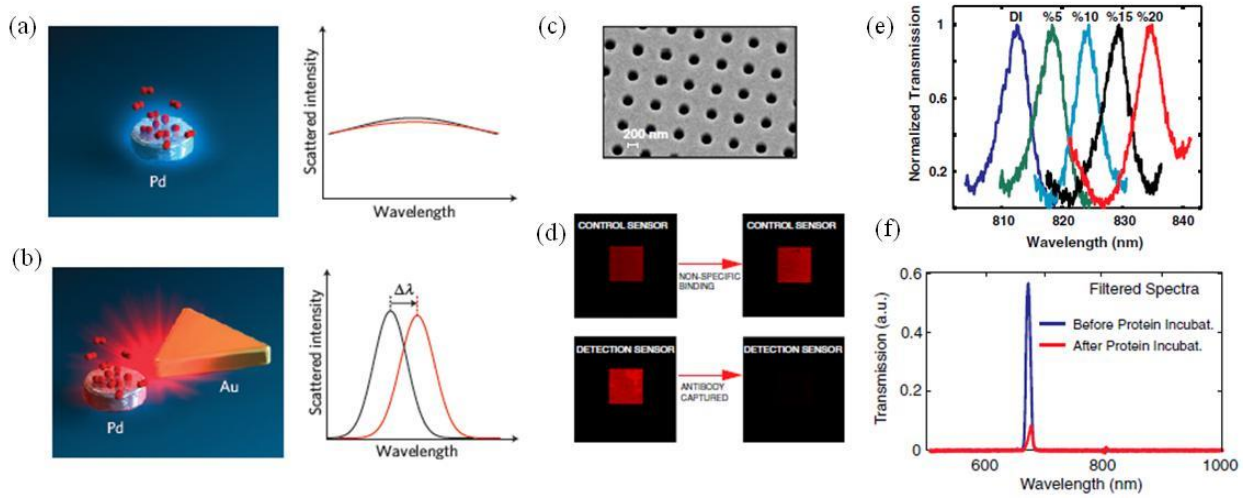

Figure 1.9: (a, b) Hydrogen detection using nanoplasmonic structure [30] (c) SEM image of the nano-hole sensor structure [31]. (d) CCD images of the transmitted light obtained from detection and control sensors. Capturing of the antibody causes a dramatic reduction of the transmitted light intensities through the detection sensors. (e) Resonance shift of transmission spectra with different NaCl concentrations. (f) Transmission spectra corresponding to figure shown in (d).

References

[1] A. L. Ingram and A. R. Parker, "A review of the diversity and evolution of photonic structures in butterflies, incorporating the work of John Huxley (The Natural History Museum, London from 1961 to 1990)," *Philosophical Transactions of the Royal Society B-Biological Sciences,* vol. 363, pp. 2465-2480, JUL 27 2008, 2008.

[2] J. Zi, X. D. Yu, Y. Z. Li, X. H. Hu, C. Xu, X. J. Wang, X. H. Liu and R. T. Fu, "Coloration strategies in peacock feathers," *Proc. Natl. Acad. Sci. U. S. A.,* vol. 100, pp. 12576-12578, OCT 28 2003, 2003.

[3] G. S. Watson and J. A. Watson, "Natural nano-structures on insects - possible functions of ordered arrays characterized by atomic force microscopy," *Appl. Surf. Sci.,* vol. 235, pp. 139-144, JUL 31 2004, 2004.

[4] A. R. Parker and H. E. Townley, "Biomimetics of photonic nanostructures," *Nature Nanotechnology,* vol. 2, pp. 347-353, JUN 2007, 2007.

[5] A. R. Parker, "The diversity and implications of animal structural colours," *J. Exp. Biol.,* vol. 201, pp. 2343-2347, AUG 1998, 1998.

[6] K. Autumn, Y. A. Liang, S. T. Hsieh, W. Zesch, W. P. Chan, T. W. Kenny, R. Fearing and R. J. Full, "Adhesive force of a single gecko foot-hair," *Nature,* vol. 405, pp. 681-685, JUN 8 2000, 2000.

[7] W. R. Hansen and K. Autumn, "Evidence for self-cleaning in gecko setae," *Proc. Natl. Acad. Sci. U. S. A.,* vol. 102, pp. 385-389, JAN 11 2005, 2005.

[8] H. J. Ensikat, P. Ditsche-Kuru, C. Neinhuis and W. Barthlott, "Superhydrophobicity in perfection: the outstanding properties of the lotus leaf." *Beilstein Journal of Nanotechnology,* vol. 2, pp. 152-61, 2011, 2011.

[9] P. S. J. Russell, "Photonic crystals: Molding the flow of light - Joannopoulos,JD, Meade,RD, Winn,JN," *Nature,* vol. 381, pp. 290-290, MAY 23 1996, 1996.

[10] N. I. Zheludev, "What diffraction limit?" *Nature Materials,* vol. 7, pp. 420-422, JUN 2008, 2008.

[11] [Anonymous], "Beyond the diffraction limit," *Nature Photonics,* vol. 3, pp. 361-361, JUL 2009, 2009.

[12] S. R. P. Pavani, M. A. Thompson, J. S. Biteen, S. J. Lord, N. Liu, R. J. Twieg, R. Piestun and W. E. Moerner, "Three-dimensional, single-molecule fluorescence imaging beyond the diffraction limit by using a double-helix point spread function," *Proc. Natl. Acad. Sci. U. S. A.,* vol. 106, pp. 2995-2999, MAR 3 2009, 2009.

[13] V. V. Doan and M. J. Sailor, "Luminescent Color Image Generation on Porous Silicon," *Science,* vol. 256, pp. 1791-1792, JUN 26 1992, 1992.

[14] K. Seo, M. Wober, P. Steinvurzel, E. Schonbrun, Y. Dan, T. Ellenbogen and K. B. Crozier, "Multicolored Vertical Silicon Nanowires," *Nano Letters,* vol. 11, pp. 1851-1856, APR 2011, 2011.

[15] J. Zhu, Z. Yu, G. F. Burkhard, C. Hsu, S. T. Connor, Y. Xu, Q. Wang, M. McGehee, S. Fan and Y. Cui, "Optical Absorption Enhancement in Amorphous Silicon Nanowire and Nanocone Arrays," *Nano Letters,* vol. 9, pp. 279-282, JAN 2009, 2009.

[16] M. D. Kelzenberg, D. B. Turner-Evans, M. C. Putnam, S. W. Boettcher, R. M. Briggs, J. Y. Baek, N. S. Lewis and H. A. Atwater, "High-performance Si microwire photovoltaics," *Energy & Environmental Science,* vol. 4, pp. 866-871, MAR 2011, 2011.

[17] F. E. Wagner, S. Haslbeck, L. Stievano, S. Calogero, Q. A. Pankhurst and P. Martinek, "Before striking gold in gold-ruby glass," *Nature,* vol. 407, pp. 691-692, OCT 12 2000, 2000.

[18] Anonymous Available: www.mpikg.mpg.de/pdf/KolloidChemie/Scripte/metnanopart.ppt.

[19] Anonymous Available: www.mpikg.mpg.de/pdf/KolloidChemie/Scripte/metnanopart.ppt.

[20] T. A. Kelf, "Light-Matter Interactions on Nano-Structured Metallic Films," 2006.

[21] X. Lu, M. Rycenga, S. E. Skrabalak, B. Wiley and Y. Xia, "Chemical Synthesis of Novel Plasmonic Nanoparticles," *Annu. Rev. Phys. Chem.,* vol. 60, pp. 167-192, 2009, 2009.

[22] W. A. Murray and W. L. Barnes, "Plasmonic materials," *Adv Mater,* vol. 19, pp. 3771-3782, NOV 19 2007, 2007.

[23] V. Giannini, A. I. Fernandez-Dominguez, Y. Sonnefraud, T. Roschuk, R. Fernandez-Garcia and S. A. Maier, "Controlling Light Localization and Light-Matter Interactions with Nanoplasmonics," *Small,* vol. 6, pp. 2498-2507, NOV 22 2010, 2010.

[24] J. B. Lassiter, J. Aizpurua, L. I. Hernandez, D. W. Brandl, I. Romero, S. Lal, J. H. Hafner, P. Nordlander and N. J. Halas, "Close encounters between two nanoshells," *Nano Letters,* vol. 8, pp. 1212-1218, APR 2008, 2008.

[25] S. Kawata, Y. Inouye and P. Verma, "Plasmonics for near-field nano-imaging and superlensing," *Nature Photonics,* vol. 3, pp. 388-394, JUL 2009, 2009.

[26] E. Verhagen, A. Polman and L. Kuipers, "Nanofocusing in laterally tapered plasmonic waveguides," *Optics Express,* vol. 16, pp. 45-57, JAN 7 2008, 2008.

[27] M. I. Stockman, "Nanofocusing of optical energy in tapered plasmonic waveguides," *Phys. Rev. Lett.,* vol. 93, pp. 137404, SEP 24 2004, 2004.

[28] M. I. Stockman, "Nanoplasmonics: The physics behind the applications," *Phys Today,* vol. 64, pp. 39-44, FEB 2011, 2011.

[29] E. Moreno, F. J. Garcia-Vidal, S. G. Rodrigo, L. Martin-Moreno and S. I. Bozhevolnyi, "Channel plasmon-polaritons: modal shape, dispersion, and losses," *Opt. Lett.,* vol. 31, pp. 3447-3449, DEC 1 2006, 2006.

[30] N. Liu, M. L. Tang, M. Hentschel, H. Giessen and A. P. Alivisatos, "Nanoantenna-enhanced gas sensing in a single tailored nanofocus," *Nature Materials*, vol. 10, pp. 631-636, AUG 2011, 2011.

[31] A. A. Yanik, A. E. Cetin, M. Huang, A. Artar, S. H. Mousavi, A. Khanikaev, J. H. Connor, G. Shvets and H. Altug, "Seeing protein monolayers with naked eye through plasmonic Fano resonances," *Proc. Natl. Acad. Sci. U. S. A.*, vol. 108, pp. 11784-11789, JUL 19 2011, 2011.

CHAPTER 2

FABRICATION OF NANOPHOTONICS AND PLASMONICS DEVICES

Introduction

Although the data processing is performed by Si based electronics, the data transferring is done optically primarily using III-V semiconductors [1]. This is due to the fact that Si is a poor light emitter because of its indirect band gap nature. The problem is going to be exacerbated with the information technology industry moving towards optical interconnects for chip-to-chip communication [2]. Hence, silicon-based optoelectronics devices are needed for easy integration to silicon-based circuits. It was proposed that one dimensional nanostructure will provide the additional momentum for the wavevector in Si to make it emit light at room temperature. Besides nanophotonics device with proper design can also be transformed in to plasmonics devices after metal deposition.

For nanophotonics and plasmonics applications generally optical diffraction limited structures are required (dimension ~ $\lambda/2$, where λ is the incident wavelength). The typical dimensions are < 300 nm. Recently many different types of one-dimensional nanostructures, such as nanowhisker, nanorod, nanowire, nanopillar, nanocone, nanotip, nanoneedle, have been proposed for the applications in electronics, photonics, energy conversion and storage devices. Here, mainly nanostructures made on silicon will be introduced and attention will be focused on nanopillar or nanocone structures due to their direct applications to sensing and energy harvesting devices. For plasmonics structure, we will describe nanopillar/nanocone and nanohole based device fabrication. The fabrication steps of such devices involve either bottom-up approaches such as synthesis or growth process or top-down approaches such as lithography or etching process. Some of the techniques used for making nanopillar structures are chemical etching, electron beam lithography, nanosphere lithography, laser ablation process, and catalytic chemical growth.

Nanophotonics device fabrication

Figure 2.1a shows a SEM image of nanopillar silicon produced by electrochemical etching of the silicon wafer. This particular class of structures is also known as porous silicon. Crystalline silicon can be etched in aqueous solution of ethanol and hydrofluoric acid (HF) electrolytes to produce porous silicon [3]. Another chemical based process to achieve silicon nanopillar is the low cost metal assisted chemical etching (MacEtch) where silicon is etched in a solution of H_2O_2 and HF catalyzed by metal (Au or Ag). Figure 2.1b shows schematically a MacEtch process to form pillar array with metal (Au) Mesh as catalyst. The corresponding SEM of the etched sample is also shown (aspect ratio ~ 93). With this process high aspect ratio nanopillar are feasible to be produced quickly [4].

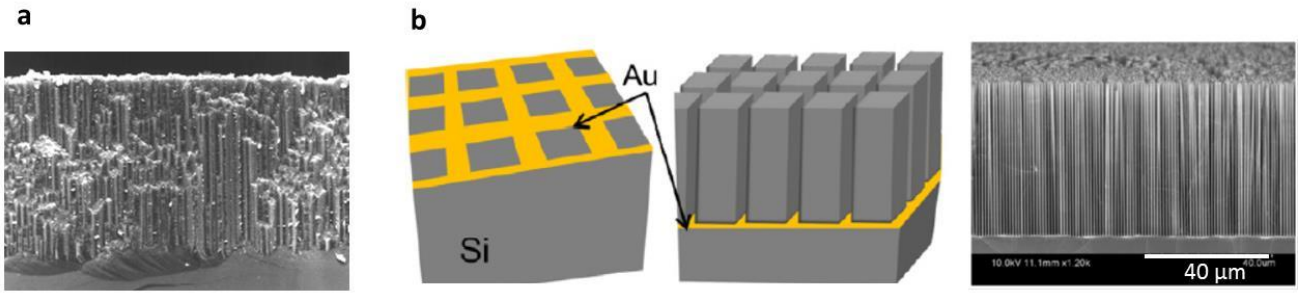

Figure 2.1: Silicon nanopillar produced using chemical etching. (a) Porous silicon, (b) Schematic of MacEtch process with gold mesh as catalyst. The Au Mesh grid pattern goes down into the substrate (Si) as the etching progresses leaving Si pillars standing. SEM image of an array of Si nanopillars with diameter of 550 nm, height of 51 µm obtained using MacEtch process. Image reproduced from [4].

Electron beam lithography (EBL) can be used to obtain silicon nanopillar with sub-100 nm resolution. Figure 2.2a shows example of different diameter of Si nanowire fabricated using e-beam lithography techniques [5]. However, the throughput of EBL process is low as it relies on serial point-by-point electron-beam writing method. This limits the maximum area to around 100 µm x 100 µm that can normally be structured using EBL. In order to overcome this problem, nanosphere lithography was invented where large area colloidal nanoparticles are first self-assembled on large area (4-inch wafer scale has been demonstrated) [6] and then etched using conventional reactive ion-etching (RIE) process to make nanopillars. Figure 2.2b shows schematically the self-assembly, size reduction (to control the diameter of the pillar), RIE, and

particle removal process. The corresponding SEM is shown below each of the figures. Besides the above mentioned techniques, other top-down methods such as femtosecond laser induced plasma [7], ablation of silicon surface with a series of femto second laser pulses, in the presence of a sulfur containing gas [8, 9] has been employed to get silicon nanopillars.

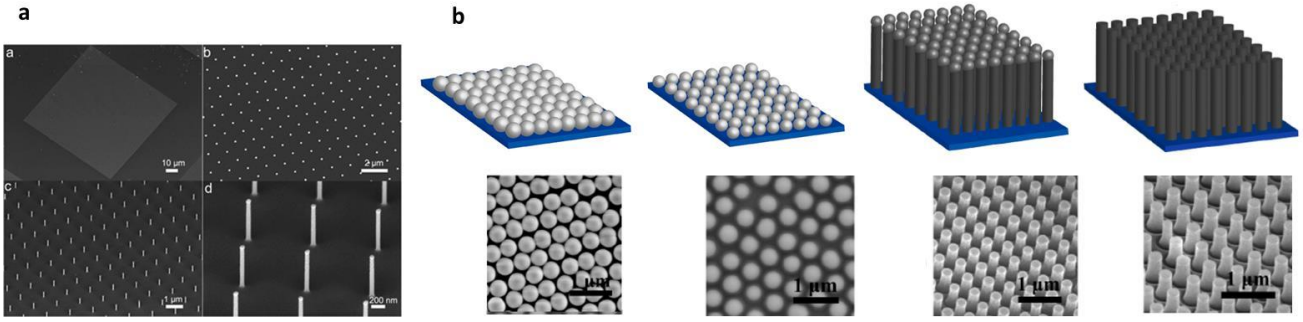

Figure 2.2: (a) Electron beam lithography [5], and (b) Nanosphere lithography based process to make silicon nanopillars [6].

Recently a bottom-up manufacturing technique has been introduced to produce micropillar structure [10]. Here, catalytic vapor–liquid–solid (VLS) chemical vapor deposition (CVD) process was used to grow crystalline Si wires for solar cell applications [10]. Figure 2.3 (d, i) shows schematically the fabrication of Si microwire arrays. Figure 2.3 (d, ii-iii) is showing the SEM images of a microwire array.

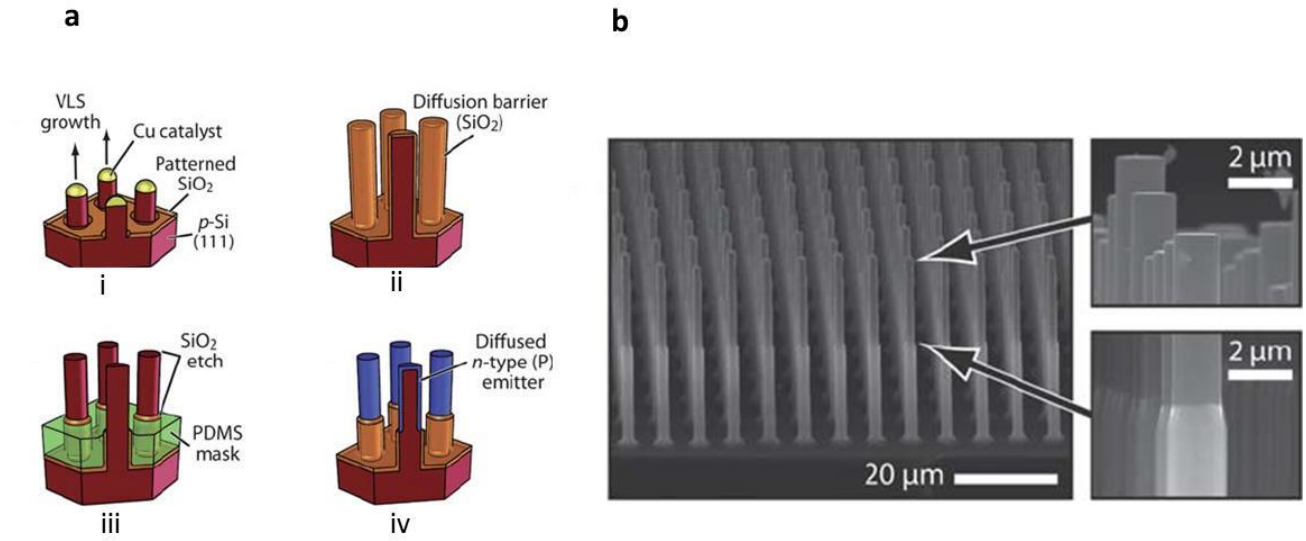

Figure 2.3: Bottom-up approach to make silicon nanopillars. (a) Schematic figure showing (i) VLS growth of p-type Si nanopillar, (ii) removal of catalyst and thermal-oxide diffusion-barrier growth, (iii) selectively removing oxide barrier using a polymer mask, (iv) thermal diffusion of radial p–n junctions. (b) SEM images of the nanopillar array with 45^0 tilt (left) and cross-section (right) [10].

The motivation behind manufacturing nanocone/ nanopillar structures ranges from potential applications in sensing, energy and light emitting devices. Particularly for photovoltaic applications, in order to increase conversion efficiency, near zero reflection over a broad spectral and angular range is desired. Usually for Si solar cell chemical (anisotropic) etching based surface texturing is employed which greatly enhances the optical path length of the incident light and reduces surface reflection. However, these techniques are not applicable to thin film silicon solar cells and are less effective for more widely used multi-crystalline silicon wafers. So, there is a need for developing new manufacturing techniques capable of making structures on any type of silicon with varying thicknesses.

We have developed a manufacturing technique to create nanostructures by combining top-down and bottom-up nanofabrication approach called simultaneous plasma enhanced reactive ion synthesis and etching (SPERISE) [11]. By using SPERISE technique high aspect ratio nanocone/ nanopillar structure can be made on any type of silicon (crystalline, polycrystalline, amorphous). The process is compatible with wafer-scale (4") manufacturing. SPERISE process uses a mixture of HBr and O_2 gas in Inductively Coupled Plasma (ICP) machine to perform the reactive ion etching (RIE) process. During etching, initially a nano-mask made of silicon oxybromide natually forms and then HBr gas etches the unmasked silicon substrate. Since HBr has a high etching selectivity of silicon to oxide (200:1), high-aspect-ratio nanocone structures are formed.

Formation of nanostructure will cause surface modification in silicon, which generally leads to a black appearance. This class of materials is also known as "black silicon", due to low optical reflectivity and high absorption from visible to infrared wavelength range. Black silicon (b-Si) was first produced by reactive ion etching (RIE) in fluorine, bromine and chlorine plasmas [12, 13]. Besides the above mentioned techniques, other methods such as femtosecond laser induced plasma [7], ablation of silicon surface with a series of femto second laser pulses, in the presence of a sulfur containing gas [8, 9], deep UV lithography method [14], using nanosphere lithography with different sizes of spheres [15], local metal-catalyzed wet chemical etching [16] and metal assisted dry etching [17] has been used to produce b-Si. Though the exact mechanism of formation of b-Si is still unknown, it is widely believed that the formation of nanopillars during RIE is due to a local variation of the Si etch rate [17]. This variation in etching rate can be

caused by the Si surface itself, for example an inhomogeneous oxide layer or incompletely removed native oxide [17]. Normally halogen-based plasmas are used for the dry etching of silicon due to their high etch rates. F-based plasmas such as SF_6 are generally used for fast isotropic etching [18]. However, Sulfur is known to introduce impurity states causing recombination [19] of the generated electron-hole pairs and hence detrimental to photovoltaic based applications. Further, Cl- and Br-based plasmas such as Cl_2 and HBr can also be used to achieve anisotropic etching profiles [20]. In the present work, we have used HBr based dry etching process to produce b-Si.

Silicon nanostructure formation

The nanocone b-Si structures are fabricated by SPERISE process [11]. First, the native oxide layer is removed from the single crystal silicon wafer (4") using a wet etch process (10:1 buffered oxide etching for 1 min). Then the polysilicon substrate is etched by HBr and oxidized by O_2 simultaneously. PlasmaTherm SLR-770 Inductively Coupled Plasma (ICP) Reactive Ion Etcher (RIE) was used for the etching process (Fig. 2.4). The temperature was set to 40 ^{o}C, the throat pressure was 20 mTorr, the RF power was 200 W and the etching time was 6 min during the fabrication process. The HBr flow rate was 20 sccm whereas the O_2 flow rate was set to 8 sccm.

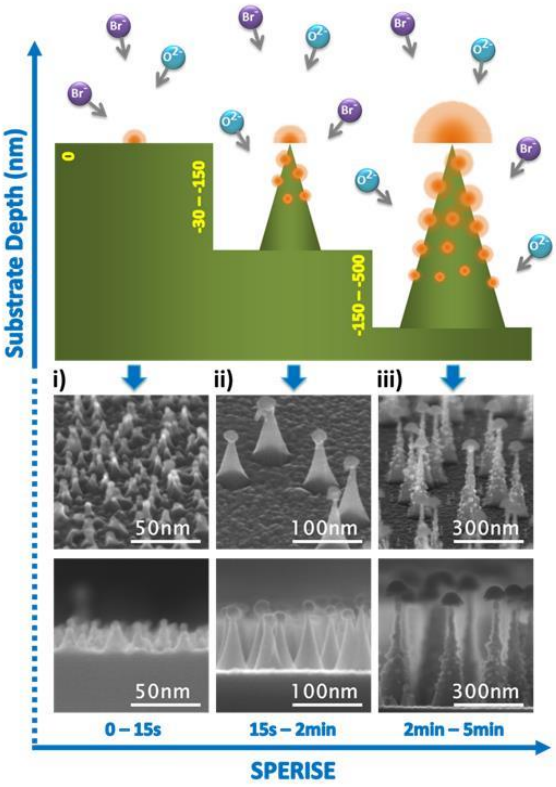

Figure 2.4: Mechanism of formation of nanocone structure using SPERISE process. Image adapted from [11].

SEM and TEM Characterization

Figure 2.5a shows the scanning electron micrograph (SEM) of the b-Si right after etching taken at 30^0 tilt angle. A close-up view showed in Fig. 2.5b revealed that the nanocones are covered with heavy oxide (shown with red arrows) during etching process. Figure 2.5c shows a cross-sectional SEM image of the b-Si after removal of heavy oxide layers using 10:1 buffered oxide etching process. Figure 2.5d shows typical TEM image of a nanocone. From the TEM image, we did not observe any appreciable damage to the crystal structure due to etching process. The optical characterization of device will be presented in Chapter 3.

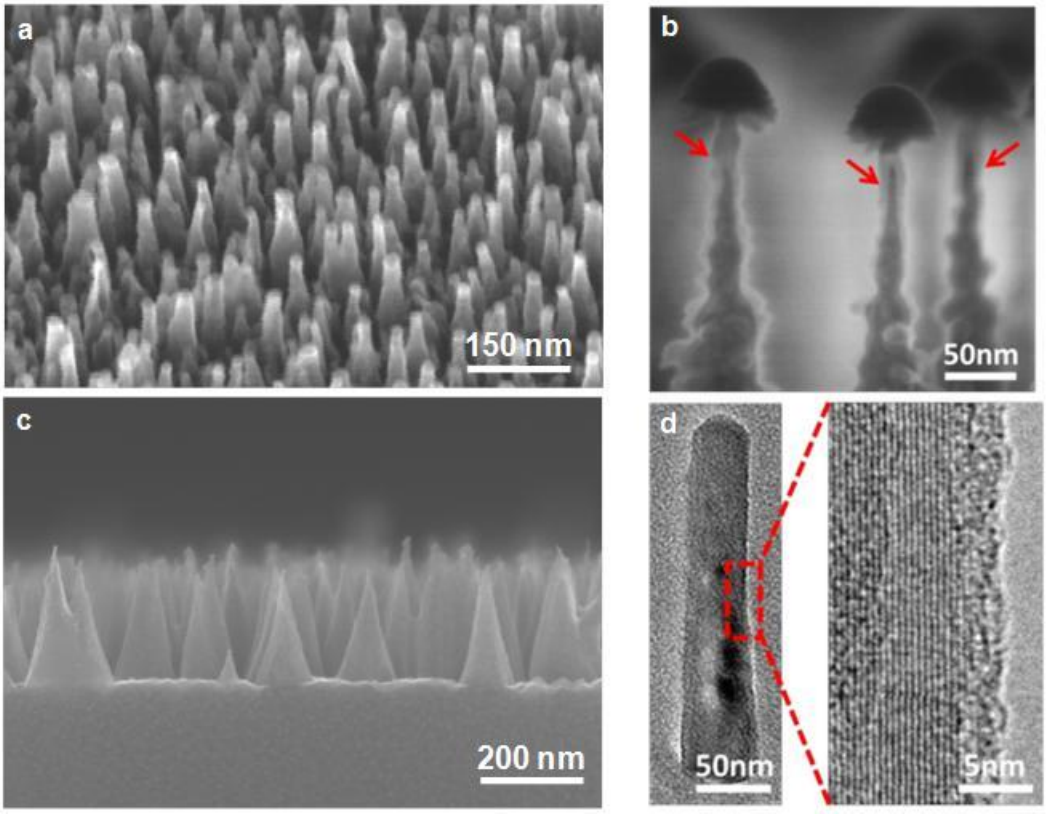

Figure 2.5: (a) 30^0 angle SEM image of the b-Si (b) High-resolution SEM of nanopillar before removal of the heavy oxide layer (shown with red arrows) (c) Cross-sectional SEM of the b-Si after removal of oxides (d) TEM image of nanopillar.

Nanofabrication of plasmonics structures

Plasmonics structures are free standing noble-metal structures or metal deposited over nanophotonics structures. Plasmonics structures have attracted attentions in recent years due to its capability to guide and manipulate light at nanoscale dimensions. Different metal nanoparticle shapes such as spheres, rods, cubes, boxes, bowls, rice, pyramids, and cages (Fig. 2.6) have been achieved through chemical synthesis process. Although solution based methods are scalable, achieving uniformity in size and shape and controlling the space between the structures within a matrix is still a challenge [21].

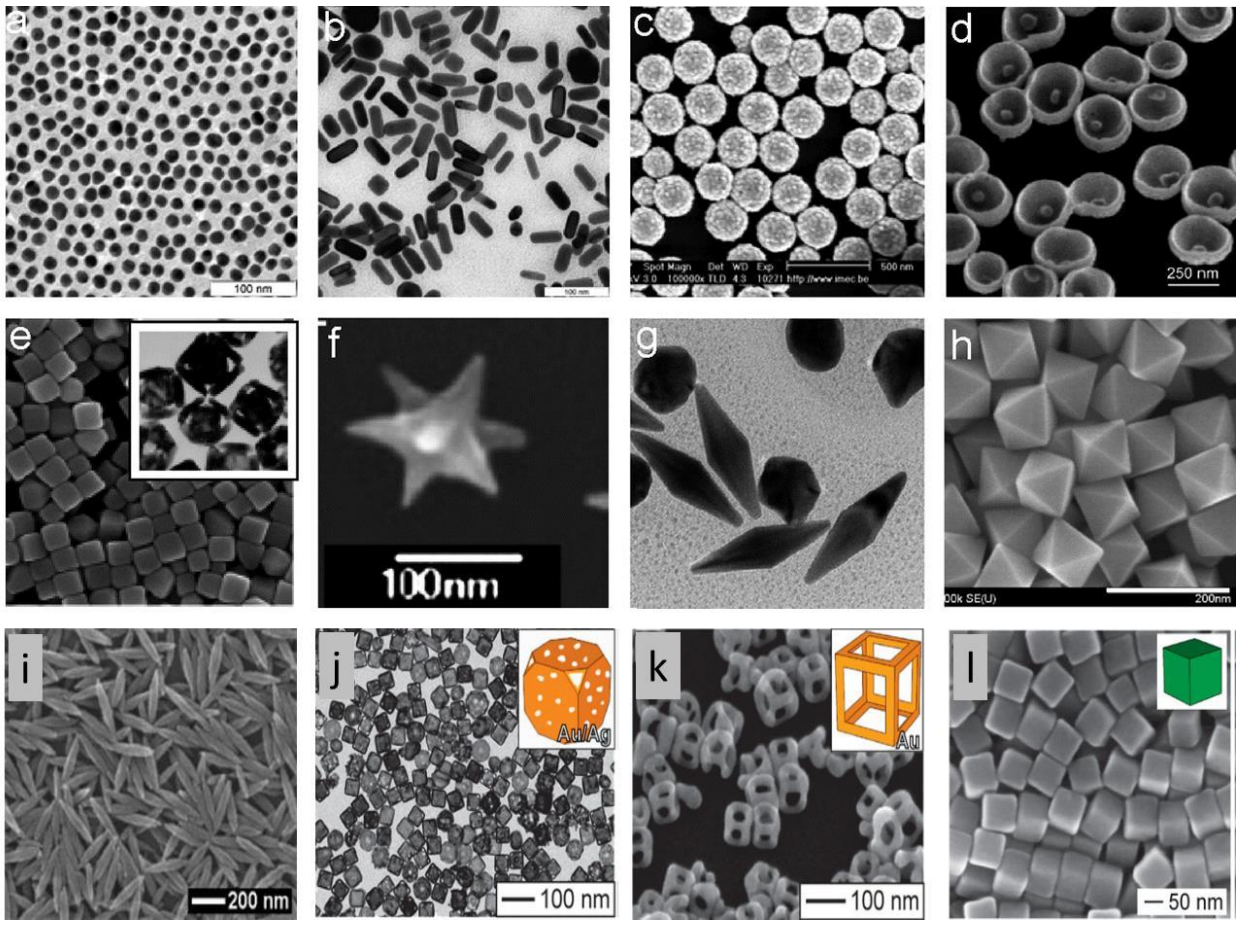

Figure 2.6: TEM images of 15 nm colloidal gold (a),15 x 50 nm gold nanorods (b),160 (core)/17 (shell)nm silica/gold nanoshells (c,SEM), 250nm Aunanobowls with 55Au seed inside (d), silver cubes and gold nanocages (insert)(e), nanostars (f), bipyramids (g), octahedral (h), nanorice (i), nanocage (j), nanoframe (k), and nanocube (l). Images (a–h) are adapted from Refs. [22]. Images (i-l) are adapted from [23].

Direct writing methods such as electron beam lithography (EBL) have also been used to generate plasmonic nanostructure. Figure 2.7 shows the popular Lena image reproduced using plasmonic nanodisc design created using EBL. Using EBL a resolution of < 10 nm can be achieved [24] and is mainly limited by electron scattering in the polymer matrix and swelling of the resist in the developer solution. Additional processing steps such as metal evaporation and photoresist lift-off are required for completing the fabrication of plasmonic metal nanostructures, which further limit the resolution.

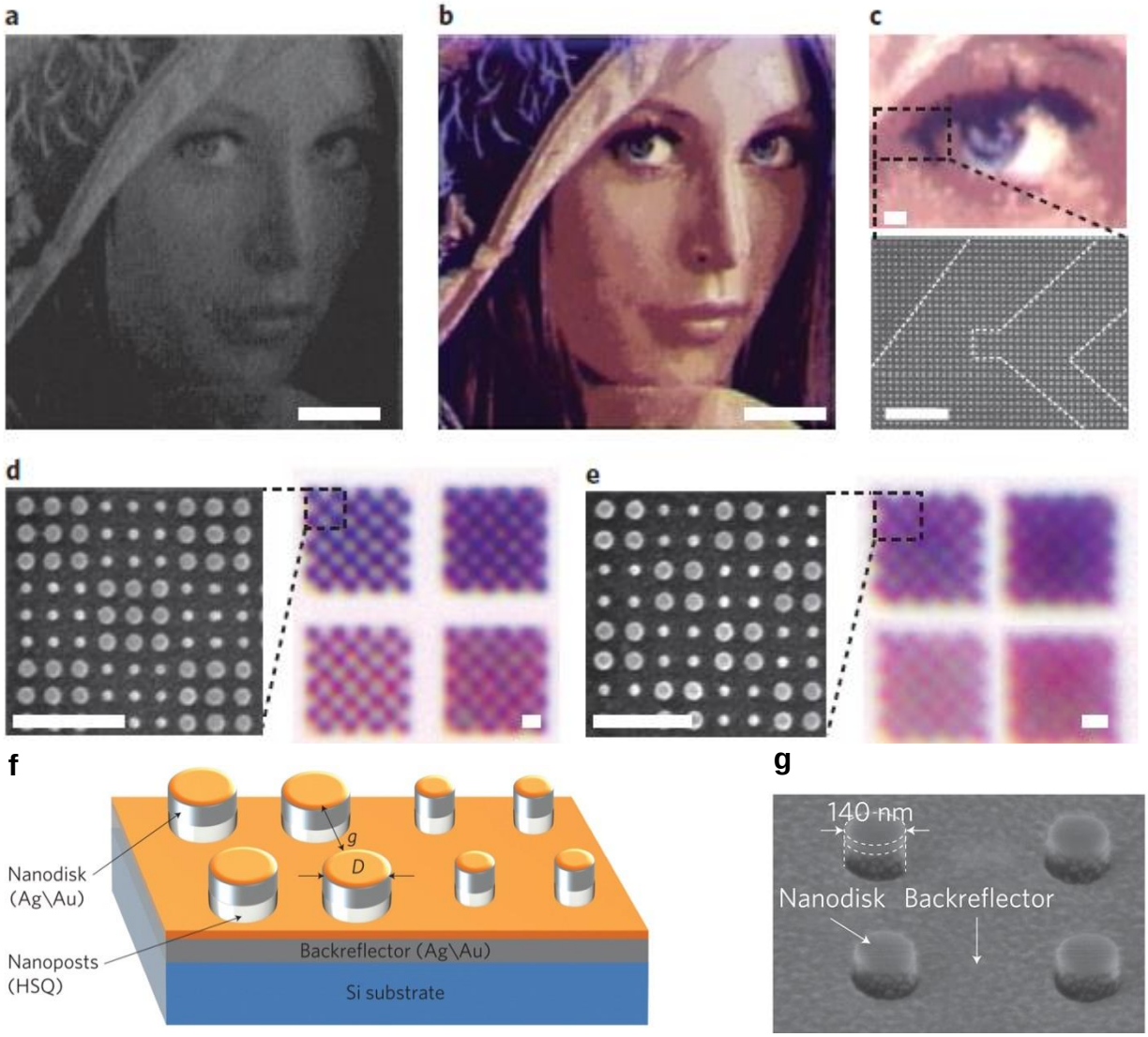

Figure 2.7: Producing Lena image using plasmonic nanodisc created using EBL. a,b, Optical micrographs of the Lena image before (a) and after (b) metal deposition. c, Details of optical image and the corresponding SEM image. d,e, Resolution test patterns. f,g, Design and SEM of the substrate after metal deposition. Scale bars: 10 μm (a, b), 1 μm (c), 500 nm (d, e). Images adapted from [25].

Another popular method of creating plasmonic nanostructure is focused ion beam (FIB) milling. Figure 2.8 shows some examples of plasmonic structures created using FIB.

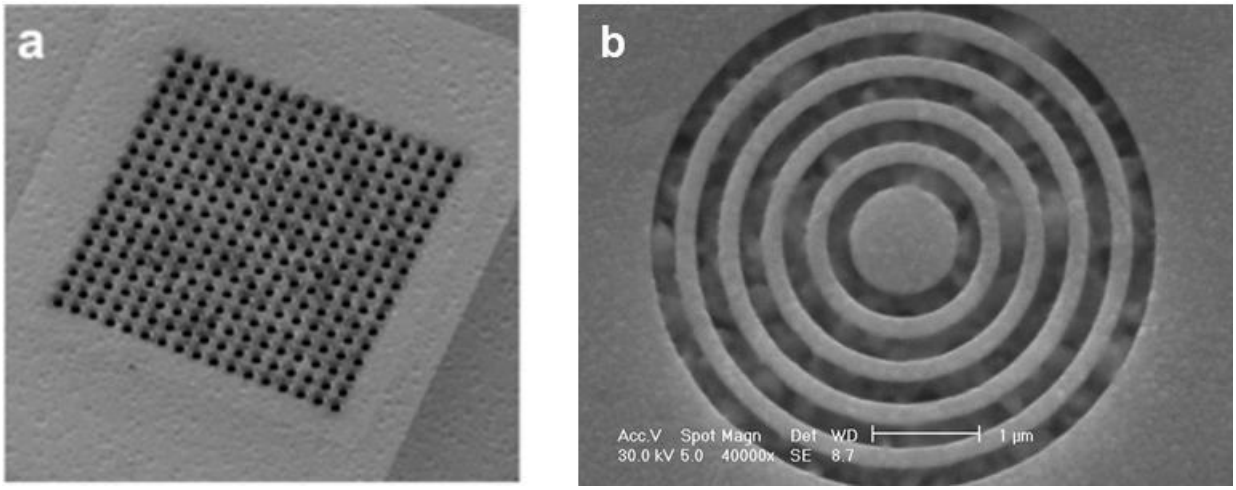

Figure 2.8: Examples of plasmonics structures created using FIB. (a) Periodic nanohole arrays in Ag film (period 600 nm) used for extraordinary optical transmission effects [26]. (b) Metallic bull's eye structure for channeling light from the concentric rings into the central, subwavelength aperture. The groove periodicity is 500 nm. Images are adapted from [27].

A shadow mask type deposition or stencil lithography is another method of creating plasmonic structure (Fig. 2.9). Typically the nanostructures free-standing mask is made up of Si or Si_3N_4 film perforated with the desired patterns. Stencil lithography is particularly useful for patterning substrates that are not compatible with standard photoresist processing [27]. For example, substrates coated with organic semiconductors or polymers which may not withstand the chemical and developing process of optical lithography and lift-off. Another case where stencil lithography would be useful is when the adhesion between a deposited metal film and the substrate is poor, which may delaminate the metal film during development.

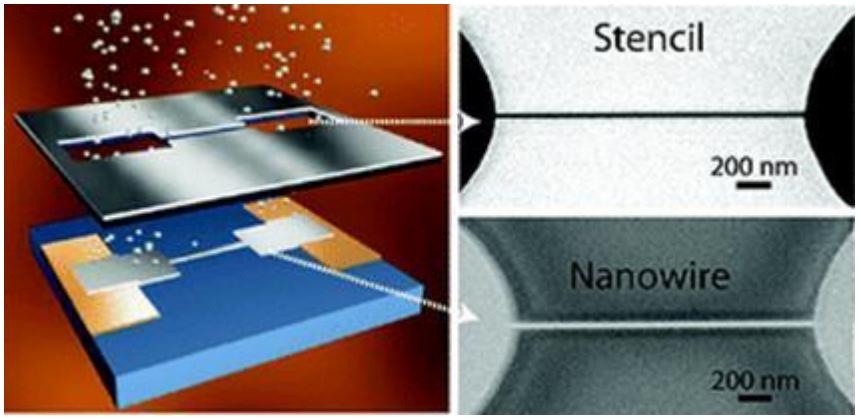

Figure 2.9: Stencil lithography. Image adapted from [28].

Achieving good film quality of plasmonic surfaces is one of the problems in previously discussed nanofabrication processes. For example, the metal films using electron beam evaporation and sputtering methods are inherently polycrystalline. The rough grain boundaries in polycrystalline noble metal surfaces fabricated by e-beam evaporation and sputtering processes also introduce undesirable scattering and ohmic losses in the plasmonic devices. In order to produce ultrasmooth plamonic surfaces, a nanomanufacturing method called template stripping (Fig. 2.10) has been introduced [29]. In general, noble metals have poor adhesion but good wettability on ultrasmooth templates such as freshly cleaved mica or silicon wafers. Template stripping takes advantage of the above properties and works in the following way. First, a metal film is deposited onto the clean template and then, an epoxy or adhesive backing layer is attached to the topside of the metal film. By peeling off the supporting polymer layer, the metal will be released from the template.

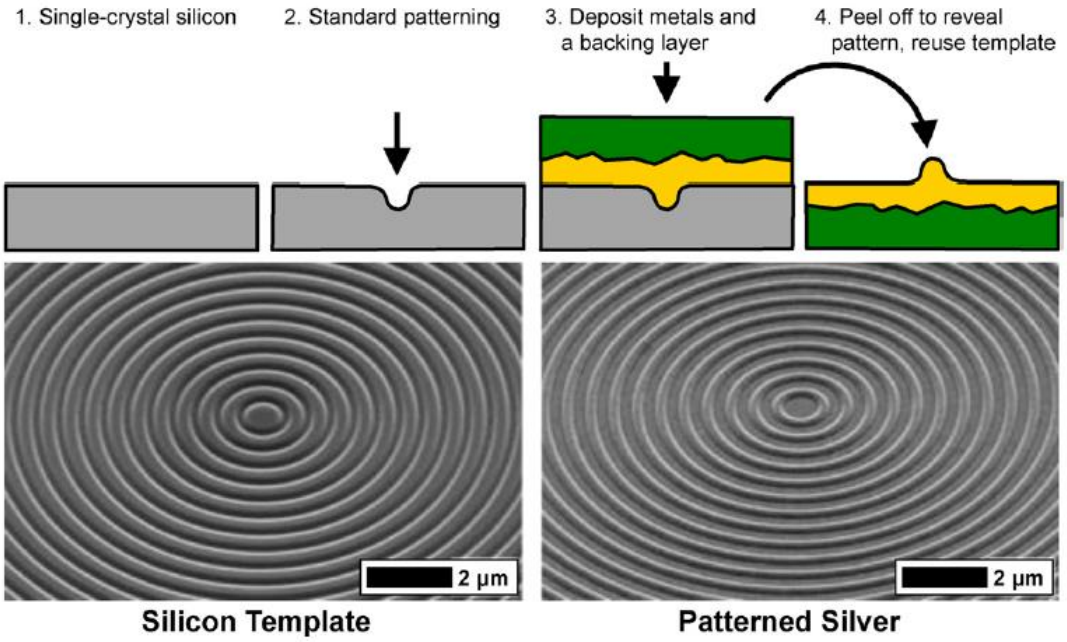

Figure 2.10: Template stripping method. Image adapted from [29].

High quality nanohole substrate has been achieved (Fig. 2.11) using template stripping method [30].

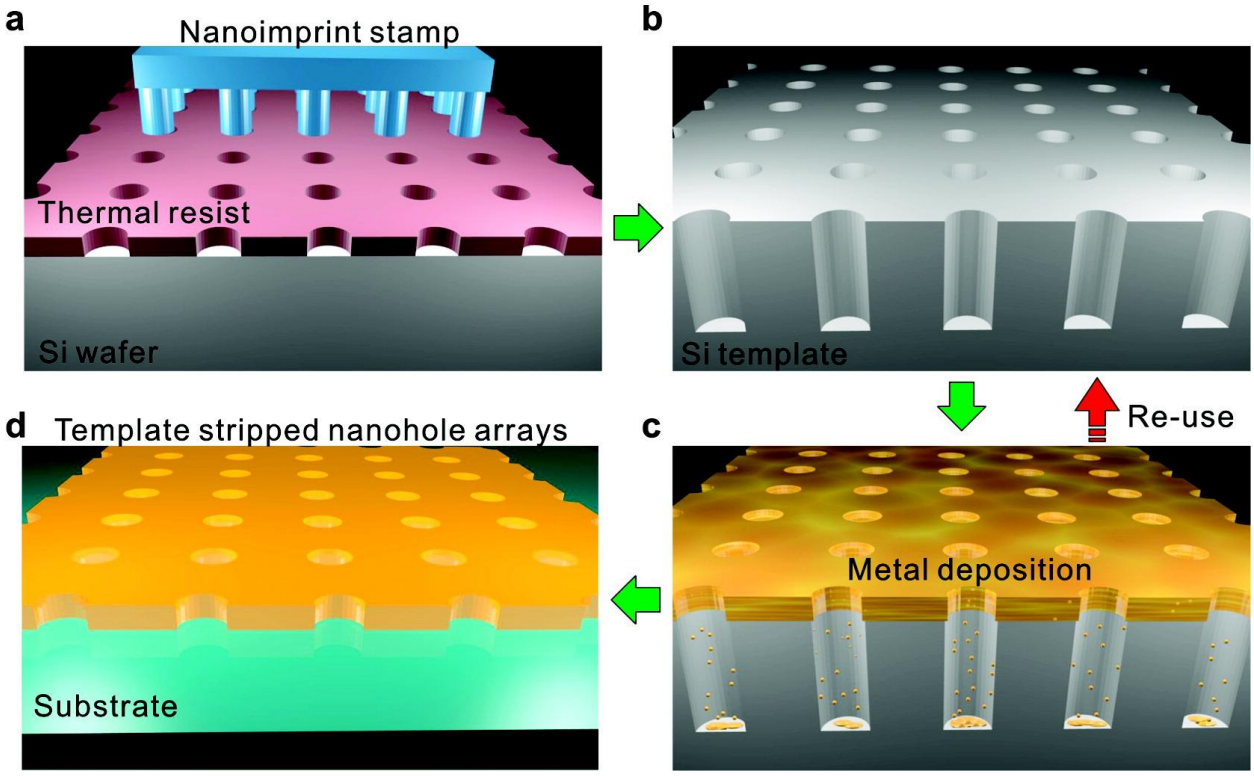

Figure 2.11: Schematic for obtaining high quality nanohole plasmonic device using template stripping method. Image adapted from [30].

Similar to template stripping methods, Teri Odom's lab at Northwestern University has developed a new technique called PEEL (combining PSP (phase-shifting photolithography), etching, electron-beam deposition, and lift-off) to transfer patterned features in a photoresist into free-standing, functional materials (Fig. 2.12).

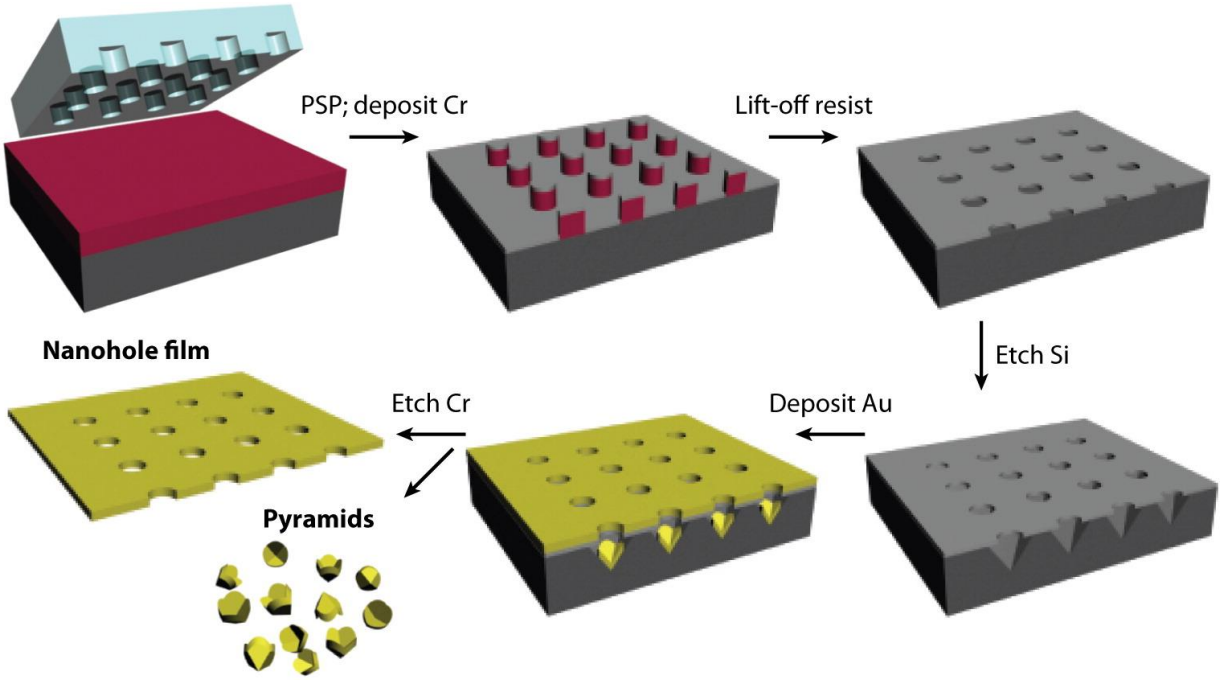

Figure 2.12: Schematic of one variation of template stripping called PEEL to transfer nanofeatures from photoresist to polymer templates. Image adapted from [21].

All of the above modes of manufacturing require expensive tools such as electron beam lithography, FIB or deep-UV projection lithography to fabricate the plasmonic device. Hence, they are not amenable for low cost, large scale fabrication of plasmonic structures. In order to overcome this problem various soft lithography based scheme has been invented initially by Whitesides' group at Harvard University [31-33]. Schematics of various soft lithography techniques such as replica molding, microcontact printing, micromolding, and microtrasfer printing are shown in Fig. 2.13. Most of these techniques find resemblance to "hot embossing" type of methods.

Another variation of soft lithography is the nanoimprint lithography (NIL). In NIL process the master template is mechanically pressed into a molded material to transfer the features from the master mold to the polymer material (generally in liquid form). Subsequently, the polymer material is hardened by curing (cooling, heating or UV light). Figure 2.14 shows schematic of the nanoimprint processes.

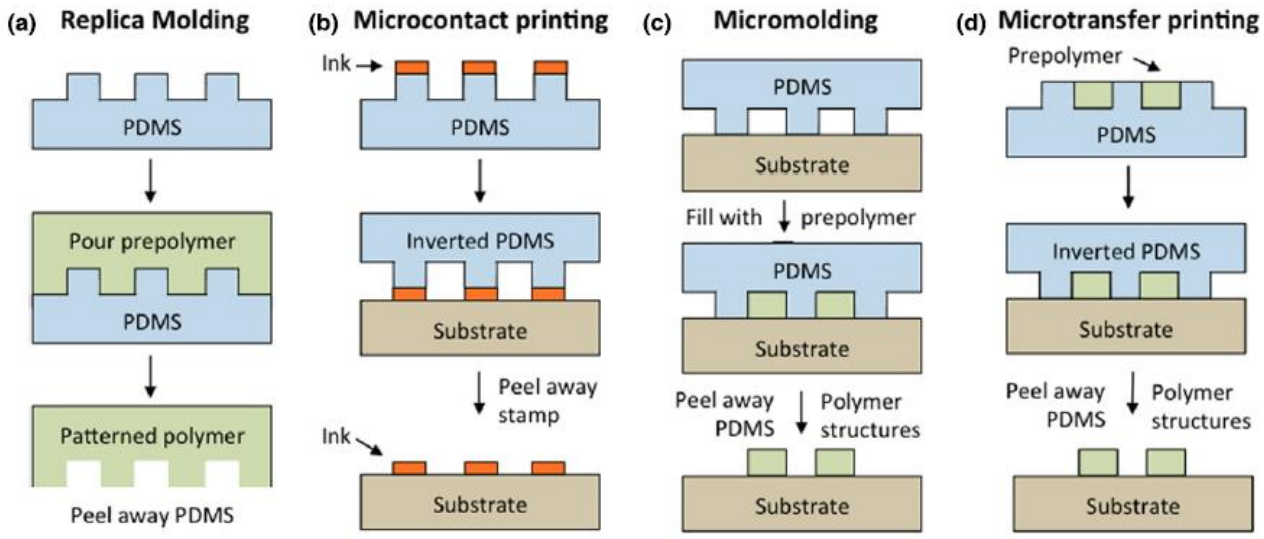

Figure 2.13: Various soft lithography techniques. (a) Replica molding, (b) microcontact printing, (c) micromolding in capillaries and (d) microtransfer printing. Image adapted from [27].

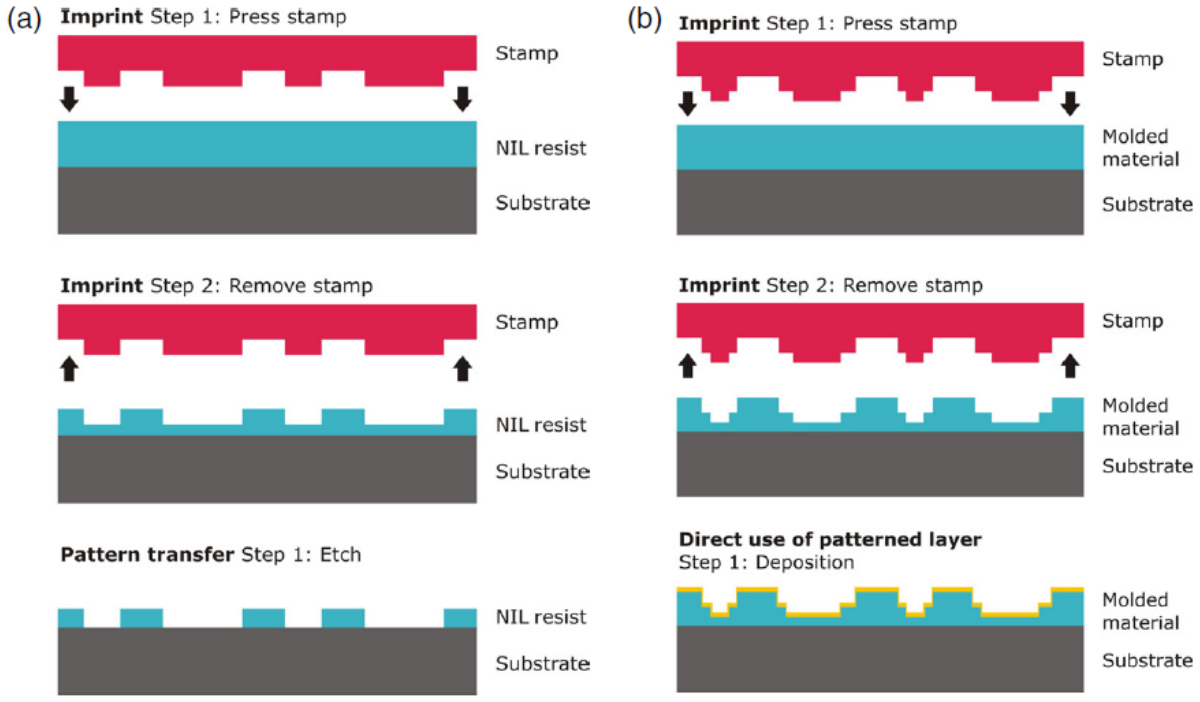

Figure 2.14: Schematics of nanoimprint processes: (a) the originally proposed nanoimprint lithography process where a resist layer is used for further pattern transfer, as in standard lithography, and (b) a method where the patterned layer is directly used. Image adapted from [34].

Recently another method called “beam pen lithography” (Fig. 2.15) has been developed by Chad Mirkin’s group at Northwestern University [35]. In this method, nanoscale holes have been drilled on the AFM polymer tips to act as lithography mask. Various controlled nanoscale feature has been achieved using this technique [35].

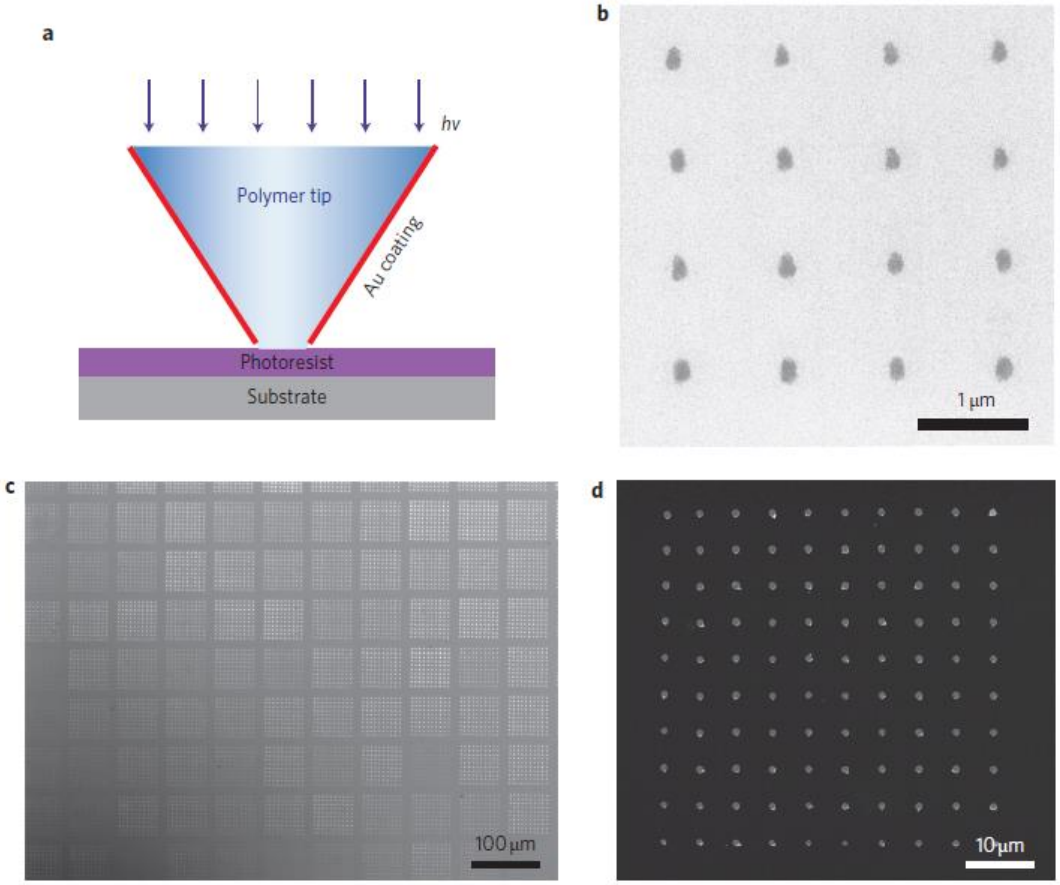

Figure 2.15: Beam pen lithography. Image adapted from [35].

Fabrication of plasmonics structures using replica molding

In the thesis, the plasmonic structure is fabricated using the replica molding process. The master nanocone pattern is first fabricated on a glass substrate using laser interference lithography technique [36, 37] with a range of different heights (h = 250, 500 and 1000 nm). Figure 2.16 shows the SEM images of the master mold.

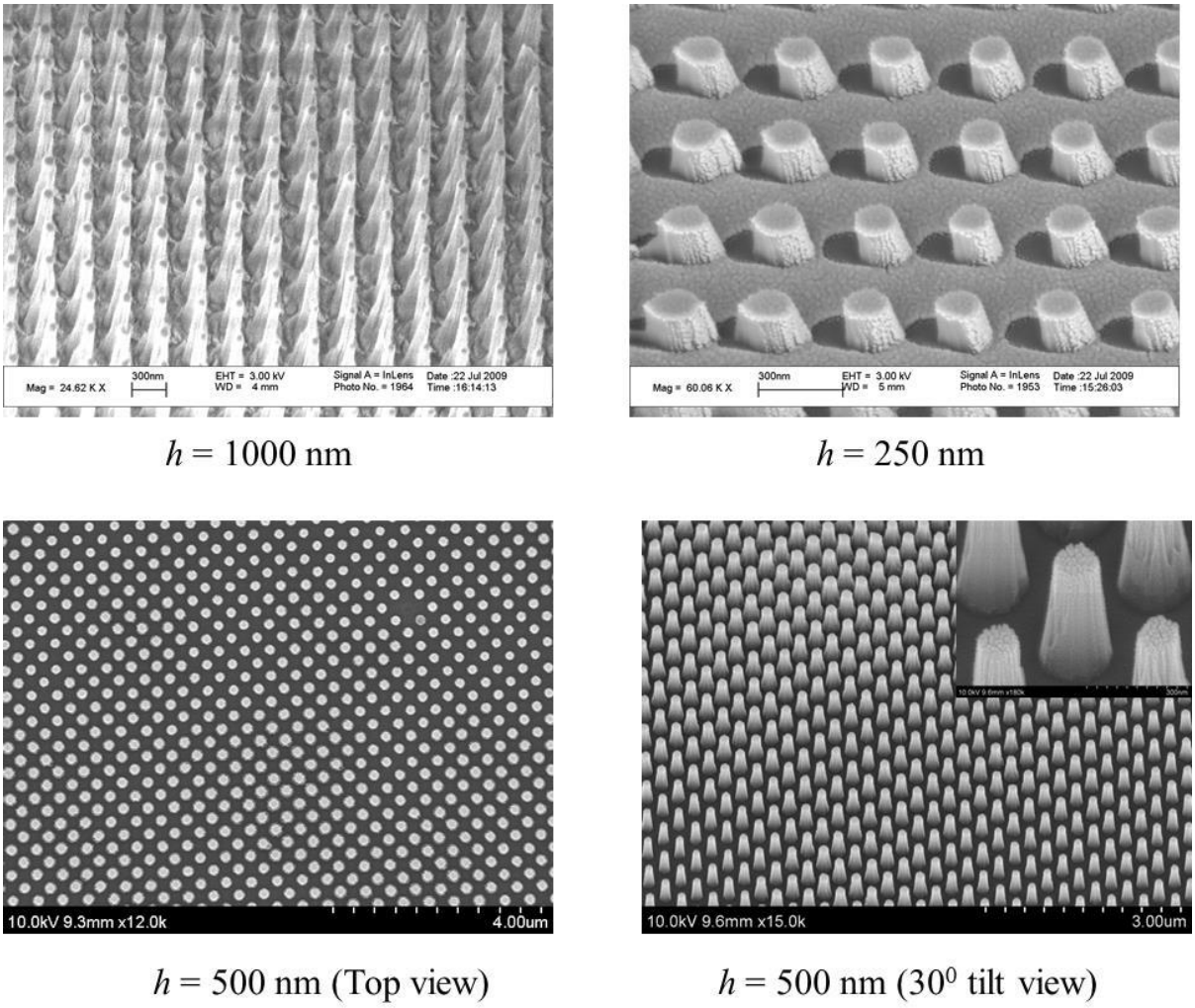

h = 1000 nm

h = 250 nm

h = 500 nm (Top view)

h = 500 nm (30^0 tilt view)

Figure 2.16: Scanning electron micrograph (SEM) of the master mold used for the fabrication of nanoplasmonic device.

The two-dimensional square lattice of master mold (pitch, p = 350 nm) was transferred to a flexible and optically transparent polyethylene terephthalate (PET) film using nanoreplica molding process. Figure 2.17 shows the schematic of the replica molding fabrication process. The nanocone master made on glass substrate was first cleaned and silanized for 30 min followed by ethanol and deionized water rinse (Fig. 2.17a). 5 μL of UV-curable polymer (NOA-61) was evenly spread on the top of the nanocone master and a PET sheet was put on top of the polymer to act as a substrate. The master with the polymer and PET sheet was exposed to UV-light (105 mW cm^{-2}) for 60 sec (Fig. 2.17b). The PET substrate with nanohole arrays was peeled off carefully from the master (Fig. 2.17c). In order to make the structure surface plasmon active,

we deposited different thickness, *t*, of silver metal layer (*t* = 40, 60, 70, 80, 90, 100 and 120 nm) (Fig. 2.17d).

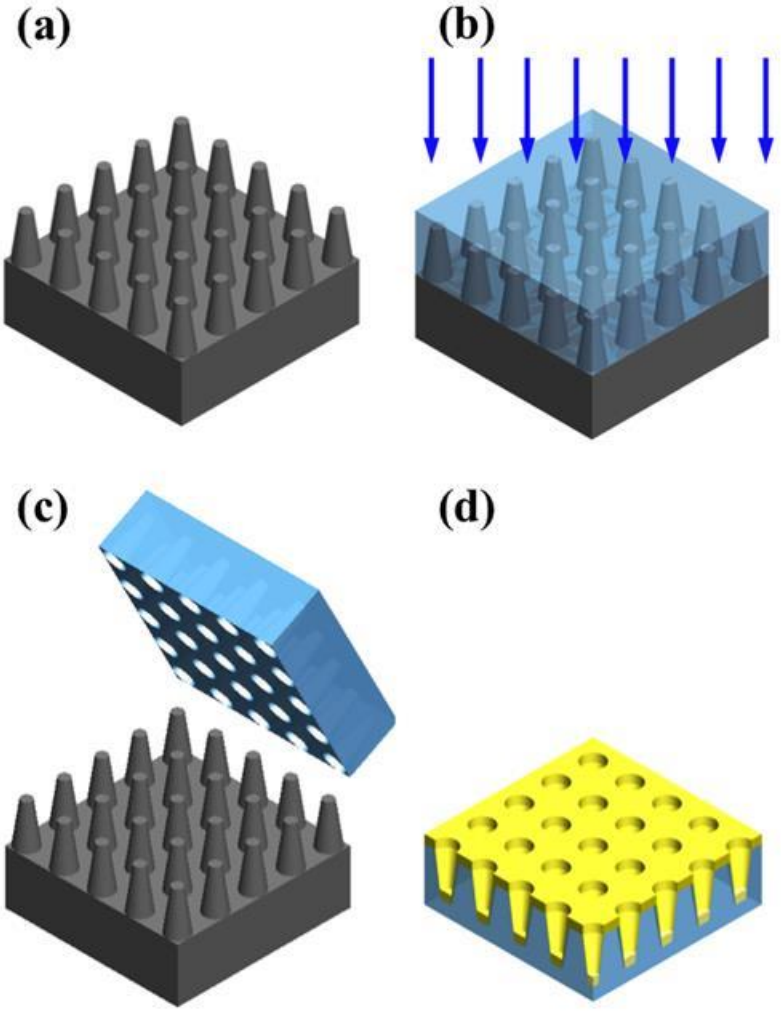

Figure 2.17: Schematic of the replica molding process to make the plasmonic device.

Figure 2.18 shows the SEM images of the plasmonic device obtained using replica molding process. It is quite clear that nanoscale features can be transferred to the polymer substrate from the original master mold with high fidelity. The nanoparticles inside the nanohole structures are also clearly visible.

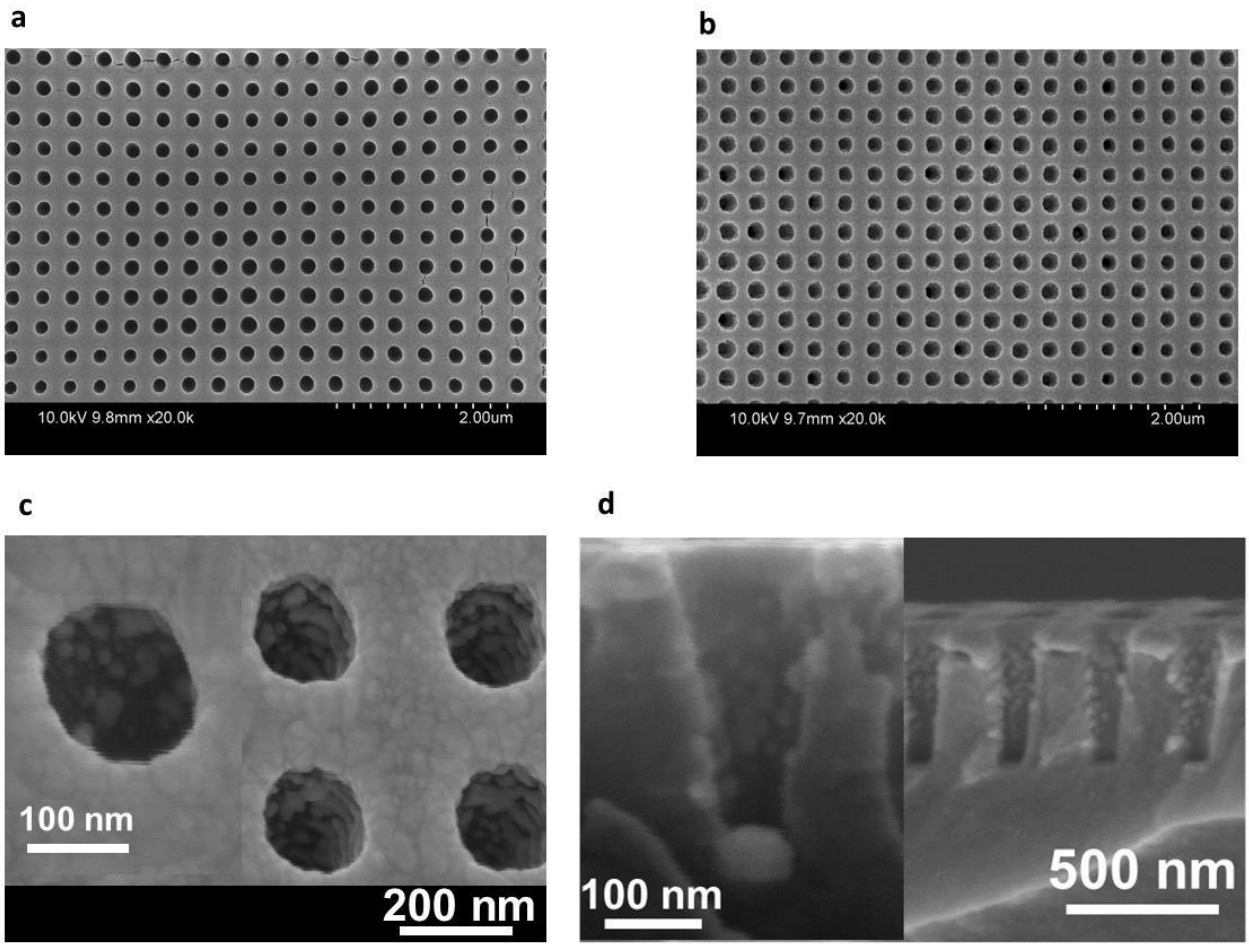

Figure 2.18: SEM image of the plasmonic device fabricated using replica molding method. (a) SEM (top view) image of polymer nanohole structure before deposition of metal. (b) SEM (top view) image of nanohole structure after 90 nm deposition of Ag. Top (c) and cross-sectional (d) view SEM images of plasmonic device showing the nanoparticles inside the nanohole structure.

Conclusions

This chapter provides an overview of different silicon based nanofabrication techniques. We have introduced a new manufacturing technique to create nanostructures on silicon by combining top-down and bottom-up nanofabrication approach called simultaneous plasma enhanced reactive ion synthesis and etching (SPERISE). High aspect ratio nanocone structure has been obtained using SPERISE process. Various plasmonic device fabrication methods including soft lithography have been discussed. In order to obtain low cost, large area plasmonic

device, we have utilized replica molding process. Replica molding offers simple, high resolution, wafer-scale fabrication of plasmonic structures and opens up opportunity for biosensing applications.

References

[1] P. Ball, "Let there be light," *Nature,* vol. 409, pp. 974-976, FEB 22, 2001.

[2] S. Godefroo, M. Hayne, M. Jivanescu, A. Stesmans, M. Zacharias, O. I. Lebedev, G. Van Tendeloo and V. V. Moshchalkov, "Classification and control of the origin of photoluminescence from Si nanocrystals," *Nature Nanotechnology,* vol. 3, pp. 174-178, MAR, 2008.

[3] V. V. Doan and M. J. Sailor, "Luminescent Color Image Generation on Porous Silicon," *Science,* vol. 256, pp. 1791-1792, JUN 26 1992, 1992.

[4] X. Li, "Metal assisted chemical etching for high aspect ratio nanostructures: A review of characteristics and applications in photovoltaics," *Current Opinion in Solid State & Materials Science,* vol. 16, pp. 71-81, APR, 2012.

[5] K. Seo, M. Wober, P. Steinvurzel, E. Schonbrun, Y. Dan, T. Ellenbogen and K. B. Crozier, "Multicolored Vertical Silicon Nanowires," *Nano Letters,* vol. 11, pp. 1851-1856, APR 2011, 2011.

[6] J. Zhu, Z. Yu, G. F. Burkhard, C. Hsu, S. T. Connor, Y. Xu, Q. Wang, M. McGehee, S. Fan and Y. Cui, "Optical Absorption Enhancement in Amorphous Silicon Nanowire and Nanocone Arrays," *Nano Letters,* vol. 9, pp. 279-282, JAN 2009, 2009.

[7] S. Liu, J. Zhu, Y. Liu and L. Zhao, "Laser induced plasma in the formation of surface-microstructured silicon," *Mater Lett,* vol. 62, pp. 3881-3883, AUG 31, 2008.

[8] C. H. Crouch, J. E. Carey, M. Shen, E. Mazur and F. Y. Genin, "Infrared absorption by sulfur-doped silicon formed by femtosecond laser irradiation," *Applied Physics A-Materials Science & Processing,* vol. 79, pp. 1635-1641, NOV, 2004.

[9] M. Y. Shen, C. H. Crouch, J. E. Carey and E. Mazur, "Femtosecond laser-induced formation of submicrometer spikes on silicon in water," *Appl. Phys. Lett.,* vol. 85, pp. 5694-5696, DEC 6, 2004.

[10] M. D. Kelzenberg, D. B. Turner-Evans, M. C. Putnam, S. W. Boettcher, R. M. Briggs, J. Y. Baek, N. S. Lewis and H. A. Atwater, "High-performance Si microwire photovoltaics," *Energy & Environmental Science,* vol. 4, pp. 866-871, MAR 2011, 2011.

[11] Y. Chen, Z. Xu, M. R. Gartia, D. Whitlock, Y. Lian and G. L. Liu, "Ultrahigh Throughput Silicon Nanomanufacturing by Simultaneous Reactive Ion Synthesis and Etching," *Acs Nano,* vol. 5, pp. 8002-8012, OCT 2011, 2011.

[12] G. S. Oehrlein, J. F. Rembetski and E. H. Payne, "Study of Sidewall Passivation and Microscopic Silicon Roughness Phenomena in Chlorine-Based Reactive Ion Etching of Silicon Trenches," *Journal of Vacuum Science & Technology B,* vol. 8, pp. 1199-1211, NOV-DEC, 1990.

[13] H. Jansen, M. Deboer, R. Legtenberg and M. Elwenspoek, "The Black Silicon Method - a Universal Method for Determining the Parameter Setting of a Fluorine-Based Reactive Ion Etcher in Deep Silicon Trench Etching with Profile Control," *J Micromech Microengineering,* vol. 5, pp. 115-120, JUN, 1995.

[14] A. G. Nassiopoulos, S. Grigoropoulos and D. Papadimitriou, "Electroluminescent device based on silicon nanopillars," *Appl. Phys. Lett.,* vol. 69, pp. 2267-2269, OCT 7, 1996.

[15] H. Xu, N. Lu, D. Qi, L. Gao, J. Hao, Y. Wang and L. Chi, "Broadband antireflective Si nanopillar arrays produced by nanosphere lithography," *Microelectronic Engineering,* vol. 86, pp. 850-852, APR-JUN, 2009.

[16] S. Koynov, M. S. Brandt and M. Stutzmann, "Black nonreflecting silicon surfaces for solar cells," *Appl. Phys. Lett.,* vol. 88, pp. 203107, MAY 15, 2006.

[17] S. Kalem, P. Werner, O. Arthursson, V. Talalaev, B. Nilsson, M. Hagberg, H. Frederiksen and U. Sodervall, "Black silicon with high density and high aspect ratio nanowhiskers," *Nanotechnology,* vol. 22, pp. 235307, JUN 10, 2011.

[18] Y. Djeridane, A. Abramov and P. R. I. CabarrocaS, "Silane versus silicon tetrafluoride in the growth of microcrystalline silicon films by standard radio frequency glow discharge," *Thin Solid Films,* vol. 515, pp. 7451-7454, JUL 16, 2007.

[19] Z. Huang, J. E. Carey, M. Liu, X. Guo, E. Mazur and J. C. Campbell, "Microstructured silicon photodetector," *Appl. Phys. Lett.,* vol. 89, pp. 033506, JUL 17, 2006.

[20] H. Jansen, H. Gardeniers, M. deBoer, M. Elwenspoek and J. Fluitman, "A survey on the reactive ion etching of silicon in microtechnology," *J Micromech Microengineering,* vol. 6, pp. 14-28, MAR, 1996.

[21] J. Henzie, J. Lee, M. H. Lee, W. Hasan and T. W. Odom, "Nanofabrication of Plasmonic Structures," *Annu. Rev. Phys. Chem.,* vol. 60, pp. 147-165, 2009.

[22] N. G. Khlebtsov and L. A. Dykman, "Optical properties and biomedical applications of plasmonic nanoparticles," *J. Quant. Spectrosc. Radiat. Transfer,* vol. 111, pp. 1-35, JAN, 2010.

[23] Y. Xia, X. Xia, Y. Wang and S. Xie, "Shape-controlled synthesis of metal nanocrystals," *MRS Bull,* vol. 38, pp. 335-344, APR, 2013.

[24] W. CHEN and H. AHMED, "Fabrication of 5-7 Nm Wide Etched Lines in Silicon using 100 Kev Electron-Beam Lithography and Polymethylmethacrylate Resist," *Appl. Phys. Lett.,* vol. 62, pp. 1499-1501, MAR 29, 1993.

[25] K. Kumar, H. Duan, R. S. Hegde, S. C. W. Koh, J. N. Wei and J. K. W. Yang, "Printing colour at the optical diffraction limit," *Nature Nanotechnology,* vol. 7, pp. 557-561, SEP, 2012.

[26] T. Ebbesen, H. Lezec, H. Ghaemi, T. Thio and P. Wolff, "Extraordinary optical transmission through sub-wavelength hole arrays," *Nature,* vol. 391, pp. 667-669, FEB 12, 1998.

[27] N. C. Lindquist, P. Nagpal, K. M. McPeak, D. J. Norris and S. Oh, "Engineering metallic nanostructures for plasmonics and nanophotonics," *Reports on Progress in Physics,* vol. 75, pp. 036501, MAR, 2012.

[28] O. Vazquez-Mena, G. Villanueva, V. Savu, K. Sidler, M. A. F. van den Boogaart and J. Brugger, "Metallic Nanowires by Full Wafer Stencil Lithography," *Nano Letters,* vol. 8, pp. 3675-3682, NOV, 2008.

[29] P. Nagpal, N. C. Lindquist, S. Oh and D. J. Norris, "Ultrasmooth Patterned Metals for Plasmonics and Metamaterials," *Science,* vol. 325, pp. 594-597, JUL 31, 2009.

[30] H. Im, S. H. Lee, N. J. Wittenberg, T. W. Johnson, N. C. Lindquist, P. Nagpal, D. J. Norris and S. Oh, "Template-Stripped Smooth Ag Nanohole Arrays with Silica Shells for Surface Plasmon Resonance Biosensing," *Acs Nano,* vol. 5, pp. 6244-6253, AUG, 2011.

[31] B. Gates, Q. Xu, J. Love, D. Wolfe and G. Whitesides, "Unconventional nanofabrication," *Annual Review of Materials Research,* vol. 34, pp. 339-372, 2004.

[32] B. Gates, Q. Xu, M. Stewart, D. Ryan, C. Willson and G. Whitesides, "New approaches to nanofabrication: Molding, printing, and other techniques," *Chem. Rev.,* vol. 105, pp. 1171-1196, APR, 2005.

[33] Y. Xia and G. Whitesides, "Soft lithography," *Annual Review of Materials Science,* vol. 28, pp. 153-184, 1998.

[34] A. Boltasseva, "Plasmonic components fabrication via nanoimprint," *Journal of Optics A-Pure and Applied Optics,* vol. 11, pp. 114001, NOV, 2009.

[35] F. Huo, G. Zheng, X. Liao, L. R. Giam, J. Chai, X. Chen, W. Shim and C. A. Mirkin, "Beam pen lithography," *Nature Nanotechnology,* vol. 5, pp. 637-640, SEP, 2010.

[36] M. R. Gartia, Z. Xu, E. Behymer, H. Nguyen, J. A. Britten, C. Larson, R. Miles, M. Bora, A. S. -. Chang, T. C. Bond and G. L. Liu, "Rigorous surface enhanced Raman spectral characterization of large-area high-uniformity silver-coated tapered silica nanopillar arrays," *Nanotechnology,* vol. 21, pp. 395701, OCT 1 2010, 2010.

[37] A. Fernandez, H. T. Nguyen, J. A. Britten, R. D. Boyd, M. D. Perry, D. R. Kania and A. M. Hawryluk, "Use of interference lithography to pattern arrays of submicron resist structures for field emission flat panel displays," *Journal of Vacuum Science & Technology B,* vol. 15, pp. 729-735, MAY-JUN 1997, 1997.

CHAPTER 3

OPTICAL CHARACTERIZATION OF NANOPHOTONICS DEVICES

Introduction

Due to the characteristics length scale, the physical, optical and electronic properties of nanostructured silicon are significantly different from that of bulk silicon. For example, as the diameter of the silicon nanowire decreases, the band gap of the nanowire widens and the quantum mechanical effects plays more important role for the optical as well as electronic property of the nanowire. Because of the unique optical and electronic properties, nanostructured silicon have been extensively studied and found application in many fields such as photovoltaics [38], optical sensor [39, 40] and detectors [41]. In spite of concerted effort to understand the properties of nanostructured systems, such as nano porous silicon [42], nano pillar silicon [43] and nanowires [44, 45], still some lingering questions remain there. For example, the mechanism of photoluminescence (PL) of nanostructured silicon, the thermoelectric properties of silicon nanowire, and enhanced solar conversion efficiency of nanostructured silicon based photovoltaics, to name a few. Hence, understanding the optical and electronic properties of the nanostructured silicon will provide information about guiding rules of various phenomena, and could further drive the applications. Chapter 3 provides detail about the optical characterization performed on the silicon nanostructured devices.

Reflectance measurement of silicon nanocone structure

The reflection spectrum is measured with wavelength range from ultraviolet to infrared regions using a UV–Vis–NIR spectrometer (Varian Cary 5G) equipped with a mirror-composed diffuse reflectance accessory. Figure 3.1a shows the comparison of diffuse reflectance (measured with integrating sphere detector) between smooth Si wafer and b-Si. The average reflectance of smooth Si was > 50% between 300-800 nm and > 30% from 800-1100 nm. We observed reflectance < 5% for b-Si between 300-1100 nm. We measured the specular reflectance using a

home-made goniometer set-up. The schematic of the set-up is shown in Fig. 3.1b. The light source was kept fixed and the angle dependent measurement was achieved by rotating the sample holding stage. The specular reflected light was collected by rotating the spectrometer on the goniometer track as shown in the schematic. The average specular reflectance for b-Si for angle between -20 to 100^0 is less than 20%, except at 20^0 for which we observed a peak in reflectance at around 430 nm.

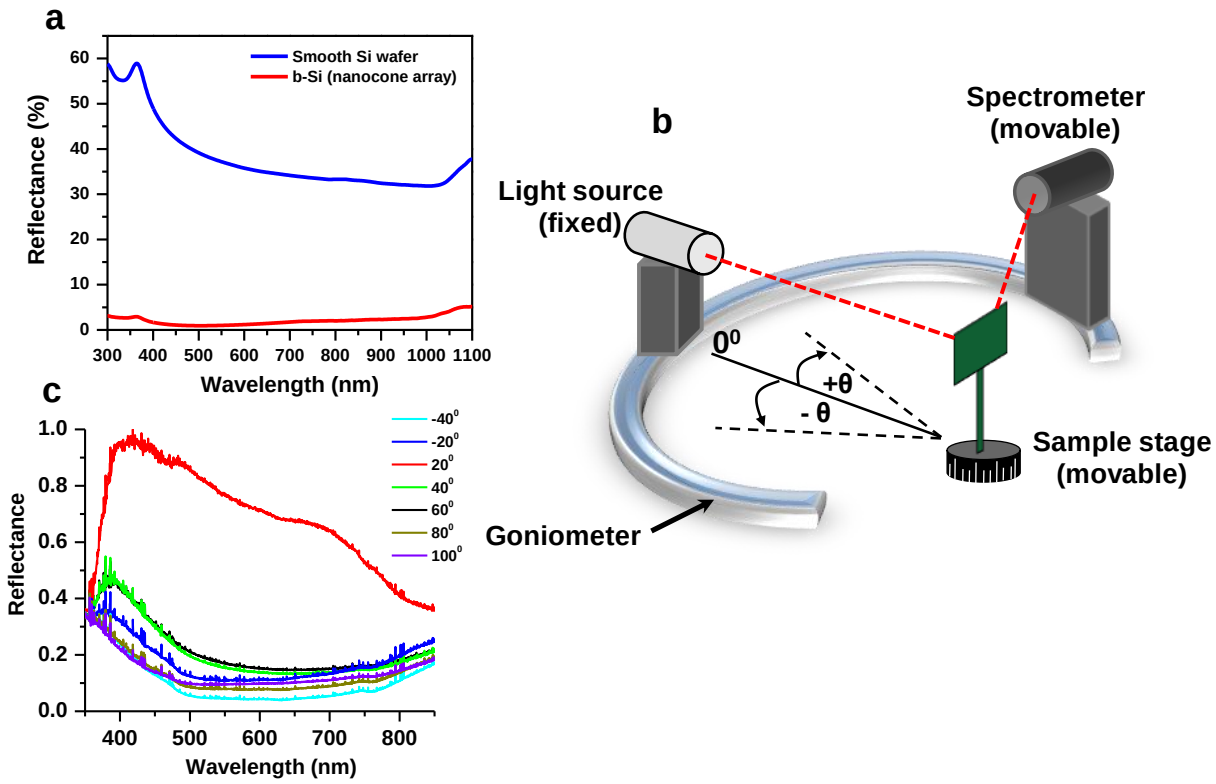

Figure 3.1: (a) Normal incident reflectance measurement on b-Si and smooth Si substrate. (b) Schematic of the goniometer set-up for angle dependent reflectance measurement. (c) Angle dependent reflectance measurement for b-Si substrate.

Cathodoluminescence (CL) measurement of silicon nanocone structure

A commercial setup (MonoCL from Gatan) with a parabolic mirror for photon collection mounted onto an SEM (JEOL JSM-7000F) was used for the CL experiment. A photomultiplier tube (PMT) having a range of 300 nm – 900 nm was used to collect the spectra. A schematic of the experimental setup is shown in Fig. 3.2a. For spectroscopy and spectrally resolved CL

imaging, the emitted light is sent through a grating monochromator before being focused on the PMT detector. For panchromatic imaging, the emitted light is directly focused on to the PMT detector, detecting photons with wavelength ranging from 300-900 nm. The spectra are taken by scanning the electron beam over a selected area of the sample with a passband of 10 nm. The excitation voltage was 15 kV and the beam current was varied from 25 – 92 nA. Secondary electron and CL images are obtained simultaneously. Figure 3.2b is the secondary electron image (SEI) of b-Si substrate which gives the topographic information about the specimen. Figure 3.2c is a panchromatic CL image (PanCL). In panchromatic mode all of the emitted light is collected by the detector and hence the intensity at each pixel represents the integrated photon counts in the sensitivity range of the detector. In general, bulk Si does not show near UV and visible range CL [46]. In contrast, PanCL image (Fig. 3.2c) clearly depicts electron induced luminescence in b-Si. The way this image is acquired is similar to SEM mapping i.e. by raster scanning the electron beam and collecting emitted photons rather than secondary electrons as done in scanning electron imaging. Figure 3.2d shows the probe current dependent CL spectra acquired at probe current of 25 nA, 50 nA and 92 nA respectively. Clearly, two CL peaks at 660 nm and 737 nm are visible.

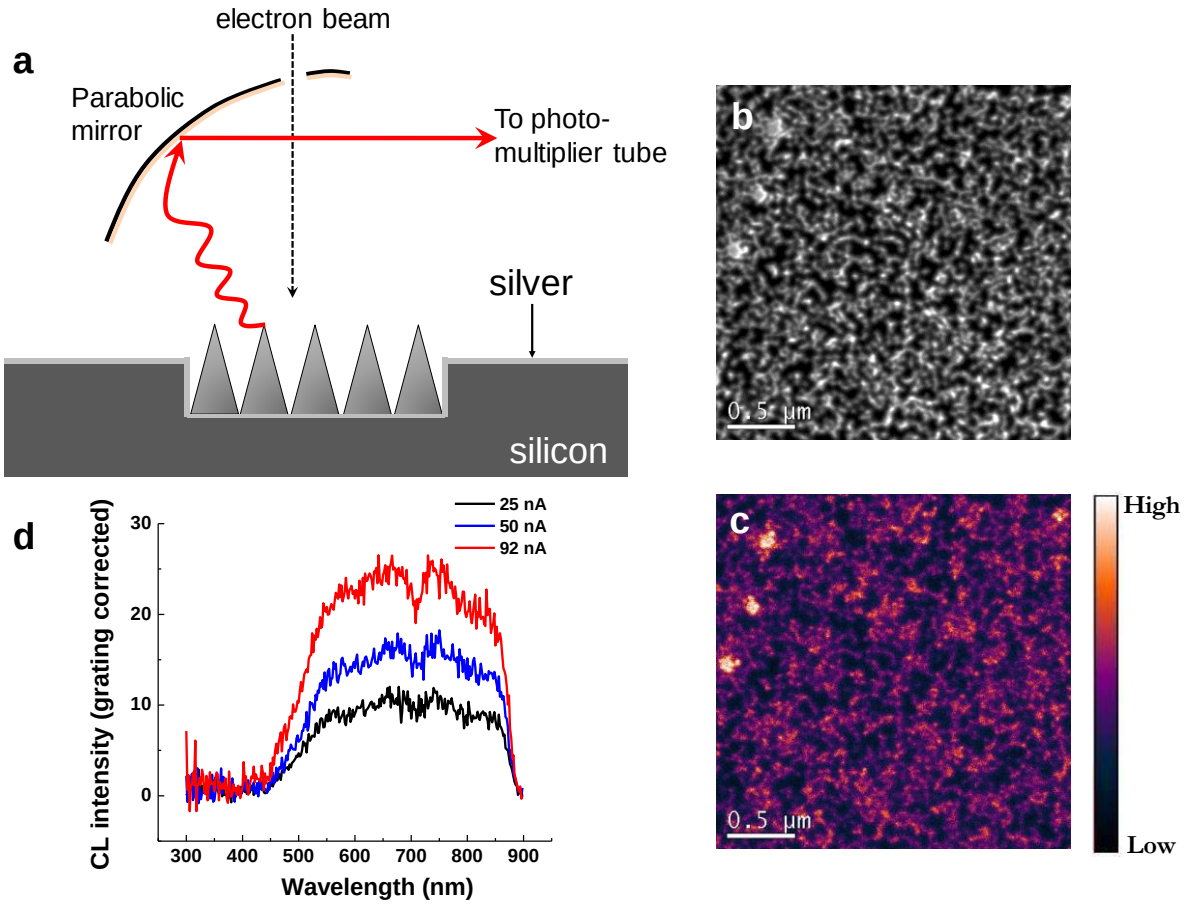

Figure 3.2: (a) Schematic of the CL measurement set-up. (b) Secondary electron image (SEI) of the b-Si. (c) PanCL image of the b-Si corresponds to image shown in (b). (d) Probe current dependent CL spectra for the b-Si substrate.

Figure 3.3a shows the CL spectrum for black Si with an excitation probe current of 25 nA. The measured CL spectra are deconvoluted and fitted to a Gaussian shape. Mainly three Gaussian bands: green, red and infrared are observed. The green CL band (565 nm or 2.2 eV) is attributed to point defects related to oxygen deficit (Si-Si bond) [47]. The observed red band (650 – 670 nm or 1.9-1.85 eV) is generally assigned to nonbridging oxygen hole centers in oxygen deficient SiO2 environment [48] or recombination via Si-nanocrystal-SiO2 interface defects [49, 50]. The band at 750 nm (1.65 eV) may also originated from a nonbridging oxygen hole center mostly at Si-SiO2 interface [51]. The infrared band (1.4-1.6 eV) is attributed to band-band transition in Si-nanocluster [47]. Figure 3.3b shows the variation of CL spectrum with increasing the probe current. The intensity of the CL spectra increases with increase in the probe current. The earlier observed PL peak at 667 nm is also observed in all CL spectra (Fig. 3.3b). The secondary

electron image (SEI) and panchromatic CL (panCL) image of the black Si over a 4 μm x 2.67 μm area is shown in Fig. 3.2b and c respectively. The bright spots are due to the presence of oxide layers on the black Si surface. The luminescence from black Si can be clearly seen from the panCL image.

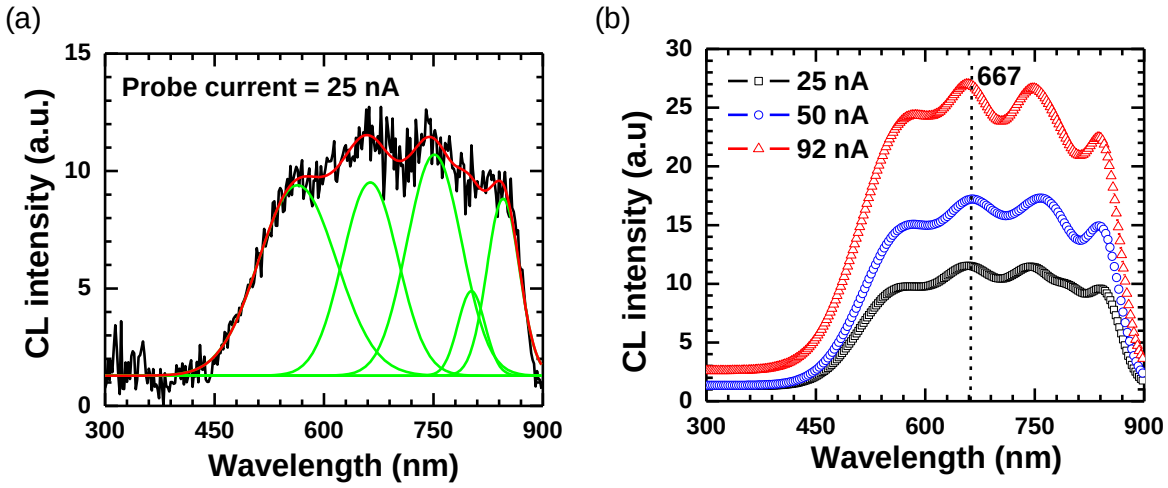

Figure 3.3: (a) Grating corrected CL spectrum of black Si using probe current of 25 nA. (b) Comparison of CL spectra with increasing the probe current.

Photoluminescence (PL) measurement of silicon nanocone structure

We obtained the PL spectra by illuminating the sample with a 442 nm laser source and measuring the luminescence from 500 to 800 nm at room temperature. Figure 3.4a shows the PL spectrum from the sample with an integration time of 300 s. After the deconvolution of the peaks and Gaussian curve fitting, the PL spectrum contains three peaks at 1.73 (718 nm), 1.86 (667 nm) and 1.95 eV (637 nm) respectively. At low temperature (77 K) the peak at 650 nm gets enhanced as compared to peak at 515 nm (Figure 3.4b). The green band (~ 510-580 nm) is generally attributed to the recombination of carriers at oxygen-related defect centers (“ defects related PL”) [52-57] and the red band (~635 -720 nm) is due to recombination of confined excitons in Si nanocluster (“ confinement related PL”) [2, 52, 56, 58]. Figure 3.4b shows an increase in intensity for band at 650 nm at low temperature. This can be explained by the quantum confinement of the excited carriers at the tips of the nanocone [56]. At low temperatures, excited carriers are localized at these weak potential wells or traps formed by the

defects. At lower temperature, there is reduced probability of non-radiative recombination through defect centers and increased zero phonon recombination probability for electron-hole pair. Hence, the intensity of PL at lower temperature (77 K) is higher as compared to PL at room temperature (300 K). Figure 3.4b shows the peak wavelength of green luminescence band remains unchanged after lowering the temperature, although there is slight increase in intensity. This provides further evidence that the green luminescence band is defects-related PL. Furthermore, with the increase in temperature, the carriers are thermally excited and move to deeper potential well close to band edges. As shown in Fig. 3.4c, the band-edge PL intensity is higher than the confinement related PL intensity. Since our system uses Si based detector, we are not able to see the whole band-edge spectrum for Si. Figure 3.4d shows PL spectra for black Si with different excitation energies. We observe a consistent red shift of PL peak with decreasing the excitation energy from 2.8-2.33 eV (442 - 532 nm). The red shift of the PL peak is an indication of defects related PL [59].

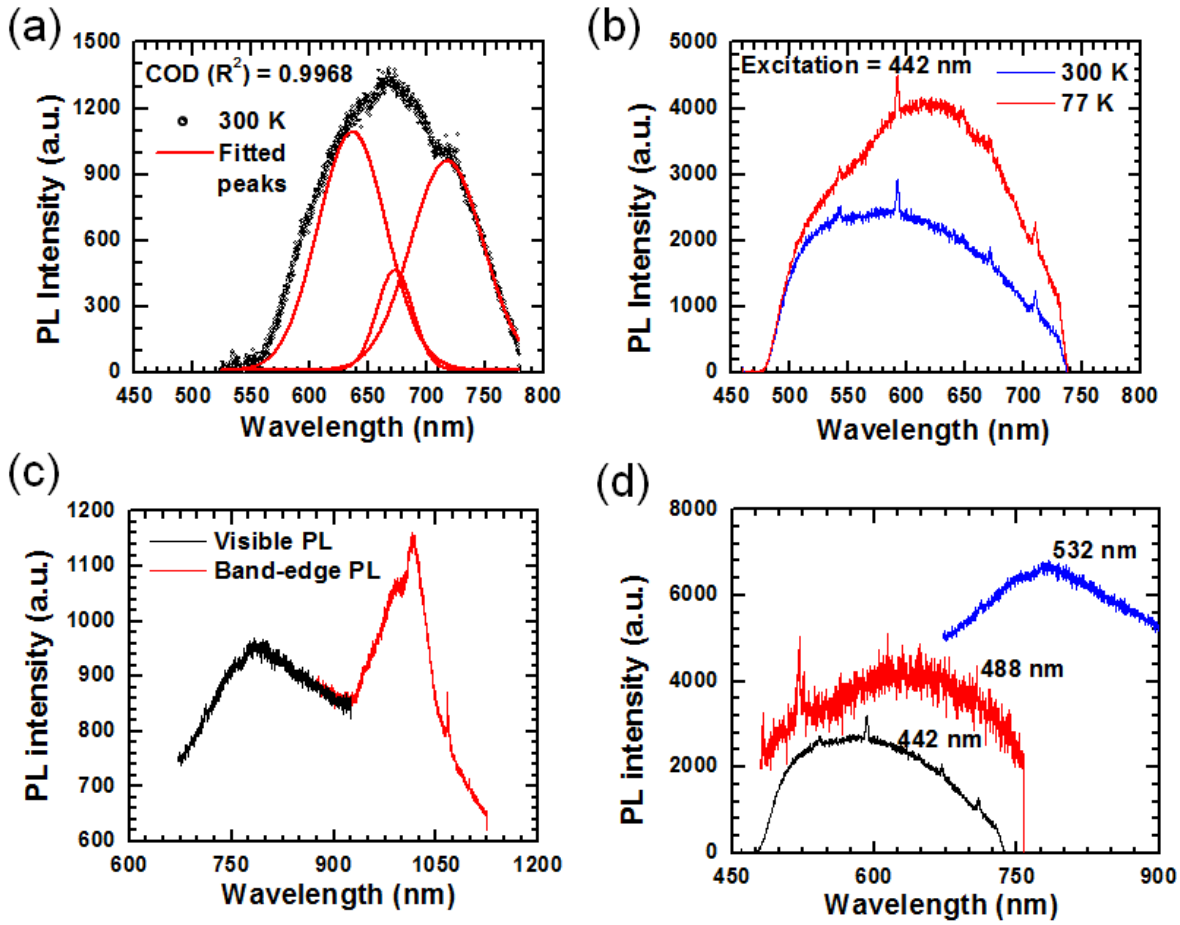

Figure 3.4: (a) PL spectrum from black Si with excitation laser of 442 nm. (b) PL at 77K and 300K using excitation wavelength of 442 nm. The integration time is 300 s. (c) Visible and bandedge PL spectra using excitation wavelength 532 nm. (d) Comparison of PL spectra using excitation wavelength of 442, 488, and 532 nm.

XPS and AES measurement of silicon nanocone structure

The presence of oxide layers on black Si surface is further studied using XPS and AES. Figure 3.5a shows the Si 2*p* and 2*s* XPS spectra for Si, black Si and black Si with heavy oxide specimen. All the spectra are calibrated with C 1s with binding energy of 285 eV. Bulk plasmon peak generally shows as equally spaced satellite structures at higher binding energy side (17.4 eV) of the core peaks [60]. The plasmon peak can be seen for Si and black Si, but not for black Si with heavy oxide. The presence of bulk plasmon indicates that the material in black Si is essentially elemental Si though some broadening is observed for black Si. The Si 2*s* spectrum of black Si with heavy oxide shifts by 2.42 eV as compared to 2*s* of black Si. This is an indication

of non-stoichiometric oxide formation on black Si (as it is well known that Si can be oxidized by electronegative elements through several oxidation states (1 to 4) and the binding energy increase associated with unit increase in oxidation state is ~ 1 eV) [61]. Figure 3.5b shows the Si 2*p* XPS spectrum of Si, Si with native oxide, black Si and black Si with heavy oxide. The peak with highest binding energy (103.35 eV) is assigned to Si^{+4} oxidation state of SiO_2 and the peak with smallest binding energy (99.24 eV) is assigned to Si^0 of the silicon crystal [62]. The inset of Fig. 3.5b shows that with native oxide formation on Si, the Si 2p spectrum shifts by around 0.6 eV, which is due to spin-orbit coupling [62]. Hence, Si^0 photoelectron peak has two contributions, Si^0 $2p_{3/2}$ with binding energy 98.94 eV and Si^0 $2p_{1/2}$ with binding energy 99.54 eV. The Si^{+4} peak has similar contributions [62].

Figure 3.5c shows XPS valence band (VB) spectra for Si and black Si sample. The XPS VB provides useful information about distribution of total density of states (DOS) of the sample. Hence, any transformation of VB spectrum indicates re-arrangement of the energy spectrum of the electronic states for black Si sample [63]. The Si 3*d* peak is generally situated ~2.4 - 4.2 eV above the Fermi level and Si 3*s* level is about 11.1 eV above the Fermi level [64]. The rearrangement of DOS on black Si can be clearly seen. The spectrum for black Si shows four main characteristic peaks labeled A-D. Taking into account the positions of Si 3*s* and 3*d* peak and O 2*p* peak from a low energy survey scan, the peak features at A-B-C appear due to strongly hybridized Si 3*d* 3*s*-O 2*p* electronic states [63]. This so called XPS VB transition layer [65] gives further indication of migration of oxygen and formation of non-stoichiometric oxide layer on black Si forming Si/SiO_x ($x<2$) interface. Figure 3.5d shows the Si KLL Auger spectrum for Si and black Si sample. The intense Auger line (KL23L23) at 1614-1616 eV (Peak-8) is for Si and smaller satellite at 1607-1609 eV (Peak-7) is for SiO_2 [66]. The peaks at 1-3 are due to KL_1L_{23} transition and peaks at 4-8 are due to $KL_{23}L_{23}$ transition [67]. The peaks are shifted to higher kinetic energy for black Si, which is further indication of formation of oxide layers [68]. We believe that nonstoichiometric oxide layer is a necessary condition for PL. The oxygen-defect centers are reported to be located in suboxide structures and migrates to the defect centers from the absorbing Si grains to produce PL [69].

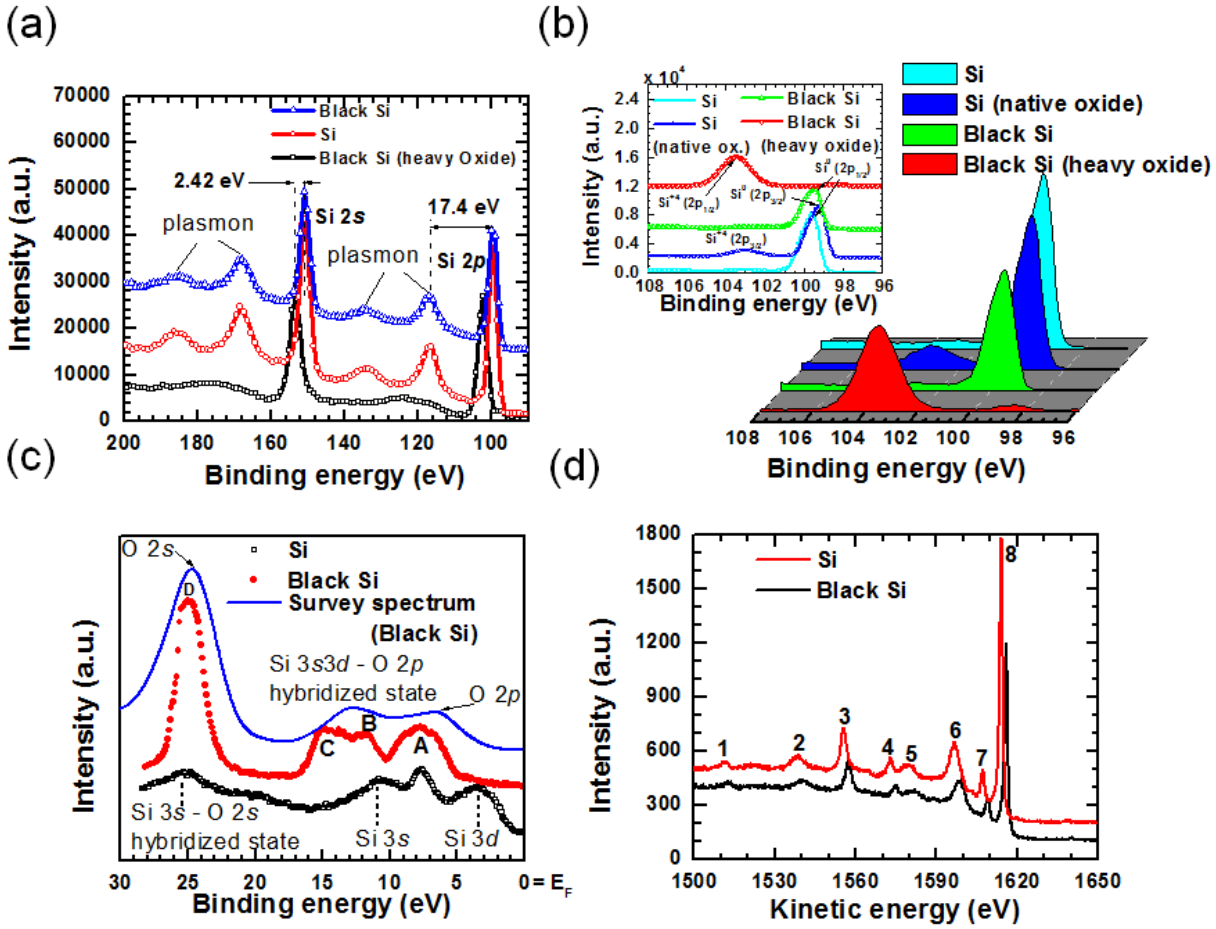

Figure 3.5: (a) Si 2*p* and 2*s* XPS spectra for Si, black Si and black Si with heavy oxide (b) High resolution Si 2*p* XPS spectra of Si, black Si with and without oxide layer (c) XPS valence band structure of Si and black Si showing variation in density of states (d) AES spectra of Si and black Si.

Raman measurement of silicon nanocone structure

Figure 3.6 shows Raman spectra of b-Si and smooth Si wafer using laser excitation of 785 nm. For pure single crystalline Si, Raman peak is observed at 520.5 cm-1 which is the energy of optical phonon at the center of Brillouin zone and due to conservation of quasi-momentum in crystals [70]. For b-Si we observed broadening and downshift of Raman peak towards lower energy indicating the presence of nanoscale crystalline structure. It is well known that the silicon optical phonon line shifts to lower frequency and becomes broader asymmetrically as the size of nanocrystal decreases [70-72]. This shifting of peak is due to the reduction in the phonon energy as a result of disturbances in the silicon lattice due to nanopillar

structure [70]. The absence of other peak in the Raman spectra also confirms the crystallinity of b-Si sample. Further, the shift and broadening in the Raman spectra suggest that the Raman signal is exclusively coming from the top nanocone layer and not from the bulk Si. Using the analytical form given by Paillard et al. [73]: $\Delta\omega = -A\left(\frac{a}{L}\right)^{\gamma}$

where a = 0.543 nm is the lattice constant of Si, L is the crystallites size, the parameters A = 52.3, and γ = 1.586, one can calculate the crystallite size from the measured Raman wavenumber shift. For example, the observed Raman shift of 1.1 cm-1 for b-Si corresponds to average crystallite size of 6.2 nm which is close to the Bohr exciton radius for bulk Si (~ 5 nm). Since the current structure is conical, the tip of the structure may be much smaller dimension and can lead to quantum confinement effect producing higher energy PL exceeding the normal bandgap for Si (~ 1.1 eV).

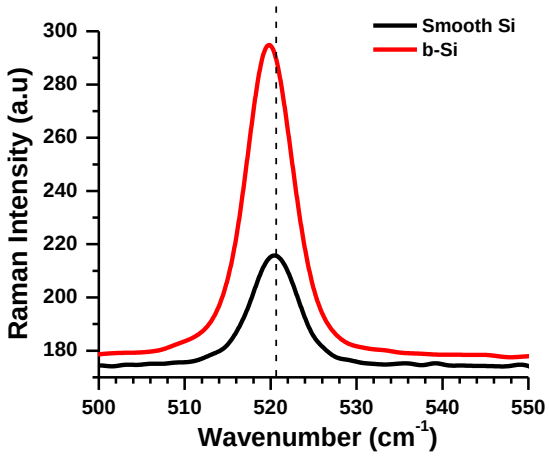

Figure 3.6: Comparison of Raman spectra for b-Si and smooth Si with laser excitation of 785 nm.

Nanocone array silicon solar cell

In order to demonstrate the photovoltaic application, single crystal p-n junction solar cells were created using SPERISE method. The fabrication process is shown schematically in Fig. 3.7 (a). First, the nanocone structure were formed on highly doped (0.001 – 0.005 Ω·cm) p-type monocrystalline silicon wafer (University Wafer) [11]. The p-n junction was formed by spin-on phosphorus doping processes (P509 Dopant from Filmtronics). After annealing at 950°C for 10 minutes, a radial junction with junction depth around 200nm was formed. For a conformal front

and back contact, ITO and Au sputtering were done respectively, followed by a rapid thermal annealing (RTA) at 400°C. Figure 3.7b, c show the I-V characteristics of nanocone black silicon and planar silicon control solar cells under AM 1.5G illumination. The average Jsc of planer solar cell are 32.2 mA/cm2 and that of nanotextured sc-Si solar cell was 35.9 mA/cm2 respectively. The Voc for nanocone and planer solar cells was found to be 631 mV and 610 mV respectively. The enhancement of Voc is due to more effective charge carrier collection through radial junction. The fill factor of 0.80 for nanocone solar cell was slightly higher than 0.78 of planar solar cell. We obtained an enhancement of 18.3% for the nanocone solar cell as compared to planar solar cell [11]. The corresponding external quantum efficiency (number of electrons produced per incident photon) is also measured. Figure 3.8 shows the comparison of external quantum efficiency (EQE) for planar (untextured) and nanocone (textured) single crystal solar cell. This shows that the loss of recombination has been improved for nanocone solar cell between 450 -850 nm. However, the EQE degrades at lower (< 450 nm) and higher (> 850 nm) wavelengths indicating higher surface recombination. We believe that carefully planning the height of nanopillar during the etching process and controlled passivation layer might further improve the solar cell efficiency.

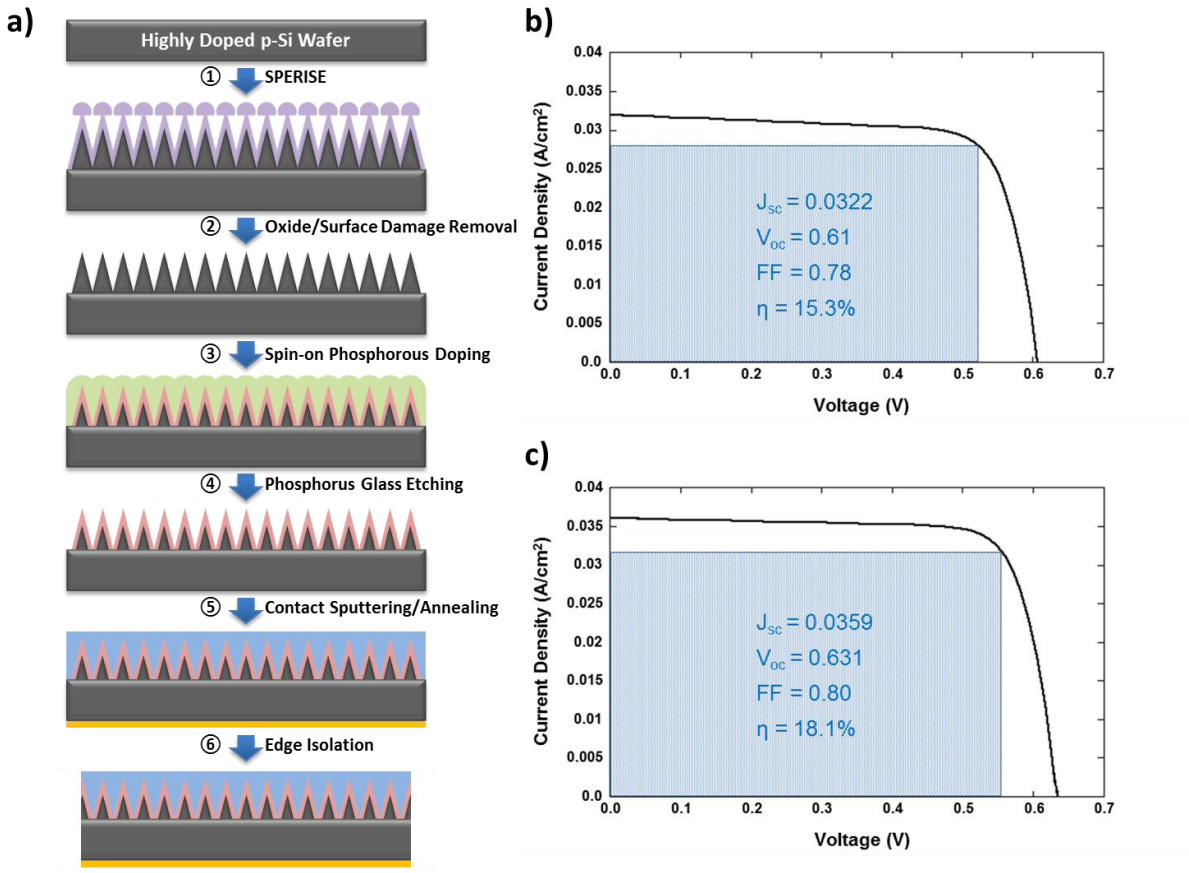

Figure 3.7: (a) Nanocone array solar cell fabrication process. I-V characteristics (b) before formation of nanocone arrays, (c) after formation of nanocone arrays. Image adapted from [11].

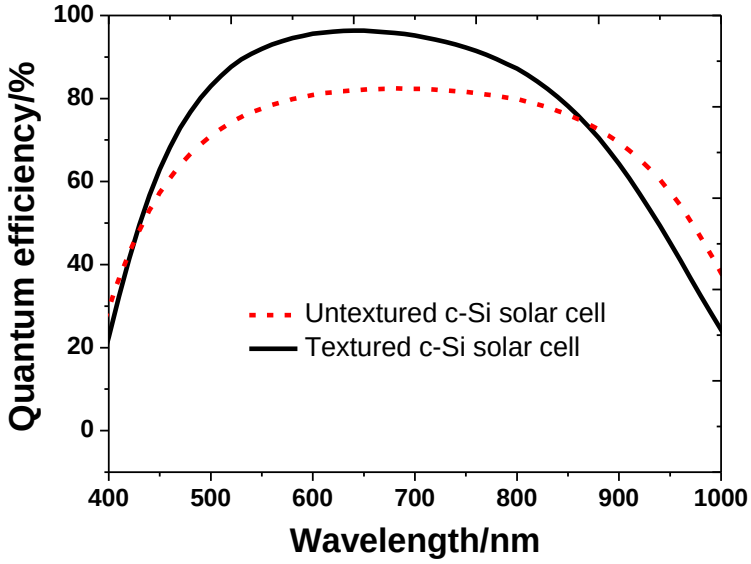

Figure 3.8: Comparison of external quantum efficiency (EQE) for planar (untextured) and nanocone (textured) single crystal solar cell.

Conclusions

In conclusion, we observe photoluminescence and cathodoluminescence from crystalline black silicon without additional thermal treatment. The PL and CL study shows three bands: the green band is associated with point defects, the red band is related to the surface and interface defects, and the infrared band can be attributed to the electronic transition between quantum confinement induced widened band gap in the vicinity of the sub-10 nm nanocone tip. Finally, XPS and AES study showed the presence of non-stoichiometric oxide layer forming Si/SiOx interface states responsible for room-temperature PL and CL. Our results indicate the potential applications of the sharp-tip nanocone black silicon structures in active silicon photonic devices. In addition, the nanocone black silicon substrate was used to fabricate photovoltaic cells. We obtained 18.3% enhancement in the conversion efficiency for textured solar cell as compared to non-textured planar solar cells.

References

[1] K. Peng, Y. Xu, Y. Wu, Y. Yan, S. Lee and J. Zhu, "Aligned single-crystalline Si nanowire arrays for photovoltaic applications," *Small,* vol. 1, pp. 1062-1067, NOV, 2005.

[2] F. Gu, L. Zhang, X. Yin and L. Tong, "Polymer single-nanowire optical sensors," *Nano Letters,* vol. 8, pp. 2757-2761, SEP, 2008.

[3] K. A. Sablon, "Polymer Single-Nanowire Optical Sensor," *Nanoscale Research Letters,* vol. 4, pp. 94-95, JAN, 2009.

[4] J. Wang, M. Gudiksen, X. Duan, Y. Cui and C. Lieber, "Highly polarized photoluminescence and photodetection from single indium phosphide nanowires," *Science,* vol. 293, pp. 1455-1457, AUG 24, 2001.

[5] O. Bisi, S. Ossicini and L. Pavesi, "Porous silicon: a quantum sponge structure for silicon based optoelectronics," *Surface Science Reports,* vol. 38, pp. 1-126, 2000.

[6] H. J. Xu, D. Y. Li and X. J. Li, "Electronic band structure and optical properties of silicon nanoporous pillar array," *Physica E-Low-Dimensional Systems & Nanostructures,* vol. 41, pp. 1882-1885, OCT, 2009.

[7] G. Broenstrup, N. Jahr, C. Leiterer, A. Csaki, W. Fritzsche and S. Christiansen, "Optical Properties of Individual Silicon Nanowires for Photonic Devices," *Acs Nano,* vol. 4, pp. 7113-7122, DEC, 2010.

[8] B. Piccione, C. Cho, L. K. van Vugt and R. Agarwal, "All-optical active switching in individual semiconductor nanowires," *Nature Nanotechnology,* vol. 7, pp. 640-645, OCT, 2012.

[9] P. Chaturvedi, K. H. Hsu, A. Kumar, K. H. Fung, J. C. Mabon and N. X. Fang, "Imaging of Plasmonic Modes of Silver Nanoparticles Using High-Resolution Cathodoluminescence Spectroscopy," *Acs Nano,* vol. 3, pp. 2965-2974, OCT, 2009.

[10] M. V. Zamoryanskaya and V. I. Sokolov, "Cathodoluminescence study of silicon oxide-silicon interface," *Semiconductors,* vol. 41, pp. 462-468, APR, 2007.

[11] H. Nishikawa, T. Shiroyama, R. Nakamura, Y. Ohki, K. Nagasawa and Y. Hama, "Photoluminescence from Defect Centers in High-Purity Silica Glasses Observed Under 7.9-Ev Excitation," *Physical Review B,* vol. 45, pp. 586-591, JAN 1, 1992.

[12] L. S. Liao, X. M. Bao, N. S. Li, X. Q. Zheng and N. B. Min, "Blue-, green-, and red-light emission from Si+-implanted thermal SiO2 films on crystalline silicon," *J Lumin,* vol. 68, pp. 199-204, MAY, 1996.

[13] J. Pezoldt, T. Kups, M. Stubenrauch and M. Fischer, "Black luminescent silicon," *Physica Status Solidi (C),* vol. 8, pp. 1021-1026, 2011.

[14] M. V. Zamoryarskaya, V. I. Sokolov and V. Plotnikov, "Cathodoluminescence study of Si/SiO2 interface structure," *Appl. Surf. Sci.,* vol. 234, pp. 214-217, JUL 15, 2004.

[15] C. Wu, C. H. Crouch, L. Zhao and E. Mazur, "Visible luminescence from silicon surfaces microstructured in air," *Appl. Phys. Lett.,* vol. 81, pp. 1999-2001, SEP 9, 2002.

[16] L. N. Dinh, L. L. Chase, M. Balooch, W. J. Siekhaus and F. Wooten, "Optical properties of passivated Si nanocrystals and SiOx nanostructures," *Physical Review B,* vol. 54, pp. 5029-5037, AUG 15, 1996.

[17] A. N. Trukhin, M. Goldberg, J. Jansons, H. -. Fitting and I. A. Tale, "Silicon dioxide thin film luminescence in comparison with bulk silica," *J. Non Cryst. Solids,* vol. 223, pp. 114-122, 1/1, 1998.

[18] T. D. Shen, I. Shmagin, C. C. Koch, R. M. Kolbas, Y. Fahmy, L. Bergman, R. J. Nemanich, M. T. McClure, Z. Sitar and M. X. Quan, "Photoluminescence from mechanically milled Si and SiO2 powders," *Physical Review B,* vol. 55, pp. 7615-7623, MAR 15, 1997.

[19] S. Kalem, P. Werner, O. Arthursson, V. Talalaev, B. Nilsson, M. Hagberg, H. Frederiksen and U. Sodervall, "Black silicon with high density and high aspect ratio nanowhiskers," *Nanotechnology,* vol. 22, pp. 235307, JUN 10, 2011.

[20] H. Wong, "Recent developments in silicon optoelectronic devices," *Microelectronics Reliability,* vol. 42, pp. 317-326, MAR, 2002.

[21] S. Godefroo, M. Hayne, M. Jivanescu, A. Stesmans, M. Zacharias, O. I. Lebedev, G. Van Tendeloo and V. V. Moshchalkov, "Classification and control of the origin of photoluminescence from Si nanocrystals," *Nature Nanotechnology,* vol. 3, pp. 174-178, MAR, 2008.

[22] T. Shimizuiwayama, S. Nakao and K. Saitoh, "Visible Photoluminescence in Si+-Implanted Thermal Oxide-Films on Crystalline Si," *Appl. Phys. Lett.,* vol. 65, pp. 1814-1816, OCT 3, 1994.

[23] Z. F. Ding, B. M. Quinn, S. K. Haram, L. E. Pell, B. A. Korgel and A. J. Bard, "Electrochemistry and electrogenerated chemiluminescence from silicon nanocrystal quantum dots," *Science,* vol. 296, pp. 1293-1297, MAY 17, 2002.

[24] R. J. Elliot and A. F. Gibson, *An Introduction to Solid State Physics and its Applications.* New York: Macmillan, 1974.

[25] Y. F. Zhang, L. S. Liao, W. H. Chan, S. T. Lee, R. Sammynaiken and T. K. Sham, "Electronic structure of silicon nanowires: A photoemission and x-ray absorption study," *Physical Review B,* vol. 61, pp. 8298-8305, MAR 15, 2000.

[26] F. Verpoort, P. Persoon, L. Fiermans, G. Dedoncker and L. Verdonck, "SiO2/Si(100) model support with AES and XPS in combination with MLCFA," *Journal of the Chemical Society-Faraday Transactions,* vol. 93, pp. 3555-3562, OCT 7, 1997.

[27] D. A. Zatsepin, P. Mack, A. E. Wright, B. Schmidt and H. -. Fitting, "XPS analysis and valence band structure of a low-dimensional SiO2/Si system after Si+ ion implantation," *Physica Status Solidi (a),* pp. n/a-n/a, 2011.

[28] K. Hirose, H. Nohira, K. Azuma and T. Hattori, "Photoelectron spectroscopy studies of SiO2/Si interfaces," *Prog Surf Sci,* vol. 82, pp. 3-54, 2007.

[29] C. D. Wagner, D. E. Passoja, H. F. Hillery, T. G. Kinisky, H. A. Six, W. T. Jansen and J. A. Taylor, "Auger and Photoelectron Line Energy Relationships in Aluminum-Oxygen and Silicon-Oxygen Compounds," *Journal of Vacuum Science & Technology,* vol. 21, pp. 933-944, 1982.

[30] T. Kantia, S. Aksela, P. Turunen, L. Partanen and H. Aksela, "KLL Auger decay of atomic silicon," *Journal of Physics B-Atomic Molecular and Optical Physics,* vol. 43, pp. 205002, OCT 28, 2010.

[31] J. A. Taylor, "Further Examination of the Si Kll Auger Line in Silicon-Nitride Thin-Films," *Appl. Surf. Sci.,* vol. 7, pp. 168-184, 1981.

[32] L. Khriachtchev, T. Nikitin, R. Velagapudi, J. Lahtinen and S. Novikov, "Light-emission mechanism of thermally annealed silicon-rich silicon oxide revisited: What is the role of silicon nanocrystals?" *Appl. Phys. Lett.*, vol. 94, pp. 043115, JAN 26 2009, 2009.

[33] R. S. Dubey and D. K. Gautam, "Fabrication and characterization of porous silicon layers for applications in optoelectronics," *Opt. Quant. Electron.*, vol. 41, pp. 189-201, FEB, 2009.

[34] F. Kozlowski and W. Lang, "Spatially Resolved Raman Measurements at Electroluminescent Porous N-Silicon," *J. Appl. Phys.*, vol. 72, pp. 5401-5408, DEC 1, 1992.

[35] Z. F. Sui, P. P. Leong, I. P. Herman, G. S. Higashi and H. Temkin, "Raman Analysis of Light-Emitting Porous Silicon," *Appl. Phys. Lett.*, vol. 60, pp. 2086-2088, APR 27, 1992.

[36] V. Paillard, P. Puech, M. A. Laguna, R. Carles, B. Kohn and F. Huisken, "Improved one-phonon confinement model for an accurate size determination of silicon nanocrystals," *J. Appl. Phys.*, vol. 86, pp. 1921-1924, AUG 15, 1999.

[37] Y. Chen, Z. Xu, M. R. Gartia, D. Whitlock, Y. Lian and G. L. Liu, "Ultrahigh Throughput Silicon Nanomanufacturing by Simultaneous Reactive Ion Synthesis and Etching," *Acs Nano*, vol. 5, pp. 8002-8012, OCT 2011, 2011.

CHAPTER 4

OPTICAL CHARACTERIZATION OF PLASMONICS DEVICES

Introduction

Surface plasmons are collective oscillation of surface bound charges due to interaction of electromagnetic waves (light) with that of free electrons. Plasmonics offer nanoscale confinement and localization of electromagnetic field. This property has been exploited for label-free surface plasmon resonance biosensing and surface enhanced Raman spectroscopy (SERS). Optical characterization of plasmonic device will provide information about the resonance behavior of the device which gives guidance about the operational regime and further improvement in the design of the sensor. Chapter 4 provides detail about the optical characterization performed on the plasmonic nanostructured devices. Here, two different plasmonic devices- one using silicon nanocone substrate, and the other one using polymer nanohole substrate will be presented.

Silicon nanocone based plasmonic substrate

The plasmonics substrate has been prepared in two steps. The first step involves preparation of the black silicon substrate (described in Chapter 2) using SPERISE nanomanufacturing process. In the second step, a thin layer of silver (80 nm) is deposited on top of the nanocone structures using e-beam evaporation to impart plasmonic property. For better adhesion of metal to the nanocone Si substrate, 5 nm of Ti layer was deposited before deposition of 80 nm Ag layer. Finally, further optical characterizations were carried out for plasmonic b-Si to probe its suitability for sensing applications. The reason for choosing silver over gold for our experiment is clear from Fig. 4.1. Gold is generally associated with high absorption losses (imaginary part of the complex dielectric function) compared to silver in the visible range (Fig. 4.1b) [74]. In fact, silver has the lowest losses in the visible spectrum with typical surface plasmon propagation distances of 10–100 μm [75].

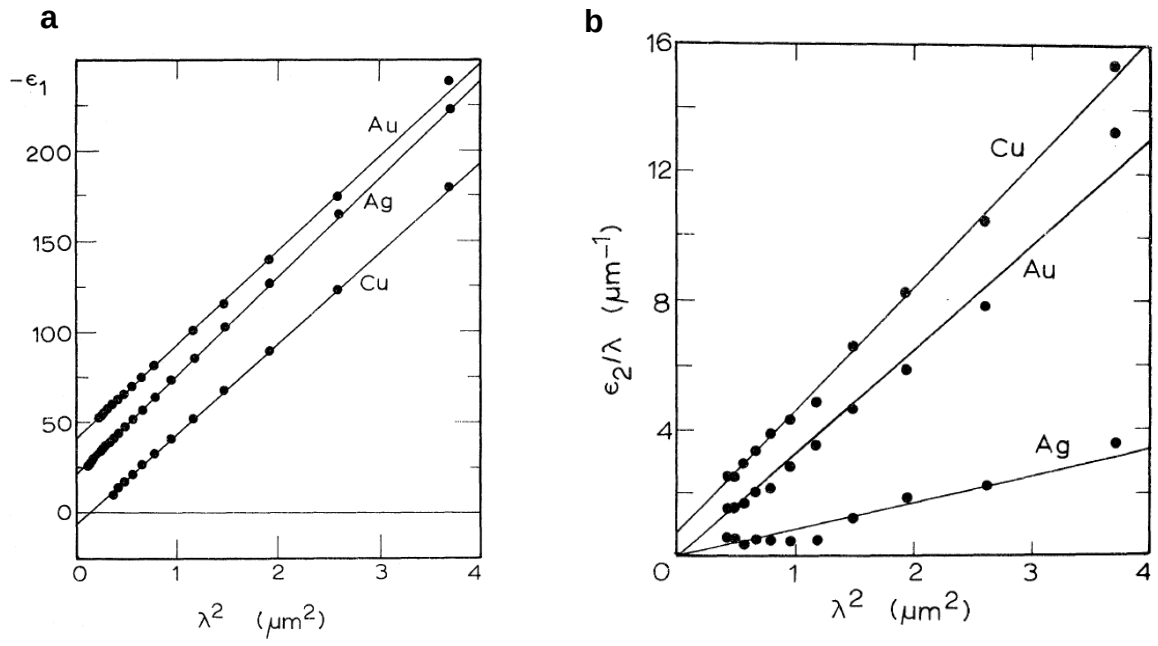

Figure 4.1: Comparison of optical properties for copper, silver and gold (a) real part of the complex dielectric function, (b) imaginary part of the complex dielectric function. Image adapted from [74].

Reflectance measurement of silicon nanocone based plasmonic substrate

Figure 4.2a shows the diffused reflectance measurement for silver coated nanocone structure in the visible range with normal incident (90^0) and unpolarized light using Varian Cary-5G equipped with integrating sphere. The observed low reflectance (< 20%) is due to b-Si surface roughness, where multiple reflections lead to strong, broad-band absorption and low reflectivity. This confirmed that most of the light incident on the nanoplasmonic substrate would be absorbed instead of reflecting back due to metal surface. A closer look at the reflectance spectrum of nanocone substrate with silver coating showed a sharp dip in the reflectivity at 317 nm (Fig. 4.2a) which corresponds to the bulk Plasmon for Ag [76]. Another dip in the reflectivity is visible at 615 nm. The inset of Fig. 4.2a also shows an SEM of the b-Si plasmonic structure. Figure 4.2b shows the angle dependent specular reflectance measurement performed using the home-made goniometer set up schematically shown in Fig. 3.1b. As shown in Fig. 4.2b, we observed higher reflectance at lower angle of incidence. We observed reflectance dip at 500 nm for 40^0 and 100^0 incident angle, a peak at 395 nm and a dip at 613 nm for 80^0 incident angles, two peaks at 430 nm and 735 nm for incident angle of 20^0 and resonance peak at 503 nm and 600 nm for incident angle of -20^0 and -40^0 respectively. The resonance dip at 615 nm observed in

normal (90^0) incident diffused reflectance measurement is quite similar to the measured resonance peak at 613 nm for 80^0 incident angle in the goniometric set up.

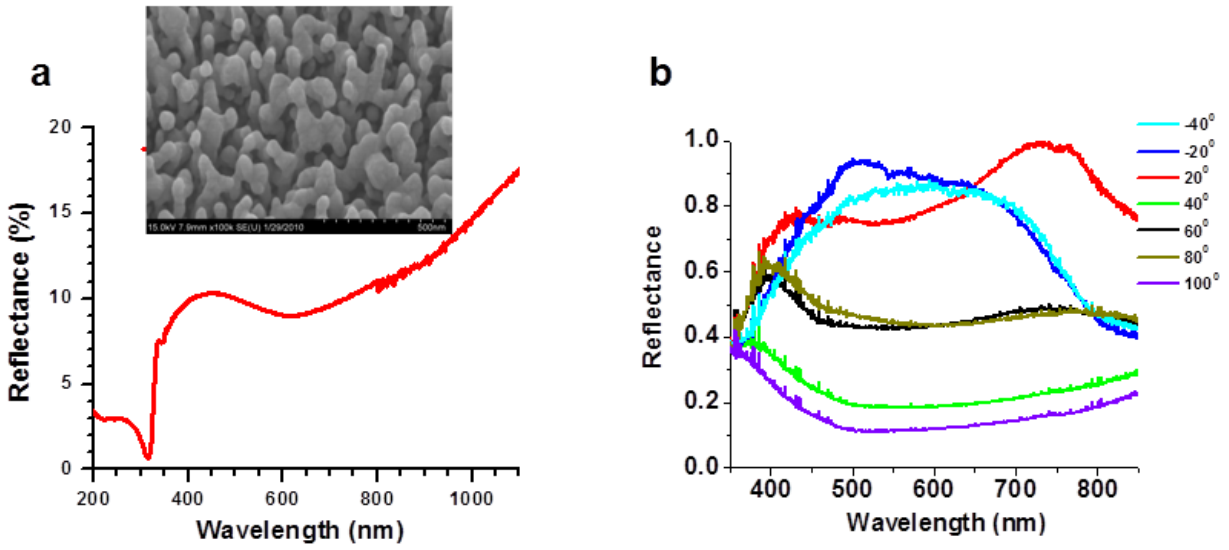

Figure 4.2: (a) Normal incident reflectance measurement for b-Si coated with 80 nm silver. (b) Angle dependent reflectance measurement for b-Si with 80 nm silver layer.

Cathodoluminescence measurement of silicon nanocone based plasmonic substrate

In cathodoluminescence (CL), when electrons beam impinges onto the metal surface, it creates a perturbation in the density of conduction electrons. This charge together with the incoming electron can be considered as an effective dipole. In case of a metal substrate the dipole can decay into two channels: direct emission into the far field (transition radiation) and generation of surface plasmons [77]. Further, in case of surface plasmon, when the excited electron comes down to original energy state, they have to give out photons for energy balance which is detected by CL detector [78]. Figure 4.3a-c shows the secondary electron images (SEI) of the nanoplasmonic structure and Fig. 4.3d-f show the corresponding panchromatic CL images. Figure 4.3g shows the line profiles from the regions indicated by dashed line in Fig. 4.3b and e. Similarly, Figure 4.3h shows the line profiles as indicated in Fig. 4.3c and f. Figure 4.3g clearly illustrates strong emission when electron beam is positioned at the center of the nanocone plasmonic structure and the intensity decreases as the electron beam moves away from the center. Also, the difference in SEI and CL image can be seen from the intensity profile. In between the edges of two nanopillar plasmonic structure for the SEI profile (Fig. 4.3g), there is

no intensity recorded (dark space in the SEI images), whereas some intensity peaks can be seen on the panCL intensity profile in the dark region due to surface plasmon propagation. Figure 4.3f clearly shows the electric field distribution due to excitation by electron beam at the center of the nanoplasmon region. In the current experimental set-up, for 15 keV electron beam the interaction length is calculated to be ~ 18 nm and spatial resolution of ~ 25 nm [79]. Therefore, we are able to spatially map the electric field distribution on an area of 100 nm x 100 nm as shown in Fig. 4.3f.

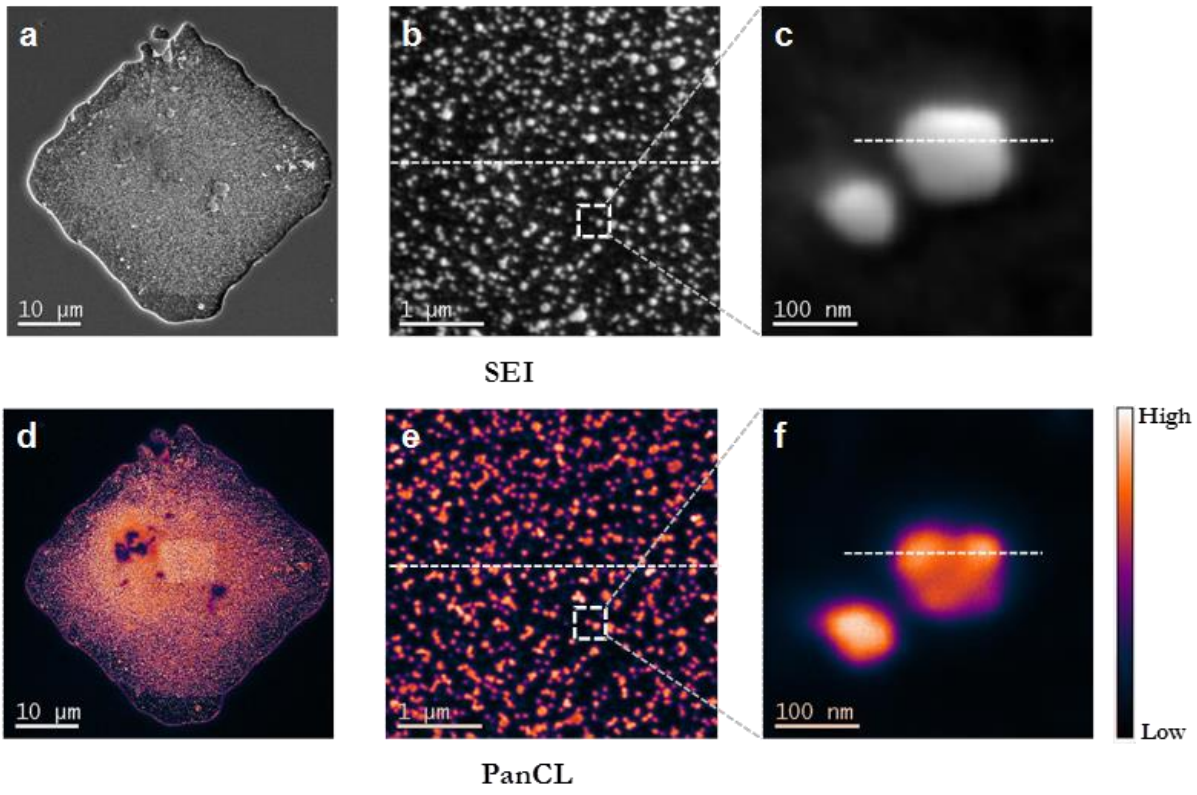

Figure 4.3: (a-c) SEI image of b-Si plasmonic structure. (d-f) Corresponding panCL images. (g) Comparison of SEI and CL intensity profile for b and e along the dashed line. (h) Comparison of SEI and CL intensity profile for c and f along the dashed line.

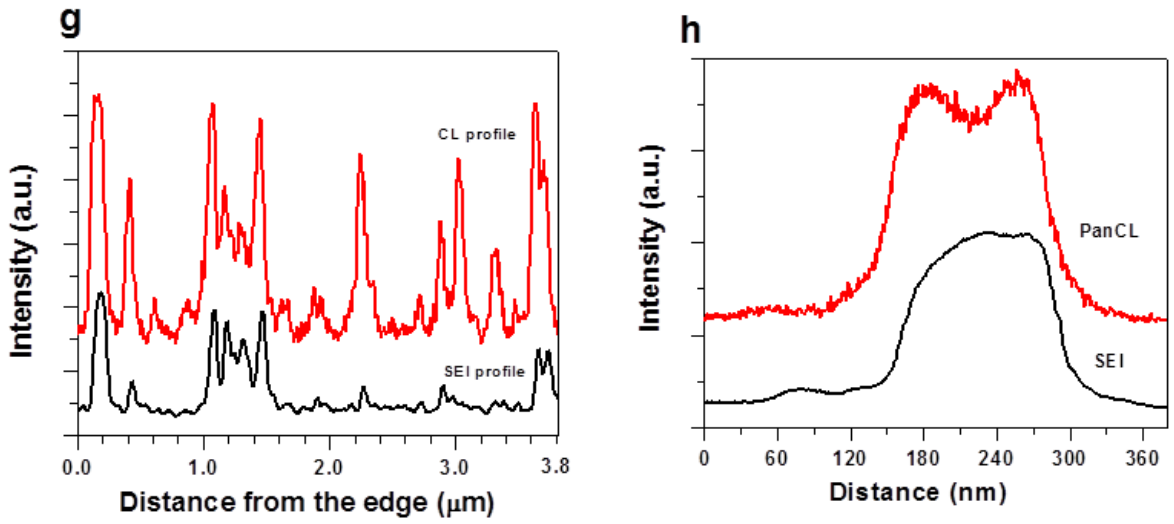

Figure 4.3 (cont.)

In order to confirm that our substrate can support surface plasmon we further carried out a through cathodoluminescence (CL) study. In traditional CL of semiconductors, the impingement of high-energy electron beam results in the excitation of valence electrons to the conduction band, leaving behind a hole. The detected photons in a CL spectroscopy experiment are a result of the recombination of electron-hole pairs. However, the detected photons in case of metallic nanostructure are a result of excited plasmons (collective motion of conduction electrons induced by fast moving electrons) [79]. The CL study for the nanocone structure showed that it can support a wide range of localized plasmonic modes and propagating surface modes. Fig. 4.4a shows a CL spectrum collected from the nanocone structure and smooth silver surface from an area of 1200 nm x 800 nm. The spectrum is corrected for grating response function. We observe a sharp peak at 331 nm and a small peak at 343 nm for the smooth silver surface. The sharp peak at 331 nm is generally attributed to the bulk plasmon peak and peak at 343 nm is generally the surface plasmon peak [79]. For nanopillar plasmonic structure we observe a sharp peak with much higher intensity than that of smooth surface at 363 nm, which corresponds to the surface plasmons at the silver-air interface [79]. In addition, light collected from larger area (60 μm x 40 μm), after the deconvolution of the experimental data and the Gaussian fit revealed several surface plasmon peaks at 410 nm, 472 nm, 654 nm and 754 nm, indicating that our sample can support resonance for broad range of wavelengths (Fig. 4.4b). Figure 4.4c describes the

Panchromatic CL image (pseudo colored) of the same area showing the intensity of surface and localized plasmon resonance. The figure clearly showed many “hot spots” for our nanocone substrate. The difference in the plasmon resonance mode observed in reflectance spectra and CL spectra may be due to the source of excitation for the plasmon. Light excitation can couple to low frequency plasmon eigen modes, but may not excite all high frequency modes due to large momentum mismatch [80]. On the other hand, electron excitation can couple to high frequency modes [81]. Combined with the CL data, it can be inferred that the nanocone substrate has the surface plasmon band in between 1.55-3.1 eV (around 400-800 nm).

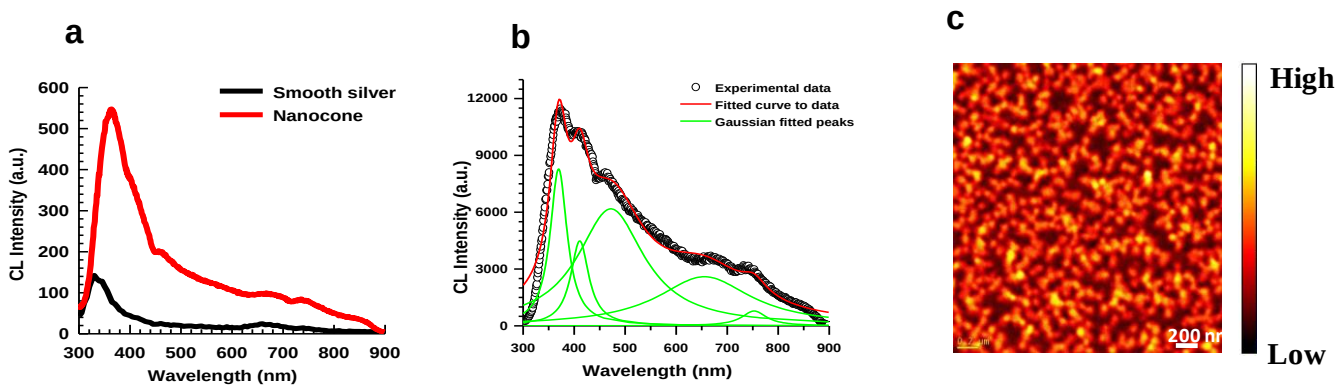

Figure 4.4: Optical characterizations of the substrate (a, b) Cathodoluminescence (CL) spectrum collected from a nanocone structure. The spectrum is corrected for grating response function. (c) Panchromatic CL image (pseudo colored) of the same area showing the intensity of surface and localized plasmon resonance.

Fluorescence enhancement measurement of silicon nanocone based plasmonic substrate

To demonstrate the utility of our substrate for sensing applications, we carried out fluorescence measurement on the substrate. First we patterned the square array region as shown in Fig. 4.5a using conventional photolithography technique where the positive photoresist is exposed and developed away. The exposed square silicon area not protected by photoresist is then turned into b-Si area using the SPERISE process described in Chapter 2. To render with plasmonic property we deposit 80 nm of silver on the substrate. An optical image of nanoplasmonic substrate is shown in Fig. 4.5a. The inset also shows the prepared sensor substrate. For the fluorescence experiment, we deposit 5µl of Rhodamine-6G (R6G) solution

with the concentration of 10 μM on both b-Si plasmonic substrate and glass slide, wait until dry and excite the fluorescence with green light (550 nm center wavelength). The image is taken with a microscope objective lens with 20x magnification and numerical aperture (NA) of 0.5. The intensity distribution is captured with a black and white CCD camera. In Fig. 4.5b and c, we present the pseudo-color fluorescence emission intensity image for the nanoplasmonic and glass substrate respectively. Figure 4.5f compares the fluorescence intensity of the images shown in Fig. 4.5b and c along the dashed line. It is clear that the intensity on the b-Si plasmonic region is much higher than the surrounding smooth silver region, and the glass substrate. Further, Fig. 4.5d shows the comparison of fluorescence emission spectra over the entire microscopic field of view (400μm x 400μm) taken on b-Si plasmonic substrate and regular glass slide, all captured with the integration time of 5 seconds. We obtain the fluorescence enhancement on the b-Si plasmonic substrate to be 40 times with respect to glass slide. Unlike most plasmonic metal nanostructures where the fluorescence emission photon is not likely to be trapped in the structure, in the case of b-Si plasmonic structure substrate, most of the fluorescence emission photons from R6G molecules should be mostly trapped within the nanocone forest without being acquired by the imaging or spectroscopy system. Even with such potential loss, we still observed ~40 times fluorescence enhancement [82]. Further, it is well known that there is strong interaction between surface plasmon and excited state of fluorophore, and hence we are expected to see modification in fluorophore properties such as lifetime and quantum yield on nanostructured surfaces. In fact, from our Fluorescence Lifetime Imaging Microscopy (FLIM), shown in Fig. 4.5e, we observed a reduction in lifetime of R6G from intrinsic 4.11 ns to around 0.5 ns on nanoplasmonic substrate. The enhancement in fluorescence intensity and at the same time the reduction in the fluorescence lifetime is good for the stability of fluorophore as it has to spend less time at the excited state after each excitation.

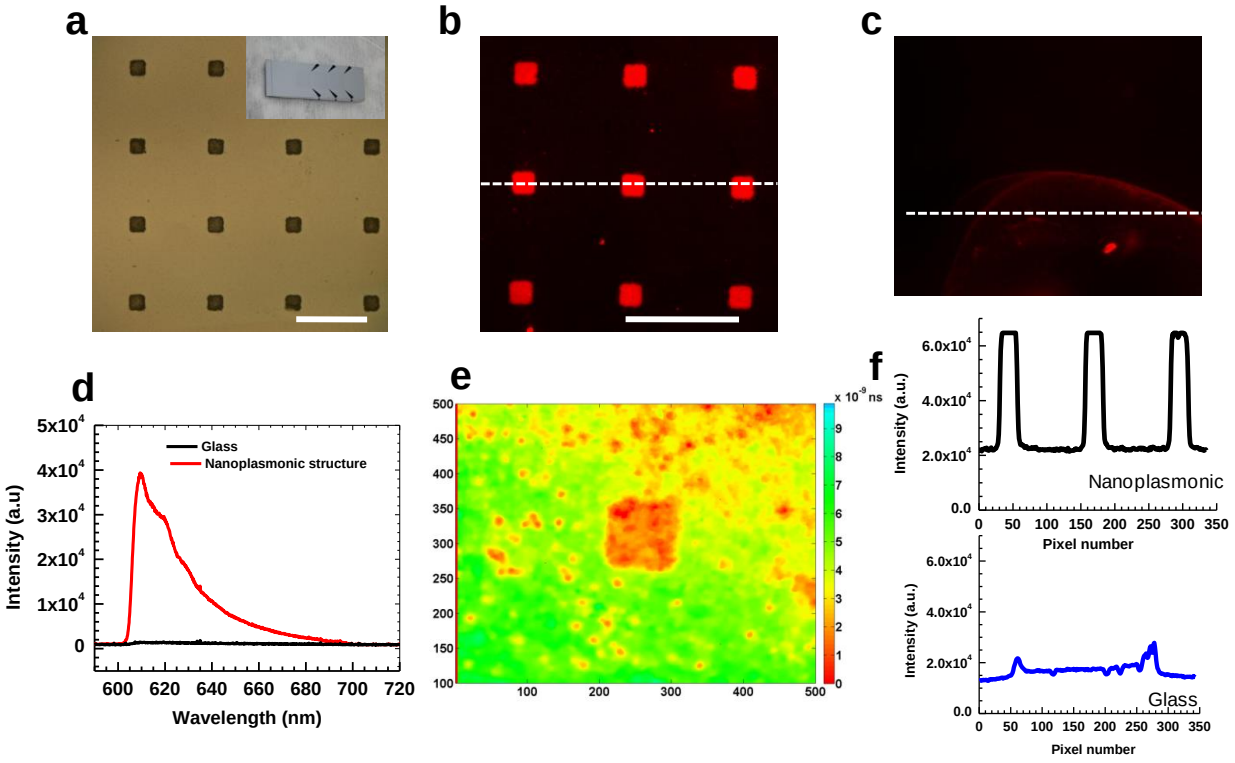

Figure 4.5: (a) Optical image of the b-Si plasmonic sensor. Inset shows the fabricated structure. The scale bar is 300 µm. (b) Fluorescence image of the R6G coated b-Si plasmonic substrate. The scale bar is 300 µm. (c) Fluorescence image of the R6G coated glass slide. (d) Fluorescence spectroscopy plot for glass and R6G coated b-Si plasmonic substrate. (e) Fluorescence Lifetime Imaging Microscopy (FLIM) for R6G coated plasmonic substrate. (f) Comparison of fluorescence intensity for b and c along dashed line.

Nanohole based plasmonic substrate

As discussed in Chapter 3, we employ the nanoimprint method to produce nanohole based plasmonic device on plastic substrate. Metal (Ag or Au) was deposited on the device by electron beam evaporation, producing metal surface on the rim of the holes, on the bottom of the holes and also nanoparticles-like structure on the sidewalls of the holes. In order to investigate the plasmonic properties of the nanohole substrate, transmission experiment with normal and angle dependent incident light are performed.

Normal incident transmission experiment

The optical properties of nanohole substrate is characterized by illuminating the device under normal incidence and collimated white light source and collecting the transmitted light

using a spectrometer. The schematic of the transmission and reflection mode is shown in Fig. 4.6.

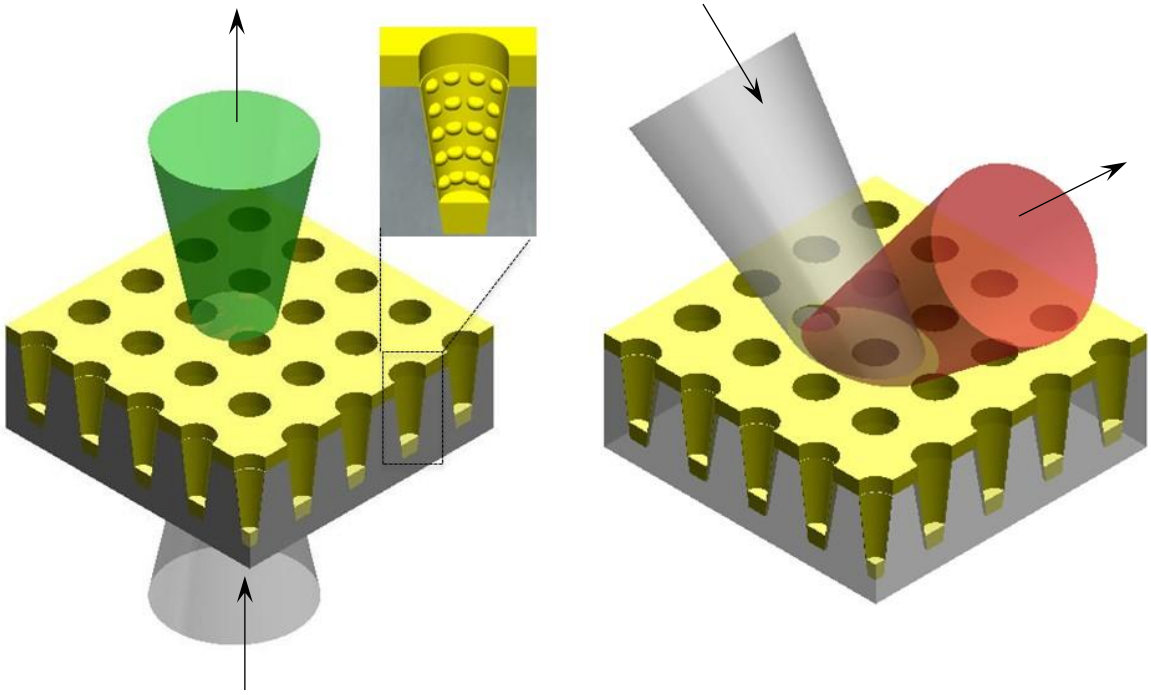

Figure 4.6: Schematic showing the nanohole plasmonic substrate in transmission and reflection mode; inset shows the nanoparticles along the sidewalls of the cup structure.

The transmission spectra are collected using Varian Cary 5G UV-Vis-NIR spectrophotometer (spectral bandwidth = 1 nm, data interval = 1 nm) with normal incidence transmission mode. The zeroth order transmission spectrum for Ag-air interface (n=1) reveals a bulk plasmon peak (Fig. 4.7) for silver at λ=320 nm [79]. The peak at λ=381 nm in Fig. 4.7 is predicted to be due to surface plasmon polariton- Bloch wave (SPP-BW) (1,0) mode at Ag-air interface (n=1) using equation (1). The SPP-BW and Wood's anomaly (WA) (due to the diffraction of light parallel to the surface) [83, 84] for a rectangular lattice structure can be approximately calculated using the relation [85]:

$$\lambda_{SPP-BW} = \frac{p}{\sqrt{i^2 + j^2}} \sqrt{\frac{\varepsilon_{Ag}(\lambda)\varepsilon_d}{\varepsilon_{Ag}(\lambda) + \varepsilon_d}} \qquad (1)$$

$$\lambda_{WA} = \frac{p}{\sqrt{i^2 + j^2}} \sqrt{\varepsilon_d} \qquad (2)$$

where, i and j are the order of SPP-BW or WA, p is the pitch and ε is the complex dielectric constant. The dip at λ=350 nm is due to (1,0) WA at Ag-air interface. The plasmonic band of (1,0) Ag-PET is predicted to be at λ= 600 nm using equation (1).

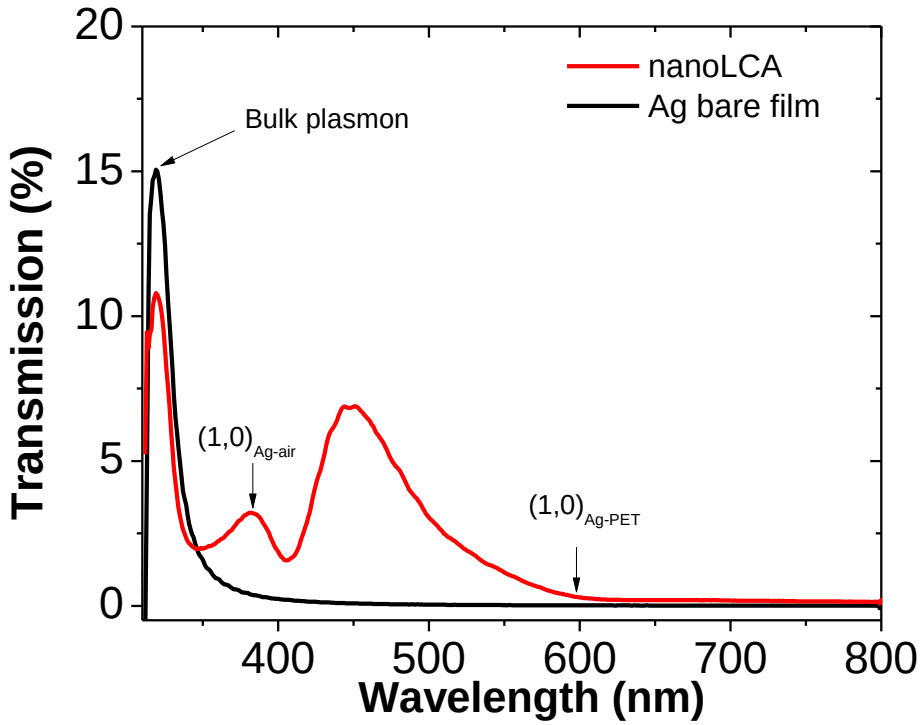

Figure 4.7: Zero order transmission spectra of Ag bare film (t = 90 nm) on PET substrate (black curve) and nanohole plasmonic substrate (t = 90 nm, h = 500 nm, p = 350 nm) (red curve).

In order to identify the origin of peak at 450 nm, resonance position of SPP-BW and WA are predicted using equation (1) and (2). The solid line in Fig. 4.8a corresponds to SPP-BW prediction results (equation (1)) and the dotted line corresponds to WA (equation (2)) prediction results. The red curves are for (1,0) modes and the black curve is for (1,1) modes. The scatter symbols are from the experiments and the positions are shown in Fig. 4.8b (P: Peak; D: Dip). All the Peak-2 experimental data correlates well with the (1,0) WA of Ag-Superstrate interface. Similarly, all the Dip-3 data are due to (1,0) SPP-BW at Ag-Superstrate and Dip-1 are due to WA (1,1) Ag-Substrate (n=1.56) interface. However, Peak-3 did not correlate well with either

SPP-BW or WA. The intense peak at λ=450 nm cannot be predicted by any lowest order SPP-BW or WA from the calculation.

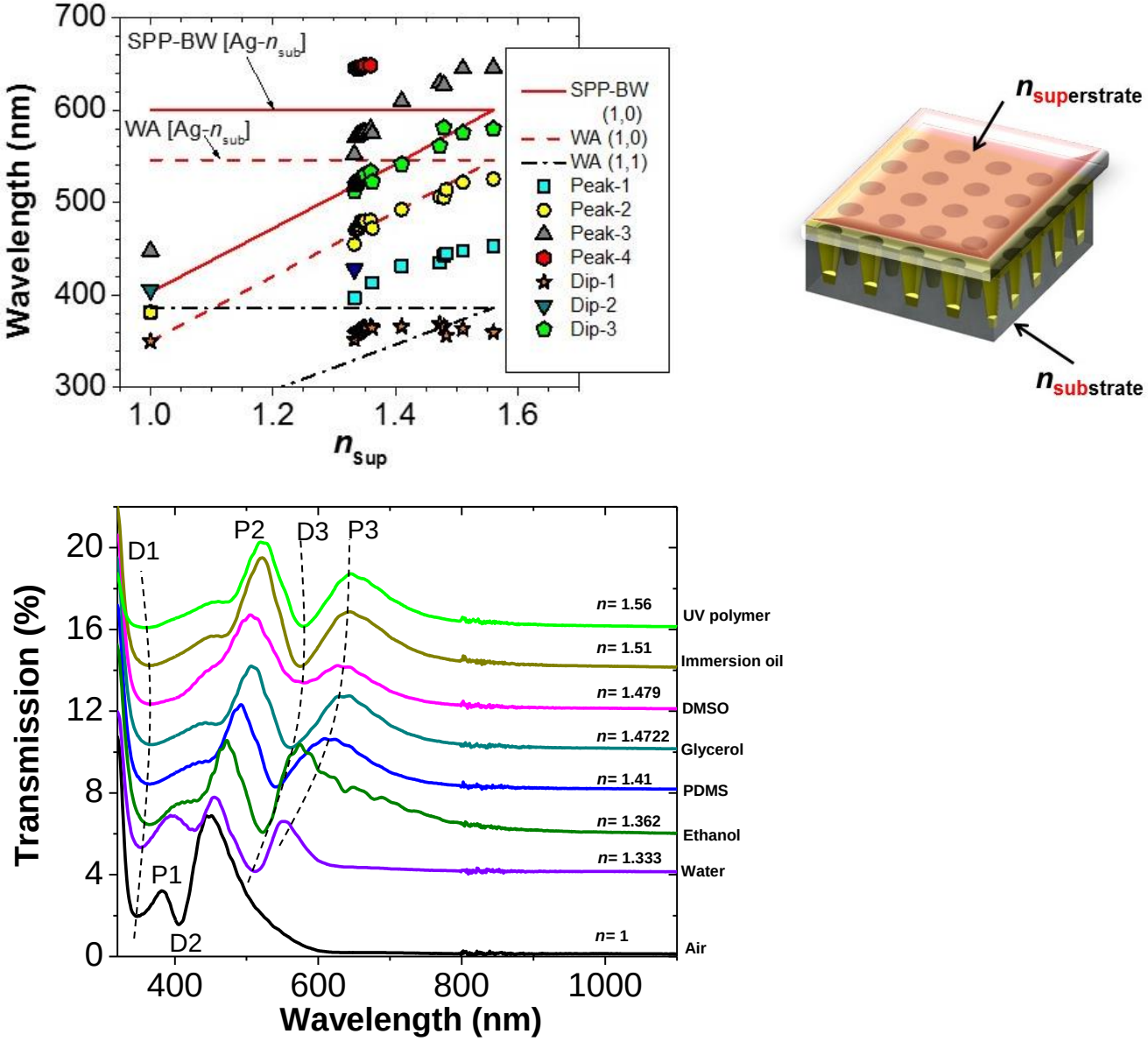

Figure 4.8: Prediction of surface plasmon polariton-Bloch wave (SPP-BW) and Wood's anomaly (WA).

Since the nanohole also contains nanoparticles structure inside, we wanted to verify whether the peak at 450 nm is related to the scattering modes of the nanoparticles. The dispersion contour was constructed by calculating the scattering spectra of the nanoparticle with varying surrounding medium (at an interval of 0.01 refractive-index unit, RIU) from n=1 to n=3. The experimental peak of λ= 450 nm can be observed corresponding to the simulated scattering

spectra for the nanoparticle with surrounding refractive index of n = 1.56 (same refractive index as PET substrate with UV-polymer). The corresponding point is shown with blue dotted line in Fig. 4.9. This gives further indication that the peak at λ= 450 nm is a LSPR mode.

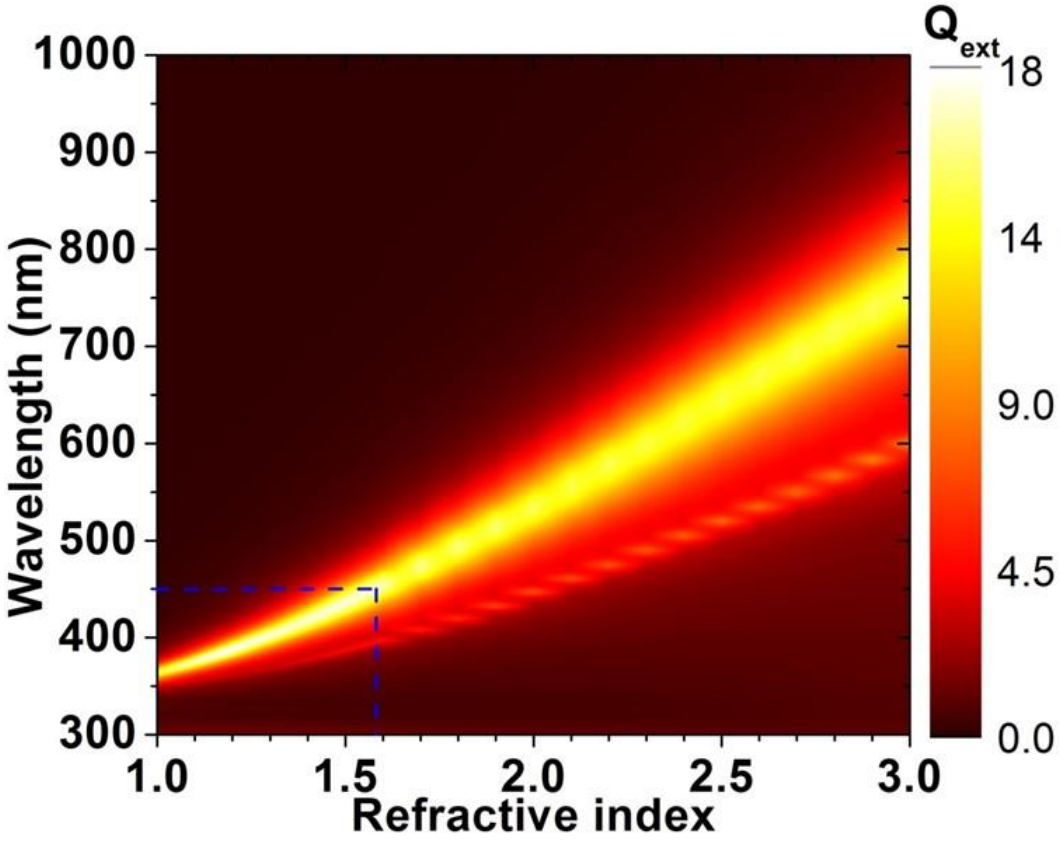

Figure 4.9: Variation of extinction coefficient for nanoparticle (*d* = 50 nm) with surrounding refractive indices using Mie scattering theory.

Transmission spectra with variation of refractive index

Figure 4.10 shows the spectroscopic results of the refractive index sensing on the nanohole plasmonic structure. The zeroth order transmission spectrum for Ag-air interface (*n* =1) reveals a bulk plasmon peak (Fig. 4.7) for silver at λ =320 nm. Upon changing the refractive index of the superstrate from air (*n* = 1) to higher refractive indices solutions, the result showed that the bulk plasmon peak at λ = 320 nm remains unchanged (Fig. 4.10); the SPP-BW and WA features are red shifted, and the Mie scattered LSPR peak was red shifted by 100 nm for water (*n* =1.333) and by almost 200 nm for immersion oil (*n* =1.51).

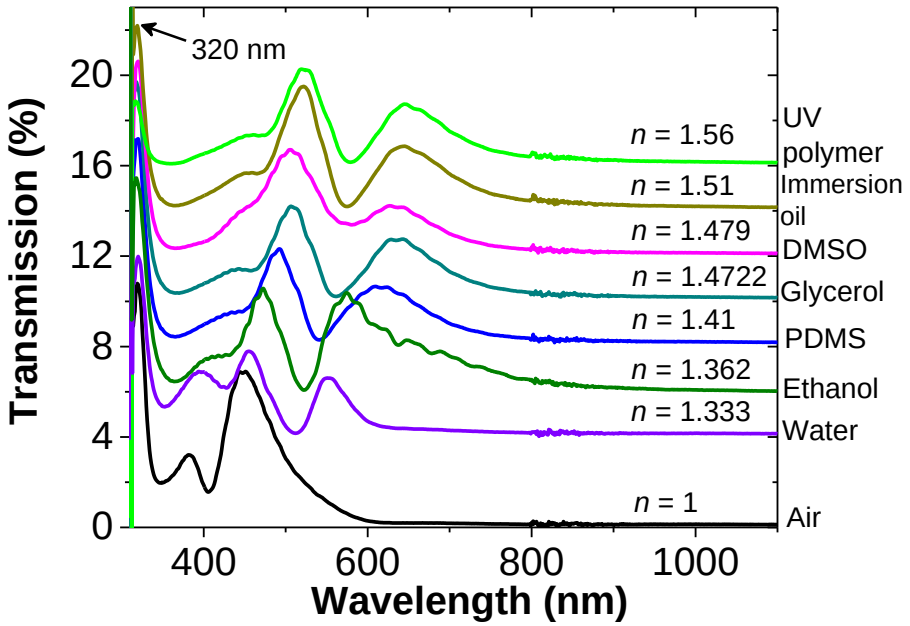

Figure 4.10: Optical properties of nanohole plasmonic substrate. Zero-order transmission spectra of sensor (h = 500, p = 350 and t = 90 nm) with different refractive index chemicals.

Transmission and reflection spectra with variation of depth

Further detailed optical characterization was carried out to reveal the property of nanohole plasmonic substrate. Figure 4.11- 4.14 demonstrate the ability to control the resonance peak position by changing the height, h, the pitch, p and the materials independently. Figure 4.11a shows the effect of nano cup depth on the quality-factor (Q-factor) of the sensor device. As we increase the depth, the Q-factor increases as shown by the increase in transmitted light. The reflectance spectra were also obtained in an inverted microscope (Zeiss Axio Observer D1) equipped with 100 W halogen light source. The light was focused on to the sample with 20x objective (NA=0.45) and the reflected light were collected by a silicon photodiode array (PDA) spectrometer (300-900 nm). Figure 4.11b shows the reflectance spectra of nanohole substrate with different depth, h. The reflectance dip becomes sharper (higher Q-factor) with the increase of h.

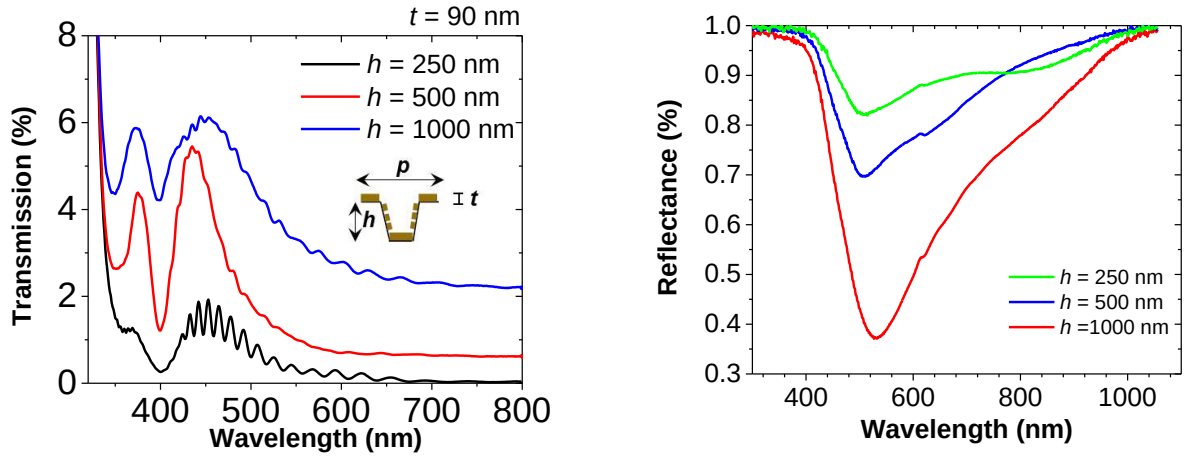

Figure 4.11: (a) Transmission spectra of nanohole plasmonic substrate with different height of nano cup, h = 250 nm (black), h = 500 nm (red), and h = 1000 nm (blue). (b) Reflectance spectra of nanohole plasmonic substrate with different height of nano cup. For all the devices the thickness of Ag was t = 90 nm.

Transmission spectra with variation of thickness of metal

Figure 4.12a shows the effect of increasing the thickness of metal layer on transmission intensities while keeping the depth of the nanohole same (h = 500 nm). The transmission intensity can be tuned by changing the metal thickness, t. The transmission intensity decreases with increase in the thickness. Figure 4.12b shows the corresponding variation of transmission intensities with metal thickness for h = 1000 nm nanohole depth.

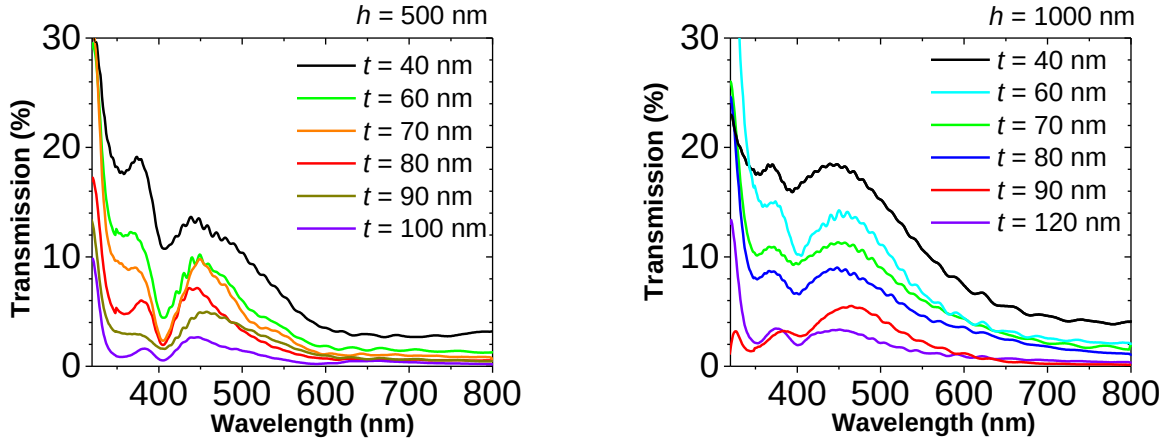

Figure 4.12: (a) Transmission spectra for nanohole substrate with different Ag thickness (t = 40-100 nm). For all the devices the height of nano cup was h = 500 nm. (b) Transmission spectra for nanohole

substrate with different Ag thickness (t = 40-120 nm). For all the devices the height of nano cup was h = 1000 nm.

Effect of variation of pitch

Figure 4.13 shows the effect of variation of the pitch on transmission property of the plasmonic device. The transmission spectrum red shifted with increase in the pitch. This shows that the resonance peak position can be tuned by using different pitch dimension. This is also obvious from equation (1), where the SPP-BW resonance wavelength is directly proportional to the pitch.

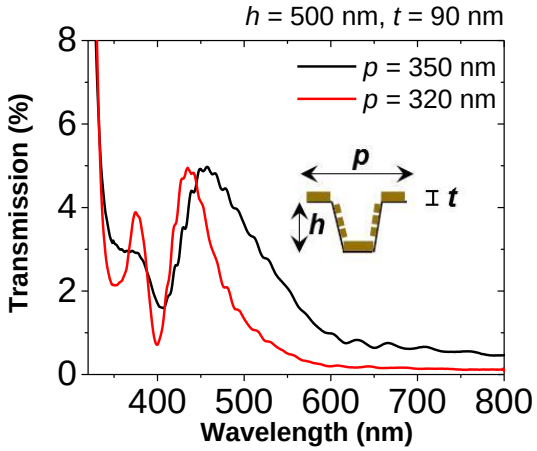

Figure 4.13: Transmission spectra of nanohole device with two different pitch of nano cup, p = 320 nm (red), p = 350 nm (black). The transmission spectrum red shifted with increase in the pitch.

Effect of variation of materials

Equation (1) shows that the SPP-BW resonance is also a function of the dielectric properties of the metal layer. Hence, the resonance position can be tuned by changing the top metallic layer over the plasmonic sensor. Figure 4.14 shows that by changing the metal from Ag to Au, we can change the resonance of the substrate from λ = 450 nm to λ = 532 nm.

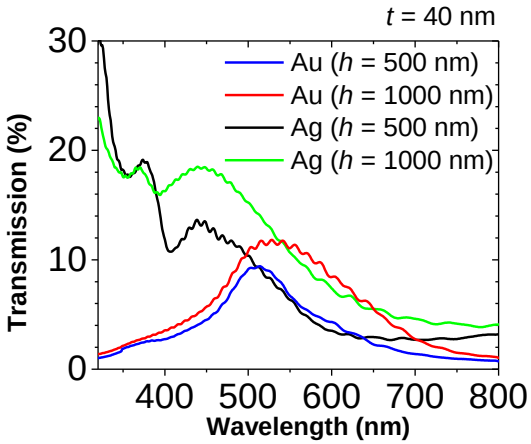

Figure 4.14: Transmission spectra with Ag (40 nm) and Au (40 nm) for two different height of nano cup (*h* = 500 nm and *h* = 1000 nm).

Angle dependent transmission spectra

The angle and polarization dependent transmission spectra were obtained by J.A. Woollam Co. variable angle spectroscopic ellipsometer. For the dispersion diagram (angle-wavelength), the transmission spectra were taken at 1^0 intervals. The angular and polarization dependent property of plasmonic substrate are shown in Fig. 4.15- 4.18. In normal transmission ($\theta = 0^0$), the transmission spectrum show two pronounced peaks at λ = 381 nm and λ = 450 nm. However, with increasing angle of incidence from $\theta = 0^0$ to $\theta = 60^0$, the intensity of peak at λ = 381 nm gradually decreases for s- polarization. Also, the peak at λ = 450 nm blue-shifted to higher energy upon increasing the incident angle for s-polarization. However, for *p*-polarization both the peaks at λ = 381 nm and λ = 450 nm shifted to lower energy (red shifted) with the increase in incidence angle. Also, for p-polarization, the coupling to SPP-BW becomes much stronger than the LSPR modes with increasing the angle of incidence. The appearance of λ = 450 nm peak for s-polarization gives further indication that the peak at λ = 450 nm is a localized surface plasmon resonance (LSPR) peak as SPP should not be excited efficiently by s-polarized incident light.

p-polarization (h=500 nm)

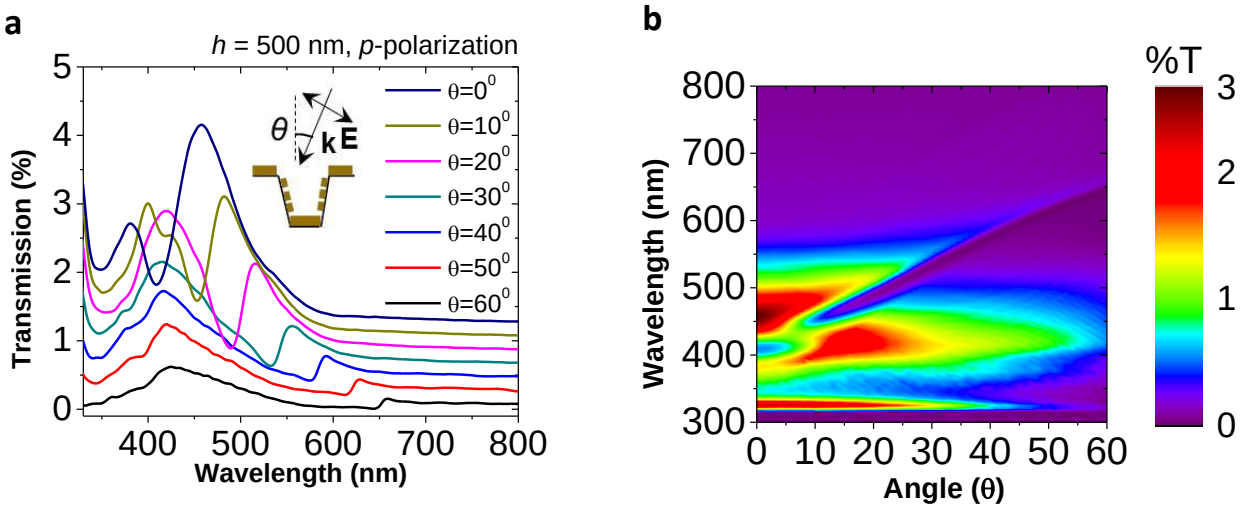

Figure 4.15: (a) Measured transmission spectra of nanohole plasmonic substrate in *p*-polarized light. The incident angle was varied from $\theta = 0^0$ to $\theta = 60^0$. (b) The corresponding dispersion curve for *p*-polarization is presented as a contour plot. The height of nano cup is $h = 500$ nm.

s-polarization (h=500 nm)

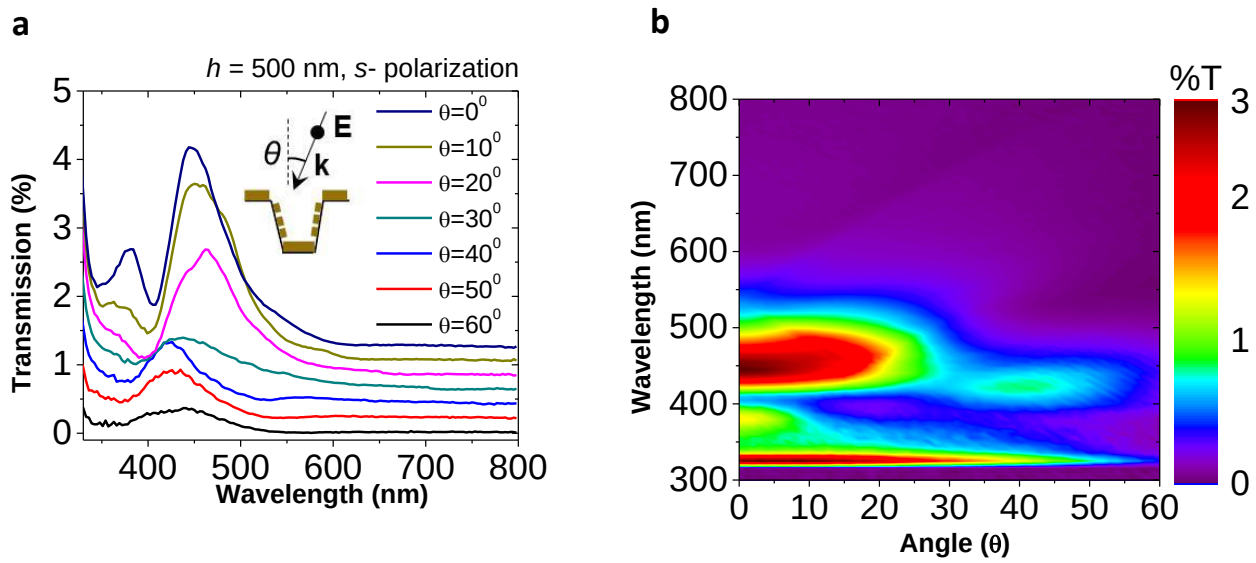

Figure 4.16: (a) Measured transmission spectra of nanohole plasmonic substrate in *s*-polarized light. The incident angle was varied from $\theta = 0^0$ to $\theta = 60^0$. (b) The corresponding dispersion curve for *s*-polarization is presented as a contour plot. The height of nano cup is $h = 500$ nm.

p-polarization (h=1000 nm)

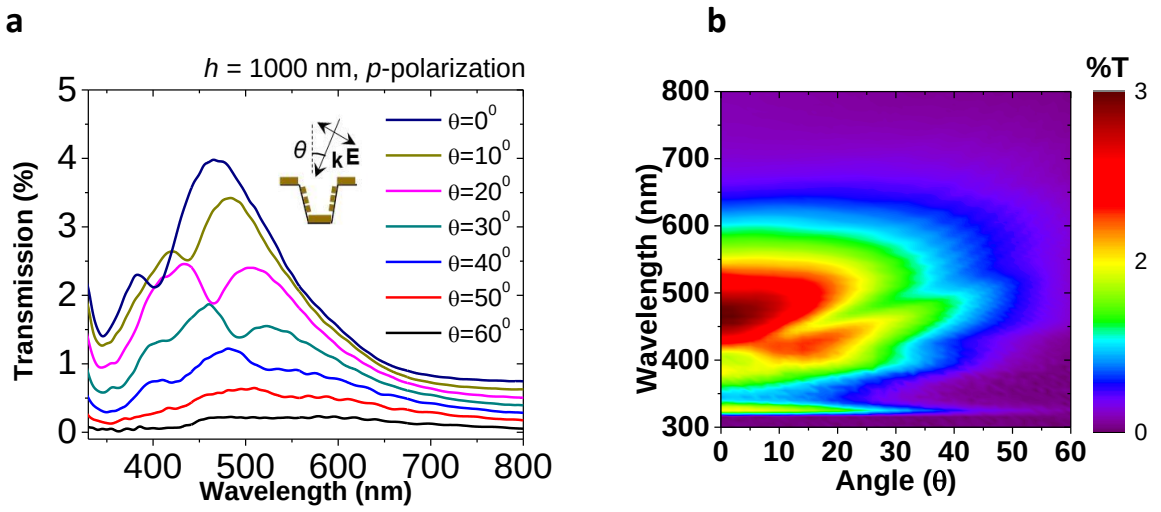

Figure 4.17: (a) Measured transmission spectra of nanohole plasmonic substrate in *p*-polarized light. The incident angle was varied from θ = 0^0 to θ = 60^0. (b) The corresponding dispersion curve for *p*-polarization is presented as a contour plot. The height of nano cup is *h* = 1000 nm.

s-polarization (h=1000 nm)

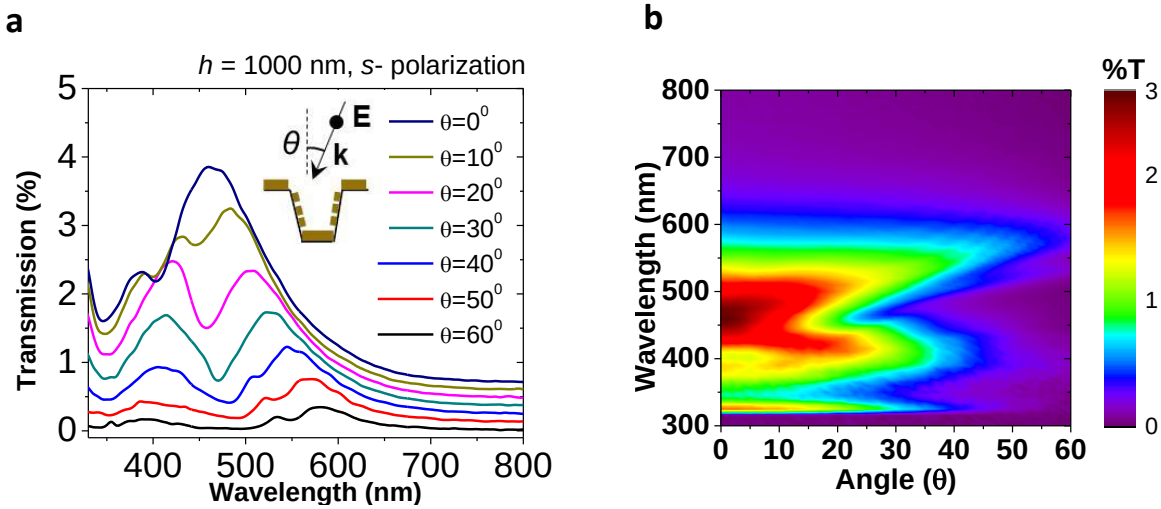

Figure 4.18: (a) Measured transmission spectra of nanohole plasmonic substrate in *s*-polarized light. The incident angle was varied from θ = 0^0 to θ = 60^0. (b) The corresponding dispersion curve for *s*-polarization is presented as a contour plot. The height of nano cup is *h* = 1000 nm.

Conclusion

In summary, we have fabricated plasmonic substrate based on nanocone black silicon structure and nanohole polymer substrate on wafer scale with a mass producible nanomanufacturing method. We obtained fluorescence enhancement of ~40 times on the nanocone plasmonic substrate. The CL characteristics showed that the nanocone substrate efficiently scatters light in the near field and supports good surface plasmon resonance property. From the FLIM results we got a shorter lifetime on the plasmonic substrate, which means fluorophore has less available time for photochemistry while in the excited state and hence more excitation-emission cycles before photo bleaching. Overall, we have demonstrated the potential of b-Si based plasmonics for sensing applications. We carried out detailed optical characterization of nanohole based plasmonic substrate. The plasmonic resonance wavelength can be independently tuned by changing the height, *h*, the pitch, *p* and the materials of the plasmonic substrate. The normal incident, angle dependent, and polarization dependent transmission spectra revealed that the major resonance wavelength (λ = 450 nm) is due to the LSPR mode of the nanoparticles inside the nanohole structures.

References

[1] P. Johnson and R. Christy, "Optical Constants of Noble Metals," *Physical Review B,* vol. 6, pp. 4370-4379, 1972.

[2] W. L. Barnes, A. Dereux and T. W. Ebbesen, "Surface plasmon subwavelength optics," *Nature,* vol. 424, pp. 824-830, AUG 14 2003, 2003.

[3] H. F. Ghaemi, T. Thio, D. E. Grupp, T. W. Ebbesen and H. J. Lezec, "Surface plasmons enhance optical transmission through subwavelength holes," *Physical Review B,* vol. 58, pp. 6779-6782, SEP 15 1998, 1998.

[4] M. Kuttge, E. J. R. Vesseur, A. F. Koenderink, H. J. Lezec, H. A. Atwater, F. J. Garcia de Abajo and A. Polman, "Local density of states, spectrum, and far-field interference of surface plasmon polaritons probed by cathodoluminescence," *Physical Review B,* vol. 79, pp. 113405, MAR, 2009.

[5] F. J. Garcia de Abajo, "Optical excitations in electron microscopy," *Reviews of Modern Physics*, vol. 82, pp. 209-275, JAN-MAR, 2010.

[6] P. Chaturvedi, K. H. Hsu, A. Kumar, K. H. Fung, J. C. Mabon and N. X. Fang, "Imaging of Plasmonic Modes of Silver Nanoparticles Using High-Resolution Cathodoluminescence Spectroscopy," *Acs Nano*, vol. 3, pp. 2965-2974, OCT, 2009.

[7] H. Raether, "Surface-Plasmons on Smooth and Rough Surfaces and on Gratings," *Springer Tracts Mod. Phys.*, vol. 111, pp. 1-133, 1988.

[8] F. J. G. de Abajo and M. Kociak, "Probing the photonic local density of states with electron energy loss spectroscopy," *Phys. Rev. Lett.*, vol. 100, pp. 106804, MAR 14, 2008.

[9] Z. Xu, Y. Chen, M. R. Gartia, J. Jiang and G. L. Liu, "Surface plasmon enhanced broadband spectrophotometry on black silver substrates," *Appl. Phys. Lett.*, vol. 98, pp. 241904, JUN 13 2011, 2011.

[10] A. G. Brolo, R. Gordon, B. Leathem and K. L. Kavanagh, "Surface plasmon sensor based on the enhanced light transmission through arrays of nanoholes in gold films," *Langmuir*, vol. 20, pp. 4813-4815, JUN 8 2004, 2004.

[11] J. M. McMahon, J. Henzie, T. W. Odom, G. C. Schatz and S. K. Gray, "Tailoring the sensing capabilities of nanohole arrays in gold films with Rayleigh anomaly-surface plasmon polaritons," *Optics Express*, vol. 15, pp. 18119-18129, DEC 24 2007, 2007.

[12] M. E. Stewart, N. H. Mack, V. Malyarchuk, J. A. N. T. Soares, T. Lee, S. K. Gray, R. G. Nuzzo and J. A. Rogers, "Quantitative multispectral biosensing and 1D imaging using quasi-3D plasmonic crystals," *Proc. Natl. Acad. Sci. U. S. A.*, vol. 103, pp. 17143-17148, NOV 14 2006, 2006.

CHAPTER 5

QUANTUM MECHANICAL SIMULATION OF METAL-MOLECULE INTERACTIONS

Introduction

Due to enormous advancement in the applications of biomolecule conjugated biochips, e.g. DNA/peptide/protein microarrays and DNA sequencing devices in recent years, it is important to study the fundamental nanoscience of biomolecule conformation, function and activity on biochip surfaces. One of such examples is the charge transfer mechanism in surface enhanced Raman spectroscopy. In this chapter, we describe a complementary interpretation of the mechanism responsible for the strong enhancement observed in Surface Enhanced Raman Scattering (SERS) using quantum mechanical simulation. The effect of a strong static local electric field due to Schottky barrier at the metal-molecule junction on SERS is systematically investigated. The study provides a viable explanation to the low repeatability of SERS experiments as well as the Raman peak shifts as observed in SERS and raw Raman spectra. It was found that strong electrostatic build-in field at the metal-molecule junction along specific orientations can result in 2-4 more orders of enhancement in SERS.

Background

Since its discovery [1-3], Surface Enhanced Raman Scattering (SERS) is progressively breaking new grounds and now even applied for the detection of more complex molecules and biologically relevant materials [4]. The single molecule detection capability [5, 6] has enhanced the prospect of using Raman probe in sensor application [7-9], hazardous materials detection [10, 11] and more recently, probing biological structures [12, 13]. Over the years three possible mechanisms for enhancement in Raman scattering have been identified [14]: (i) the surface plasmon resonance in the metal particle (or Electromagnetic mechanism) [2,3, 15-19] (ii) a charge transfer resonance involving transfer of electrons between the molecule and metal energy

level (or simply Charge Transfer mechanism) [16, 20-27] (iii) resonance within the molecule itself [14]. The well-known electromagnetic (EM) mechanism can be described as follows: when the incident laser frequency (or wavelength) is in resonance with the plasmon mode of the nanoparticle, a large amount of energy can be "concentrated" by the nanoparticle [28]. Subsequently the nanoparticle re-emits a portion of the EM energy by Mie scattering, thereby creating an intense surface field with very high energy density at or near the particle surface. In general, EM enhancement should amplify the Raman scattering non-selectively irrespective of type of molecules adsorbed on a particular surface [29]. However, the molecules CO and N_2 differ by a factor of 200 in their SERS intensities under the same experimental conditions [26]. Another interesting example is that of water. While many SERS studies are conducted in aqueous systems, there is rarely an enhancement in the Raman spectrum of water. These results cannot be explained by invoking only electromagnetic enhancement. Further, when the coupling of chemical enhancement effect of the nanoparticles is considered, the EM enhancement of SERS can be up to the order of 10^{10} [30]. The huge enhancement factor (10^{14}-10^{15}) as seen in many single-molecule experiments are normally attributed to the low concentration level of the analyte in SERS experiments and hence, mainly due to the difference in the number of molecules showing scattering in SERS as compared to bulk Raman [31]. However, the contribution from electromagnetic coupling and chemical binding are clearly inseparable in experiments due to the fact that the SERS detection itself depends on the electromagnetic enhancement process [32]. Thus the kind of charge transfer (CT) contribution in those high enhancement experiments (10^{14} -10^{15}) is still unknown. In the charge transfer model [33], an incident photon excites an electron from the metal surface into an adsorbed molecule, creating a negatively charged excited molecule. The molecular geometry of this excited molecule differs from that of the neutral species. This charge transfer induces a nuclear relaxation within the excited molecule, which results in, the return of the electron to the metal surface, the creation of an excited neutral molecule and the emission of a wavelength shifted (Raman) photon [18]. In principle in the CT an adsorbed molecule can, under specific conditions, interact with a metal surface in such a way that there is a large increase in molecular polarizability (change), α. Further, it was shown experimentally that the charge transfer can occur in both directions (that is, metal cluster-to-molecule or molecule-to-metal cluster) depending on the relative energies of the metal Fermi level and the HOMO (highest occupied molecular orbital) and LUMO (lowest unoccupied

molecular orbital) levels of the adsorbed molecule [22]. For example, molecules with low-lying unfilled π-orbitals (such as pyridine) experienced metal-to-molecule transfer, while those without low-lying unfilled orbitals (such as NH_3 or piperidine) tended to transfer electrons to the metal [14, 22].

It is also important to realize that the aforementioned three mechanisms are not independent of each other, but rather the total enhancement is due to the result of combine effect of one or more of the three mechanisms depending on the wavelength used in the experiment and the specific adsorbate and metal [34]. Even though it may not always be possible to separate these different mechanisms experimentally or theoretically, certain limits can be established where one mechanism is more dominating than the others. In fact, to isolate the CT enhancement, SERS has been studied for adsorbates on smooth surfaces, which are known to be incapable of supporting large surface plasmons. These studies showed only small (10^1-10^2) enhancements [35, 36]. However, recent theoretical [37] as well as experimental [38, 39] studies has shown that under certain conditions the CT enhancement can be much larger than is usually predicted earlier. In addition, large SERS enhancements have also been observed for molecules interacting with small nanoclusters or nanocrystalline semiconductor surfaces, both of which are not expected to support plasmon resonances and thus should show only small EM enhancement [40-42]. Though, the CT mechanism has been widely studied and fairly gives an intuitive picture of the chemical enhancement, it mostly relies on phenomenological parameters [16, 24]. In this context, it is increasingly important to understand the microscopic nature of SERS using first principle modeling [43]. It is now widely believed that the chemical bonding effects in SERS can be simulated just by considering the local environment of a molecule which is also consistent with the adatom model [26, 44]. The adatom model assumes that the atomic-scale roughness features determine the hot spots on a metal surface and invariably discount the electromagnetic enhancement due to the excitation of surface plasmons in the metal as well as the effect of interference between the chemical and the electromagnetic mechanism if any. Indeed in such approach the CT and EM effects enter in multiplicative fashion in the total enhancement factor [45]. Also, in most of the previous theoretical studies of SERS, only a few metal atoms were used to model the molecule/surface interaction. For example, Aroca et al. [46] did the simulation with just a single silver atom to mimic the chemisorption of phthalimide on a silver surface and

obtained a reasonable agreement with experiments. Similarly, resonance Raman calculation [47], SERS study of pyridine adsorbed on silver clusters [34, 37, 48] and SERS simulation for Benzenethiol adsorbed on Ag surface [44] have been performed with fair success by using a few tens of atoms. It has also been shown using rigorous density functional theory (DFT) computation by using large surface unit cells, that the ($\sqrt{3}\times\sqrt{3}$) unit cell is sufficient to treat the single molecule adsorption of Benzenethiol on Au (1 1 1) surface in the low coverage limit [49]. A full coverage can be defined as one thiol molecule per three Au surface atoms, which is consistent with our simulation approach. The STM experiments for structure of Benzenethiol adsorbed on gold (111) showed surface coverage of about 0.306 for the Benzenethiol molecule [50]. In this paper, simulations for chemical bonding effects on Raman scattering have been performed for Benzenethiol using 1-3 gold atoms.

The various issues considered so far in the context of chemical enhancement includes the binding geometry of the adsorbate [51], the effects of adsorption on various noble and transition metal surfaces [52], the influence of positively charged atoms at the metal surface [53, 54], the effect of adsorbed chloride anions [55], the effect of nonzero static electric fields [56], and the solvent effects in the calculations [57]. Although there is clear evidence of the existence of a solid-liquid electrochemical interface (electric double layer) in all aqueous SERS experiment as well as metal-molecule interface in non-aqueous SERS experiments, there is no systematic study so far to elucidates these effects. It is also well known that the strong electric field present at such an interface perturbs the vibrational frequencies of the adsorbed species—the vibrational Stark effect (VSE) [1, 58]. In addition, the electric field also changes the adsorbate vibrational line strength—the vibrational intensity effect (VIE) [59, 60]. Here we present a systematic study of both of these effects on a model SERS molecule, Benzenethiol, by assuming an interfacial static electric field between metal-molecule interface whose magnitude and direction are taken as parameters of the model. The external static electric field can be seen as a perturbation to the system Hamiltonian. Our present computational approach is also motivated by the goal of interpretation of potential dependent SERS studies [61, 62]. In recent experiment, an enhancement of the order of 10^5-10^9 was observed upon application of external electric field to glutamic acid adsorbed on Ag substrate [63]. The present study aims to provide a microscopic insight to any such studies and may lead to achieving applied electric field controllable SERS

intensity module. To present a simplified picture of metal-molecule interface, the molecule has been considered as a semiconductor (the justification is described below) and the magnitude of the static electric field so developed is calculated based on metal-molecule Schottky barrier mechanism.

Molecule as semiconductor

Most organic materials are electrical insulators with values of electrical conductivity at room temperature in the range 10^{-9} - 10^{-14} S cm^{-1} [64] (10^{9} - 10^{14} Ω cm resistivity). To obtain a larger conductivity and hence semiconducting behaviour, the HOMO–LUMO gap needs to be reduced; this can be achieved with extensive π-bonding. This reduced band gap allows electrons to more easily jump between conduction and valence bands and gives rise to the semiconductive properties [65]. In crystalline semiconductor technologies, n-type and p-type refer to the type of dopant, and therefore majority carrier, in a semiconductor. In crystalline materials both holes and electrons can usually be transported reasonably well. It is, nevertheless, common in the literature to refer to hole transporting disordered (doped) semiconductor materials as p-type and electron transporting materials as n-type because this describes their majority carriers and semiconducting behavior.

On the other hand, aromatic rings contain alternating single and double bonds that lead to overlapping p-orbitals, which form π-bonds. In π-bonds, electrons delocalize and are shared between the atoms on the ring's backbone. Similar to conduction due to a delocalized “sea of electrons" in metals, free movement of delocalized π-electrons in organic compounds allows organic molecules to conduct electricity and behave as semiconductors [66]. Then how to distinguish p-type or n-type organic semiconductor? In view of popular organic semiconductor field, electron-rich conjugated polymers are termed as p-type and electron-poor ones are termed as n-type [67]. For example, in Benzenethiol, the hydrogen atoms which surround the carbon backbone are less electronegative than the carbon backbone itself and lend some electron density to the delocalized π-electron cloud. The electron rich conjugated molecule has difficulty accepting another electron, but is able to lose an electron with relative ease. As a consequence, positive charge carriers expected to dominate transport in Benzenethiol molecule [66]. In other

words, molecules involving π-conjugation have high HOMO levels and exhibit electron-donating properties. Hence, these molecules are good candidates for p-type semiconductors [68].
However, it should be recognized here that the view of holes and electrons pi-orbital molecule as free carriers is rather simplistic. It allows us to make some general predictions about the trends in energy levels if we use it carefully, but may not extend well to all polymers [66]. It should also be recognized that the expected carrier mobility in such organic semiconductor is typically low (~ 1 $cm^2V^{-1}s^{-1}$) as compared to traditional inorganic semiconductors (for silicon crystal ~ 300-900 $cm^2V^{-1}s^{-1}$).

Metal-Molecule interface

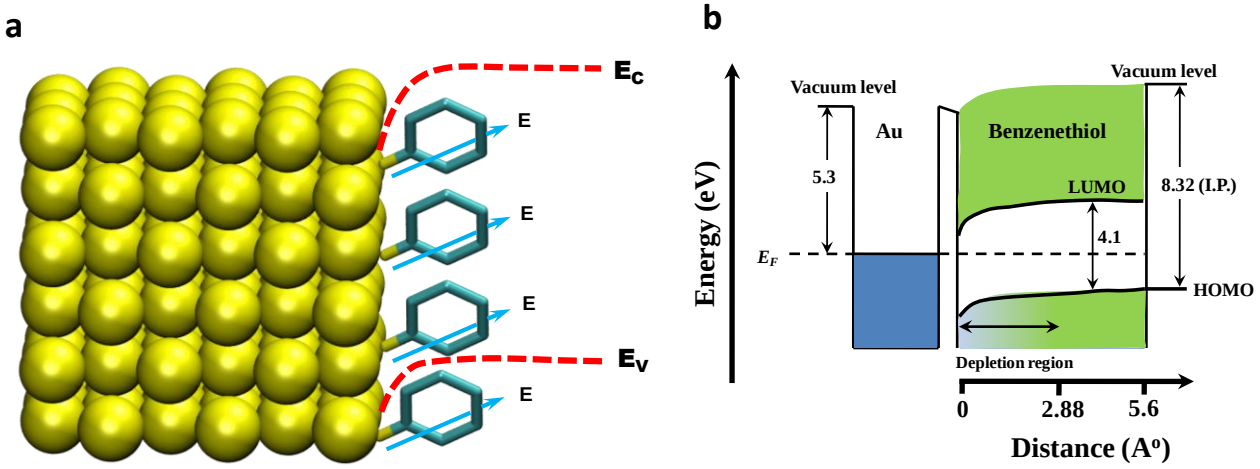

Figure 5.1: (a) Schematic of metal-molecule Schottky barrier junction, the monolayer of Benzenethiol molecules on gold cluster surface with perpendicular electric field orientation. (b) Schematic energy-band diagram of the Gold/Benzenethiol Schottky junction interface. E_F is the Fermi energy of metal, and I.P. is the ionization potential.

It is well known that a potential barrier known as Schottky barrier forms at a metal-semiconductor junction [69, 70] and the build-in electrostatic field strength can be as high as a few volts per angstrom. The formation of Schottky barrier between metal electrode and organic electronics materials has been extensively studied both theoretically [71-73] and experimentally [74-77] in recent years. In addition, the application of SAMs (Self Assembled Monolayers) of π-conjugated thiols for single-molecule electronics have been extensively studied [78]. Herein we assume the Benzenethiol molecule is equivalent to a highly doped p-type semiconductor and the

gold-Benzenethiol junction is equivalent to a metal-semiconductor Schottky barrier junction as shown in Fig. 5.1a. Providing a self-assembly monolayer coverage of $6.8\times10^{14} cm^{-2}$ for Benzenethiol on gold surface [79, 80], the packing density of Benzenethiol or equivalently the electron donor concentration can be calculated to be $N_D = 1.36\times10^{22} cm^{-3}$. The depletion width at the metal-molecule junction can be calculated using the relation $W = \left[\frac{2\varepsilon_s \phi_s}{qN_D}\right]^{1/2}$ where ε_s is the permittivity of Benzenethiol molecule, ϕ_s is the surface potential, q is the fundamental electric charge. The maximum surface potential ϕ_s is approximated as half of the energy band gap of the Benzenethiol molecule, which is about 2 eV. Taking relative permittivity (ε_r) of Benzenethiol as 4.38 [81] the depletion width of our system was thus found to be 2.88 A^0. The build-in electric field was calculated using the simple relation $E_0 = \frac{q}{\varepsilon} W N_D$ and found to be 1.41 V/Å. It should be noted that this estimated electric field strength is the maximum value and the real build-in electric field should be slightly lower than this value. Figure 5.1b displays the schematic of the energy-band diagram of a gold/Benzenethiol Schottky junction, using the parameters obtained in our analysis. The work function of Au is 5.3 eV [82], the ionization potential (IP) of Benzenethiol is 8.32 eV [83, 84]. The band gap of Benzenethiol was calculated to be 4.1 eV. The difference between Fermi energy of metal and HOMO (highest occupied molecular orbital) is known as HIB (hole injection barrier) and difference in Fermi level and that of LUMO (lowest unoccupied molecular orbital) of organic molecule is known as EIB (electron injection barrier) [71, 77]. In the present study HIB is calculated to be ~ 2.06 eV and EIB is calculated to be ~ 2.04 eV.

Now, the interface between metal and organic semiconducting layers can be described with the help of screening parameter (S parameter) [85] which is defined as $S = \frac{d\phi_B^P}{d\phi_m}$, where ϕ_m and ϕ_B^P denote the work function of the metal and the barrier height for carrier injection at the interface for holes (HIB), respectively. S = 0 corresponds to the so called Bardeen limit for which Fermi level pinning occurs. Similarly, S = 1 corresponds to an ideal Schottky barrier at the interface (Schottky limit) [86]. For metal−organic molecule interfaces formed by chemical bonds, it is reasonable to interpret the Bardeen limit as the situation where strong orbital

interactions between frontier orbitals of metals and the HOMO of molecule occurs and the Schottky limit as the situations where weak orbital interactions occurs between them. In other words, when molecules have large energy gaps between the HOMO and the LUMO, as in the present study, Schottky limit holds well [86]. In fact the value of S was calculated to be 0.5 experimentally for Au and Benzenethiol system [86]. Again the density of states $D(E_F)$ of interfacial electronic states can be calculated using the relation, $S = (1 + e^2\delta D(E_F)/\varepsilon)^{-1}$,[85-87] where e, δ, and ε denote the elementary charge, width of the metal−molecule interface, and dielectric constant, respectively. Taking δ and ε to be 5.7 Å and 4.38 for Benzenethiol [81] respectively, $D(E_F)$ is estimated to be 4.2×10^{13} states/(cm^2·eV), which is less than 20% of the density of states of Au at the Fermi level [88]. Even though small, the existence of a finite density of states for the frontier orbitals of the molecule near the Fermi level, indicates that electrons pass through hybrid orbitals composed of frontier orbitals of the metal and molecule supporting the charge transfer mechanism.

Computational approach and details

Using a simple model we have estimated the built-in electric field of the order of few V/A^o. The effect of such high build-in electric field on the molecular conformation, electronic and vibrational properties was probed using a quantum mechanical simulation. The theoretical simulations were performed using Density Functional Theory (DFT) implemented in Amsterdam Density Functional (ADF) program package [89, 90]. DFT methods are based on the Hohenberg-Kohn theorem which states that the ground state electronic energy of a molecule can be expressed exactly as the electron density of the molecule. The Becke-Perdew (BP86) XC-potential [91, 92] and a triple-ζ polarized slater type (TZP) basis set from the ADF basis set library were used in our simulation. For metal adsorbed molecule, a frozen core was chosen for Au during the vibrational frequency calculation to reduce the computational time. The zeroth order regular approximation (ZORA) was employed to account for the scalar relativistic effects. For neat Benzenethiol calculation, a large core without relativity and with an integration accuracy of 4.0 was used. The SCF convergence criterion was kept at 10^{-8}. Frequencies preset were run in the ADF-GUI mode to obtain the Raman frequencies. Automatic Electron Smearing

(in case of problematic SCF convergence) was disabled. All frequency calculations are run after geometry convergence is achieved. The polarizability derivative and Raman frequencies are calculated internally by ADF-GUI module (no external numerical calculation was performed). The validity of using DFT and ADF for quantum mechanical SERS calculation has already been proven by many researchers [37-48]. Further, in the present study the validity of our results has been checked by comparing the computational results for the Raman as well as SERS spectra with the experimental results. The details of the experiments have been given elsewhere [93]. The simulated results match fairly well with the experiments as shown in Fig. 5.2. Comparison of results obtained from DFT study with experiments for neat Raman is shown in Fig. 5.2a. Similarly, the result for SERS spectra of Benzenethiol calculated by DFT simulation and obtained from experiment is shown in Fig. 5.2b. Clearly the characteristics peaks observed in the experiments are captured by the DFT simulation.

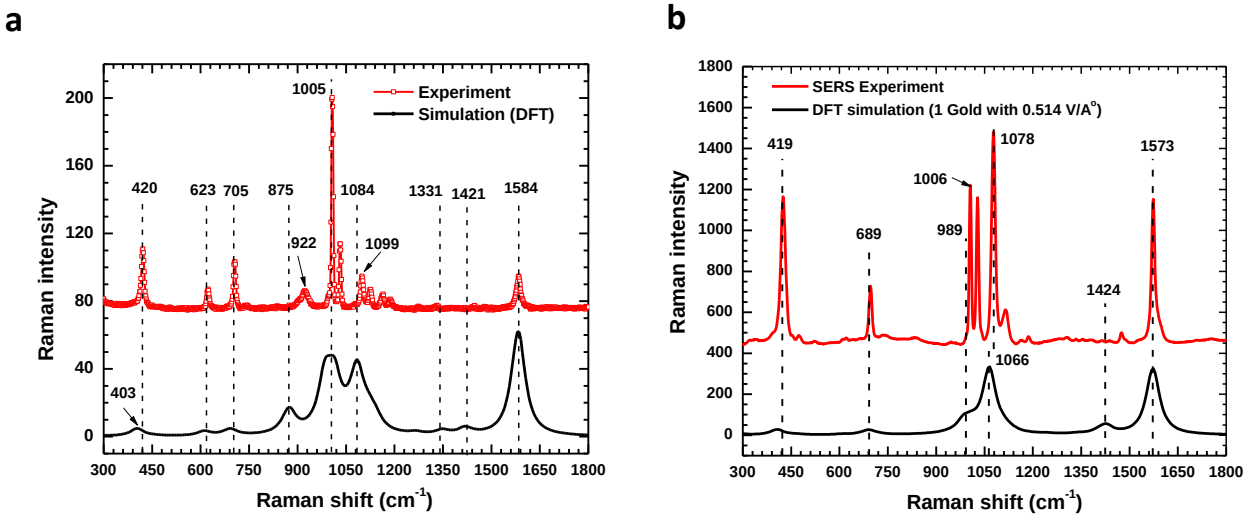

Figure 5.2: (a) Comparison of results obtained from DFT study with experiments. The spectra shown are for neat Raman (b) Comparison of SERS spectra of Benzenethiol calculated by DFT simulation and obtained from experiment.

Results and discussion

The polarization effect of SERS has already in observed in single molecule experiment [5] and recently been verified with a computational model [94]. Here, we investigate the effect of built-in electric field direction on the Raman scattering process. To model such a system, first a static electric field is applied on the Benzenethiol molecule along various directions to simulate

the build-in field of Schottky barrier developed at the metal-molecule junction. The molecular conformation under different conditions is found through the energy minimization process in each case. Here, all the directions are related to the molecular co-ordinates and hence positive Z-direction should be normal to the Benzene ring structure. Figure 5.3a shows the deformation in

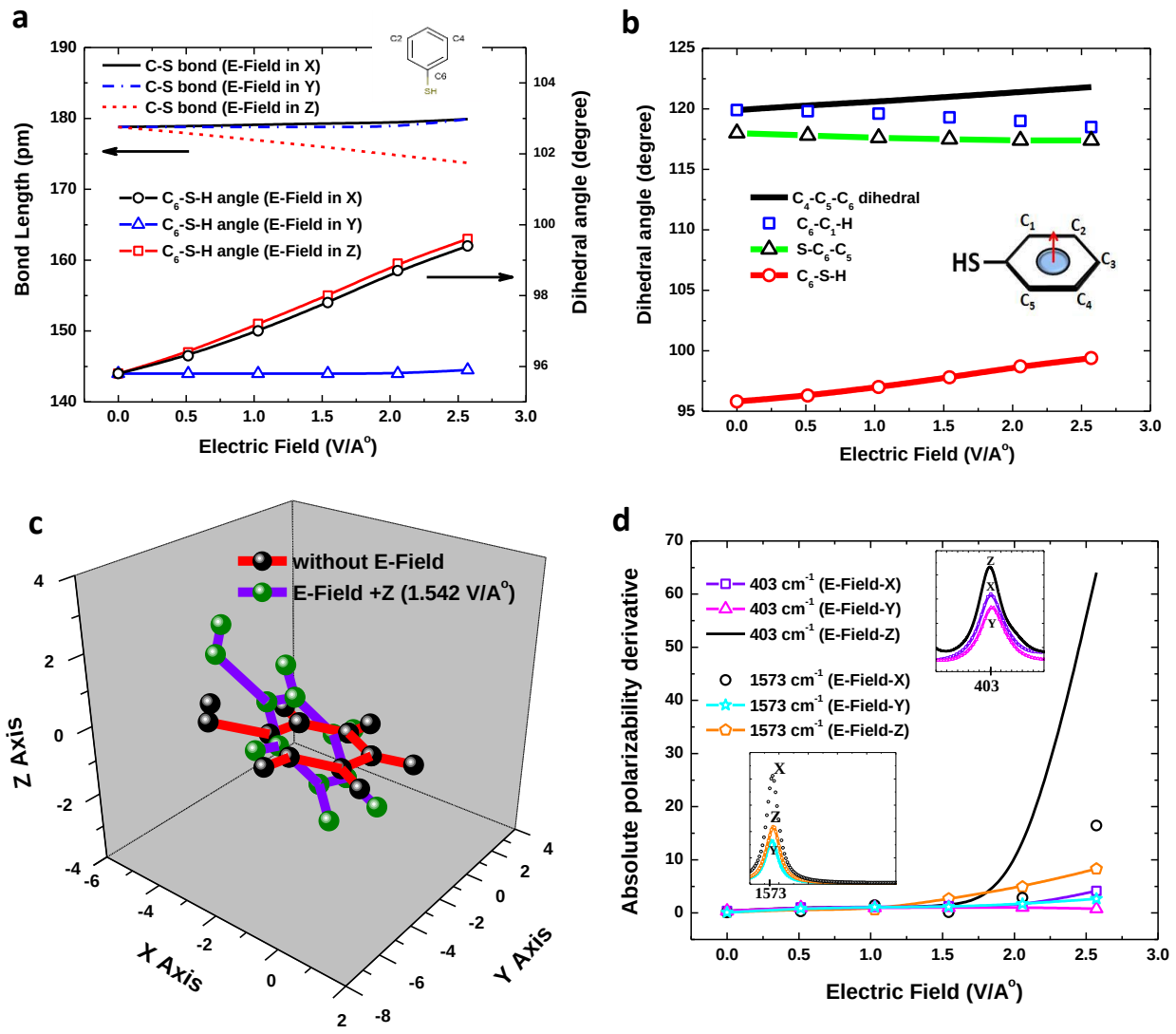

Figure 5.3: (a) The change in the C-S bond length and C-S-H dihedral angle as a function of electric field applied in X, Y and Z direction relative to the Benzenethiol molecule. (b) The dihedral angle variation with build-in electric field perpendicular to the ring structure. (c) The change in orientation of the molecule due to application of electric field. (d) The absolute polarizability derivative (modulus of the polarizability derivative) at two Raman peaks (403 cm^{-1} and 1573 cm^{-1}).

chemical bond length of Benzenethiol molecule due to application of electric fields. In general, it was found that the extent of the bond length change is proportional to the build-in electric field. Depending on the relative orientations between the molecule and the build-in electric field,

different trends show for the length change of various chemical bonds such as the carbon-sulfur bond and carbon6-sulfur bond. The largest change in bond length and dihedral angle was seen when the build-in field was perpendicular to the Benzene ring (positive Z-direction). The dihedral bond angle also changes as shown in Fig 5.3b. One can clearly see that the build-in field leads to a large variation in bond length and dihedral angle at specific orientations. To emphasize the change in bond orientation and length under application of electric field, the actual conformation of Benzenethiol molecule is shown as obtained from our simulation in Fig. 5.3c. The molecular conformation change will inherently induce dipole moment and polarizability changes since the inter-atomic distance and angle are altered. The direct correlation between the build-in electric field and the polarizability derivative of two dipoles in Benzenethiol molecule is shown in Fig. 5.3d. These two dipoles correspond to the vibrational modes at 403 cm^{-1} and 1573 cm^{-1} respectively. The trend in the change of bond length and change in the polarizability is consistent with other theoretical prediction [37, 44].

The close-up of the peaks is also shown in the inset. The large enhancement of a peak in particular direction can be assigned to the largest change in the polarizability derivative in that direction. In the particular case shown here, for example, the largest change in polarizability derivative for 403 cm^{-1} peak is in +Z direction (perpendicular to Benzene ring) and hence, the largest enhancement one could see for that peak is in +Z direction. Similarly, for 1573 cm^{-1} peak, the largest change in polarizability derivative observed was in +X direction (parallel to Benzene ring structure). That's why the largest enhanced 1573 cm^{-1} peak corresponds to electric field applied in +X direction. For a similar molecule, Pyridine, Arenas et al. [95] found experimentally that the modes at 410, 598, 1204 and 1573 cm^{-1} shows the strongest dependence on the electrode potential. The theoretical TDDFT simulation for Benzenethiol adsorbed on silver cluster shows similar trend [44] which is in agreement with current simulation results.

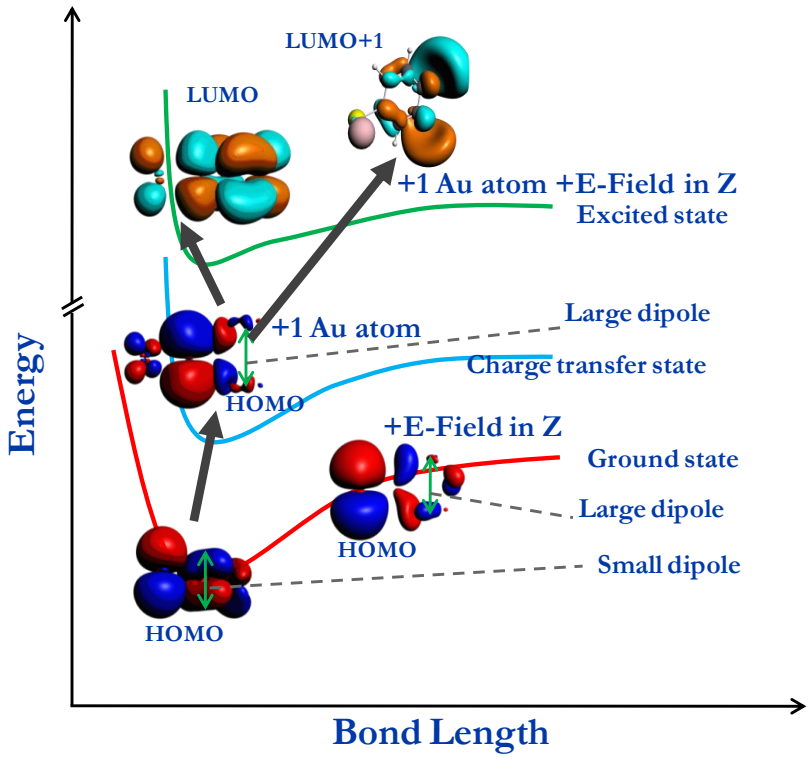

Figure 5.4: Sketch showing the schematic of charge transfer scheme explained in terms of HOMO and LUMO state of the molecule. The enhancement in Raman scattering cross-section due to large dipole moment change because of application of electric field, creation of intermediate state due to attachment of gold atom and the combined effect of above two are shown.

The graphical explanation for the effect of build-in field at the Schottky barrier on molecular dipole moment is shown in Fig. 5.4. The molecular quantum states can be described based on the Born-Oppenheimer separation of nuclear and electronic degrees of freedom. The electrons are much lighter than nuclei and can adjust rapidly to the instantaneous nuclear configuration (which is also known as Franck-Condon principle). Therefore molecules are characterized by "potential energy surfaces" - plots of energy versus internuclear separation and there is a separate surface for each electronic configuration [96]. Figure 5.4 shows schematically that there must be an intermediate state created due to adsorption of Benzenethiol to gold atoms as the excitation incident wave (532 nm or 2.33 eV) is far below the purely intramolecular electronic transitions level (4.1 eV) which is also supported by recent theoretical model [44].The increase in polarizability derivative (and subsequent enhanced Raman intensity) can be explained by the large change in the dipole moment due to change in molecular conformation (and increase in the bond length as shown in Fig. 5.4). The increased dipole moment ($p = q*d$) is depicted by a

larger separation of two charges described by red and blue color as observed for the HOMO level of Benzenethiol. Since the polarizability of the molecule is related to the vibrational co-ordinates and the dipole moment, an increased in polarizability is expected. We also observed an increase in the absolute polarizability derivative (modulus of the polarizability derivative) along with increase in dipole moment (Fig. 5.3d). The Raman scattering cross-section is proportional to the square of polarizability derivative $\frac{d\sigma}{d\Omega}\alpha\left(\frac{d\alpha}{dr}\right)^2$ [97]. Hence, an increase in Raman scattering cross-section is expected as a result of large change in polarizability derivative even in the absence of electronic transition.

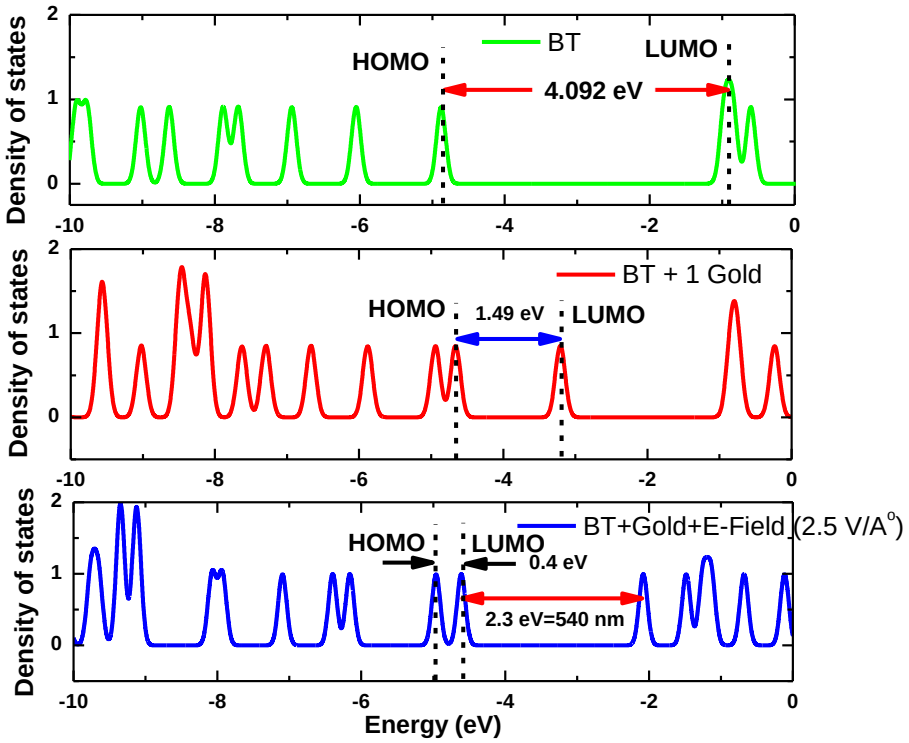

Figure 5.5: The density of state plot for isolated Benzenethiol (BT), the molecule adsorbed on one gold atom and when build-in electric field is applied to molecule adsorbed on the gold atom.

The metal-molecule Schottky barrier also induces the change of energy band gap of Benzenethiol molecule. As shown in Fig. 5.5, the band gap of isolated Benzenethiol molecule is in ultraviolet region which makes the electronic level transition forbidden for visible excitations. The Fermi (HOMO) level of gold is somewhere in the middle of the molecule energy band gap. The energy difference between gold Fermi level and HOMO of isolated molecule shows the viability of charge transfer scheme where charges can transfer from metal atom cluster to the

molecule or from the molecule to the metal cluster. Due to attaching gold atoms the density and number of accessible states in the hybrid system increase. In addition, the band gap shrinks due to attachment of gold atoms which may make it possible to induce resonance Raman for visible excitations. It should be noted that the band gap of Benzenethiol calculated in the present study is 4.092 eV which is in close agreement to the value of 4.027 eV calculated by Morton and Jensen [34]. Similarly the band gap calculated in the present study for Benzenethiol with three gold atoms configuration is 0.75 eV whereas for similar system the value calculated by Letardi and Cleri [98] was 0.76 eV. The prediction of shrinking band gap due to adsorption is also in good agreement with the theoretical study by Saikin et al. [44] for Benzenethiol adsorbed on a silver cluster. The build-in electric field further shrinks the band gap, increasing the probability of transition to higher excited states and further enlarging the Raman scattering cross-section.

The reason for shrinkage of band gap (Fig. 5.6a and b) due to adsorption to metal atoms can be described as follows. The ionic cores in the metal are assumed to give rise to a square potential well for the electrons and all states are filled up to the Fermi level, E_F [71]. The energy difference between E_F and the potential energy of an electron in the vacuum above this hypothetical surface, U_{vac}, is generally referred to as the *intrinsic* work function, Φ', (or chemical potential) of the metal (e.g. for gold it is 5.3 eV) (Fig. 5.6c). However, because the potential well is not infinitely deep, there is always a finite probability of finding electrons outside the potential well, that is, electron density is "leaking out" from the metal into the vacuum [99]. Consequently, a dipole layer is formed with a positively charged region below the surface (red region) and negatively charged region (light blue) just outside the metal surface. This dipole layer is commonly referred to as the *surface dipole* and gives rise to a potential step across the metal surface (Fig. 5.6d) [71]. The surface dipole raises *U*vac directly above the metal surface relative to E_F and leads to the *observed* work function, Φ, of the metal surface [99].

Now when a Benzenethiol molecule appears near the metal surface, there exist a mismatch of ionization potential (IP ~ 8.32 eV)) of the molecule and the work function of metal (~ 5.3 eV). As we pointed out earlier, this will lead to a Schottky barrier which will give rise to a built-in electric field directed from metal surface to the organic molecule. The developed electric field will oppose further leakage of electrons from metal. So even for a weakly interacting (physisorbed or van der Waal interacting) species or for a strongly interacting (covalent bonded)

species, the electron cloud leaking out of the metal surface is pushed back into the metal (Fig. 5.6e) [100].

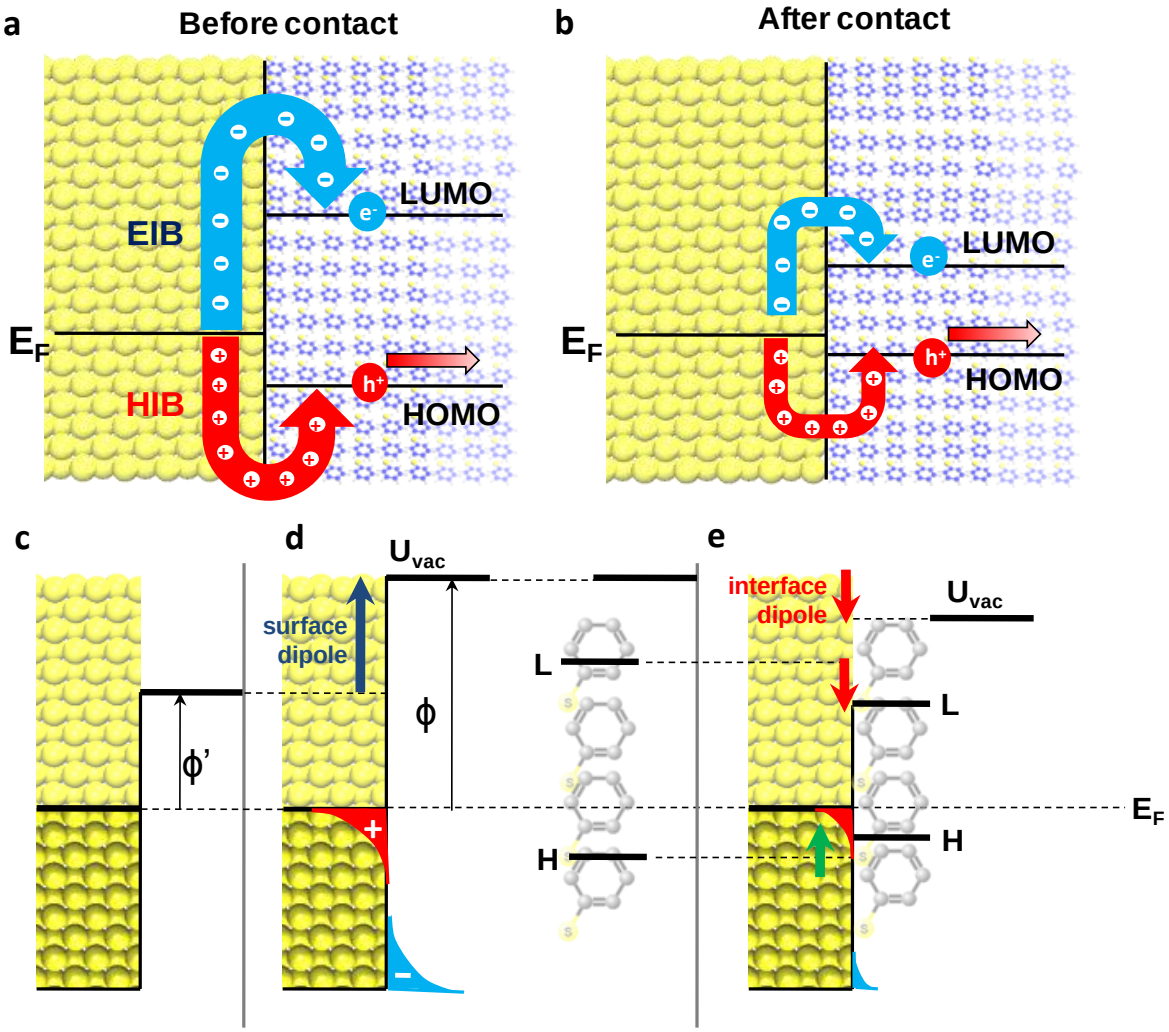

Figure 5.6: (a) Schematic energy-level diagram at a metal/organic molecule interface. (a) the position of the highest occupied molecular orbital (HOMO: H) and the lowest unoccupied molecular orbital (LUMO: L) of Benzenethiol with respect to the Fermi level (E_F) of Au before contact.. After contact (b), the HIB and EIB can be reduced. (c) Model of a metal surface (square potential well in the absence of a surface dipole; (d) As electrons leak out of the potential well forming surface dipole (e) Upon interaction of the molecules, the electrons are pushed back into the metal, reducing the surface dipole and charge-carrier injection barriers.

This *push-back* (or *pillow*) effect always contributes to reduce the surface dipole and lower U_{vac} relative to E_F and, consequently, leads to a reduced work function, Φ_{mod}, of the sample [71]. The amount by which the surface dipole is reduced is generally known as the *interface dipole* [71]. The interface dipole is expected to lower the LUMO level of the organic molecule too. In the

present study we have observed a reduction of ~ 2.54 eV for Benzenethiol LUMO level. In addition, an interface dipole with its negative pole pointing toward the organic layer and its positive pole toward the metal is expected to increase the metal work function (i.e., decreases the Fermi energy) and increases the HOMO energy of the organic layer by adding an electrostatic energy [101]; as a result, the hole injection barrier (HIB) should be reduced (Fig. 5.6b and e). In fact, in our simulation, we have observed an increase of 1.37 eV for the HOMO level of Benzenethiol up on conjugation to gold which reduces the HIB from 2.06 eV before conjugation to 0.69 eV after conjugation.

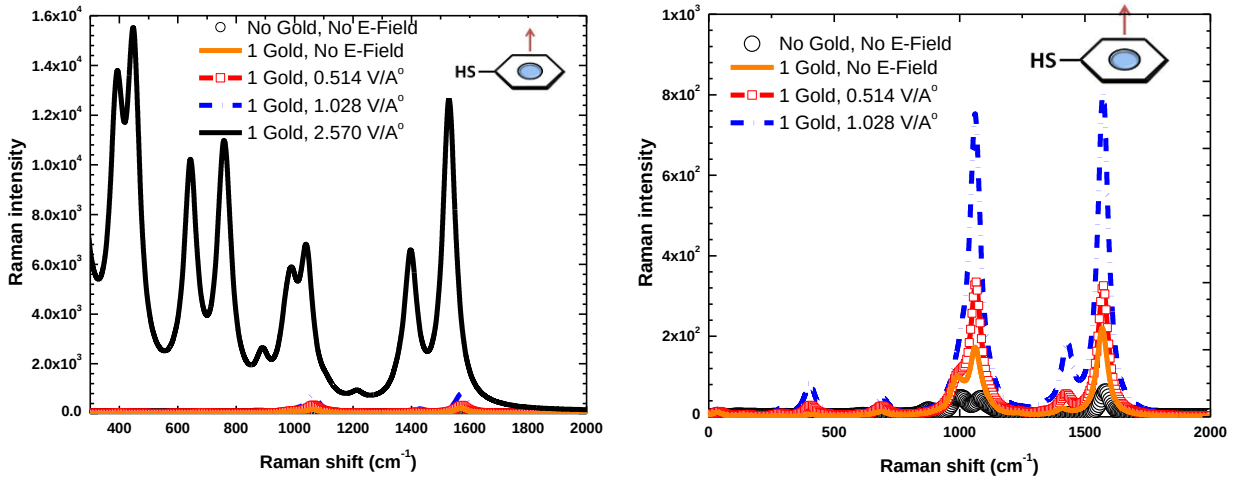

Figure 5.7: Enhancement due to Gold-Benzenethiol Schottky barrier.

To elucidate the effect of magnitude of build-in electric field on Raman intensity, the Raman scattering spectra are simulated by calculating the Raman intensity as the function of applied electric field. Figure 5.7 shows that with application of local build-in electric field of 1.028 V/A^{o} (which is slightly lower than the theoretical electric field calculated earlier using simple model), one extra order of Raman enhancement was achieved in addition to the enhancement from the gold atom attachment. This shows that build-in electric field can actually bridge the gap between high enhancement experimental observations and previous theoretical simulations. In fact, with an application of a high build-in field of 2.570 V/A^{o} we achieved a 2~4 more orders of enhancement, which points to the importance of a metal-molecular junction for the potential 10^{14} Raman enhancement.

Effect of direction of electric field

The intensity of a vibrational mode is proportional to the square of scalar product of the electric field and the dipole moment derivative of the mode $(d\vec{\mu}/dQ)$ as $I\alpha\left|\frac{d\vec{\mu}}{dQ}\vec{E}\right|^2=\left|\frac{d\vec{\mu}}{dQ}\right|^2\left|\vec{E}\right|^2\cos^2\beta$[102], where β is the angle between electric field, $\vec{E}$ and $d\vec{\mu}/dQ$. This shows that there is a strong dependence of Raman peak intensity to direction of electric field. In fact, in our DFT simulation, we observed that applying electric field in a direction parallel to the aromatic ring decreases the SERS enhancement as shown in Fig. 5.8. Further, aligning the electric field in Gold-Sulfur bond direction improved the signals. Finally, with the application of electric field perpendicular to the aromatic ring further increases SERS enhancement. This concludes that molecular orientations relative to build-in electric field in the junction dictate in this enhancement mechanism. The reorientation of molecule relative to surface due to changes in the electrode potential has been reported by Moskovits et al. [103]. Subsequent detailed study using high resolution electron energy loss spectroscopy (HREELS) by Wan et al. [50] for Benzenethiol adsorption to Au (111) surface further confirms our hypothesis that molecule orientation relative to built-in electric field is playing an important role for the charge transfer mechanism in SERS.

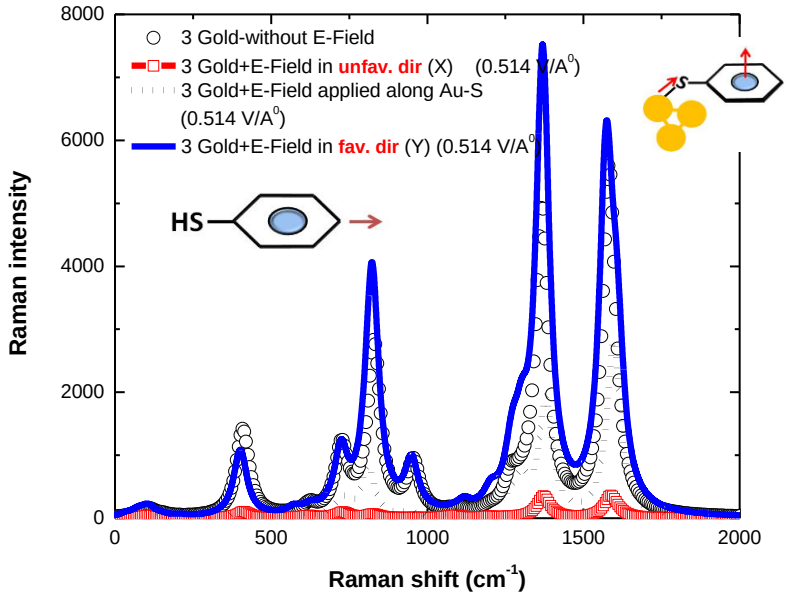

Figure 5.8: The effect of molecular orientation relative to build-in electric field.

Vibrational shift in SERS

In general, all the Raman peak positions in SERS spectra are never consistent with those of original Raman spectra [44, 104-107]. The frequency shifts of seven commonly observed modes in Benzenethiol are compared to experimental SERS and DFT calculated data in Table 5.1. The values of the vibrational frequencies (termed as Freq. PhSH) are taken for neat Benzenethiol from our experiments [93]. The vibrational band at ω_1 = 1005 cm^{-1} is assigned to the ring breathing mode (β_{CCC}), and the band at ω_2 = 1032 cm^{-1} corresponds to a ring deformation mode (β_{CH}). The C–S stretching mode (β_{CCC} + ν_{CS}), is given at ω_3 = 1099 cm^{-1} while the computed Raman band at ω_4 = 1584 cm^{-1} is associated with a totally symmetric ring stretching mode (ν_{CC}). The other important modes are ω_5 = 420 (ν_{CS}+β_{CCC}), ω_6 = 705 (β_{CCC} +ν_{CS}) and 922 cm^{-1} (β_{SH}). Note that the 922 cm^{-1} generally disappears in SERS spectra due to thiolate bond formation. The large shift in the C-S stretching mode (1099 cm^{-1}) in SERS can be attributed to the proximity affect as the vibrational mode is strongly enhanced by the interaction with Au cluster [44].

As described above, the C-C bond stretch mode on the aromatic ring was observed at 1584 cm^{-1} in the original Raman spectrum which is consistent with our DFT simulation results. In a parallel SERS experiment reported in the paper [93, 107], the SERS peak for the same mode was observed at 1573 cm^{-1}. Apparently the Raman peak position shifts in the SERS spectrum in comparison with the original Raman spectrum. Although with only one gold atom conjugation there is a shift of Raman peak position in our simulation from 1584 cm^{-1} to 1560 cm^{-1}, but it is not consistent with the experimental observation, where it shifts to 1573 cm^{-1}. On the other hand, with including the build-in electric field effect (1.028 V/A^o) in our DFT simulation we observed the SERS peak at 1573 cm^{-1} which exactly matches with the experimental observation (Fig. 5.9). Similarly, the large enhancement of 420 cm^{-1} peak (βCCC+ νCS), is obtained in our simulation only after taking into account of the metal molecular Schottky junction (Fig. 5.9), which is also consistent with the experimental observations [93, 107] and theoretical prediction [44].

Table 5.1: The frequency shifts of Benzenethiol Raman active vibrational modes due to binding to the metal and application of electric field (in DFT). The frequencies are given in cm^{-1}; PhSH: Benzenethiol; The numbers in the bracket are the electric field value in V/A^{o} applied in DFT simulations.

Mode	ω_1	ω_2	ω_3	ω_4	ω_5	ω_6	ω_7
Freq. PhSH [93]	1005	1032	1099	1584	420	705	922
PhS-Ag (SERS) [93]	1006	1028	1078	1573	425	696	---
PhSH-DFT	1002	---	1084	1584	403	691	875
PhSH-DFT (0.51)	991	---	1084	1580	403	696	882
PhSH-DFT (1.03)	992	---	1084	1578	403	691	882
PhSH-DFT (1.54)	989	---	1079	1570	400	676	882
PhSH-DFT (2.05)	981	---	1071	1564	426	631	869
PhSH-DFT (2.57)	---	1018	1047	1549	410	715	840
Ref-105	1003	1027	1076	1576	422	695	---
Ref-106	1000	1025	1075	1575	420	695	---
Ref-107	1002	1026	1073	1573	420	693	---
Ref- 44	1003	1024	1076	1574	419	697	907
PhS-Au_1 [Present work]	---	---	1062	1560	403	693	---
PhS-Au_1 (0.51)	---	---	1064	1571	408	693	---
PhS-Au_1 (1.03)	988	---	1061	1573	409	693	---
PhS-Au_1 (1.54)	983	---	1053	1563	409	693	---
PhS-Au_1 (2.05)	979	---	1059	1551	382	712	---
PhS-Au_1 (2.57)	1009	1035	1090	1571	408	713	922

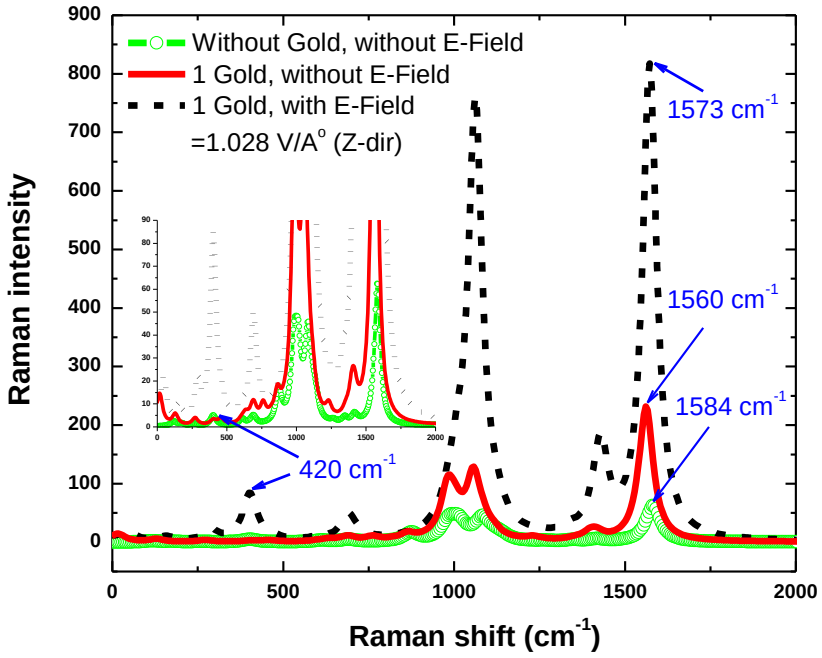

Figure 5.9: Explanation for Raman peak shift. The inset shows the 420 cm^{-1} Raman peak position.

Finally, Fig. 5.10 shows the vibrational shift observed in our DFT simulation when we applied electric field of different magnitude perpendicular to the ring structure. The plot is shown for a characteristic peak of 1573 cm^{-1} and corresponds to the case when Benzenethiol molecule is not attached to any gold atom (so this will discount any interference of charge transfer from gold cluster and thus represents the effect purely due to electric field only). We observed a closely linear fall of vibrational shift of ring stretching mode (ν_{CC}) with electric field and the stark tuning rate was calculated to be 13.2 cm^{-1}/ (V/A^{o}). In fact this value is very close to the vibrational shift observed (which ranges from ~ 10-13 cm^{-1}) in many SERS experiments for this particular characteristics peak [105-107]. In spite of not having enough statistics to prove our hypothesis, the results clearly points to a possible role of electric field of strength ~1 V/A^{o}. In addition, though the accuracy and precision of DFT is in doubt [108], still the correct trend of vibrational shift can be inferred from the present simulation. Since the inclusion of build-in electric field contribution leads to correct prediction of Raman peak shifts, we believe that the build-in electric field is playing an important role in SERS process.

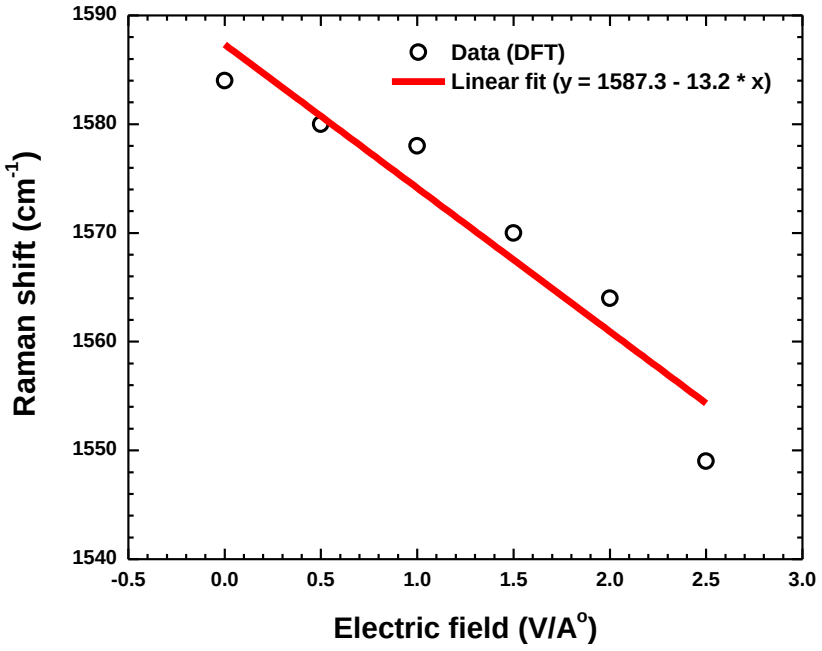

Figure 5.10: Effect of electric field on Raman vibrational shift

Conclusions

In summary, we have performed a quantum mechanical simulation to study the effect of build-in electric field due to a Schottky barrier formed between the molecule monolayer and metallic SERS substrate. We found that the application of build-in electric field changes the bond lengths and dihedral angles which lead to an alteration in the dipole moment. Further, this build-in field also causes a modification in the polarizability and polarizability derivatives of the molecule, which are mainly responsible for the drastic change in scattering cross-section observed in SERS. We have also shown that the order of enhancement that can be obtained in Raman scattering cross section is highly dependent on the direction of the build-in electric field. This help to explain the non-repeatability of many SERS experiments. Finally, by adding strong electrostatic build-in field can result in 2-4 more orders of enhancement in SERS for Benzenethiol molecules.

References

[1] Fleischmann, M.; Hendra, P. J.; McQuillan, A. J. Raman Spectra of Pyridine Adsorbed at a Silver Electrode. *Chemical Physics Letters* **1974**, *26*, 163-166.

[2] Jeanmaire, D. L.; Van Duyne, R. P. Surface Raman Spectroelectrochemistry: Part I. Heterocyclic, Aromatic, and Aliphatic Amines Adsorbed on the Anodized Silver Electrode. *J Electroanal Chem* **1977**, *84*, 1-20.

[3] Albrecht, M. G.; Creighton, J. A. Anomalously Intense Raman Spectra of Pyridine at a Silver Electrode. *J. Am. Chem. Soc.* **1977**, *99*, 5217.

[4] Cotton, T. M.; Schultz, S. G.; Van Duyne, R. P. Surface-Enhanced Resonance Raman Scattering from Cytochrome c and Myoglobin Adsorbed on a Silver Electrode. *J. Am. Chem. Soc.* **1980**, *102*, 7962.

[5] Nie, S.; Emory, S. R. Probing Single Molecules and Single Nanoparticles by Surface-Enhanced Raman Scattering. *Science* **1997**, *275*, 1102-1106.

[6] Kneipp, K.; Wang, Y.; Kneipp, H.; Perelman, L. T.; Itzkan, I.; Dasari, R. R.; Feld, M. S. Single Molecule Detection using Surface-Enhanced Raman Scattering (SERS). *Phys. Rev. Lett.* **1997**, *78*.

[7] Lyandres, O.; Shah, N. C.; Yonzon, C. R.; Walsh, J. T.; Glucksberg, M. R.; Van Duyne, R. P. Real-Time Glucose Sensing by Surface-Enhanced Raman Spectroscopy in Bovine Plasma Facilitated by a Mixed Decanethiol/Mercaptohexanol Partition Layer. *Anal. Chem.* **2005**, *77*, 6139.

[8] Lyandres, O.; Yuen, J. M.; Shah, N. C.; Van Duyne, R. P.; Walsh, J. J. T.; Glucksberg, M. R. Progress Toward an in Vivo Surface-Enhanced Raman Spectroscopy Glucose Sensor. *Diabetes technology therapeutics* **2008**, *10*, 257.

[9] Yonzon, C.; Lyandres, O.; Shah, N.; Dieringer, J.; Van Duyne, R. Glucose Sensing with Surface-Enhanced Raman Spectroscopy. **2006**, *103*, 367.

[10] Zamarion, V. M.; Timm, R. A.; Araki, K.; Toma, H. E. Ultrasensitive SERS Nanoprobes for Hazardous Metal Ions Based on Trimercaptotriazine-Modified Gold Nanoparticles. *Inorg. Chem.* **2008**, *47*, 2934.

[11] Zhang, X.; Shah, N. C.; Van Duyne, R. P. Sensitive and Selective chem/bio Sensing Based on Surface-Enhanced Raman Spectroscopy (SERS). *Vibrational Spectroscopy* **2006**, *42*, 2-8.

[12] Qian, X.; Peng, X.; Ansari, D. O.; Yin-Goen, Q.; Chen, G. Z.; Shin, D. M.; Yang, L.; Young, A. N.; Wang, M. D.; Nie, S. In Vivo Tumor Targeting and Spectroscopic Detection with Surface-Enhanced Raman Nanoparticle Tags. *Nature Biotechnology* **2008**, *26*, 90.

[13] Fujita, K.; Ishitobi, S.; Hamada, K.; Smith, N. I. Time-Resolved Observation of Surface-Enhanced Raman Scattering from Gold Nanoparticles during Transport through a Living Cell. *J. Biomed. Opt.* **2009**, *14*, 024038.

[14] Lombardi, J. R.; Birke, R. L. A Unified View of Surface-Enhanced Raman Scattering. *Accounts of Chemical Research* **2009**, *42*, 742.

[15] Moskovits, M. Surface Roughness and the Enhanced Intensity of Raman Scattering by Molecules Adsorbed on Metals. *J. Chem. Phys.* **1978**, *69*, 4159.

[16] Lombardi, J. R.; Birke, R. L.; Lu, T.; Xu, J. Charge-Transfer Theory of Surface Enhanced Raman Spectroscopy: Herzberg-Teller Contributions. *J. Chem. Phys.* **1986**, *84*, 4174.

[17] Lombardi, J. R.; Birke, R. L. A Unified Approach to Surface-Enhanced Raman Scattering. *J. Phys. Chem. C*, **2008**, *112*, 5617.

[18] Campion, A.; Kambhampati, P. Surface-Enahnced Raman Scattering. *Chem. Soc. Rev.* **1998**, *27*, 241.

[19] Kneipp, K.; Kneipp, H.; Itzkan, I.; Dasari, R. R.; Feld, M. S. Surface-Enhanced Raman Scattering and Biophysics. *Journal of physics.Condensed matter* **2002**, *14*, R597.

[20] Furtak, T. E.; Macomber, S. H. Voltage-Induced Shifting of Charge-Transfer Excitations and their Role in Surface-Enhanced Raman Scattering. *Chemical Physics Letters* **1983**, *95*, 328-332.

[21] Pockrand, I.; Otto, A. Surface Enhanced and Disorder Induced Raman Scattering from Silver Films. *Solid State Commun.* **1981**, *37*, 109-112.

[22] Lombardi, J. R.; Birke, R. L.; Sanchez, L. A.; Bernard, I.; Sun, S. C. The Effect of Molecular Structure on Voltage Induced Shifts of Charge Transfer Excitation in Surface Enhanced Raman Scattering. *Chemical Physics Letters* **1984**, *104*, 240-247.

[23] Burstein, E.; Chen, Y. J.; Chen, C. Y.; Lundquist, S.; Tosatti, E. "Giant" Raman Scattering by Adsorbed Molecules on Metal Surfaces. *Solid State Commun.* **1979**, *29*, 567-570.

[24] Persson, B. N. J. On the Theory of Surface-Enhanced Raman Scattering. *Chemical Physics Letters* **1981**, *82*, 561-565.

[25] Gersten, J. I.; Birke, R. L.; Lombardi, J. R. Theory of Enhanced Light Scattering from Molecules Adsorbed at the Metal-Solution Interface. *Phys. Rev. Lett.* **1979**, *43*,147– 150.

[26] Moskovits, M. Surface-Enhanced Spectroscopy. *Reviews of modern physics* **1985**, *57*, 783.

[27] Otto, A.; Mrozek, I.; Grabhorn, H.; Akemann, W. Surface-Enhanced Raman Scattering. *Journal of Physics: Condensed Matter* **1992**, *4*, 1143.

[28] Jin, R. Nanoparticle Clusters Light Up in SERS. *Angewandte Chemie (International ed.in English)* **2010**, *49*, 2826 – 2829.

[29] Sun, M.; Li, Z.; Liu, Y.; Xu, H. Direct Visual Evidence for Chemical Mechanisms of SERRS Via Charge Transfer in Au20-Pyrazine-Au20 Junction. *J. Raman Spectrosc.* **2009**, *40*, 1942.

[30] Xu, H. X.; Bjerneld, E. J.; Käll, M.; Börjesson, L. Spectroscopy of Single Hemoglobin Molecules by Surface Enhanced Raman Scattering. *Phys. Rev. Lett.* **1999**, *83*.

[31] General Discussion. *Faraday Discuss.* **2006**, *132*, 227 - 247.

[32] Lazorenko-Manevich, R. M. Adatom Hypothesis as a Predominant Mechanism of Surface Enhanced Raman Scattering: A Review of Experimental Argumentation. *Russian J. Electrochem.* **2005**, *41*, 799.

[33] Otto, A.; Timper, J.; Billmann, J.; Kovacs, G.; Pockrand, I. Surface Roughness Induced Electronic Raman Scattering. *Surf. Sci.* **1980**, *92*, L55.

[34] Morton, S. M.; Jensen, L. Understanding the Molecule-Surface Chemical Coupling in SERS. *J. Am. Chem. Soc.* **2009**, *131*, 4098.

[35] Udagawa, M.; Chou, C.; Hemminger, J. C.; Ushioda, S. Raman Scattering Cross Section of Adsorbed Pyridine Molecules on a Smooth Silver Surface. *Phys. Rev. B* **1981**, *23*.

[36] Jiang, X.; Campion, A. Chemical Effects in Surface-Enhanced Raman Scattering: Pyridine Chemisorbed on Silver Adatoms on Rh (100). *Chemical Physics Letters* **1987**, *140*, 95-100.

[37] Zhao, L. L.; Jensen, L.; Schatz, G. C. Surface-Enhanced Raman Scattering of Pyrazine at the Junction between Two Ag_{20} Nanoclusters. *J. Am. Chem. Soc.* **2006**, *6*, 1234.

[38] Nikoobakht, B.; Wang, J.; El-Sayed, M. A. Surface-Enhanced Raman Scattering of Molecules Adsorbed on Gold Nanorods: Off-Surface Plasmon Resonance Condition. *Chemical Physics Letters* **2002**, *366*, 17-23.

[39] Fromm, D. P.; Sundaramurthy, A.; Kinkhabwala, A.; Schuck, P. J.; Kino, G. S.; Moerne, W. E. Exploring the Chemical Enhancement for Surface-Enhanced Raman Scattering with Au Bowtie Nanoantennas. *J. Chem. Phys.* **2006**, *124*, 061101.

[40] Peyser-Capadona, L.; Zheng, J.; Gonzalez, J. I.; Lee, T. H.; Patel, S. A.; Dickson, R. M. Nanoparticle-Free Single Molecule Anti-Stokes Raman Spectroscopy. *Phys. Rev. Lett.* **2005**, *94*, 058301.

[41] Zheng, J.; Ding, Y.; Tian, B.; Wang, Z. L.; Zhuang, X. Luminescent and Raman Active Silver Nanoparticles with Polycrystalline Structure. *J. Am. Chem. Soc.* **2008**, *130*, 10473.

[42] Yang, L.; Jiang, X.; Ruan, W.; Zhao, B.; Xu, W.; Lombardi, J. R. Observation of Enhanced Raman Scattering for Molecules Adsorbed on TiO_2 Nanoparticles: Charge-Transfer Contribution. *J. Phys. Chem. C* **2008**, *112*, 20098.

[43] Jensen, L.; Aikens, C. M.; Schatz, G. C. Electronic Structure Methods for Studying Surface-Enhanced Raman Scattering. *Chem. Soc. Rev.* **2008**, *37*, 1061.

[44] Saikin, S. K.; Olivares-Amaya, R.; Rappoport, D.; Stopa, M.; Aspuru-Guzik, A. On the Chemical Bonding Effects in the Raman Response: Benzenethiol Adsorbed on Silver Clusters. *Physical chemistry chemical physics* **2009**, *11*, 9401.

[45] Otto, A. The Chemical (Electronic) Contribution to Surface-Enhanced Raman Scattering. *J. Raman Spectrosc.* **2005**, *36*, 497.

[46] Aroca, R. F.; Clavijo, R. E.; Halls, M. D.; Schlegel, H. B. Surface-Enhanced Raman Spectra of Phthalimide. Interpretation of the SERS Spectra of the Surface Complex Formed on Silver Islands and Colloids. *J. Phys. Chem. A* **2000**, *104*, 9505.

[47] Jensen, L.; Zhao, L. L.; Autschbach, J.; Schatz, G. C. Theory and Method for Calculating Resonance Raman Scattering from Resonance Polarizability Derivatives. *J. Chem. Phys.* **2005**, *123*, 174110.

[48] Jensen, L.; Zhao, L. L.; Schatz, G. C. Size-Dependence of the Enhanced Raman Scattering of Pyridine Adsorbed on Ag_n (n= 2-8, 20) Clusters. *The Journal of Physical Chemistry.C* **2007**, *111*, 4756.

[49] Nara, J.; Higai, S.; Morikawa, Y.; Ohno, T. Density Functional Theory Investigation of Benzenethiol Adsorption on Au (111). *J. Chem. Phys.* **2004**, *120*, 6705.

[50] Wan, L.; Terashima, M.; Noda, H.; Osawa, M. Molecular Orientation and Ordered Structure of Benzenethiol Adsorbed on Gold (111). *J. Phys. Chem. B* **2000**, *104*, 3569.

[51] Vivoni, A.; Birke, R. L.; Foucault, R.; Lombardi, J. R. Ab Initio Frequency Calculations of Pyridine Adsorbed on an Adatom Model of a SERS Active Site of a Silver Surface. *J. Phys. Chem. B* **2003**, *107*, 5557.

[52] Wu, D. Y.; Duan, S.; Ren, B.; Tian, Z. Q. Density Functional Theory Study of Surface-Enhanced Raman Scattering Spectra of Pyridine Adsorbed on Noble and Transition Metal Surfaces. *J. Raman Spectrosc.* **2005**, *36*, 533.

[53] Cardini, G.; Miranda, M. M. Density Functional Study on the Adsorption of Pyrazole Onto Silver Colloidal Particles. *The Journal of Physical Chemistry.B* **2002**, *106*, 6875.

[54] Wu, D. Y.; Ren, B.; Jiang, Y. X.; Xu, X.; Tian, Z. Q. Density Functional Study and Normal-Mode Analysis of the Bindings and Vibrational Frequency Shifts of the Pyridine-M (M) Cu, Ag, Au, Cu+, Ag+, Au+, and Pt) Complexes. *The Journal of Physical Chemistry.A* **2002**, *106*, 9042.

[55] Cardini, G.; Muniz-Miranda, M.; Pagliai, M.; Schettino, V. A Density Functional Study of the SERS Spectra of Pyridine Adsorbed on Silver Clusters. *Theor. Chem. Acc.* **2007**, *117*, 458.

[56] Johansson, P. Illustrative Direct Ab Initio Calculations of Surface Raman Spectra. *Physical chemistry chemical physics* **2005**, *7*, 475.

[57] Wu, D. Y.; Hayashi, M.; Lin, S. H.; Tian, Z. Q. Theoretical Differential Raman Scattering Cross-Sections of Totally-Symmetric Vibrational Modes of Free Pyridine and pyridine–metal Cluster Complexes. *Spectrochimica Acta Part A: Molecular and Biomolecular Spectroscopy* **2004**, *60*, 137-146.

[58] Lambert, D. K. Vibrational Stark Effect of Adsorbates at Electrochemical Interfaces. *Electrochim. Acta* **1996**, *41*, 623-630.

[59] Lambert, D. K. Electric Field Induced Change of Adsorbate Vibrational Line Strength. *J. Chem. Phys.* **1991**, *94*, 6237.

[60] Nart, F. C.; Iwasita, T. Static Field Effect on the Band Intensity of Adsorbed Sulfate Ions. *Electrochim. Acta* **1996**, *41*, 631-636.

[61] Pomfret, M. B.; Pietron, J. J.; Owrutsky, J. C. Measurement of Benzenethiol Adsorption to Nanostructured Pt, Pd, and PtPd Films using Raman Spectroelectrochemistry. *Langmuir* **2010**, *26*, 6809.

[62] Gomez, R.; Perez, J. M.; Gullon, J. S.; Montiel, V.; Aldaz, A. In Situ Surface Enhanced Raman Spectroscopy on Electrodes with Platinum and Palladium Nanoparticle Ensembles. *The journal of physical chemistry.B* **2004**, *108*, 9943.

[63] Sawai, Y.; Takimoto, B.; Nabika, H.; Ajito, K.; Murakoshi, K. Control of Near-Infrared Optical Response of Metal Nano-Structured Film on Glass Substrate for Intense Raman Scattering. *Faraday Discuss.* **2006**, *132*, 179.

[64] Kilitziraki, M.; Moore, A. J.; Petty, M. C.; Bryce, M. R. Evaporated Thin Films of Tetrathiafulvalene Derivatives and their Charge-Transfer Complexes. *Thin Solid Films* **1998**, *335*, 209-213.

[65] Geiser, U. *Toward crystal design in organic conductors and superconductors;* **1999**, Proceedings of the 28th International School of Crystallography, Erice, Italy, May 1999.

[66] Horowitz, G. Organic Field-Effect Transistors. *Adv Mater* **1998**, *10*, 365.

[67] Kymissis, I. *Organic Field Effect Transistors, Theory, Fabrication and Characterization;* Springer: 2009; Chap. 2.

[68] Yamashita, Y. Organic Semiconductors for Organic Field-Effect Transistors. *Science and technology of advanced materials* **2009**, *10*, 024313.

[69] Schottky, W. *Phs. Z* **1940**, *41*, 570.

[70] Bardeen, J. Surface States and Rectification at a Metal Semi-Conductor Contact. *Physical review* **1947**, *71*, 717.

[71] Heimel, G.; Romaner, L.; Zojer, E.; Bredas, J. The Interface Energetics of Self-Assembled Monolayers on Metals. *Accounts of Chemical Research* **2008**, *41*, 729.

[72] Heimel, G.; Romaner, L.; Brédas, J.; Zojer, E. Organic/metal Interfaces in Self-Assembled Monolayers of Conjugated Thiols: A First-Principles Benchmark Study. *Surf. Sci.* **2006**, *600*, 4548-4562.

[73] Heimel, G.; Romaner, L.; Bredas, J.; Zojer, E. Interface Energetics and Level Alignment at Covalent Metal-Molecule Junctions: π-Conjugated Thiols on Gold. *Phys. Rev. Lett.* **2006**, *96*, 196806.

[74] Ishii, H.; Sugiyama, K.; Ito, E.; Seki, K. Energy Level Alignment and Interfacial Electronic Structures at organic/metal and organic/organic Interfaces. *Adv Mater* **1999**, *11*, 605.

[75] Campbell, I. H.; Davids, P. S.; Smith, D. L.; Barashkov, N. N.; Ferraris, J. P. The Schottky Energy Barrier Dependence of Charge Injection in Organic Light-Emitting Diodes. *Appl. Phys. Lett.* **1998**, *72*, 1863.

[76] Betti, M. G.; Kanjilal, A.; Mariani, C.; Vazquez, H.; Dappe, Y. J.; Ortega, J.; Flores, F. Barrier Formation at Organic Interfaces in a Cu (100)-Benzenethiolate-Pentacene Heterostructure. *Phys. Rev. Lett.* **2008**, *100*, 027601.

[77] de Boer, B.; Hadipour, A.; Mandoc, M. M.; van Woudenbergh, T.; Blom, P. W. M. Tuning of Metal Work Functions with Self-Assembled Monolayers. *Adv Mater* **2005**, *17*, 621.

[78] Chen, J.; Reed, M. A.; Rawlett, A. M.; Tour, J. M. Large on-Off Ratios and Negative Differential. *Science* **1999**, *286*, 1550.

[79] Whelan, C. M.; Smyth, M. R.; Barnes, C. J. HREELS, XPS, and Electrochemical Study of Benzenethiol Adsorption on Au(111). *Langmuir* **1999**, *15*, 126.

[80] Pauling, L. The Nature of the Chemical Bond. Application of Results obtained from the Quantum Mechanics and from a Theory of Paramagnetic Susceptibility to the Structure of Molecules. *J. Am. Chem. Soc.* **1931**, *53*, 1367. Also in Pauling,L. The nature of the Chemical Bond, 3rd ed.; Cornell University Press: New York (1960).

[81] Valiskó, M.; Boda, D. Relative Permittivity of Polar Liquids. Comparison of Theory, Experiment, and Simulation. *The journal of physical chemistry.B* **2005**, *109*, 6355.

[82] Peisert, H.; Knupfer, M.; Fink, J. Energy Level Alignment at organic/metal Interfaces: Dipole and Ionization Potential. *Appl. Phys. Lett.* **2002**, *81*, 2400.

[83] Nam, P. C.; Nguyen, M. T.; Chandra, A. K. Theoretical Study of the Substituent Effects on the S-H Bond Dissociation Energy and Ionization Energy of 3-Pyridinethiol: Prediction of Novel Antioxidant. *J. Phys. Chem. A* **2006**, *110*, 10911.

[84] Ionization potential of Benzenethiol. *http://www.bis.fm/assets/documents/faxdatasheets/Ion%20Science%20PhoCheck+2000%2010.6eV%20Gas%20Detection%20Table.pdf* (accessed 07/09, 2010).

[85] Sze, S. M. In *Physics of Semiconductor Devices;* John Wiley Sons, Inc.: Hoboken, 2007; 2nd ed.

[86] Yokota, K.; Taniguchi, M.; Kawai, T. Metal−Molecule Interfaces Formed by Noble-Metal−Chalcogen Bonds for Nanoscale Molecular Devices. *J. Phys. Chem. C* **2010**, *114*, 4050.

[87] Braun, S.; Salaneck, W. R.; Fahlman, M. Energy-Level Alignment at organic/metal and organic/organic Interfaces. *Adv Mater* **2009**, *21*, 1450.

[88] Tian, W.; Datta, S.; Hong, S.; Reifenberger, R.; Henderson, J. I.; Kubiak, C. P. Conductance Spectra of Molecular Wires. *J. Chem. Phys.* **1998**, *109*, 2874.

[89] ADF: Amsterdam Density Functional software. *http://www.scm.com.*

[90] Velde, Te. G.; Bickelhaupt, F. M.; Baerends, E. J.; Guerra, C. F.; Van Gisbergen, S. J. A.; Snijders, J. G.; Ziegler, T. Chemistry with ADF. *Journal of computational chemistry* **2001**, *22*, 931.

[91] Becke, A. D. Density-Functional Exchange-Energy Approximation with Correct Asymptotic Behavior. *Physical review.A, Atomic, molecular, and optical physics* **1988**, *38*, 3098.

[92] Perdew, J. P. Density-Functional Approximation for the Correlation Energy of the Inhomogeneous Electron Gas. *Phys. Rev. B* **1986**, *33*.

[93] Gartia,M.R.; Xu, Z.; Behymer, E.; Nguyen, H.; Britten , J.A.; Larson, C.; Miles, R.; Bora, M.; Chang, A.S.P.; Bond, T.C.; Liu, G.L. Rigorous Surface Enhanced Raman Spectral Characterization of Large-Area Ultrahigh-Uniformity Silver-Coated Tapered Silica Nanopillar Arrays. Nanotechnology **2010**, 21, 395701.

[94] Etchegoin, P. G.; Galloway, C.; Le Ru, E. C. Polarization-Dependent Effects in Surface-Enhanced Raman Scattering (SERS). *Physical chemistry chemical physics* **2006**, *8*, 2624.

[95] Arenas, J. F.; Woolley, M. S.; Otero, J. C.; Marcos, J. I. Charge Transfer Processes in Surface-Enhanced Raman Scattering. Franck-Condon Active Vibrations of Pyridine. *J. Phys. Chem.* **1996**, *100*, 3206.

[96] Garraway, B.; Stenholm, S.; Suominen, K. A. Adventures in Wave Packet Land. *Physics World* **1993**, *46*.

[97] van Gisbergen, S. J. A.; Snijders, J. G.; Baerends, E. J. Application of Time-Dependent Density Functional Response Theory to Raman Scattering. *Chemical Physics Letters* **1996**, *259*, 599-604.

[98] Letardi, S.; Cleri, F. Interaction of Benzene Thiol and Thiolate with Small Gold Clusters. *J. Chem. Phys.* **2004**, *120*, 10062.

[99] Lang, N. D.; Kohn, W. Theory of Metal Surfaces: Work Function. *Phys. Rev. B* **1971**, *3*.

[100] Witte, G.; Lukas, S.; Bagus, P. S.; Woll, C. Vacuum Level Alignment at organic/metal Junctions: "Cushion" Effect and the Interface Dipole. *Appl. Phys. Lett.* **2005**, *87*, 263502.

[101] Crispin, X.; Geskin, V.; Crispin, A.; Cornil, J.; Lazzaroni, R.; Salaneck, W. R.; Bredas, J. L. Characterization of the Interface Dipole at Organic/Metal Interfaces. *J. Am. Chem. Soc.* **2002**, *124*, 8141.

[102] Allara, D. L.; Nuzzo, R. G. Spontaneously Organized Molecular Assemblies. 2. Quantitative Infrared Spectroscopic Determination of Equilibrium Structures of Solution-Adsorbed n –Alkanoic Acids on an Oxidized Aluminum Surface. *Langmuir* **1985**, *1*, 66.

[103] Moskovits, M.; DiLella, D. P.; Maynard, K. J. Surface Raman Spectroscopy of a Number of Cyclic and Molecular Reorientation Aromatic Molecules Adsorbed on Silver: Selection Rules and Molecular Reorientation. *Langmuir* **1988**, *4*, 76.

[104] Joo, T. H.; Kim, M. S.; Kim, K. Surface-Enhanced Raman Scattering of Benzenethiol in Silver Sol. *J. Raman Spectrosc.* **1987**, *18*, 57.

[105] Biggs, K. B.; Camden, J. P.; Anker, J. N.; Van Duyne, R. P. Surface-Enhanced Raman Spectroscopy of Benzenethiol Adsorbed from the Gas Phase Onto Silver Film Over Nanosphere Surfaces: Determination of the Sticking Probability and Detection Limit Time. *J. Phys. Chem. A* **2009**, *113*, 4581.

[106] Carron, K. T.; Hurley, L. G. Axial and Azimuthal Angle Determination with Surface-Enhanced Raman Spectroscopy: Thiophenol on Copper, Silver, and Gold Metal Surfaces. *J. Phys. Chem.* **1991**, *95*, 9979.

[107] Aggarwal, R. L.; Farrar, L. W.; Diebold, E. D.; Polla, D. L. Measurement of the Absolute Raman Scattering Cross Section of the 1584-cm^{-1} Band of Benzenethiol and the Surface-Enhanced Raman Scattering Cross Section Enhancement Factor for Femtosecond Laser-Nanostructured Substrates. *J. Raman Spectrosc.* **2009**, *40*, 1331.

[108] Cohen, A. J.; Sánchez, P. M.; Yang, W. Insights into Current Limitations of Density Functional Theory. *Science* **2008**, *321*, 792.

CHAPTER 6

CLASSICAL SIMULATION OF LIGHT-MATTER INTERACTION IN PLASMONIC DEVICE

Introduction

The theoretical explanation of light-matter interaction is dated back to 1871 when Lord Rayleigh theoretically derived the scattering of light by a dielectric particle with size much smaller than the wavelength [86]. For example, to explain the blueness of sky, he showed that the scattering of light by a diluted gas follows a ω^4 law, where $\omega = 2\pi/\lambda$, is the angular frequency of the incident light [86, 87]. That is, air molecules scatter blue light (high frequency) more efficiently than red light (low frequency) giving rise to blue color of the sky. In 1908, Mie expanded Rayleigh's formulation to include any arbitrary size of the particles and derived absorption as well as scattering cross sections of the spherical particles [88]. Gans extended Mie and Rayleigh's approached to ellipsoidal particles to understand shape dependent scattering behavior [89]. Since, analytical solution is available for only simple geometries (sphere, ellipse), for any other complex structures and shape require to solve Maxwell's equation. In Chapter 6, we present the classical simulation of plasmonic structures, which explains the electromagnetic enhancement mechanism of SERS and plasmonic resonances in general.

Basics of electromagnetics in metal and metal surfaces

The interaction of metals with electro-magnetic fields can be described by classical Maxwell equations:

$$\nabla \cdot \mathbf{D} = \rho \qquad (1)$$

$$\nabla \cdot \mathbf{B} = 0 \qquad (2)$$

$$\nabla \times \mathbf{E} = -\partial \mathbf{B} / \partial t \qquad (3)$$

$$\nabla \times \mathbf{H} = \mathbf{J} + \partial \mathbf{D} / \partial t \qquad (4)$$

Maxwell equation connects the macroscopic fields (dielectric displacement **D**, electric field **E**, magnetic field **H** and magnetic induction **B**) with an external charge density ρ and current density **J**. The dielectric displace **D** is connected to the electric field **E** through the frequency dependent dielectric function. The magnetic induction is related to the magnetic field.

$$\mathbf{D} = \varepsilon_0 \, \varepsilon(\omega)\mathbf{E} \qquad (5)$$

$$\mathbf{B} = \mu_0 \mathbf{H} \qquad (6)$$

The complex dielectric constant can be written as a function of real (ε') and imaginary (ε'') part as:

$$\varepsilon = \varepsilon' + i\varepsilon'' \qquad (7)$$

The complex index of refraction can be presented as

$$n = n + i\kappa = \sqrt{\varepsilon} \qquad (8)$$

Dielectric constant and index of refraction can be obtained from each other as:

$$\varepsilon' = n^2 - \kappa^2 \qquad \varepsilon'' = 2n\kappa \qquad (9)$$

$$n^2 = \frac{\varepsilon'}{2} + \frac{1}{2}\sqrt{\varepsilon'^2 + \varepsilon''^2} \qquad \kappa = \frac{\varepsilon''}{2n} \qquad (10)$$

The real part of the refractive index n (ω) describe the dispersion in the medium, the imaginary part (κ) describe the absorption coefficient (or extinction coefficient or losses in the metal). The absorption coefficient can be calculated using Beer's law as: $I = I_0 \exp(-\alpha x)$, where absorption coefficient, $\alpha(\omega) = 2\kappa(\omega)\omega/c$.

Plasma oscillation model

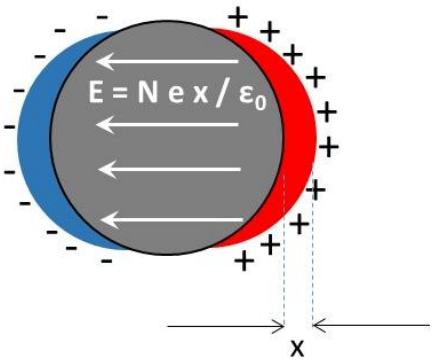

Figure 6.1: Schematic of idealized depiction of the displacement of electrons relative to metal atom, which occurs during plasma oscillations.

Let's assume that under electromagnetic field of **E** (t) = $\mathbf{E}_0$ exp (-$i\omega t$), the electron starts oscillating with a mean displacement of *x*. The damping rate due to collision with metal atoms is $\gamma = 1/\tau$ (interactions with the lattice vibrations: electron--phonon scattering). The equation of motion can be described as

$$m\frac{d^2x}{dt^2} + m\gamma\frac{dx}{dt} = -e\,\mathbf{E}(t) \qquad (11)$$

with the solution

$$x(t) = \frac{e}{m(\omega^2 + i\gamma\omega)}\mathbf{E}(t) \qquad (12)$$

The dipole moment of one electron due to this displacement = -*ex*

The polarization generated due to the displacement of electron **P** = -*Nex*

where *N* is the electron density.

The dielectric displacement, $\mathbf{D} = \varepsilon_0\,\mathbf{E} + \mathbf{P} = \varepsilon\,\varepsilon_0\,\mathbf{E}$ (13)

$$\varepsilon(\omega) = \frac{\mathbf{D}}{\varepsilon_0\mathbf{E}} = \frac{\varepsilon_0\mathbf{E} + \mathbf{P}}{\varepsilon_0\mathbf{E}} = 1 + \frac{\mathbf{P}}{\varepsilon_0\mathbf{E}} = 1 - \frac{Nex}{\varepsilon_0\mathbf{E}} \qquad (14)$$

Replacing *x* from equation (12) $\varepsilon(\omega) = 1 - \frac{Ne^2}{m\varepsilon_0}\frac{1}{(\omega^2 + i\gamma\omega)}$ (15)

Introducing, bulk plasmon frequency, $\omega_p^2 = \frac{Ne^2}{m\varepsilon_0}$

$$\varepsilon(\omega) = 1 - \frac{\omega_p^2}{(\omega^2 + i\gamma\omega)} \quad (16)$$

With $\gamma = 1/\tau$, $\varepsilon(\omega) = 1 - \frac{\omega_p^2\tau^2}{(\omega^2\tau^2 + i\omega\tau)}$ (17)

For large frequency approximation $\omega\tau >> 1$, and $i\omega\tau$ in equation (17) can be neglected.

$$\varepsilon(\omega) = 1 - \frac{\omega_p^2}{\omega^2} \quad (18)$$

Equation (16) can also be written as

$$\varepsilon(\omega) = \varepsilon_r + i\varepsilon_{im} = 1 - \frac{\omega_p^2}{\omega^2 + \gamma^2} + \frac{i\omega_p^2\gamma}{\omega(\omega^2 + \gamma^2)} \quad (19)$$

Equation (19) is called Drude model.

Figure 6.2 plots equation (18). It should be noticed that there is no propagation of wave for $\varepsilon(\omega) < 0$, that is, electromagnetic waves are totally reflected from the medium. When $\varepsilon(\omega) > 0$, electromagnetic wave propagates without damping. Similarly, there is no propagation of wave below $\omega < \omega_{p.}$ The plasma frequency in most of the metals lies in the ultra-violet regime, with energies ranging from 5-15 eV. Hence, bulk plasmon is not generally excited by visible lights. Also bulk plasmons are longitudinal propagating waves and hence bulk plasmons cannot couple to transversal electro-magnetic fields and thus cannot be excited from or coupled to direct irradiation.

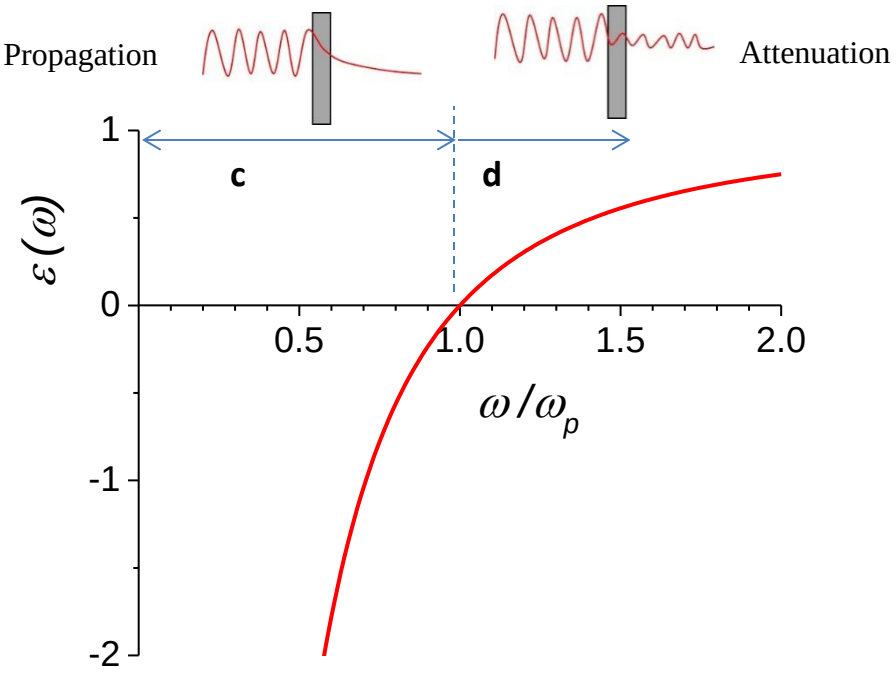

Figure 6.2: Dispersion relation of free electron gas.

To combine optoelectronics with plasmonics one has to convert light (photons) into plasmons. Bulk plasmons are longitudinal oscillations (parallel to the propagation direction), while photons are transverse (perpendicular to the propagation). Hence, they do not match. Surface plasmons are transverse, but they are mismatched to photons in their momentum. It is possible to provide the necessary momentum $\hbar k$ by a grating, which transfers the $\Delta k = 2\pi/a$ (a = line spacing).

Surface plasmon resonance

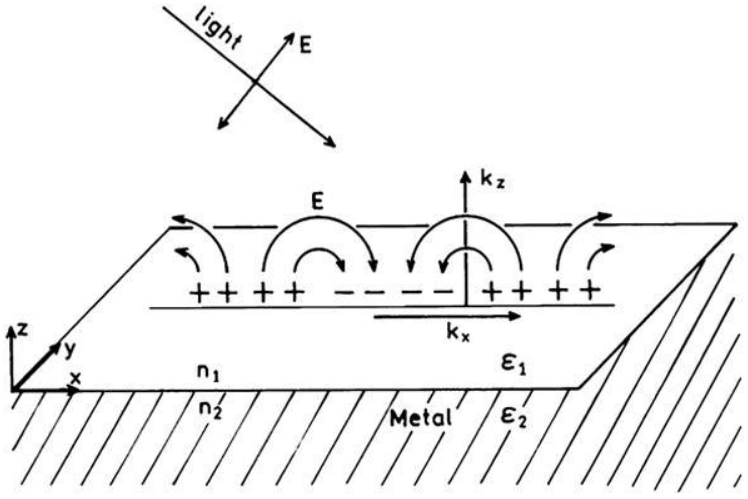

Figure 6.3: Interface along the x-y plane between a dielectric (top, index 1), and a metal (bottom, index 2).

Since, surface plasmon wave exists only for transverse magnetic (TM) mode, the electric field of incident light in x-z plane can be written as (i = 1, 2):

$$\mathbf{E}_i = \left(\mathbf{E}_{i,x}, 0, \mathbf{E}_{i,z}\right)\exp\left[i\left(\mathbf{k}_i \cdot \mathbf{r} - \omega t\right)\right] \qquad (20)$$

$$\mathbf{H}_i = \left(0, \mathbf{H}_{i,y}, 0\right)\exp\left[i\left(\mathbf{k}_i \cdot \mathbf{r} - \omega t\right)\right] \qquad (21)$$

$$\mathbf{D}_i = \varepsilon_0 \varepsilon_i \mathbf{E}_i \ , \qquad \mathbf{B}_i = \mu_0 \mathbf{H}_i \qquad (22)$$

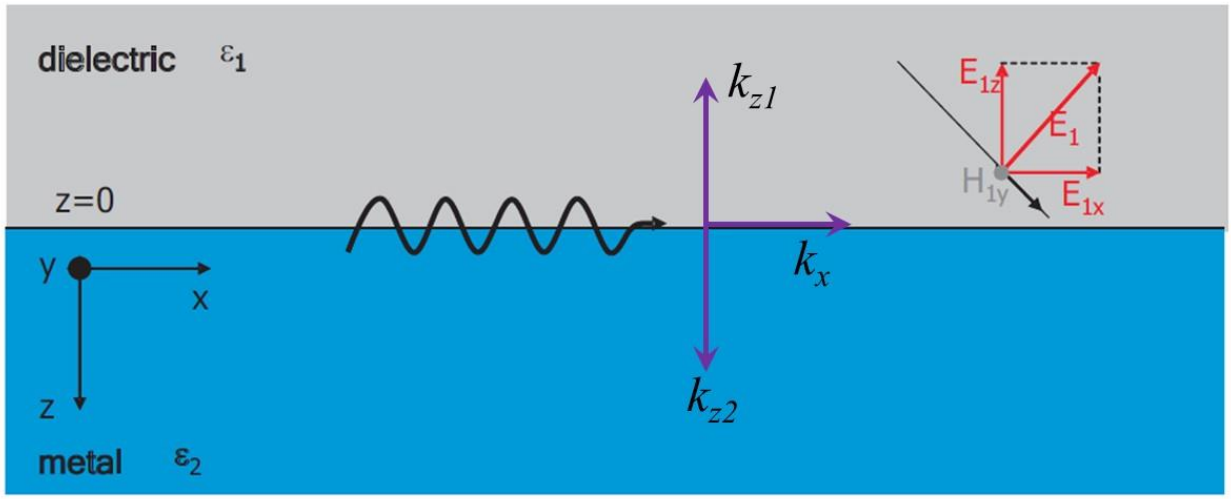

Figure 6.4: Wavevector showing the continuity conditions at the interface (x-z plane).

The incident field in x-z plane can be written as:

$\mathbf{E} = \mathbf{E}_0 \exp\left[i\left(k_x x + k_z z - \omega t\right)\right]$ with the wavevector $\mathbf{k} = \left(k_x, 0, k_{i,z}\right)$. In the absence of charge and currents (ρ = 0, **J** = 0), equation (1-4) and equation (20-22) gives:

$$\frac{k_{z1}}{\varepsilon_1} + \frac{k_{z2}}{\varepsilon_2} = 0 \qquad (23)$$

$$k_x^2 + k_{z1}^2 = \varepsilon_1 \left(\frac{\omega}{c}\right)^2 \qquad (24)$$

$$k_x^2 + k_{z2}^2 = \varepsilon_2 \left(\frac{\omega}{c} \right)^2 \qquad (25)$$

Solving equation (23-25) we can obtain the surface plasmon wave propagating on the surface as:

$$k_x = \left(\frac{\omega}{c} \right) \sqrt{\frac{\varepsilon_1 \varepsilon_2}{\varepsilon_1 + \varepsilon_2}} \qquad (26)$$

Electromagnetic simulation of plasmonic structures

For simulation, in the thesis we use commercially available electromagnetic field solvers such as rigorous coupled-wave analysis (RCWA), finite element methods (FEM) based COMSOL and finite difference time domain (FDTD) based Lumerical. Electromagnetic field solvers are either domain discretization type or boundary discretization type. Domain discretization techniques are more popular as they offer both time domain and frequency domain versions [90]. The suitability of techniques and software depends on specific properties of the problem to be solved keeping in mind the computation time and memory requirement [90].

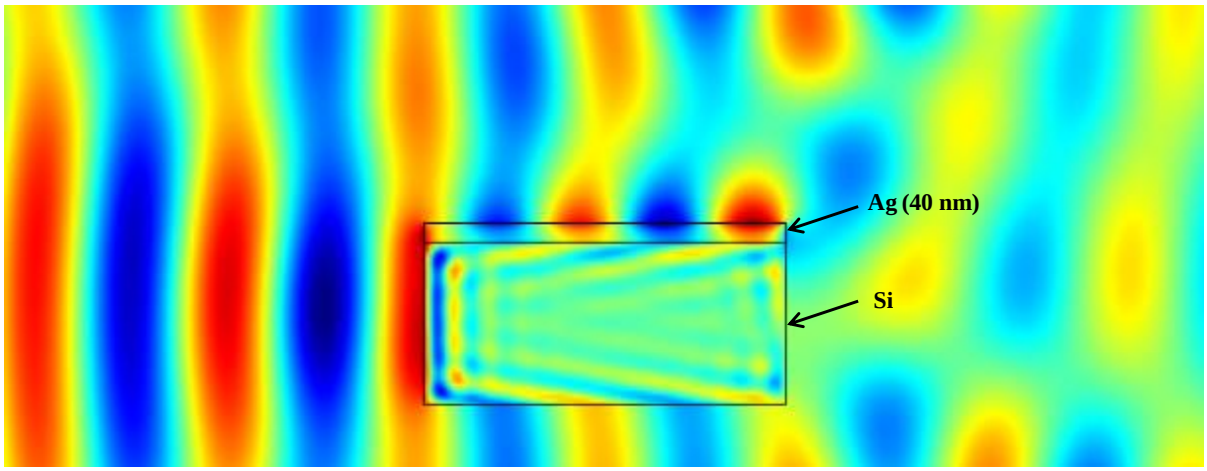

Figure 6.5: Surface Plasmon Resonance for smooth Silver surface at wavelength = 370 nm.

As an example, Figure 6.5 shows the surface plasmon resonance simulation of a thin (40 nm) Ag film on Si surface using FEM code COMSOL. Plane wave is launched from the left and the TM electric field distribution is shown in Fig. 6.5. The red and blue color signify high and

low electric field magnitude respectively. The bulk surface plasmon can be clearly seen on the Ag film.

Nanocone plasmonic structure

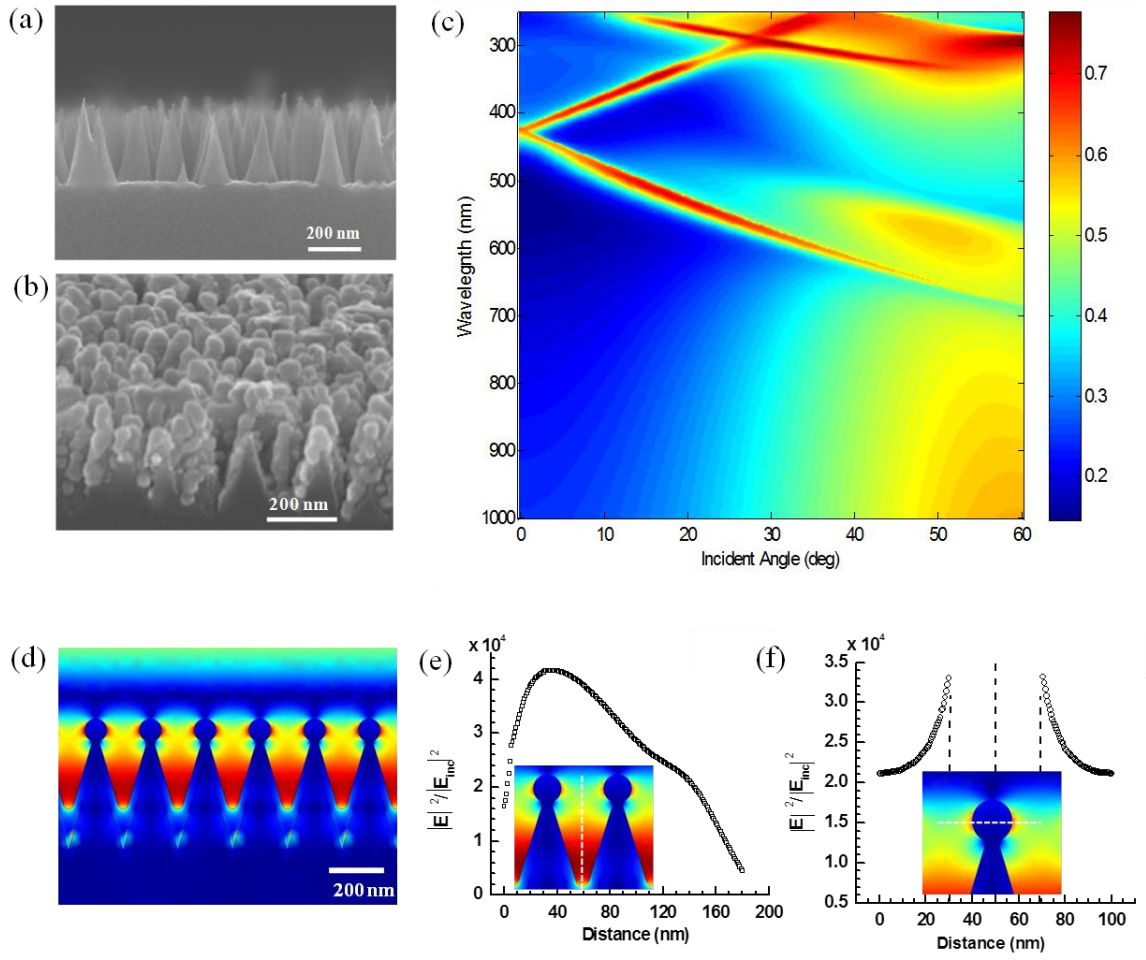

Figure 6.6: (a) SEM image of the nanocone silicon based photonic structure. (b) SEM image of the nanoplasmonic structure fabricated from the nanophotonic structure shown in (a) by depositing 80 nm of silver using electron beam evaporation. (c) Dispersion diagram of the nanoplasmonic structure shown in (b) using RCWA method. (d) Calculated electromagnetic field for the nanoplasmonic structure. (e) Gap mode surface plasmon resonance and the corresponding enhancement of the electromagnetic field calculated using COMSOL. (f) Tip mode localized surface plasmon resonance and the corresponding enhancement of the electromagnetic field at the tip of the plasmonic structure.

Figure 6.6a shows a SEM image of nanophotonic structure fabricated on silicon using SPERISE process as discussed in Chapter 2. The details of the fabrication process are given in [91, 92]. The height of the nanocone structures are about 200 nm, the base of the cones are 120

nm and the distance between two cone structures is about 300 nm. SEM of the nanoplasmonic structure after deposition of 80 nm silver on the nanophotonic structure is shown in Fig. 6.6b. The presence of surface plasmon resonance (SPR) in our fabricated nanoplasmonic structure is independently verified by using two commercially available electromagnetic simulation packages (DIFFRACTMOD, RSoft Design and COMSOL). DIFFRACTMOD uses rigorous coupled-wave analysis (RCWA) and can provide information about diffraction efficiency as a function of wavelength. The absorption maxima (or reflection minima) of the calculated spectra can be utilized to identify the resonant mode. For the RCWA simulation, we used a silicon cone structure with height 200 nm, base 120 nm, with a period of 300 nm. The thickness of silver layer on the top of the silicon cones are 80 nm. The absorption efficiency (also the reflection efficiency) of the TM resonant mode was calculated in the wavelength range of $200 < \lambda < 900$ nm and the incident angle was varied from $0° < \theta < 60°$. Figure 6.6c presents the dispersion diagram of the above mentioned nanoplasmonic structure. The dispersion diagram clearly shows that the nanocone plasmonic substrate can support broadband SPR supporting many incident wavelengths in the ranges 200 to 700 nm covering various incident angles from 0 to 60 degree. The electromagnetic field distribution within the nanocone plasmonic structure is simulated by COMSOL. The complex optical constants of silver and silicon are taken from Palik's handbook [93]. Figure 6.6d shows the excited scattering field in TM mode for an incident wavelength of 785 nm. The different colors indicate the magnitude of normalized amplitude of scattering electric field with respect to that of incident electric field, red indicating high field and blue indicating low field [94]. Two different localized surface plasmon resonance (LSPR) modes, namely, the "gap" mode (Fig. 6.6e) and the "tip" mode (Fig. 6.6f) can be clearly seen in the simulation. The gap mode is due to the confinement of electromagnetic field in the close proximity (< 30 nm) between two adjacent nanocone plasmonic structures. The field intensity is enhanced maximum up to $4x10^4$ times as compared to the incident field intensity ($I_{inc} = |E_{inc}|^2$). The high electromagnetic field at the top of cone structure is due to LSPR at the sub 20 nm silver nanobead structures, similar to LSPR observed for metallic naoparticles [95]. The exponential decaying nature of the surface plasmon near field away from the metal surface can be clearly seen in Fig. 6.6f.

Nanohole plasmonic structure

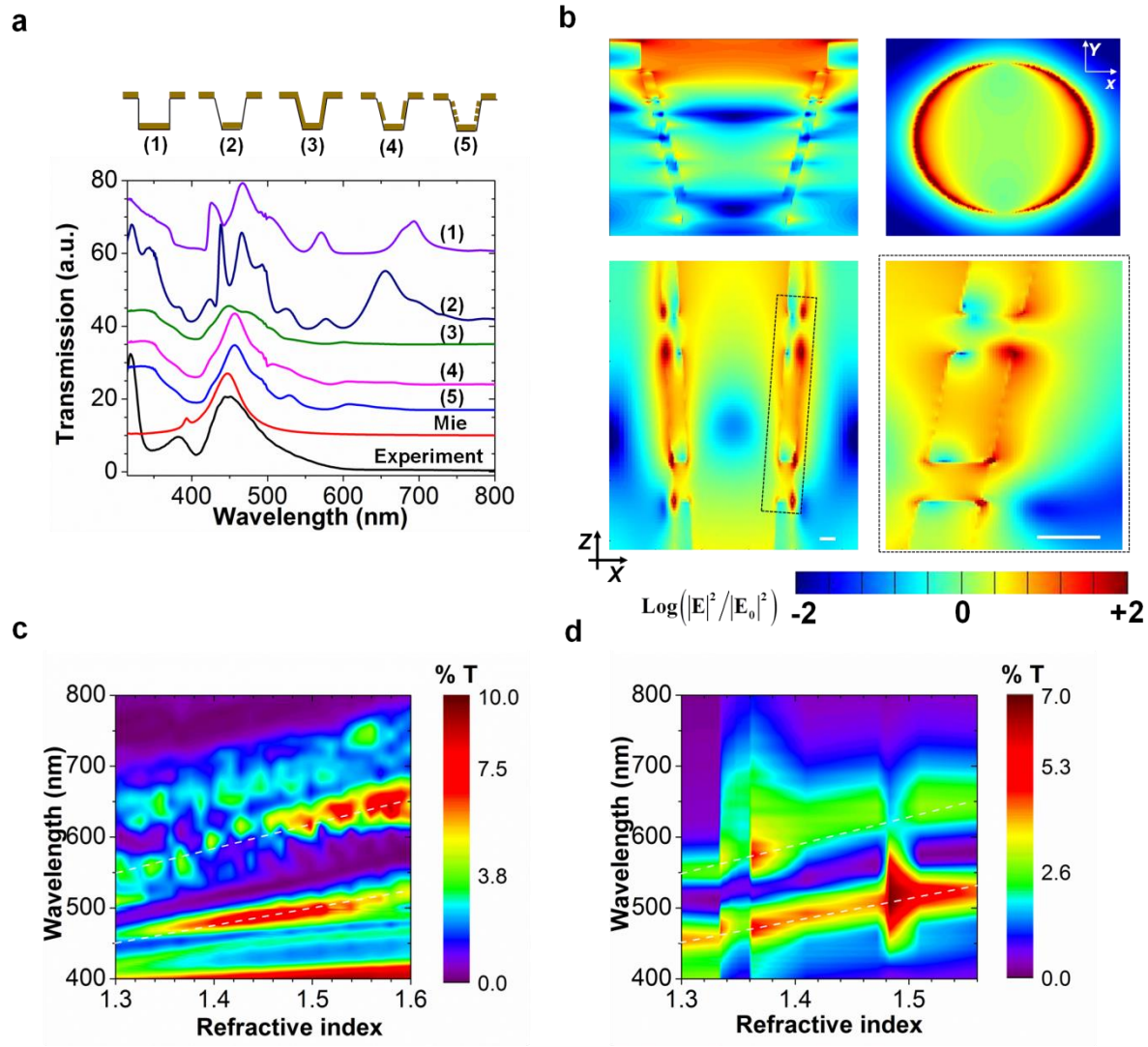

Figure 6.7: FDTD simulation for nanohole plasmonic structure.

To further understand the physics behind the experimental observations shown in Chapter 4, full 3-D finite difference time domain (FDTD) simulations are performed. The detailed simulation procedure is described in Appendix A. To highlight the importance of cup shape and the side wall nanoparticles, we have simulated five different nanohole shapes (labeled 1-5) in Fig. 6.7a. Figure 6.7a shows the FDTD simulated transmission spectra for different shaped nanohole plasmonic device labeled (1)-(5). For all the simulations, h =500 nm, t = 90 nm. The experimental transmission spectrum (black line) and calculated extinction spectrum for a

nanoparticle (d = 50 nm) in a surrounding refractive-index of n = 1.56 (red line) is also presented. As expected nanohole without metal film on the sidewalls and continuous metal film on the side walls (similar to quasi 3D plasmonics crystal or EOT structures) shows multiple transmission peaks in the simulation (case 1-3) and do not match with the experimental observations. However, with incorporation of discrete metal film on the sidewalls and multiple particle-like structures (case-4 and 5) as the analogy to the Lycurgus cup, we started to observe similar peak features as in the experiment (the slight discrepancy in the experiment and simulations are due to the difficulties in exactly simulating the randomly decorated nanoparticles on the wall). The intense peak at $\lambda = 450\,\text{nm}$ is due to the LSPR mode at the gap between the nanoparticles and at the rim of the nanohole plasmonic substrate.

The corresponding variation in the electric field intensity ($|E|^2$) is shown in Fig. 6.7b. The top (x-y) and cross-sectional (x-z) views of the intensity distribution represents the electric field enhancement ($Log|E/E_{inc}|^2$) associated with the corresponding plasmon resonances. The LSPR mode of the particle at Ag-PET interface at $\lambda = 450\,\text{nm}$ is clearly visible in Fig. 6.7b. The cavity mode (SPP-BW) can also be found in Fig. 6.7b. Detailed near-field intensity distribution for nanoLCA for different environment is presented later in this chapter. In order to predict the sensitivity of the device to refractive index variation of the surrounding medium, we perform a simulation to calculate the transmission spectrum by changing the refractive index of superstrate on nanohole plasmonic substrate. Figure 6.7c shows the FDTD simulated contour plot showing the variation of transmission spectra by changing the refractive index (RI) of surrounding medium for nanohole plasmonic substrate. The result showed appearance of two distinct peaks with increasing RI. Also, the first peak red-shifted from λ = 450 nm to λ = 525 nm and the second peak is red-shifted from λ = 550 nm to λ = 650 nm with the increase of RI. As observed in the experiment, the simulation results also showed red shift of both modes (SPP-BW and LSPR) with RI increase. The corresponding measured variation of transmission as a function of RI is shown in Fig. 6.7d. Figure 6.7d shows experimentally obtained contour plot showing the variation of transmission spectra of nanoLCA in presence of different RI liquids. The experimental contour plot showed remarkable resemblance to the FDTD simulated contour plot with appearance of two distinctive peaks and similar red-shift of resonance peaks. The

simulation results are strikingly similar with the experimental results about the appearance of two peaks and red shifting with the increase of RI.

Figure 6.8 shows the FDTD simulated cross-sectional (x-z) and top (x-y) intensity distribution for straight nanohole array at λ = 467 nm. Maximum intensity enhancement factor $\left(|E|^2/|E_0|^2\right)$ of 316 ($\cong 10^{2.5}$) was estimated for the resonance mode at λ = 467 nm.

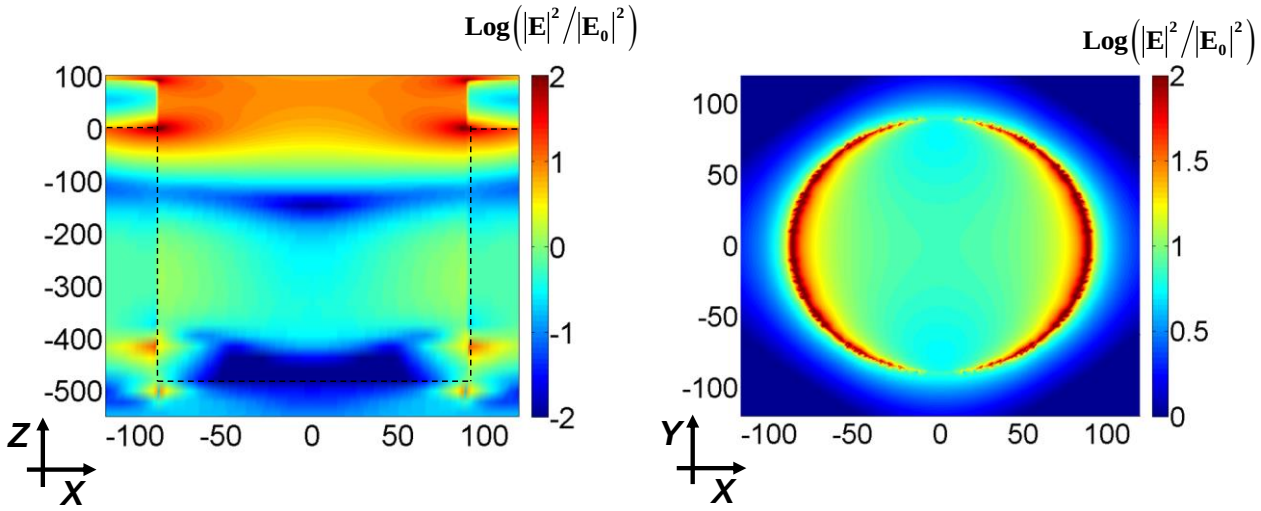

Figure 6.8: Near field intensity calculation for straight nanohole array structures.

Figure 6.9a shows the cross-sectional (x-z) intensity distribution of nanohole plasmonic substrate for air (at λ = 450 nm) and for water (at λ = 525 nm) environment. The right-hand side images are close-up view of the region marked with black dotted rectangles. The scale bar corresponds to 20 nm. The LSPR mode with high electric field intensity at Ag-PET interface and at the corner of the nanoparticle is clearly observed. Figure 6.9b shows the cross-sectional (y-z) intensity distribution of nanohole plasmonic substrate for air (at λ = 450 nm) and for water (at λ = 525 nm) environment.

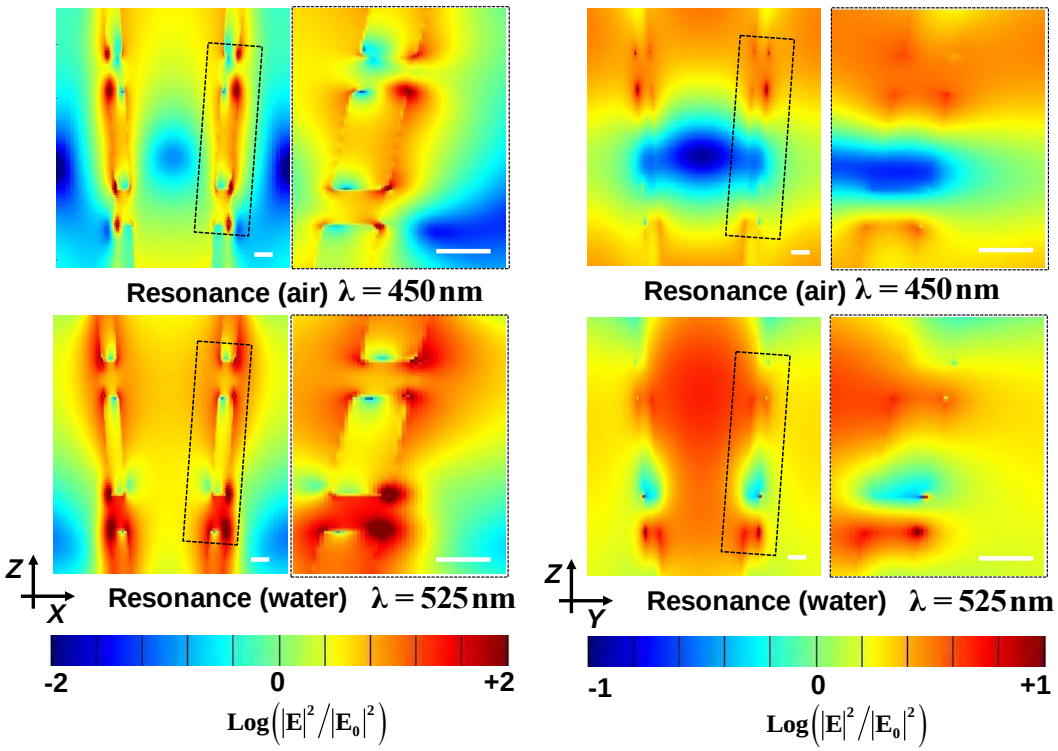

Figure 6.9: Near field intensity calculation for nanoLCA in air and water environment.

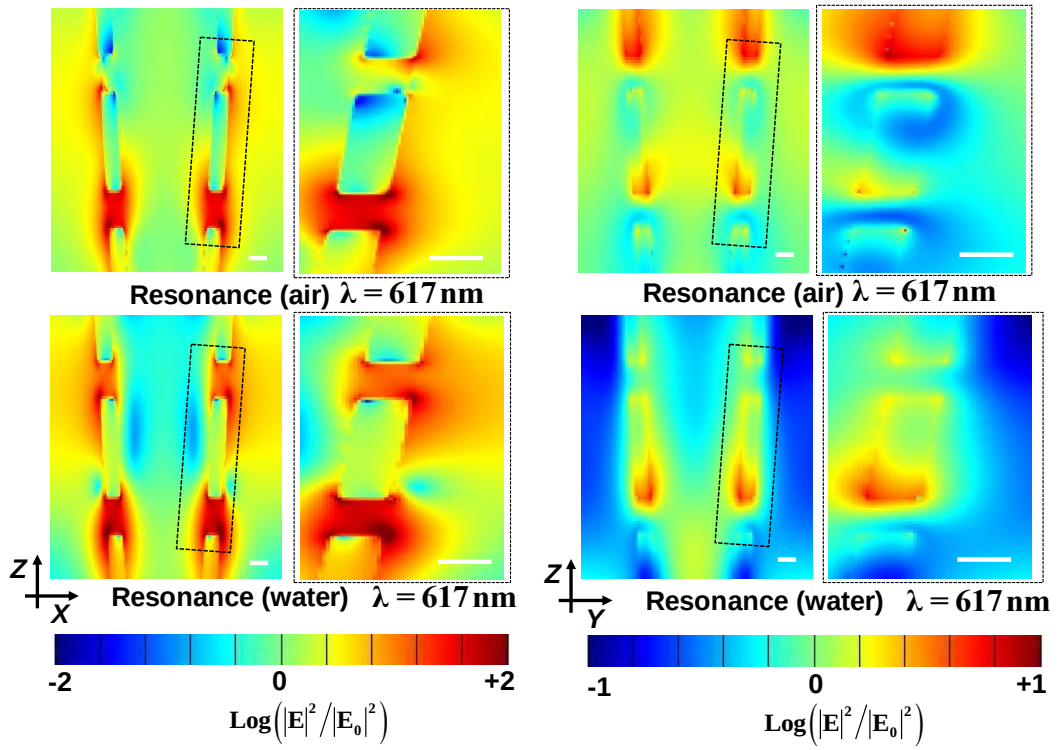

Figure 6.10: Near field intensity calculation for nanoLCA in air and water environment at λ = 617 nm.

Figure 6.10a shows the cross-sectional (x-z) intensity distribution of nanohole plasmonic substrate for air (at λ = 617 nm) and for water (at λ = 617 nm) environment. The right-hand side images are close-up view of the region marked with black dotted rectangles. The scale bar corresponds to 20 nm. Figure 6.10b shows the cross-sectional (y-z) intensity distribution of nanohole plasmonic substrate for air (at λ = 617 nm) and for water (at λ = 617 nm) environment.

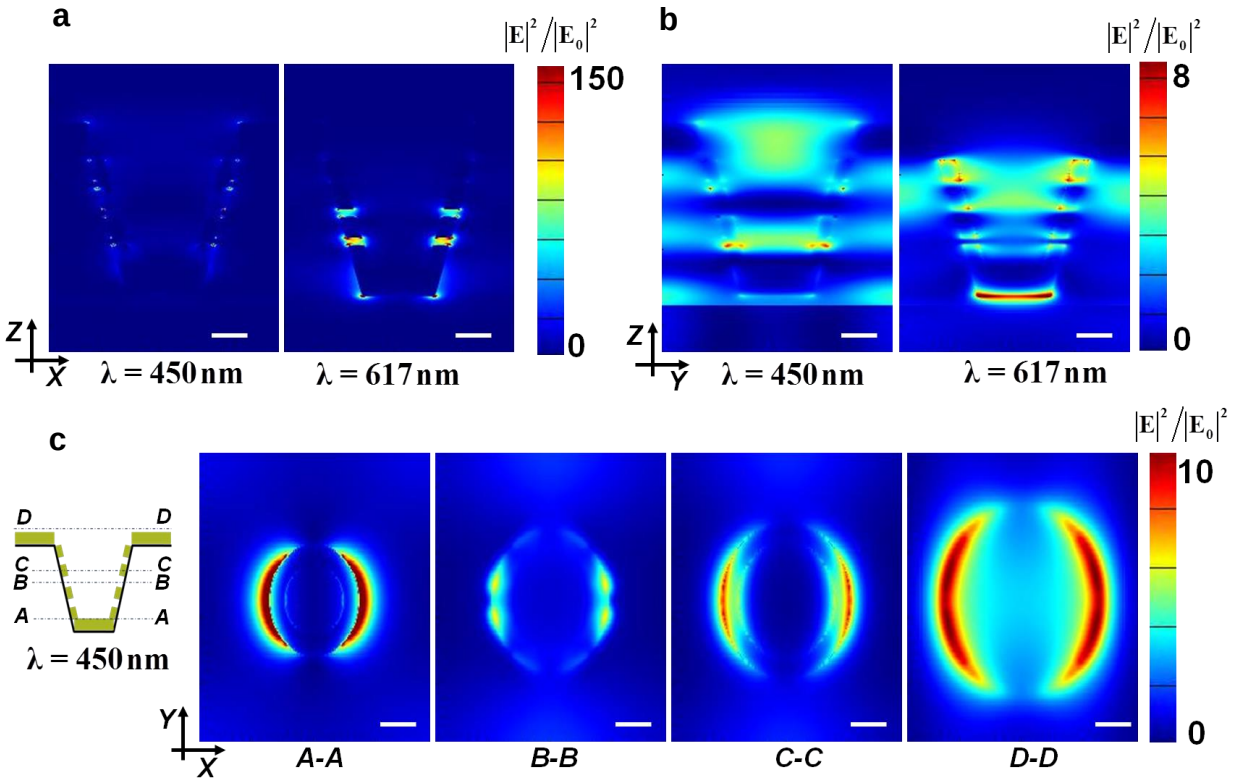

Figure 6.11: Near field intensity distribution across different position of nanohole substrate.

Figure 6.11 shows the near field intensity profile at different cross section of the nanohole plasmonic substrate. Figure 6.11a shows the field at λ = 450 and 617 nm in (x-z) plane and Figure 6.11b shows the field in (y-z) orientation. Figure 6.11c shows cross-sectional (x-y) distribution of electric field intensity at different locations shown schematically at the left figure.

Conclusions

The concept of surface plasmon polariton has been introduced in terms of classical Maxwell's equation. The fabricated surface plasmon supporting substrate (nanocone, nanohole) has been simulated using RCWA, FEM, and FDTD based methods. The simulation showed that LSPR and SPR mode can be excited using nanocone and nanohole based plasmonic substrate.

References

[1] L. Rayleigh, "On the light from the sky, its polarization and colour," *Phil. Mag.*, vol. 107, pp. 274, 1871.

[2] V. Giannini, A. I. Fernandez-Dominguez, Y. Sonnefraud, T. Roschuk, R. Fernandez-Garcia and S. A. Maier, "Controlling Light Localization and Light-Matter Interactions with Nanoplasmonics," *Small*, vol. 6, pp. 2498-2507, NOV 22, 2010.

[3] G. Mie, *Ann. Physik*, vol. 25, pp. 377, 1908.

[4] R. Gans, *Ann Phys, Leipzig*, vol. 37, pp. 881, 1912.

[5] J. Hoffmann, C. Hafner, P. Leidenberger, J. Hesselbarth and S. Burger, "Comparison of electromagnetic field solvers for the 3D analysis of plasmonic nano antennas," *arXiv:0907. 3570*, 2009.

[6] M. R. Gartia, Y. Chen and G. L. Liu, "Photoluminescence and cathodoluminescence from nanostructured silicon surface," *Appl. Phys. Lett.*, vol. 99, pp. 151902, OCT 10 2011, 2011.

[7] Y. Chen, Z. Xu, M. R. Gartia, D. Whitlock, Y. Lian and G. L. Liu, "Ultrahigh Throughput Silicon Nanomanufacturing by Simultaneous Reactive Ion Synthesis and Etching," *Acs Nano*, vol. 5, pp. 8002-8012, OCT 2011, 2011.

[8] E. Palik, *Handbook of Optical Constants of Solids.* Burlington, Massachusetts, United States: Academic Press, 1997.

[9] Z. Xu, Y. Chen, M. R. Gartia, J. Jiang and G. L. Liu, "Surface plasmon enhanced broadband spectrophotometry on black silver substrates," *Appl. Phys. Lett.*, vol. 98, pp. 241904, JUN 13 2011, 2011.

[10] W. A. Murray and W. L. Barnes, "Plasmonic materials," *Adv Mater*, vol. 19, pp. 3771-3782, NOV 19 2007, 2007.

CHAPTER 7

SURFACE PLASMON COUPLING TO FLUORESCENCE MOLECULES

Introduction

In this chapter, we report the fluorescence lifetime imaging and quantum yield measurement of five different fluorescence dyes spanning different quantum yield and excitation wavelength ranges in solution as well as on irregular nanoplasmonic substrate surface. Due to a distribution of dye molecules at random distances and orientation to the metal nanoplasmonic structure, the dyes showed multi-component lifetime decays on the surface. We have simulated the distribution of lifetime on the surface based on fractional intensity relative to steady-state value and derived an average lifetime with species fraction. From the quantum yield and fluorescence lifetime measurements we calculated the modified radiative and non-radiative decay rates for the dyes due to energy coupling on the substrate. We measured up to 100 fold fluorescence enhancement on nanoplasmonic substrate and all molecule fluorescence showed not only considerably higher radiative decay rate but also higher non-radiative decay rate.

Background

For a spontaneous emission process, the rate of transition from an excited state *k* to another state *l* can be calculated using Fermi's golden rule, which can be written as $w_{kl} = \frac{2\pi}{\hbar}\rho\left(\frac{E_k - E_l}{h}\right)\left|M_{kl}\right|^2$. M_{kl} is the transition matrix element between the excited and lower energy state. The value of M_{kl} is determined by the wavefunctions associated with those levels. $\rho\left(\frac{E_k - E_l}{h}\right) = \rho(\nu)$, is the density of states at the transition frequency, $\nu = \frac{E_k - E_l}{h}$; $\rho(\nu)$ is also known as the Photonic Mode Density (PMD) – the number of photon modes available at the

frequency ν [1]. Hence, the rate of fluorescence emission can be influenced by changing $\rho(\nu)$ [2]. Increasing PMD leads to faster decay rates [3]. For instance, a fluorophore close to a metal nanoparticle or surface can experience an increase in the PMD available for spontaneous emission at a particular frequency, ν, shortening the natural radiative lifetime. In addition, the proximity of a metal particle or surface can increase the magnitude of the impinging electromagnetic field surrounding a fluorophore, thereby increasing the rate of absorption (or stimulated emission). The latter also increases the measured fluorescence intensity by increasing the rate of forming excited molecules for a certain impinging light intensity.[1, 3] This modification in the emission properties of a fluorophore in close proximity to metals, is known as surface enhanced fluorescence (SEF) [4] - or metal enhanced fluorescence (MEF). It can be used to increase the signal level when imaging fluorescent molecules. As a result the long time stability of dyes is increased because the rate of leaving the excited state is faster (lowering the relative probability of going to the triplet state, decreasing the rate of photolysis). In addition, the limit of detectable concentrations for many fluorescent materials will become lower [5, 6].

The enhancement of fluorescence due to the augmentation of electric field near a metal nanostructure is attributed to two different mechanisms: (1) an increase in the excitation field due to the reflection of the excitation light and also redirection of the emitted light by the metal surface toward the objective lens increasing the collection efficiency (mirror effect) [7] (2) surface plasmon resonance at the surface of the metal nanostructure brought about by the electric field of the incident light interacting with the free electrons on the surface of the metal [6]. If the Frohlich condition is met, maximum polarizability and resonance will occur resulting in the amplification of the near field both inside and outside of the nanostructure [6]. The enhanced excitation of the fluorescent molecule is due to the amplification of near field outside of the nanostructure [8, 9]. The degree of interaction (transfer of energy) between the metal and fluorophore depends strongly on the distance between the dye and the surface as well as the overlap between the scattering spectra of the surfaces and the absorption/emission spectra of fluorophore (for better enhancement due to surface plasmon resonance) [10]. When the fluorophore is too close to the metal surfaces (< 5 nm) a damping of the oscillation of the molecule's dipole may occur that generally leads to fluorescence quenching (usually this has a d^{-3} dependence where d is the distance between the metal surface and dye molecule) [11].

Another issue of the emission process is whether the observed fluorescence is emitted by the fluorophore or by the surface plasmon. In the process known as radiative decay engineering (RDE), the fluorophore resonantly interacts with the metal nanostructure resulting in enhanced fluorescence being emitted by the fluorophore, itself [12]. Observation of directional emission from a fluorophore at short distances prompted the idea of surface plasmon coupled emission (SPCE), where non-radiative energy transfer occurs from an excited fluorophore to surface plasmon electrons in the metallic nanostructure. Under certain boundary conditions, radiation is thought to be emitted by surface plasmons [13].

Although the coupling between fluorophores and nanostructures with simple geometries is relatively well understood, the fluorescence emission patterns of more complex nanostructures, such as percolated or roughened metallic thin films, are under active investigation.[4] For example, on an irregular corrugated metallic structure, the surface plasmon wave vector behaves differently than the Bragg-scattered bound-mode features on a grating. For a grating with periodicity *a*, the surface plasmon wave vector is $k'_{sp} = k_{sp} \pm n\, g_B = k_{sp} \pm n(2\pi/a)$ where k_{sp} is surface plasmon (SP) wave vector at the metal-air interface and g_B is the grating or Bragg wave vector [4]. The periodic grating structure imposes a very strict condition on photon momentum for coupling to SPs (hence usually both coupling as well as emission can only occur at certain angles), whereas a random nanostructure relaxes this condition allowing broadly distributed angles for coupling to SPs. In addition, the randomness of the structure leads to the possibility of strong constructive interference of SPs at certain locations which will give rise to very high electromagnetic fields ("hot spots"), also known as Anderson localization [14, 15]. Hence, the resulting electric field associated with SPs is expected to be more intense for the case of random metallic nanostructure as compared to smooth metal surface or glass substrate. This provides additional enhancement for the excitation field and consequently greater fluorescence enhancement.

Determining different decay rate constants (radiative and non-radiative pathways of deactivation) requires measuring both the lifetimes and quantum yields on the surface. Although both the lifetime and the quantum yield of a fluorophore conjugated to nanoparticles have been measured [16-19], only the lifetime of the fluorophore has been measured on the surface of substrate [20-22]. This is because the quantum yield of the fluorophore is generally measured by

using the methods of Williams and Winfield [23], where the absorbance and emission of the dyes are compared with that of a known reference compound. However, when the samples significantly scatter light, the photons scattered by the structure will be further absorbed by the dyes and will give rise to additional light emission leading to overestimation of the quantum yield rendering the previously described method invalid [24]. Therefore, we have measured the fluorescence lifetime (with fluorescence lifetime imaging microscopy (FLIM)) and the quantum yield of five different dyes free in solution as well as on irregular nanoplasmonic substrates. We have chosen the dyes to span different quantum yield ranges (low, medium and high) and also different excitation wavelength ranges (blue, green).

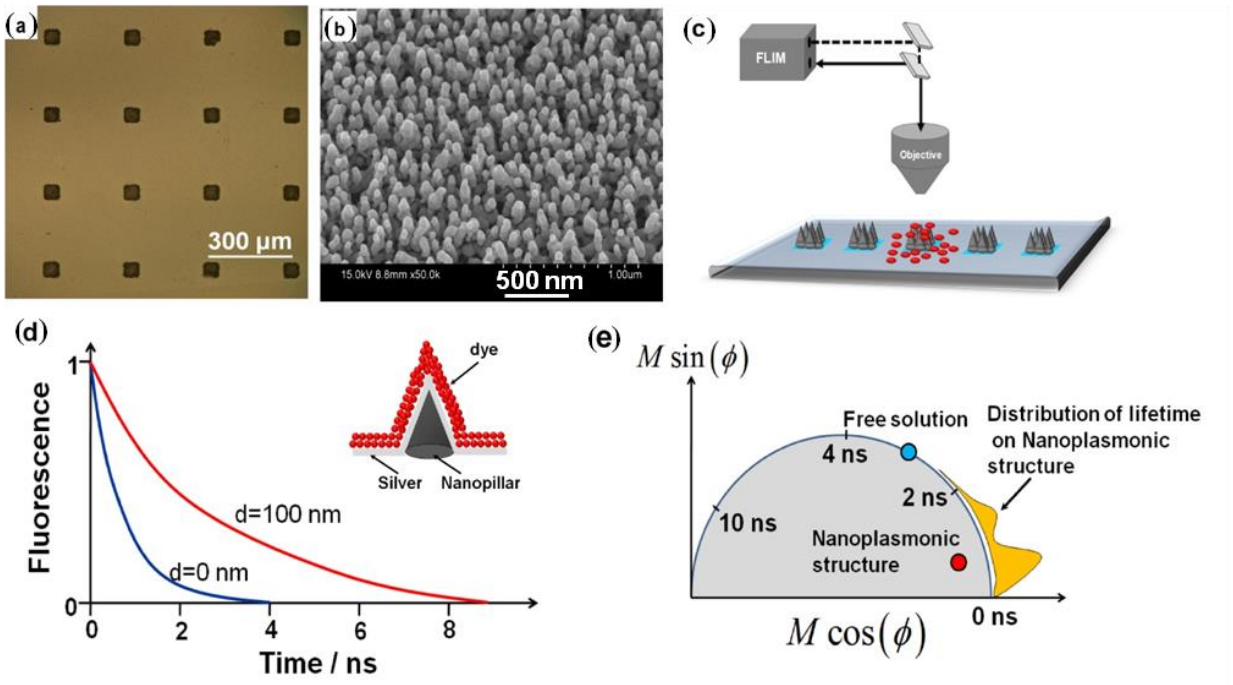

Figure 7.1: (a) Bright field image of the nanoplasmonic substrate. The square region contains the nanostructure. (b) Angular (30^{o}) SEM image of the nanostructure region after 80 nm Ag deposition. (c) Schematic diagram of FLIM experimental set-up. (d) Schematic of lifetime distribution of dyes ($I(t)=\sum_{i=1}^{n}\alpha_i \exp(-t/\tau_i)$, α_i are the amplitudes and τ_i are the lifetimes) on nanoplasmonic substrate. Here, 'd' is the distance of the dye from the nanoplasmonic substrate. (e) Sketch of polar plot and lifetime distribution for the population of dyes on nanoplasmonic substrate. Here, ϕ is the phase corresponding to lifetime component.

Figure 7.1a shows the bright field image of the prepared nanoplasmonic substrate. After a photolithographic step to prepare the square pattern, the nanopillar structures are created inside the square area using a mask-less ICP-RIE process (inductively coupled plasma-reactive ion etching) with a mixture of HBr and O_2 gases (described in details in Chapter 2). Figure 7.1b presents the angular view (30^0) SEM image of the nanostructure region after metallization (80 nm Ag) to render the structure with plasmonic property. For all the experiments 5 µl of 10 µM dyes (which typically makes a drop of about 3 mm diameter) are dropped on to the surface covering several square patterns. The FLIM system used is shown in Figure 7.1c. Since the modulation of the lifetime is nonlinearly dependent on the distance from the metal surface [20] and fluorophores are randomly distributed on the metallic nanostructure, we expect a distribution of lifetime component on the nanoplasmonic substrate instead of a single lifetime component. Figure 7.1d shows an example of exponential decays for two different distances "*d*" from the metal nanostructure surface. The lifetime of single fluorophore in direct contact (d = 0) to the metal surface is zero and increases non-linearly with increasing distance from the metal surface reaching asymptotically the free fluorophore (without metal surface) lifetime [20]. The polar plot is shown in Fig. 7.1e where the positions of lifetimes for free solution and those on nanoplasmonic substrate are shown. The data points on the polar plot, in this case due to a multi-component decay kinetics of fluorophore on nanoplasmonic surface, lie inside the semicircle of the polar plot as shown in Fig. 7.1e. Except for emission of a molecule that is excited via an excited state reaction, polar plot points due to a distribution of lifetime values will always lie inside this semi-circle.

Five different dyes, Rhodamine6G or R6G ($\lambda_{ex} = 532$ nm), Fluorescein ($\lambda_{ex} = 440$ nm), Acridine Orange ($\lambda_{ex} = 440$ nm), Rhodamine-B ($\lambda_{ex} = 532$ nm) and Eosin-Y ($\lambda_{ex} = 532$ nm) are chosen to cover different quantum yields and ranges of excitation wavelength (λ_{ex}). The quantum yields for the dyes are determined experimentally using R6G as a reference with a known quantum yield $Q_R \sim 0.90$ in aqueous media [25]. The quantum yield was calculated as [23] $Q = Q_R \frac{I}{I_R} \frac{OD_R}{OD} \frac{n^2}{n_R^2}$ where Q is the quantum yield, I is the fluorescence intensity integrated over the wavelengths of emission. OD is the optical density and n is the refractive index; the suffix R indicates the reference (R6G). Figure 7.2a shows a typical absorbance and fluorescence

measurement for Rhodamine-B (Rh-B) used for a quantum yield calculation (results for other dyes can be found in supporting information). The phase delay and modulation ratio of the dyes free in solution are detected using a frequency-domain FLIM system. Here, the modulation ratio and phase delay are projected as coordinates on the polar plot [26, 27]. The measured lifetime of the dyes are reported in Table 7.1 and are comparable to those reported in the literature. Using the quantum yield and lifetime data, the radiative and nonradiative decay rates of the fluorophore in free solution were calculated as: $\Gamma_0 = Q_0/\tau_0$ and $(k_{nr})_0 = \frac{1}{\tau_0} - \Gamma$, the results are shown in Table 7.1. We modified Nikon E600FN microscope set up to measure the quantum yield of dyes on the nanoplasmonic substrate. The camera of the microscope was replaced by a spectrometer (B&W Tek Inc.) and the emission filter was removed to register both the excitation as well as emission spectra during the experiment.

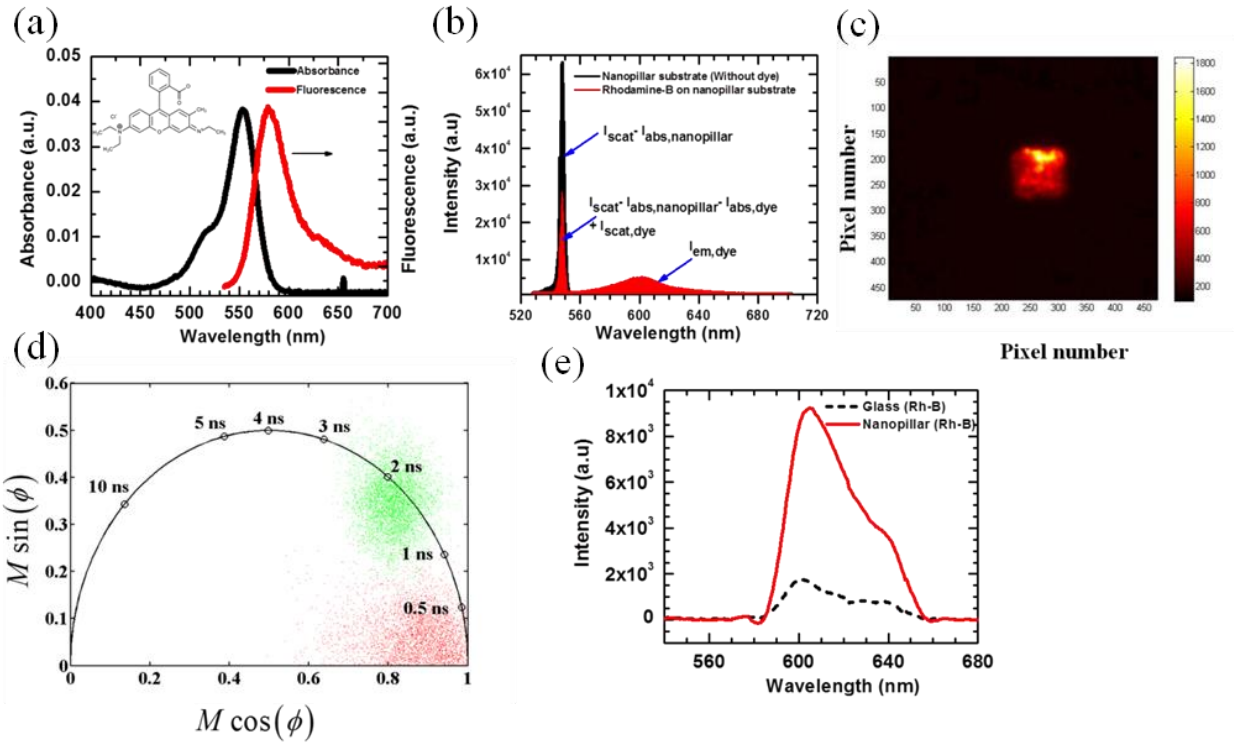

Figure 7.2: (a) Absorbance and fluorescence spectra for Rh-B in aqueous solution. (b) Emission spectra of the Rh-B on the nanoplasmonic substrate. (c) Fluorescence intensity image of Rh-B on the nanoplasmonic substrate. The increase is fluorescence intensity on the nanoplasmonic substrate (square region) compared to surrounding smooth metal (Ag) region is apparent. (d) Polar plot representation of lifetime for Rh-B in free solution (Petri Dish) and on nanoplasmonic substrate (Nanopillar). (e) Comparison of the fluorescence spectroscopy result for Rh-B on nanoplasmonic substrate and on glass substrate.

The absorption and emission spectra of the Rh-B on the nanoplasmonic substrate are shown in Figure 7.2b. The emission spectrum of the surface without dye (black curve) is a measure of the difference between scattering intensity and absorption intensity by the surface $(I_{scat} - I_{abs,nanopillar})$. The spectrum for surfaces with the dye (red curve) is due to the combination of absorption and emission spectrum from the dye. The absorption part of spectrum is a result of scattering from the surface and dye lowered by absorption by the surface and by the dye, $(I_{scat} + I_{scat,dye} - I_{abs,nanopillar} - I_{abs,dye})$. The emission spectrum $(I_{em,dye})$ describes the fluorescence of the dye on the surface. The difference between integrated area of absorption spectra with and without the dye corresponds to the relative intensity of absorption by the dye on the surface ($I_{abs,dye}$) neglecting the scattering from the dye. The integrated area of the emission spectrum is a measure of total emission intensity by the dye while on the surface ($I_{em,dye}$). Hence, we can estimate the quantum yield of dye on the surface from the ratio of emission intensity of the dye to the absorption intensity of the dye ($Q_{\mathrm{mod}} = I_{em,dye} / I_{abs,dye}$).

Figure 7.2c shows the fluorescence intensity image of Rh-B on the nanoplasmonic substrate. The intensity showed typical spatial heterogeneity with several brighter spots due to "hot spots" of the substrate. The phase-sensitive images of frequency domain FLIM were used to calculate the apparent phase (τ_{Φ}) and modulation (τ_M) lifetimes. Also, the polar plot coordinates for the Rh-B FLIM data on the nanopillar substrate are shown in Figure 7.2d; the data clearly moved toward the region of lower lifetimes on the polar plot as compared to the dye free in solution. Figure 7.2e compares the fluorescence spectroscopy result for Rh-B on nanoplasmonic and glass substrate. The ratio between integrated fluorescence intensity of Rh-B on nanoplasmonic substrate and that on glass substrate provide an estimate for the fluorescence enhancement (far field) experienced by the dye. The fluorescence enhancement for Rh-B was measured to be 5.13 on the nanoplasmonic substrate. The maximum enhancement factor observed for various dyes are reported in Table 7.1. The signal enhancement can be explained by the radiative conversion of energy transferred from the dyes to SPs. On glass substrate, the energy transferred from the dyes only dissipates in the glass and cannot be detected. On the other hand, roughened metal nanostructure enhances the light scattering and allow the efficient

coupling between light and SPs. Thus, the energy transferred from the dye to metal surface can be recovered by the re-radiation by the SPs [28].

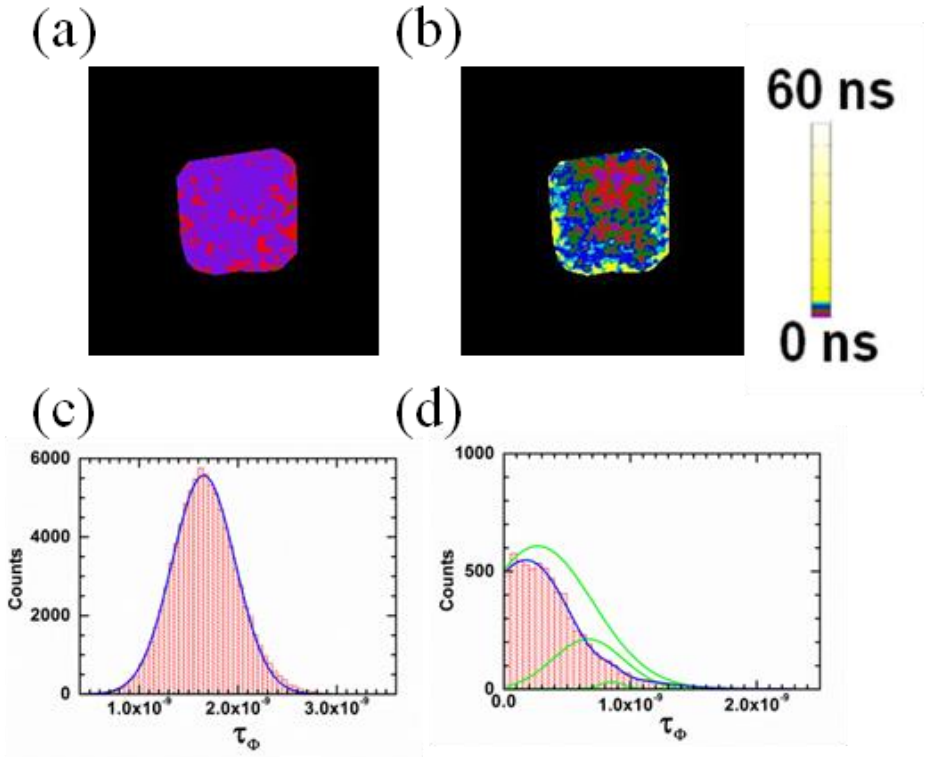

Figure 7.3: (a) Fluorescence phase lifetime image of Rh-B on nanoplasmonic substrate. (b) Fluorescence modulation lifetime images of Rh-B on the nanoplasmonic substrate. (c) Histogram for lifetime measurement of Rh-B in free solution. (d) Histogram for lifetime measurement of Rh-B on nanoplasmonic substrate.

Figures 7.3a and b shows the spatial distribution of the effective lifetimes derived from the measured phase delay τ_{Φ} and modulation ratio τ_{M} from the nanoplasmonic substrate respectively. The corresponding histograms of phase delay for free solution and dye on nanoplasmonic substrate are shown in Figure 7.3c, d. For a multiexponential decay process, the apparent phase lifetime is shorter than the apparent modulation lifetime [29]. The lifetimes determined from both the phase delay and modulation ratio were found to be reduced on the nanoplasmonic substrate. The observation of $\tau_{\Phi} < \tau_{M}$ (shown in Fig. 7.4e) is consistent with a multiexponential decay on the nanoplasmonic substrate.

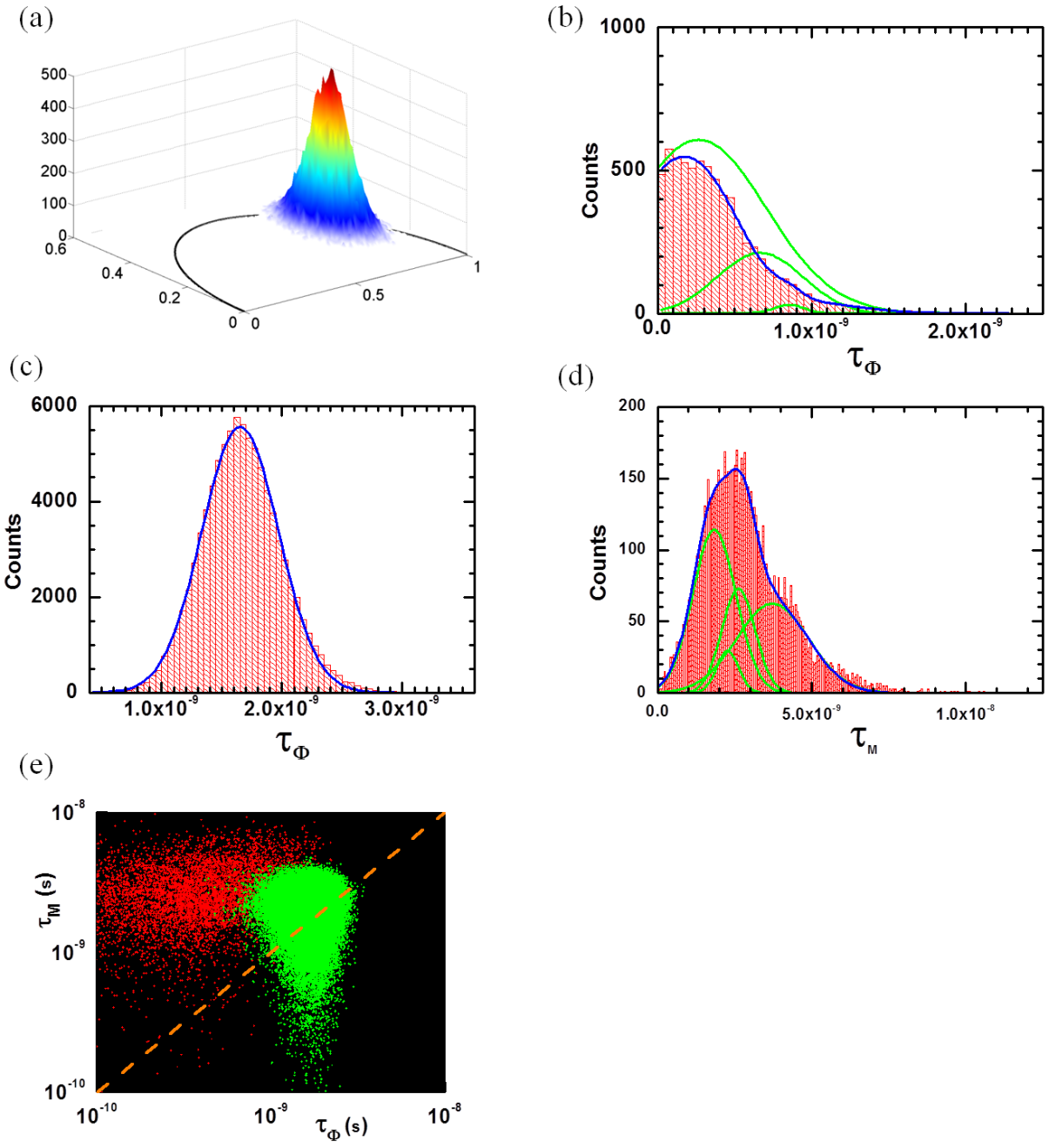

Figure 7.4: (a) 3-D polar plot for Rh-B dye in free solution showing lifetime has single component on petridish. (b) Statistical distribution of phase lifetime for Rh-B on nanoplasmonic surface. Gaussian curve fitting yields three lifetime components. The statistical average was determined to calculate the decay rates. (c) Statistical distribution of phase lifetime for Rh-B in free solution. (d) Statistical distribution of modulus lifetime for Rh-B on nanoplasmonic surface. (e) Correlation between the phase and modulation lifetime of Rhodamine B (Rh-B) shown as a scatter plot. Green represents lifetime in free solution and red represents lifetime on nanoplasmonic structure.

The data collected on the FLIM system was analyzed with a set of simulations on the polar plot. All simulations performed on the polar plot were based on the analysis of fractional intensities on the polar plot. When the phase delay (ϕ_{TOT}) and modulation ratio (M_{TOT}) are projected as a polar coordinate, variations of the fractional intensities (α) in the fluorescent species can easily be monitored. In other words, for a complicated fluorescent sample, the contribution of each constituent fluorophore's emission to the measured steady-state intensity (α_i) determines the position of the polar coordinate of the sample relative to the polar coordinates of the constituent contributing fluorescence species (i) with the following equations: $x = \sum_i \alpha_i M_i \cos(\phi_i) = M_{TOT} \cos(\phi_{TOT}), y = \sum_i \alpha_i M_i \sin(\phi_i) = M_{TOT} \sin(\phi_{TOT})$

In the above equations, (M_i) is the modulation factor associated with lifetime component (i) and (ϕ_i) is phase corresponding to lifetime component (i). $M_i = \frac{1}{\sqrt{1+(\omega\tau_i)^2}}$. $\phi_i = \tan^{-1}(\omega\tau_i)$.

The resulting polar coordinate of a sample characterized by many single lifetimes must lie inside the universal semi-circle.[26, 27]

Simulation of distribution of lifetime on plasmonic substrate

We assume that there is distribution of lifetimes each representing a population of fluorophores contributing fluorescence intensity (photons) to the measurement. This distribution represents a double Gaussian mixed with an exponential function. In the simulations, an array of lifetimes was created. The range of lifetimes was determined from 0 ns to the actual lifetime of the sample. For example, for fluorescein the lifetimes ranged from 0ns to 4.3 ns. For Acridine Orange, the lifetimes ranged from 0 ns to 2 ns. For Rhodamine 6G, the lifetimes ranged from 0 ns to 4.11 ns. Essentially, we assumed that depending on the distance of the dye to the surface, all of the lifetimes would be valid. We have lifetime ~ 0 ns near the surface. The lifetime would increase as you went further away and eventually approach the lifetime that we measured in

solution. This is the assumption that we made based on metal-enhanced fluorescence to model our data.

Next, it was assumed that the lifetimes on the surface existed as two Gaussian distributions. In other words, two distributions of lifetimes existed. Each discrete lifetime in these distributions contributed to the intensity measured. Therefore, each point in these Gaussian distributions related how much a specific lifetime contributed to the intensity measured. These Gaussians were then dampened by an exponential decay. Finally, as required, the resulting curve describing the fractional contribution to the measured steady-state intensity was normalized.

The centers of these Gaussians represent the two populations that we think exist here. The amplitude (height) of the resulting distribution represents the fractional contribution to measured steady-state intensity that each constituent fluorophore has. Therefore, if a portion of the sample with specific lifetime is emitting lots of photons (many individual fluorescent molecules), this portion of the distribution is high in amplitude. If this same component however, (even though it is bright) has a low concentration the fractional contribution to the steady-state intensity will be smaller as will the amplitude in the simulated distribution.

Polar coordinates were then simulated for each lifetime (paragraph 1) weighted by the fractional intensities in these Gaussian distributions. A mean polar coordinate was then made which by virtue of the distributions was pulled a little into the universal semi-circle. Background was then introduced to make the simulations match experimental conditions. Backgrounds were determined for each dye used by examining the regions in the image without any pillar.

As discussed, movement of the polar coordinate is premised on the fractional contribution to the steady-state intensity. If the measured steady-state intensity is being dominated by a specific fluorescent species, the measured polar coordinate moves toward the polar coordinate of that species. Therefore, if a fluorophore is very bright, it may take a low concentration of that fluorophore to actually cause a large change in polar coordinate in a mixed sample.

However, it should be noted that our simulations do not reflect or indicate the actual quantum yield of our sample. It simply reflects how much each constituent lifetime contributes to the measured steady-state intensity. More detailed measurements will need to be conducted to

determine the quantum yields (brightness) of each of the constituent components in the simulation.

The extent to which the polar coordinate generated by a large distribution of lifetimes lies inside the semi-circle depends on the intensity weighting of the fractional intensities of the single lifetimes in the distribution. A graphical representation of such distributions is presented on the polar plot (Figure 7.5a). In this work, polar plot data were simulated as a set of two Gaussian lifetime distributions (Figure 7.5b). As shown, there was a definite decrease in lifetime accompanied by an increase in fractional intensity, consistent with metal-enhanced fluorescence (Figure 7.5a). The measured polar coordinates for the nanopillar, smooth silver film and background were used in the simulations (Figure 7.5c).

(a)

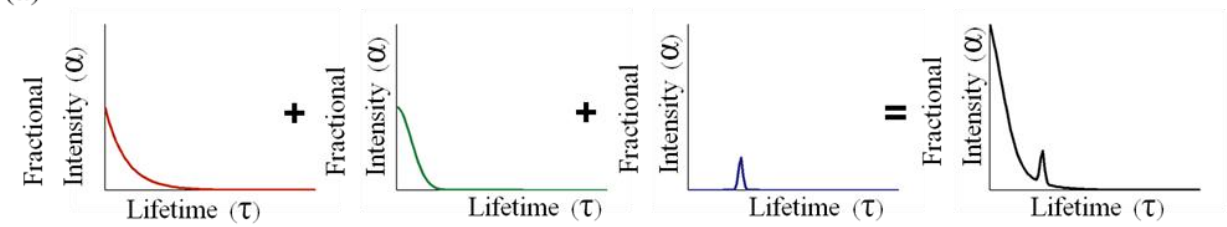

(b)

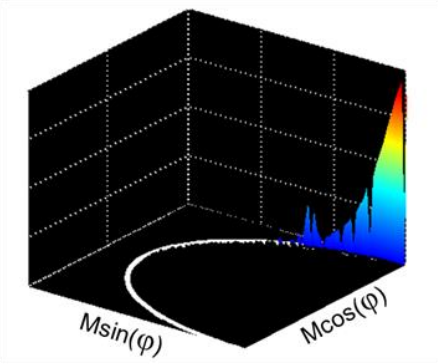

(c)

	Nanopillar (x,y)	Smoothsilver (x,y)	Background Nanopillar (x,y)
Rhodamine B	(0.9138,0.03438)	(0.8212,0.1793)	(0.2638,0.06805)
Fluorescein	(0.8678,.0596)	(0.8171,0.3563)	(0.4214,0.1277)
Rhodamine 6G	(0.9142,.05354)	(0.8636,0.06757)	(0.575,.05059)

Figure 7.5: Descriptions of life time simulations. (a) The principle components of the distributions of lifetimes are displayed as a function of fractional intensities. An exponentially decreasing set of lifetimes as function of fractional intensities (far left panel) is combined with Gaussian distributions (middle two panels) each representing the smooth-silver and nanopillar separately to determine the final distribution (far right panel). (b) A three dimensional view of the general profile of the simulated distributions is presented on the polar plot. The color hue represents an increasing fractional intensity (blue to red). (c) These measured polar coordinates were applied to the simulations to establish the locations of the nanopillar and smooth silver film distributions. Background was factored in separately.

The measured quantum yield of Rh-B on the nanopillar surface was 86%, which was a 2-fold increase from the value in solution. Generally, the quantum yield of a fluorophore reflects a competition between radiative and non-radiative decay processes, and the natural radiative rate does not change.[3] The lifetime of a fluorophore is the average time an ensemble of molecules remains in the excited state; therefore, the lifetime is influenced by all the de-excitation pathways - fluorescence, dynamic quenching, non-radiative decay, energy transfer etc. – that are available for exiting the excited state. The shortened lifetime on the surface can be explained by the fact that the proximity of the metal provides an additional pathway of de-excitation, which increases the rate at which the molecule will leave the excited state.

The modified decay rates on the surface are calculated from the quantum yield and lifetime measurement as $\Gamma_{\text{mod}} = Q_{\text{mod}} / \tau_{\text{mod}}$ and $(k_{nr})_{\text{mod}} = \frac{1}{\tau_{\text{mod}}} - \Gamma_{\text{mod}}$. The modified decay rates are reported in Table 7.1. The increased quantum yield on the surface is primarily due to increase in radiative decay rate for Rh-B. For the high quantum yield dyes in free solution, the ratio of radiative to non-radiative decay rates (r) are usually greater than 1 (e.g. $r_{Fluorescein} = 19.0,\ r_{R6G} = 9.0$) (Figure 7.6 and 7.7). The ratios for other dyes in free solution with lower quantum yield are less than 1 ($r_{AO} = 0.41, r_{EY} = 0.46, r_{Rh-B} = 0.70$) (Fig. 7.8 and Fig. 7.9). However, on nanostructure the ratio of radiative to non-radiative decay rates is always greater than 1 for all the dyes. The largest change in quantum yield was found for Eosin-Y where the quantum yield increased by 2.67 fold from that in free solution dye. However, the fluorescence enhancement for Eosin-Y measured on the nanosctructure as compared to glass substrate was the lowest. The variation of fluorescence enhancement is highly non-linear and did not necessarily follow any discernable trend. In general, the enhancement decreases with increasing non-radiative decay rate. [30]

Figure 7.6 shows the fluorescence lifetime and fluorescence intensity data obtained for R6G dye molecule. The radiative and non-radiative decay rates are calculated using the data and presented in Table 7.1.

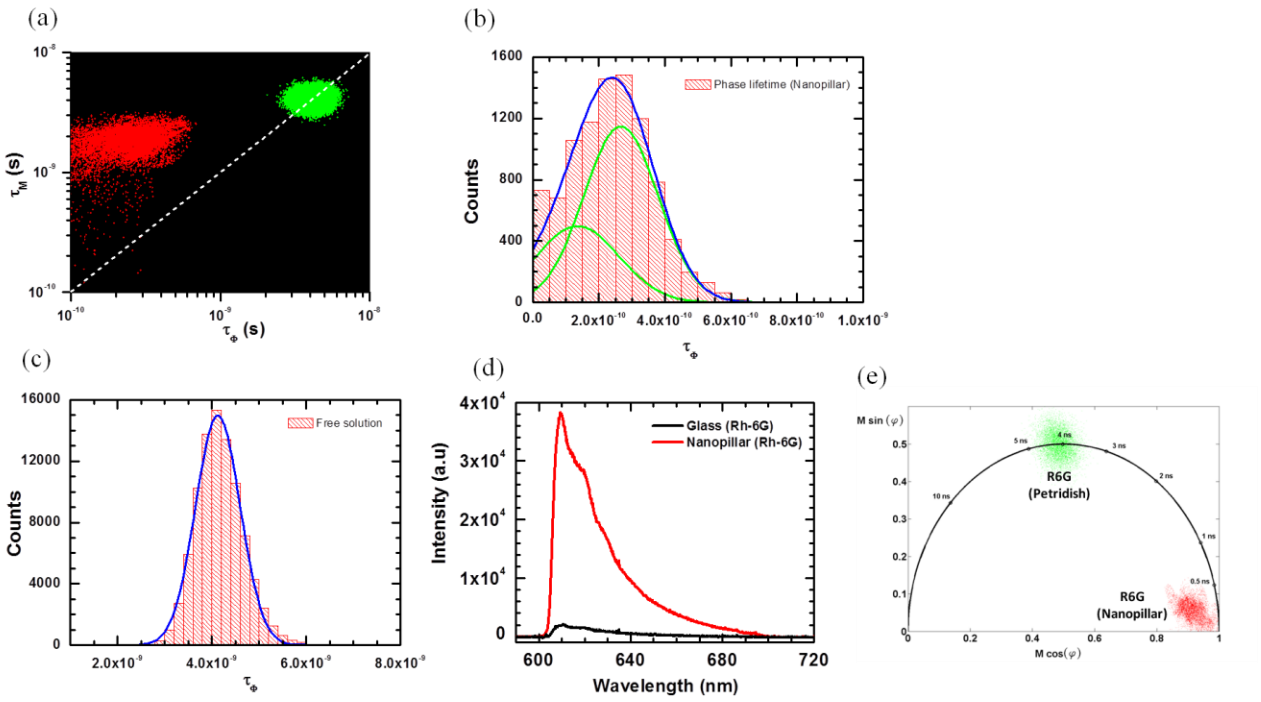

Figure 7.6: (a) Correlation between the phase and modulation lifetime of Rhodamine 6G (R6G) shown as a scatter plot. Green represents lifetime in free solution and red represents lifetime on nanoplasmonic structure. The dye on the nanoplasmonic structure has higher modulus lifetime as compared to phase lifetime. (b) Statistical distribution of phase lifetime for R6G on nanoplasmonic surface. (c) Statistical distribution of phase lifetime for R6G in free solution. (d) Comparison of the fluorescence spectroscopy result for R6G on nanoplasmonic substrate and on glass substrate. (e) Polar plot representation of lifetime for R6G in free solution (Dish) and on nanoplasmonic substrate (Nanopillar).

Figure 7.7 shows the fluorescence lifetime and fluorescence intensity data obtained for Fluorescein dye molecule. The radiative and non-radiative decay rates are calculated using the data and presented in Table 7.1.

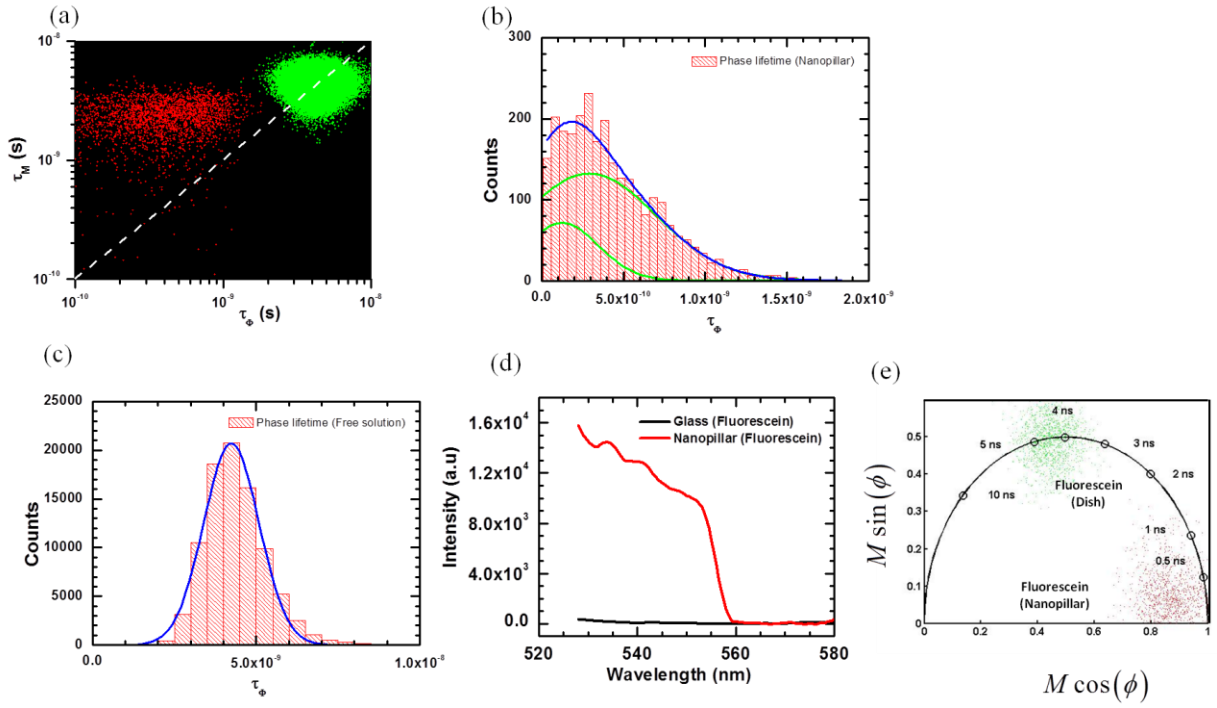

Figure 7.7: (a) Correlation between the phase and modulation lifetime of Fluorescein shown as a scatter plot. Green represents lifetime in free solution and red represents lifetime on nanoplasmonic structure. The dye on the nanoplasmonic structure has higher modulus lifetime as compared to phase lifetime. (b) Statistical distribution of phase lifetime for Fluorescein on nanoplasmonic surface. (c) Statistical distribution of phase lifetime for Fluorescein in free solution. (d) Comparison of the fluorescence spectroscopy result for Fluorescein on nanoplasmonic substrate and on glass substrate. (e) Polar plot representation of lifetime for Fluorescein in free solution (Dish) and on nanoplasmonic substrate (Nanopillar).

Figure 7.8 shows the fluorescence lifetime and fluorescence intensity data obtained for Eosin-Y dye molecule. The radiative and non-radiative decay rates are calculated using the data and presented in Table 7.1.

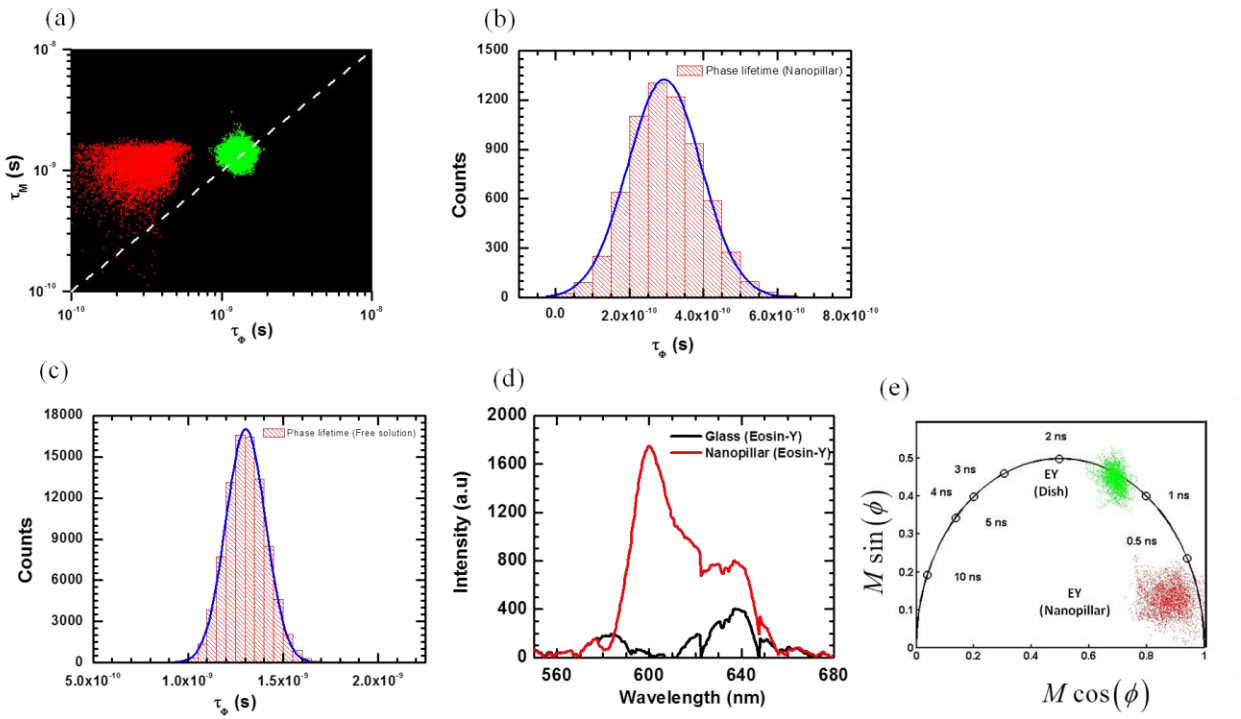

Figure 7.8: (a) Correlation between the phase and modulation lifetime of Eosin-Y (EY) shown as a scatter plot. Green represents lifetime in free solution and red represents lifetime on nanoplasmonic structure. The dye on the nanoplasmonic structure has higher modulus lifetime as compared to phase lifetime. (b) Statistical distribution of phase lifetime for Eosin-Y on nanoplasmonic surface. (c) Statistical distribution of phase lifetime for Eosin-Y in free solution. (d) Comparison of the fluorescence spectroscopy result for Eosin-Y on nanoplasmonic substrate and on glass substrate. (e) Polar plot representation of lifetime for Eosin-Y in free solution (Dish) and on nanoplasmonic substrate (Nanopillar).

Figure 7.9 shows the fluorescence lifetime and fluorescence intensity data obtained for Acridine Orange (AO) dye molecule. The radiative and non-radiative decay rates are calculated using the data and presented in Table 7.1.

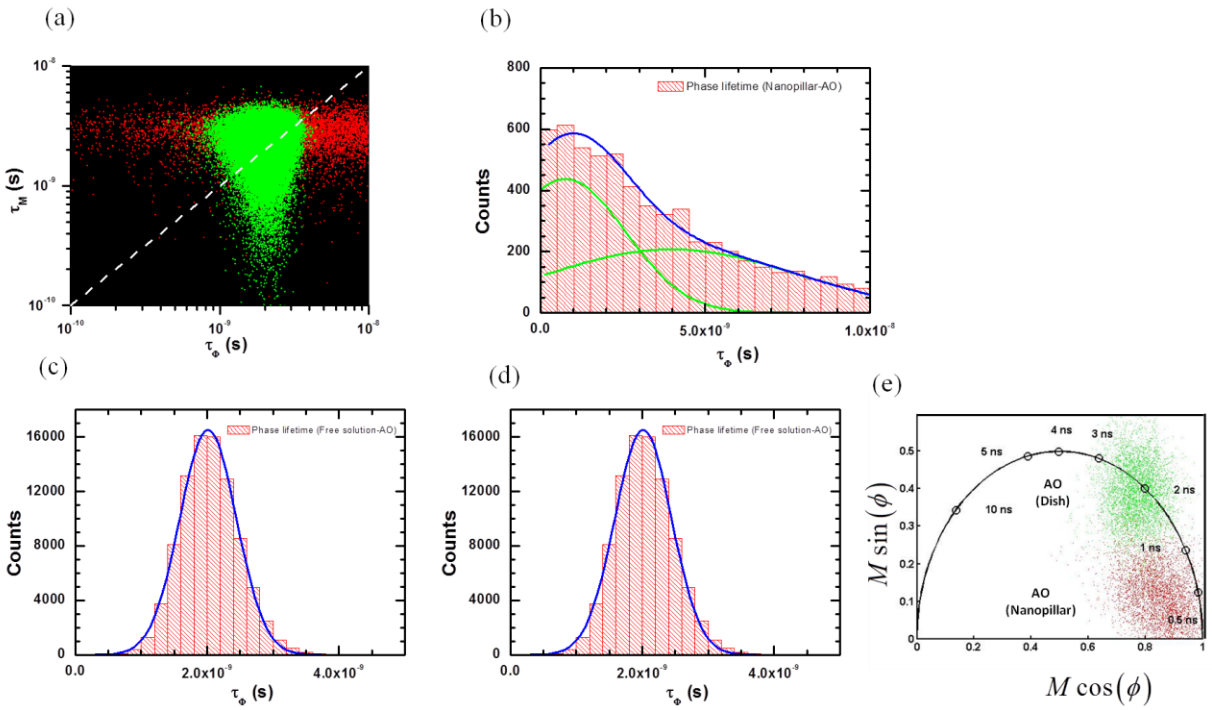

Figure 7.9: (a) Correlation between the phase and modulation lifetime of Acridine Orange (AO) shown as a scatter plot. Green represents lifetime in free solution and red represents lifetime on nanoplasmonic structure. The dye on the nanoplasmonic structure has higher modulus lifetime as compared to phase lifetime. (b) Statistical distribution of phase lifetime for AO on nanoplasmonic surface. (c) Statistical distribution of phase lifetime for AO in free solution. (d) Comparison of the fluorescence spectroscopy result for AO on nanoplasmonic substrate and on glass substrate. (e) Polar plot representation of lifetime for AO in free solution (Dish) and on nanoplasmonic substrate (Nanopillar).

The corresponding absorption and emission spectra of the dye molecules are shown in Figure 7.10.

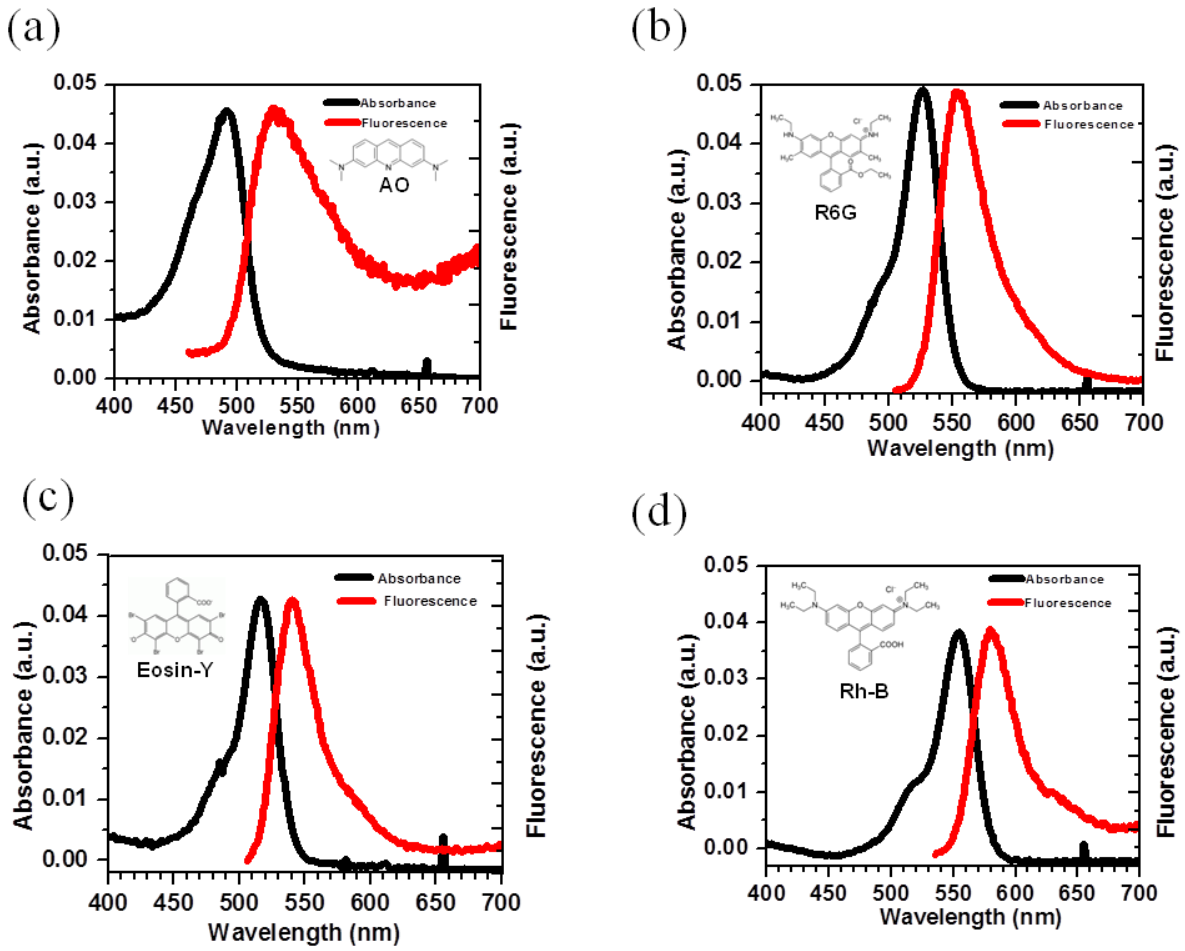

Figure 7.10: Absorbance and Fluorescence spectroscopy for (a) Acridine Orange (b) Rhodamine 6G (c) Eosin-Y and (d) Rhodamine-B solution.

Table 7.1: Fluorescence lifetime analysis: I_{nano}, fluorescence intensity on the nanoplasmonic structure; I_{glass}, fluorescence intensity on glass substrate; *EF*, Fluorescence enhancement factor.

Fluorophore	τ_0 **(ns)**	Q_0	Γ_0 **(s^{-1})**	$(k_{nr})_0$ **(s^{-1})**	τ_{mod} **(ns)**	Q_{mod}	Γ_{mod} **(s^{-1})**	$(k_{nr})_{mod}$ **(s^{-1})**	***EF*** **(I_{nano}/I_{glass})**
R6G	4.11	0.90	2.19×10^8	2.43×10^7	0.219	0.992	4.52×10^9	3.65×10^7	20.5
Fluorescein	4.38	0.95	2.17×10^8	1.14×10^7	0.182	0.991	5.45×10^9	4.84×10^7	100
Acridine Orange	2.04	0.29	1.42×10^8	3.48×10^8	0.443	0.753	1.70×10^9	5.58×10^8	8.34
Rhodamine-B	1.67	0.41	2.46×10^8	3.53×10^8	0.104	0.857	8.20×10^9	1.37×10^9	5.13
Eosin-Y	1.31	0.32	2.42×10^8	5.21×10^8	0.277	0.845	3.05×10^9	5.60×10^8	4.3

Increase of photostability on the plasmonic substrate

Lifetime is the average time the fluorophore spends in its excited state. When the lifetime decreases (on nanoplasmonic substrate), the fluorophore will spend less time in the excited state, and thus, decreasing the probability for photochemical reactions and photobleaching [30-33].

The probability of photobleaching of the dye is reduced (and hence photostability is enhanced) due to efficient energy transfer as well. The lifetime of surface plasmon are very short, typically 10 fs [34]. This suggests that energy transfer is from fluorophore to metal [13].

So we can consider fluorophore as DONOR molecule and surface plasmon as ACCEPTOR molecule. It has been shown experimentally [35, 36], that the presence of efficient acceptor molecules considerably decreases the rate of photobleaching. By transfer of energy from donors to acceptors, the excited state, in which molecules are sensitive to bleaching, is depopulated more quickly, making bleaching a less probable process. Depopulation of the excited state takes place by energy migration to sites where radiationless decay occurs.

In addition, we have also performed time-lapse imaging of fluorescein molecules on glass and on nanoplasmonic substrate respectively. The images are shown in Figure 7.11. The mean intensity derived from the images (after background correction which is set to 10% of the maximum intensity) is shown in Figure 7.12. Identical microscope settings were used for both the imaging (50x magnification, 500 ms exposure time, gain =1, Filter used: FITC). The fluorescence intensity is higher on nanoplasmonic substrate to start with. Also, the decay constant for photobleaching is also higher on nanoplasmonic substrate. This showed some indication of higher photostability (less photobleachability) on nanoplasmonic substrate compared to glass.

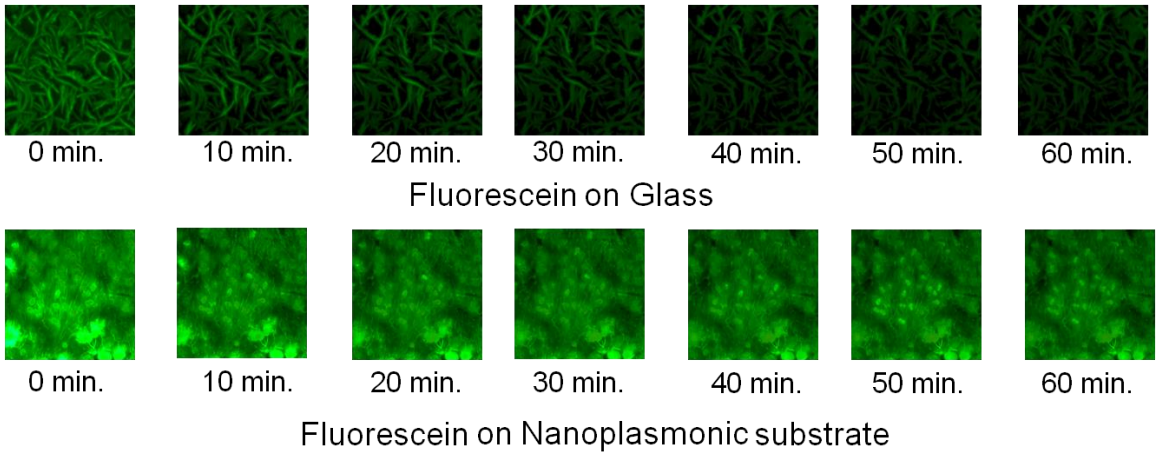

Figure 7.11: Comparison of fluorescence images for fluorescein on glass and nanoplasmonic substrate with time.

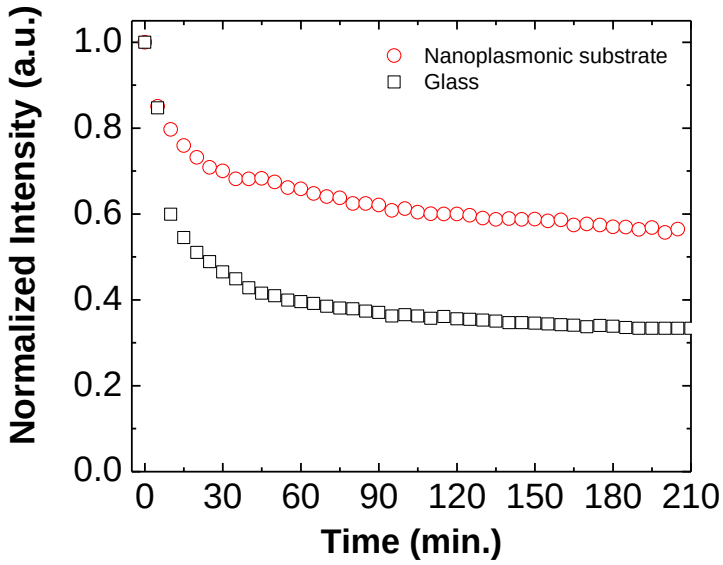

Figure 7.12: Comparison of fluorescence intensity on glass and nanoplasmonic substrate with time.

Conclusions

In conclusion, we measured the steady-state fluorescence to determine the quantum yields and we used frequency-domain FLIM to determine the time-dependent decay of five different dyes in free solution as well as on irregular nanoplasmonic substrate. We obtained a surface fluorescence enhancement of ~100 folds for fluorescein on the nanoplasmonic substrate compared to that on glass. The results provide a way to determine the quantum yield of dyes on highly scattering surfaces and analyze lifetime data for the population of fluorophores randomly distributed on a nanoplasmonic substrate.

References

[1] W. L. Barnes, "Fluorescence near interfaces: the role of photonic mode density," *Journal of Modern Optics,* vol. 45, pp. 661-699, APR, 1998.

[2] E. M. Purcell, "Spontaneous emission probabilities at radio frequencies," *Physical Review,* vol. 69, pp. 681, 1946.

[3] C. D. Geddes and J. R. Lakowicz, "Metal-enhanced fluorescence," *J. Fluoresc.,* vol. 12, pp. 121-129, JUN, 2002.

[4] E. Fort and S. Gresillon, "Surface enhanced fluorescence," *Journal of Physics D-Applied Physics,* vol. 41, pp. 013001, JAN 7, 2008.

[5] J. Fu, B. Park, G. Siragusa, L. Jones, R. Tripp, Y. Zhao and Y. Cho, "An Au/Si hetero-nanorod-based biosensor for Salmonella detection," *Nanotechnology,* vol. 19, pp. 155502, APR 16, 2008.

[6] S. Guo, J. J. Heetderks, H. Kan and R. J. Phaneuf, "Enhanced fluorescence and near-field intensity for Ag nanowire/nanocolumn arrays: evidence for the role of surface plasmon standing waves," *Optics Express,* vol. 16, pp. 18417-18425, OCT 27, 2008.

[7] J. Kummerlen, A. Leitner, H. Brunner, F. R. Aussenegg and A. Wokaun, "Enhanced Dye Fluorescence Over Silver Island Films - Analysis of the Distance Dependence," *Mol. Phys.,* vol. 80, pp. 1031-1046, DEC 10, 1993.

[8] M. Moskovits, "Surface-Enhanced Spectroscopy," *Reviews of Modern Physics,* vol. 57, pp. 783-826, 1985.

[9] P. Anger, P. Bharadwaj and L. Novotny, "Enhancement and quenching of single-molecule fluorescence," *Phys. Rev. Lett.,* vol. 96, pp. 113002, MAR 24, 2006.

[10] K. Lee, L. D. Hahn, W. W. Yuen, H. Vlamakis, R. Kolter and D. J. Mooney, "Metal-Enhanced Fluorescence to Quantify Bacterial Adhesion," *Adv Mater,* vol. 23, pp. H101-H104, MAR 25, 2011.

[11] A. Campion, A. R. Gallo, C. B. Harris, H. J. Robota and P. M. Whitmore, "Electronic-Energy Transfer to Metal-Surfaces - a Test of Classical Image Dipole Theory at Short Distances," *Chemical Physics Letters,* vol. 73, pp. 447-450, 1980.

[12] J. R. Lakowicz, "Radiative Decay Engineering: Biophysical and Biomedical Applications," *Anal. Biochem.,* vol. 298, pp. 1-24, 11/1, 2001.

[13] J. R. Lakowicz, "Radiative decay engineering 5: metal-enhanced fluorescence and plasmon emission," *Anal. Biochem.,* vol. 337, pp. 171-194, 2/15, 2005.

[14] K. Arya, Z. B. Su and J. L. Birman, "Localization of the Surface-Plasmon Polariton Caused by Random Roughness and its Role in Surface-Enhanced Optical Phenomena," *Phys. Rev. Lett.,* vol. 54, pp. 1559-1562, 1985.

[15] D. S. Wiersma, P. Bartolini, A. Lagendijk and R. Righini, "Localization of light in a disordered medium," *Nature,* vol. 390, pp. 671-673, DEC 25, 1997.

[16] R. Bardhan, N. K. Grady, J. R. Cole, A. Joshi and N. J. Halas, "Fluorescence Enhancement by Au Nanostructures: Nanoshells and Nanorods," *Acs Nano,* vol. 3, pp. 744-752, MAR, 2009.

[17] F. E. Hernandez, S. J. Yu, M. Garcia and A. D. Campiglia, "Fluorescence lifetime enhancement of organic chromophores attached to gold nanoparticles," *J Phys Chem B,* vol. 109, pp. 9499-9504, MAY 19, 2005.

[18] H. S. Muddana, T. T. Morgan, J. H. Adair and P. J. Butler, "Photophysics of Cy3-Encapsulated Calcium Phosphate Nanoparticles," *Nano Letters,* vol. 9, pp. 1559-1566, APR, 2009.

[19] M. E. Sanborn, B. K. Connolly, K. Gurunathan and M. Levitus, "Fluorescence properties and photophysics of the sulfoindocyanine Cy3 linked covalently to DNA," *J Phys Chem B,* vol. 111, pp. 11064-11074, SEP 20, 2007.

[20] M. Berndt, M. Lorenz, J. Enderlein and S. Diez, "Axial Nanometer Distances Measured by Fluorescence Lifetime Imaging Microscopy," *Nano Letters,* vol. 10, pp. 1497-1500, APR, 2010.

[21] J. R. Lakowicz, Y. B. Shen, S. D'Auria, J. Malicka, J. Y. Fang, Z. Gryczynski and I. Gryczynski, "Radiative decay engineering 2. Effects of silver island films on fluorescence intensity, lifetimes, and resonance energy transfer," *Anal. Biochem.,* vol. 301, pp. 261-277, FEB 15, 2002.

[22] Y. Zhang, K. Aslan, M. J. R. Previte and C. D. Geddes, "Metal-enhanced fluorescence: Surface plasmons can radiate a fluorophore's structured emission," *Appl. Phys. Lett.,* vol. 90, pp. 053107, JAN 29, 2007.

[23] A. T. R. Williams, S. A. Winfield and J. N. Miller, "Relative Fluorescence Quantum Yields using a Computer-Controlled Luminescence Spectrometer," *Analyst,* vol. 108, pp. 1067-1071, 1983.

[24] M. Martini, M. Montagna, M. Ou, O. Tillement, S. Roux and P. Perriat, "How to measure quantum yields in scattering media: Application to the quantum yield measurement of fluorescein molecules encapsulated in sub-100 nm silica particles," *J. Appl. Phys.,* vol. 106, pp. 094304, NOV 1, 2009.

[25] D. Magde, R. Wong and P. G. Seybold, "Fluorescence quantum yields and their relation to lifetimes of rhodamine 6G and fluorescein in nine solvents: Improved absolute standards for quantum yields," *Photochem. Photobiol.,* vol. 75, pp. 327-334, APR, 2002.

[26] G. I. Redford and R. M. Clegg, "Polar plot representation for frequency-domain analysis of fluorescence lifetimes," *J. Fluoresc.,* vol. 15, pp. 805-815, SEP, 2005.

[27] S. Matsubara, Y. Chen, R. Caliandro, Govindjee and R. M. Clegg, "Photosystem II fluorescence lifetime imaging in avocado leaves: Contributions of the lutein-epoxide and

violaxanthin cycles to fluorescence quenching," *Journal of Photochemistry and Photobiology B-Biology,* vol. 104, pp. 271-284, JUL-AUG, 2011.

[28] E. Le Moal, S. Leveque-Fort, M. Potier and E. Fort, "Nanoroughened plasmonic films for enhanced biosensing detection," *Nanotechnology,* vol. 20, pp. 225502, JUN 3, 2009.

[29] S. Murata, P. Herman, H. J. Lin and J. R. Lakowicz, "Fluorescence lifetime imaging of nuclear DNA: Effect of fluorescence resonance energy transfer," *Cytometry,* vol. 41, pp. 178-185, NOV 1, 2000.

[30] J. Zhang, Y. Fu, D. Liang, R. Y. Zhao and J. R. Lakowicz, "Enhanced Fluorescence Images for Labeled Cells on Silver Island Films," *Langmuir,* vol. 24, pp. 12452-12457, NOV 4, 2008.

[31] C. D. Geddes and J. R. Lakowicz, "Metal-enhanced fluorescence," *J. Fluoresc.,* vol. 12, pp. 121-129, JUN, 2002.

[32] J. Zhang, Y. Fu, M. H. Chowdhury and J. R. Lakowicz, "Plasmon-coupled fluorescence probes: Effect of emission wavelength on fluorophore-labeled silver particles," *Journal of Physical Chemistry C,* vol. 112, pp. 9172-9180, JUN 26, 2008.

[33] S. GAROFF, D. WEITZ, M. ALVAREZ and J. GERSTEN, "Electrodynamics at Rough Metal-Surfaces - Photochemistry and Luminescence of Adsorbates Near Metal-Island Films," *J. Chem. Phys.,* vol. 81, pp. 5189-5200, 1984.

[34] M. Scharte, R. Porath, T. Ohms, M. Aeschlimann, J. Krenn, H. Ditlbacher, F. Aussenegg and A. Liebsch, "Do Mie plasmons have a longer lifetime on resonance than off resonance?" *Applied Physics B-Lasers and Optics,* vol. 73, pp. 305-310, SEP, 2001.

[35] A. Imhof, M. Megens, J. Engelberts, D. de Lang, R. Sprik and W. Vos, "Spectroscopy of fluorescein (FITC) dyed colloidal silica spheres," *J Phys Chem B,* vol. 103, pp. 1408-1415, MAR 4, 1999.

[36] R. Young, J. Arnette, D. Roess and B. Barisas, "Quantitation of Fluorescence Energy-Transfer between Cell-Surface Proteins Via Fluorescence Donor Photobleaching Kinetics," *Biophys. J.,* vol. 67, pp. 881-888, AUG, 1994.

CHAPTER 8

APPLICATION OF NANOPLASMONICS FOR SURFACE ENHANCED RAMAN SPECTROSCOPY (SERS)

Introduction

Surface-Enhanced Raman spectroscopy (SERS) has been increasingly utilized as an analytical technique with significant chemical and biological applications [132-138]. However, production of a robust, homogeneous and large-area SERS substrate with the same ultra high sensitivity and reproducibility still remain an important issue. Here, we describe a large-area ultrahigh-uniformity tapered silver nanopillar array made by laser interference lithography on the entire surface of a 4-inch wafer. Also presented is the rigorous optical characterization method of the tapered nanopillar substrate to accurately quantify the Raman enhancement factor, uniformity and repeatability. An average homogeneous enhancement factor of close to 10^8 was obtained for benzenethiol adsorbed on a silver coated nanopillar substrate.

History of Raman scattering

By definition, scattering is redirection of light or electromagnetic wave due to an obstacle or inhomogeneity (such as solid, liquid or gas) [139, 140]. Scattering is not just "bouncing" of a photon off a molecule, but it's a two-photon process [139]. In this process the incident non-resonant photon is absorbed and simultaneously another photon is emitted with the same energy (Rayleigh scattering) or different energy (Raman scattering). The characteristic of both scattering processes is that the molecule changes its polarizability (which is defined as the ability of a molecule's electrons to be distorted by an externally applied electric field). The intensity of Rayleigh scattering at any frequency of light is proportional to the fourth power of that frequency. Hence, light with high-frequency is much more susceptible to scattering than is lower-frequency light. The energy of outgoing Rayleigh scattered photon is same as the energy of incident photon. If during the change of polarizability, the molecular co-ordinates (symmetry rule) allow the molecules to vibrate, then additional photon energy will be spent on vibration.

That is, if a change in polarizability occurs during the course of the vibration then the outgoing photon will have different energy, frequency, and wavelength than the incoming photon [139]. The amount of energy difference between the incoming and outgoing photons (ΔE_{photon}) is equal to an energy difference between two quantized energy levels of the molecules that are causing the scattering ($\Delta E_{molecule}$). These energy differences of the photons are independent of the initial energy, wavelength, and frequency of the incoming light [139]. Rather, the energy differences are characteristic of the molecules and thus, Raman spectroscopy acts as a molecular "finger-printing" by differentiating molecules by their characteristic Raman scattering of photons [139]. The two scattering processes are shown in the simplified Jablonski diagram in Fig. 8.1. A typical Raman spectra is given in Fig. 8.2 which shows that different molecule will give rise to different Raman vibration and can be used to identify the molecule.

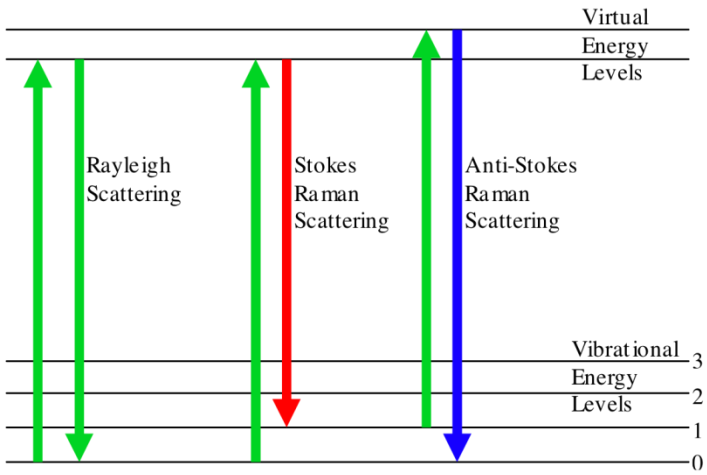

Figure 8.1: Simplified Jablonski diagram illustrating different scattering processes [141]

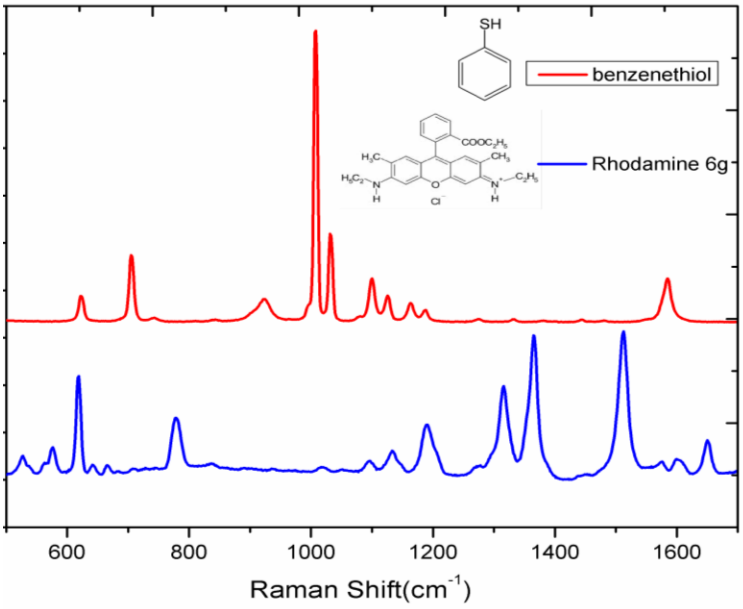

Figure 8.2: Raman spectra of Benzenethiol and Rhodamine 6-G solution

The inelastic scattering process was first predicted by Adolf Smekal [142] in 1923 and experimentally observed by C.V. Raman in 1928 [143]. The extensive use of Raman spectroscopy as a bio-molecule detection tool is still restricted due to its weak sensitivity as compared to other scattering mechanisms (roughly only 1 in 10^8 photons ends up in Raman scattering) [144] and also due to typical lower scattering cross-sections of Raman process (~ 10^{-30} cm^2) which is around 15 orders of magnitude lower than fluorescence emission [145]. In order to get detectable Raman scattering it is necessary to use an array of filtering techniques or to enhance the Raman scattering process. The latter of the two can be achieved using Surface Enhanced Raman Spectroscopy (SERS).

A brief history of SERS

SERS effect was first reported by Fleischmann et al. [146] in 1974 while doing experiment with Pyridine adsorbed on a roughened silver surface. The electric field enhancement mechanism responsible for the observed high Raman intensity was proposed by Jeanmaire and Van Duyne (1977) [147]. In the same year, Albrecht and Creighton (1977) [148] proposed a

separate mechanism, called Charge Transfer mechanism where the increase in Raman intensity was due to interaction between molecular electronic states and metal Fermi levels.

In 1997, Kneipp et al. [149] reported that SERS might be capable of single molecule detection. Nie and Emory [150]also independently confirmed the findings and proposed the concept of "hot particles" which are capable of producing very high enhancement ($\sim 10^{14}$), which can be used for single-molecule detection. The single molecule SERS experiment by Nie and Emory [150] was done with dry silver colloidal particles with Rhodamine 6G molecules, whereas Kneipp et al. [149] did the experiments with crystal violet dye molecule in aqueous colloidal silver solution. The concentrations in both the cases were ultra-low so that there are a small number of analytes per colloids, typically ~0.1 molecule/colloid. The single-molecule nature of the signals was inferred from the ultra low concentration of the sample. Because of low analyte concentration, it was statistically suggested that there cannot be more than about one molecule per colloid or an average one molecule in the scattering volume if several colloids are present. So, if any SERS signal is observed then it must originate from a single molecule. In the context of single molecule SERS experiment, it should be noted that the experiments were performed with very strong dye molecules (Rhodamine 6G (R6G) and crystal violet), which inherently have Raman cross sections much larger than 10^{-30} cm^2 due to resonance effects (e.g. isolated R6G has a resonance Raman cross section of $\sim 10^{-24}$ cm^2/sr). Hence, single-molecule detection of R6G can be achieved even with a surface enhancement factor of about 1010. However, above these SERS active substrate preparation processes are hampered by the need to use more time consuming bio-conjugation process of molecule to the colloids. The inherent statistical distribution of colloids in the solution also makes it difficult to get uniform and reproducible detection (and enhancement factor) consistently.

On the other hand, the dramatic development of nanotechnology opens the possibilities of new SERS substrate design and fabrication. One of the many approaches that has been tried includes micro- or nanoscale "roughening," either in the form of electrochemical texturing of a surface before metal sputtering [151], or as a metal colloid either bonded to a surface [152, 153], or in close proximity to a surface. In the last technique, the sample molecules are placed onto a sol-gel matrix of silver particles coating the inside of a glass vial — the molecules are injected into the vial in solution, permitting SERS of those which then leave the solution and embed

themselves into the matrix [154, 155]. The nanoscale approaches also includes (self-) assemblies of latex nanoparticles, which, when electroplated and subsequently dissolved away, leave behind nanovoids or nanoholes (ordered and irregular, respectively) [156, 157]. This popular nanosphere lithography technique has also been applied to create ordered 2D nanoparticle arrays (often called a Fischer pattern), typically using a colloid crystal as evaporation or etching mask [158-160]. In addition, the straightforward binding of molecules to single metal nanoparticles has also been reported to have yielded Raman signal enhancement, leading to the detection of single molecule Raman spectra [149, 150, 161, 162]. In general, reported signal enhancements are as much as six orders of magnitude or more. However, a mature and sizeable level of commercial success is yet to be achieved by these technologies. In spite of having a fairly reliable manufacturing process in replicating those surfaces, the level of enhancement measured across a single surface remains unacceptably inconsistent. Enhancement is observed only at so-called "hot spots," regions where the Raman signal is very high, while neighboring regions might exhibit little or even no significant signal enhancement. This situation is exacerbated further by an inconsistency of performance between different but essentially identical substrates [163]. Overall, these two aspects together effectively have prevented SERS from being widely recognized as a quantifiable spectroscopic technique [164].

In this chapter, we describe a rigorous SERS characterization experiment with a substrate made up of silver-coated silica nanopillar arrays produced by large scale laser interference lithography and following metal deposition. The pillars have shown to have great tunability potential [165] and with an adiabatic taper of ~25 degree offer the additional advantage of nanofocusing and impedance matching [166, 167]. This low cost yet highly-uniform SERS substrate is field deployable, robust and designed for reproducible detection platform for bio-molecules. Here, we describe the optical characterization experiments with the standard Raman molecule Benzenethiol (C_6H_6S), due to its ready nature to form a uniform self assembled monolayer (SAM) on noble metal material such as silver and gold [168, 169] (which are also the preferred material coating for tapered nanopillar SERS substrates because of their optimal plasmon properties in visible range) [165].

SERS substrate preparation

The nanopillar SERS substrates were prepared using the following method. Firstly a 4-inch-diameter silicon dioxide wafer is coated with an average 0.45 μm thick photoresist and then exposed by 413 nm wavelength laser interference illumination with a dose of ~ 40 mJ/cm^2. After the photoresist development, the wafer is covered by a uniform array of nanoscale circular photoresist mask of 150 nm in diameter and 350 nm in spacing distance [37]. Secondly the wafer is subject to ion milling deep reactive ion etching by using a highly directional Bosch process. The unprotected silicon diode area was etched down for 500 nm leaving behind the array of silicon dioxide nanopillars. As there is also the lateral etching to the photoresist-protected area, or "undercut", although at a much slower etch rate, the silicon dioxide nanopillars are tapered and have sharp tips at the top. Finally after completely stripping the photoresist, the wafer covered with nanopillar array structures on the entire surface was subject to metal deposition.

In order to make the nanopillar surfaces SERS active, e-beam evaporation of an 80-nm thick film of silver onto the nanopillar surface was performed. The film was deposited at a rate of 0.1 nm s^{-1}, with no heating or cooling applied to the substrate during deposition. To make the deposition uniform, the sample was kept on a hemispherical mounting rotating with 50 rpm (revolution per minute) inside the e-beam chamber. Figure 8.3a and b show the scanning electron microscope image of the LLNL (Lawrence Livermore National Laboratory) nanopillar SERS substrate before depositing silver and after coated with 80 nm of silver respectively.

(a) (b)

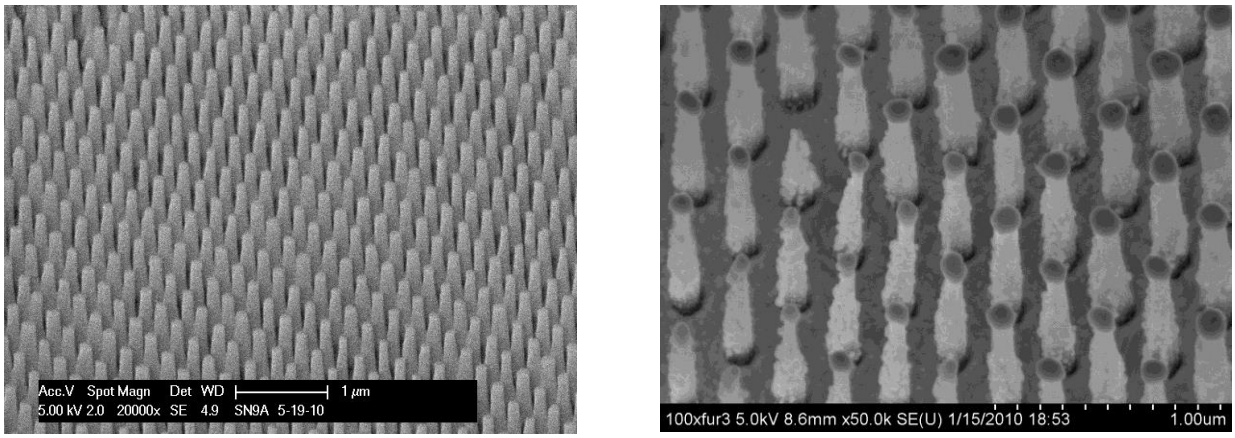

Figure 8.3: (a) SERS substrate before deposition of silver. (b) Side view (25^{o}) of SERS substrate after depositing 80 nm silver.

After the deposition, the silver-coated LLNL substrates were then functionalized with a SAM of benzenethiol using an earlier described procedure [170]. The substrates were submerged in 4-mM solutions of benzenethiol made with ethanol for 1 h and then gently rinsed in neat ethanol for 1 min, followed by drying under a stream of nitrogen.

Experimental Setup

The normal Raman and the SERS spectra of Benzenethiol were measured in a Raman spectrometer system with 785-nm laser excitation. The system comprised a semiconductor 785-nm CW diode laser, a microscopy system and a thermoelectric cooled (−80 ◦C) CCD camera (PIXIS-400, Princeton Instruments). The spectral resolution of the spectrometer was approximately 1.5 cm^{-1} in the near-infrared range. A 10x microscope objective lens (Mitutoyo infinity-corrected long working distance objectives, Edmund Optics, Part No. NT46-144) with an effective focal length of 20 mm and diameter of 24 mm was used to focus the excitation laser beam onto the sample and to collect the backscattered radiation for input into the Raman spectrometer. Figure 8.4 shows schematic of the SERS experimental set up.

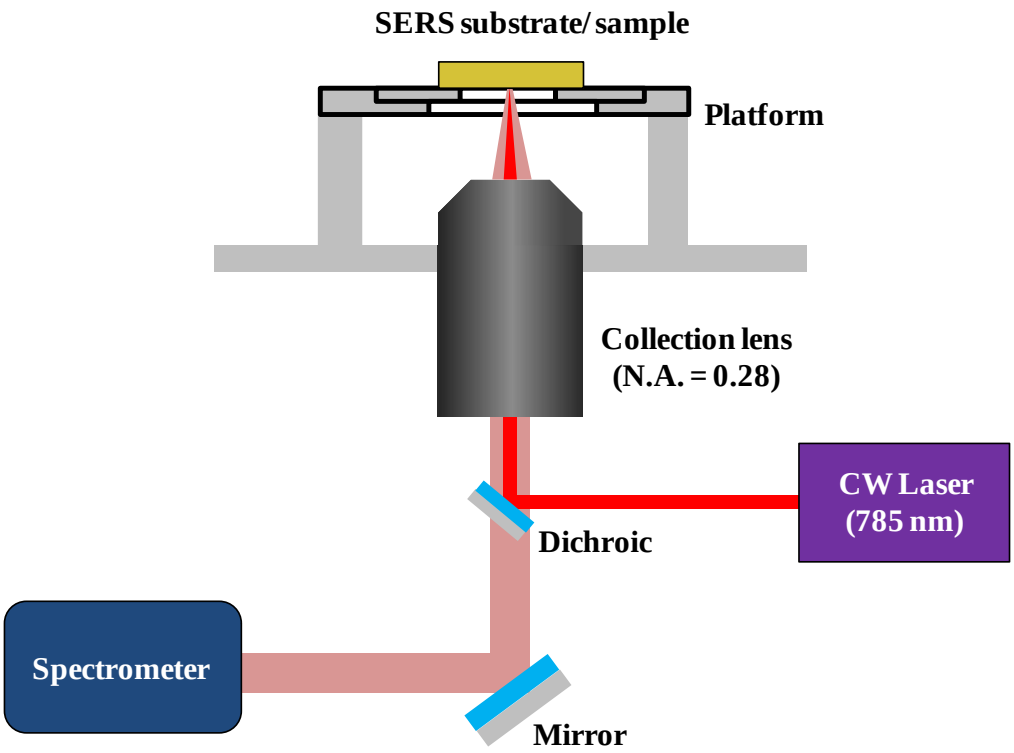

Figure 8.4: Schematic of SERS experimental set-up.

Normal Raman scattering cross-section

Benzenethiol (> 99% purity) was purchased from Sigma-Aldrich. About 0.5 ml of neat benzenethiol was poured into a PDMS cell of thickness 0.5 mm to perform the normal Raman spectra. Figure 8.5 shows the background corrected RS spectrum of neat benzenethiol obtained using 35.0 mW of 785-nm CW laser and 1-s integration time in a 20 μm spot size. Consistent with earlier reported findings [170-176] strong Raman bands are observed at 419 ($\beta_{CCC}+\nu_{CS}$), 621 ($\beta_{CCC}+\nu_{CS}$), 704 ($\beta_{CCC}+\nu_{CS}$), 919 (β_{SH}), 1006 (β_{CCC}), 1032 (β_{CH}), 1099 ($\beta_{CCC}+\nu_{CS}$), 1125 (β_{CH}), 1164 (β_{CH}), 1187(β_{CH}) and 1584 (ν_{CC}) cm^{-1}. Here, β and ν indicate the in-plane bending and the stretching modes respectively. Full width at half maximum (FWHM) of the fully resolved 1584 cm^{-1} band is 25 cm^{-1}. The normal Raman intensity was calculated by integrating the area under the 1584 cm^{-1} band and was found to be 124 counts.

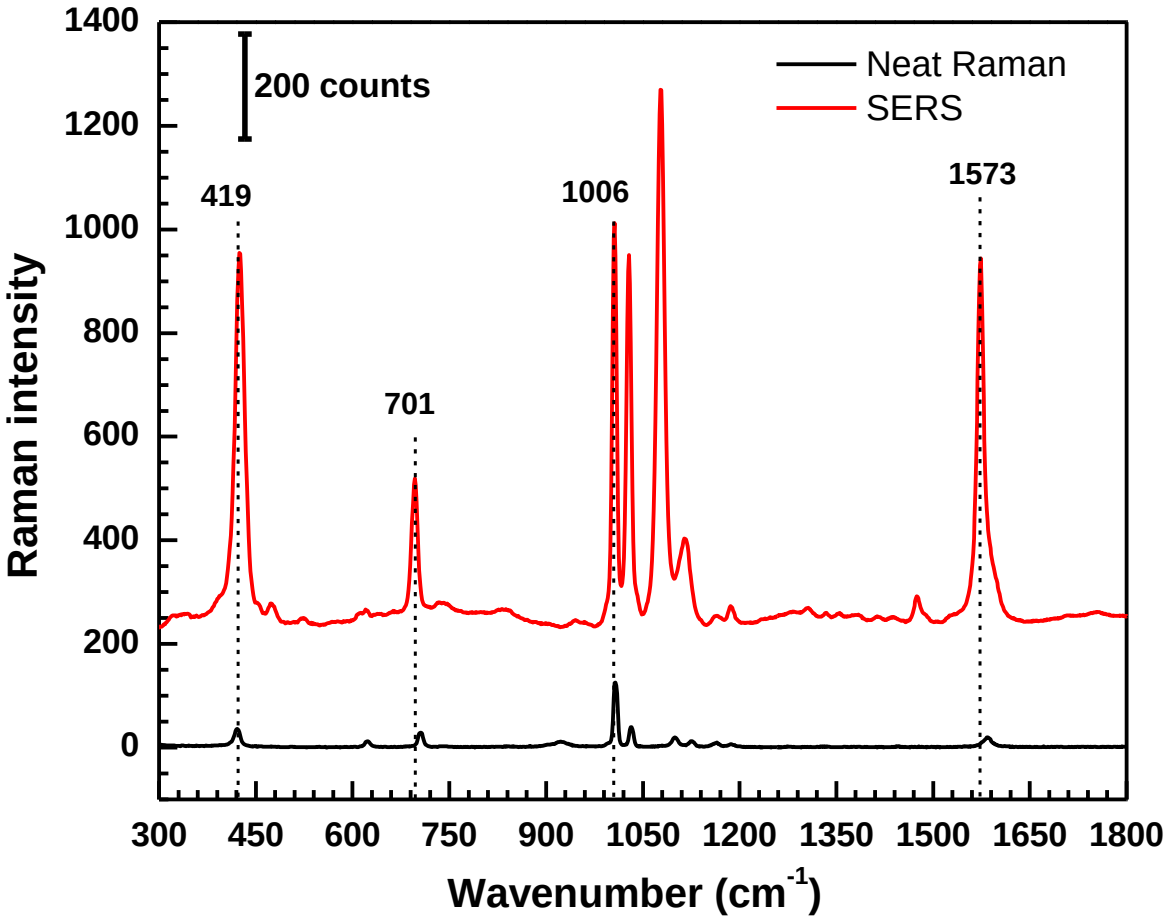

Figure 8.5: Normal Raman and SERS spectrum of benzenethiol, obtained using 35.0 mW of 785-nm pump power and 1-s integration time.

Surface Enhanced Raman scattering cross-section

The SERS spectrum for the monolayer of benzenethiol on LLNL nanopillar substrate with an 80-nm silver coating is shown in Figure 8.5. This is a typical plot of SERS spectrum averaged over four measurements at the same spot. As seen from Fig. 8.5, it is clear that the normal Raman spectrum and SERS spectrum differ in their Raman intensities bands which means that the enhancement factors not same for all the Raman bands. Also the 919 cm^{-1} (β_{SH}) band disappeared from the SERS spectra confirming that the benzenethiol is bonded to the silver surface through the thiol bond. The shifts in Raman bands are consistent with the observations of Joo et al. [171] and Roshan et al. [170]. We have considered the Raman intensities of 1584 (ν_{CC})

cm^{-1} band (C-C stretching mode) to calculate the approximate enhancement factor because of its regular appearance in both normal Raman and SERS spectrum. It should be noted that there is a slight shift in the Raman band for normal Raman spectrum which occurs at 1584 cm^{-1} as compared to that of SERS spectrum which occurs at 1573 cm^{-1}. This observation is quite similar to that reported by Roshan et al. Full width at half maximum (FWHM) of the fully resolved 1573 cm^{-1} band is 12 cm^{-1}. The SERS intensity was calculated by integrating the area under the 1573 cm^{-1} band and was found to be 44593 counts.

Raman scattering length

The Raman scattering length is an important factor in calculating the average enhancement factor of the SERS substrate. For characterizing the Raman scattering length, the neat benzenethiol was carefully mounted in a PDMS cell with a depth of 0.5 mm. The PDMS cell depth was chosen based on the knowledge of depth of focus of the laser system we are using (rule of thumb says the depth of cell should be close or smaller than the depth of focus). The Raman spectrum was taken when the stage was at the equilibrium position (focused position). Subsequently the stage was moved up and down relative to the equilibrium position. Finally, the scattering length was deduced as the length at which the Raman intensity reduced by a factor half of (1/e) as compared to the initial equilibrium position intensity. Figure 8.6a and b show a series of Raman spectrum acquired at a regular distance interval of 50 μm covering the total depth of the cell and for the cases when the stage is moving up and down relative to the equilibrium position respectively.

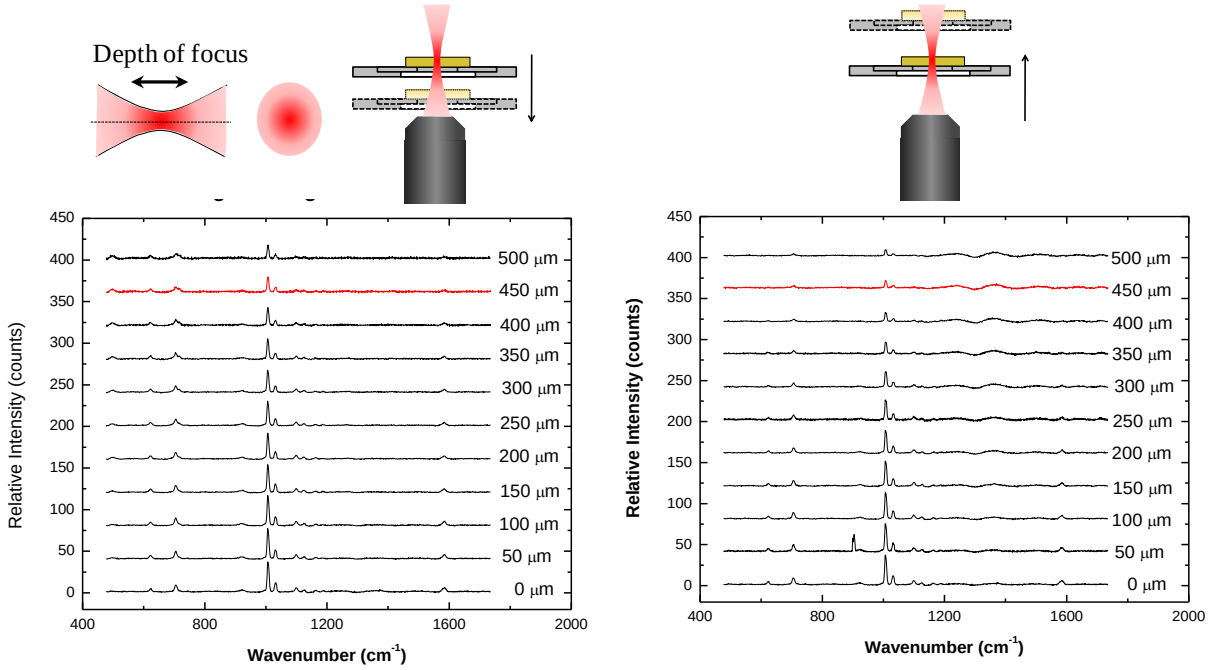

Figure 8.6: (a) Raman intensity plot when the stage is moving in down direction relative to the equilibrium stage position. (b) Raman intensity plot when the stage is moving in up direction relative to the equilibrium stage position

The variation of Raman intensity as a function of position compared to equilibrium position has also been plotted. Figure 8.7 shows the variation of Raman intensity of 1584 cm^{-1} band as a function of position when the stage is moving in down and up direction respectively. As shown in the figure, the intensity keeps on reducing while moving away from the focused position. From the study, it was found that the scattering length for our instrument is 450 μm (distance at which the intensity falls up to 50% of the 1/e value of the maximum).

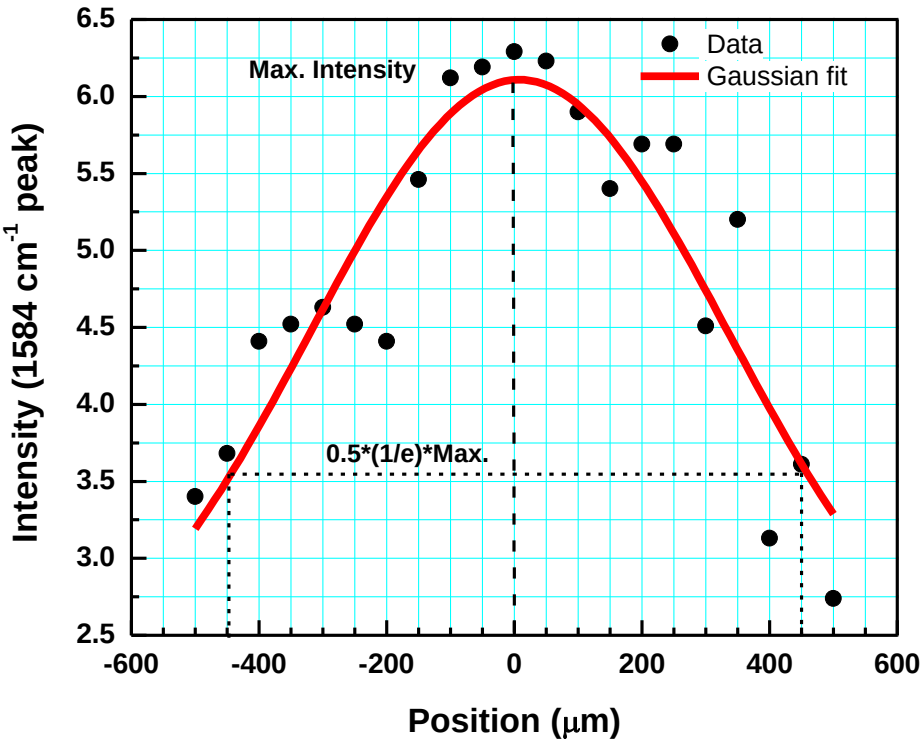

Figure 8.7: Variation of Raman intensity for 1584 cm^{-1} band (obtained using 35.0 mW of 785-nm pump power and 1-s integration time) with distance when the stage is moving in up and down direction relative to the equilibrium stage position.

Area Multiplication Factor

Due to creation of nanopillars, the effective surface area available for formation of monolayer of benzenethiol is increased as compared to flat surface. This factor has to be taken into consideration while calculating the average enhancement factor for the SERS substrate. With a special deposition technique with hemispherical mounting and having the sample at a tilt angle of 25^{o} as well as rotation of 50 rpm, we successfully deposited silver on the side wall of tapered pillars (as shown in the SEM at the inset in Fig. 8.8c). The schematic of nanopillar distribution and shape of the pillar are shown in Fig. 8.8a and b respectively. With considering a pillar radius of 75 nm and pillar height of 750 nm, m was calculated to be 2.44 using the relation:

$$m = \frac{\left[A_{1x1} - 9 * \pi r^2 + 9 * A_{cone}\right]}{A_{1x1}} \qquad (1)$$

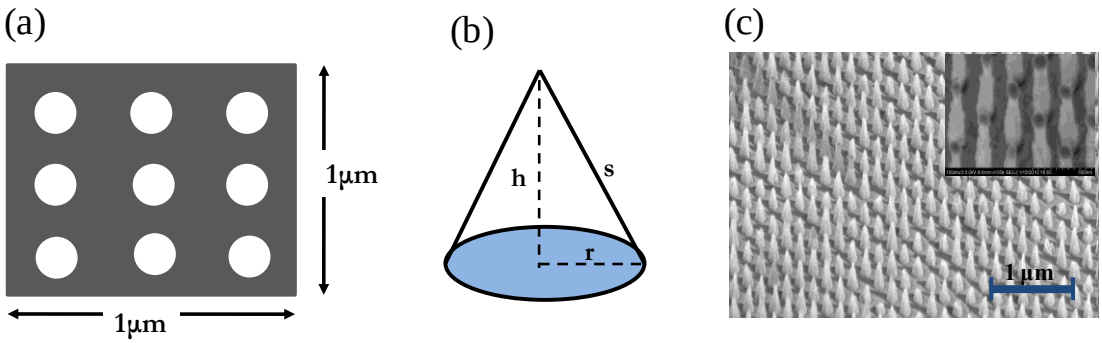

Figure 8.8: (a) Schematic of average number of pillars per unit area. (b) Assumed structure for the nanopillar. (c) SEM of LLNL nanopillar substrate with 80 nm silver deposited pillar shown at the inset.

Enhancement Factor

The absolute Raman cross-section of Benzenethiol has already been calculated by Roshan et al. [170]. Hence, instead of calculating the absolute Raman cross-section, here focus has been shifted to characterize the effectiveness of current SERS substrate, prepared using a novel laser interference technique, by calculating the enhancement factor (EF). As described in details by Roshan et al.[170], the expression for the enhancement factor can be given as:

$$EF = \frac{I_{SERS}}{I_{RS}} * \frac{N_{RS} L}{N_{SERS}\, m} * \frac{1}{n^2} \qquad (2)$$

Where I_{SERS} and I_{RS} are the Raman intensity from SERS substrate and neat Benzenethiol respectively, N_{RS} is the molecular density of the benzenethiol, N_{SERS} is the areal density of benzenethiol on a flat surface, L is that Raman scattering length, m is multiplier that accounts for the increased surface area of the nanostructured surface and *n* is the refractive index of benzenethiol. Substituting the values of 1.56 for *n* [177], 44593 for I_{SERS}, 3.3 x 10^{14} cm^{-2} for N_{SERS}, 124 for I_{RS}, and 5.9 x 10^{21} cm^{-2} for N_{RS} [170], 0.045 cm (450 µm) for *L*, 2.44 for m, we obtain a value of average enhancement factor of EF_{ave}= 0.4873 x 10^8 for our tapered nanopillar SERS substrate.

Repeatability of SERS experiment

The repeatability and uniformity of SERS signal across the SERS substrate is an important parameter for designing a robust SERS substrate. The robustness of LLNL nanopillar SERS substrate was characterized by taking several SERS spectrum by scanning the laser across the substrate. The SERS substrate was mounted on a motorized platform which was controlled by LABVIEW program. The sample was scanned for total of 57 data points and at each point, the measurement was repeated 4 times (total sample space of 228 points). A typical 5x5 arrays 2-D scanning result is reported in Fig. 8.9. The surface plot showing the 2-D scanning result has been shown in Fig. 8.9. The distributions for all the peaks are found to be following a Gaussian distribution.

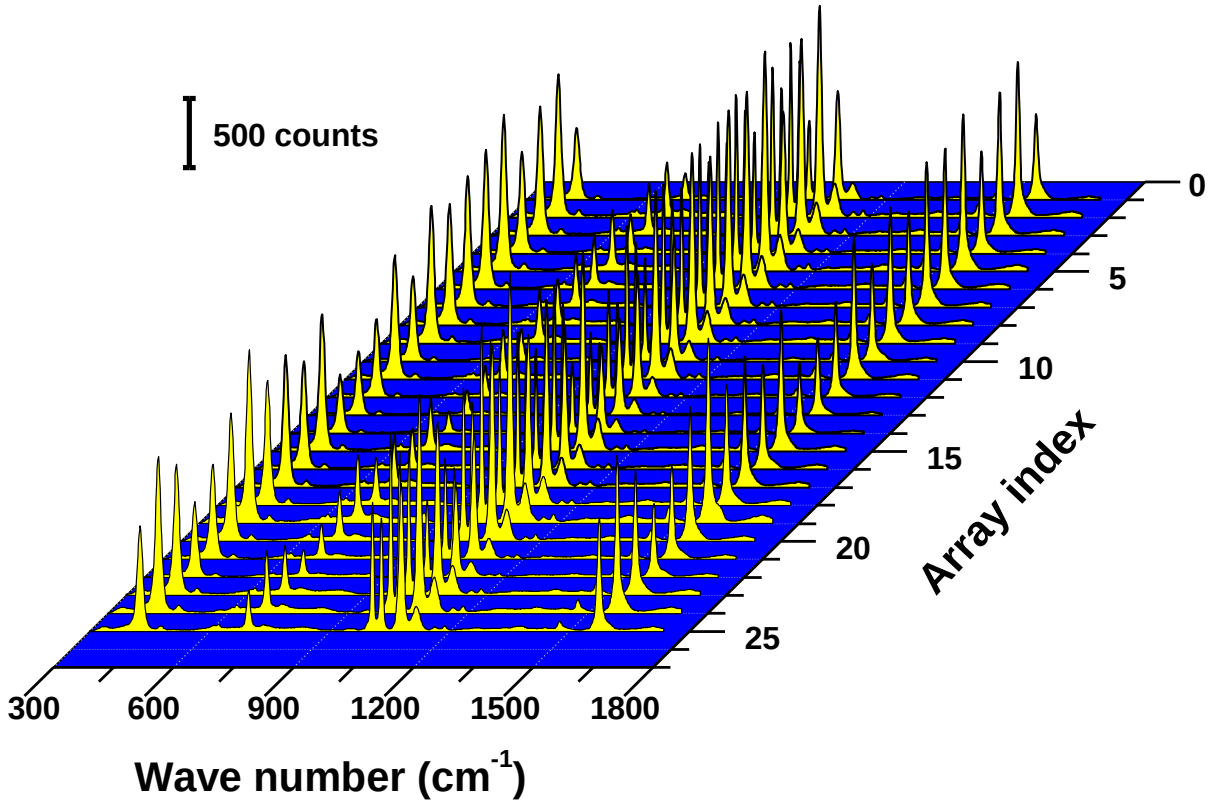

Figure 8.9: Surface plot of 2-D scanning SERS data for the LLNL nanopillar substrate obtained using 35.0 mW of 785-nm pump power and 1-s integration time.

However, 1573 cm^{-1} peak, which was used for calculating SERS enhancement factor, was found to be fairly uniform. Finally, Fig. 8.10 shows the probability distribution of the enhancement factor calculated for the entire substrate. This follows a Gaussian distribution with a maximum

enhancement factor of 0.487 x 10^8 and an average enhancement factor of 0.14 x 10^8. This showed the uniformity of the SERS substrate and confirmed that LLNL nanopillar SERS substrate is fairly robust.

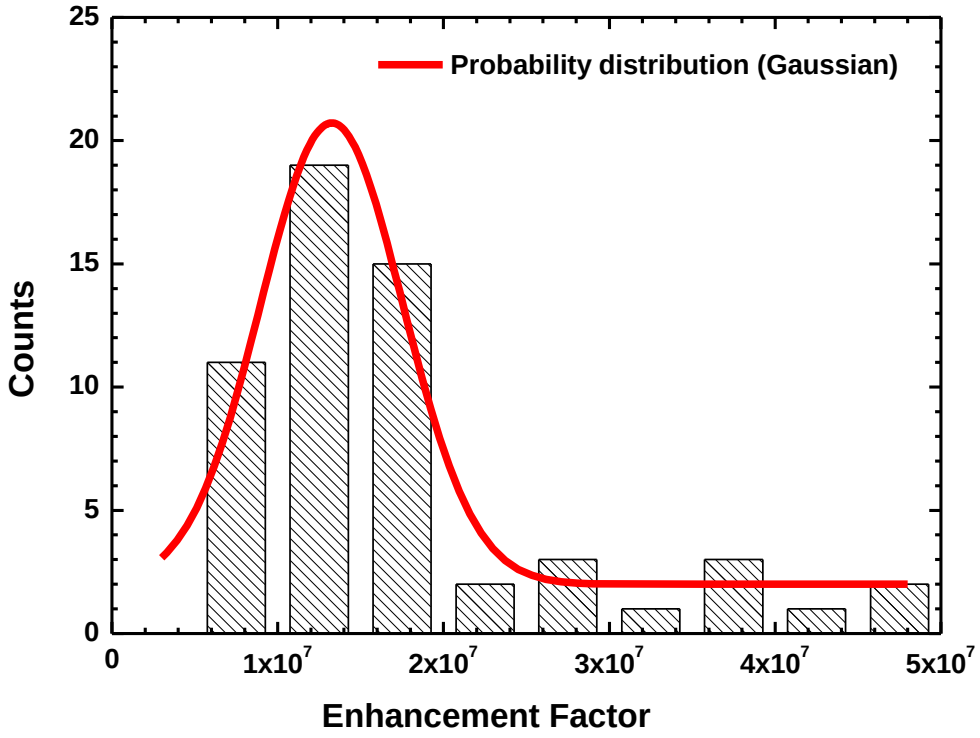

Figure 8.10: Probability distribution showing the enhancement factor calculated for the entire substrate.

Conclusions

In conclusion, we have produced a highly ordered Ag coated nanopillar SERS substrate using a novel laser interference nano-lithography technique. A uniform enhancement of ~ 0.5 x 10^8 (with peaks at 0.14x10^8) has been demonstrated using a SAM of benzenethiol on the SERS substrate. From the results, it can be inferred that the laser interference based approach is capable of fabricating large area uniform SERS active substrates. This simple and straightforward method for fabricating SERS substrates offers considerable potential for the batch fabrication as well as commercialization of such robust substrate, and hence opens the door for practical sensor chips based on SERS.

References

[1] X. Qian, X. Peng, D. O. Ansari, Q. Yin-Goen, G. Z. Chen, D. M. Shin, L. Yang, A. N. Young, M. D. Wang and S. Nie, "In vivo tumor targeting and spectroscopic detection with surface-enhanced Raman nanoparticle tags," *Nat. Biotechnol.*, vol. 26, pp. 83-90, JAN 2008, 2008.

[2] K. Fujita, S. Ishitobi, K. Hamada, N. I. Smith, A. Taguchi, Y. Inouye and S. Kawata, "Time-resolved observation of surface-enhanced Raman scattering from gold nanoparticles during transport through a living cell," *J. Biomed. Opt.*, vol. 14, pp. 024038, MAR-APR 2009, 2009.

[3] I. -. Chou, M. Benford, H. T. Beier, G. L. Cote, M. Wang, N. Jing, J. Kameoka and T. A. Good, "Nanofluidic biosensing for beta-amyloid detection using surface enhanced Raman spectroscopy," *Nano Letters*, vol. 8, pp. 1729-1735, JUN 2008, 2008.

[4] M. Culha, D. Stokes, L. R. Allain and T. Vo-Dinh, "Surface-enhanced Raman scattering substrate based on a self-assembled monolayer for use in gene diagnostics," *Anal. Chem.*, vol. 75, pp. 6196-6201, NOV 15 2003, 2003.

[5] K. A. Willets, "Surface-enhanced Raman scattering (SERS) for probing internal cellular structure and dynamics," *Analytical and Bioanalytical Chemistry*, vol. 394, pp. 85-94, MAY 2009, 2009.

[6] X. X. Han, B. Zhao and Y. Ozaki, "Surface-enhanced Raman scattering for protein detection," *Analytical and Bioanalytical Chemistry*, vol. 394, pp. 1719-1727, AUG 2009, 2009.

[7] M. Y. Sha, H. Xu, M. J. Natan and R. Cromer, "Surface-Enhanced Raman Scattering Tags for Rapid and Homogeneous Detection of Circulating Tumor Cells in the Presence of Human Whole Blood," *J. Am. Chem. Soc.*, vol. 130, pp. 17214-+, DEC 24 2008, 2008.

[8] D. W. Ball. Rayleigh and raman scattering. *Spectroscopy 16(2)*, pp. 15. 2001.

[9] D. W. Hahn, "Raman scattering theory introduction," .

[10] Anonymous (). . Available: http://en.wikipedia.org/wiki/Raman_spectroscopy.

[11] A. Smekal, "Zur Quantentheorie der Dispersion," *Naturwissenschaften*, vol. 11, pp. 873-875, 1923.

[12] C. V. Raman and K. S. Krishnan, "A new type of secondary radiation," *Nature*, vol. 121, pp. 501-502, 1928.

[13] R. M. Jarvis and R. Goodacre, "Discrimination of bacteria using surface-enhanced Raman spectroscopy," *Anal. Chem.*, vol. 76, pp. 40-47, JAN 1 2004, 2004.

[14] T. Vo-Dinh, L. R. Allain and D. L. Stokes, "Cancer gene detection using surface-enhanced Raman scattering (SERS)," *J. Raman Spectrosc.*, vol. 33, pp. 511-516, JUL 2002, 2002.

[15] Fleischm.M, P. J. Hendra and Mcquilla.Aj, "Raman-Spectra of Pyridine Adsorbed at a Silver Electrode," *Chemical Physics Letters*, vol. 26, pp. 163-166, 1974, 1974.

[16] D. L. Jeanmaire and R. P. Vanduyne, "Surface Raman Spectroelectrochemistry .1. Heterocyclic, Aromatic, and Aliphatic-Amines Adsorbed on Anodized Silver Electrode," *J Electroanal Chem*, vol. 84, pp. 1-20, 1977, 1977.

[17] M. G. Albrecht and J. A. Creighton, "Anomalously Intense Raman-Spectra of Pyridine at a Silver Electrode," *J. Am. Chem. Soc.*, vol. 99, pp. 5215-5217, 1977, 1977.

[18] K. Kneipp, Y. Wang, H. Kneipp, L. T. Perelman, I. Itzkan, R. Dasari and M. S. Feld, "Single molecule detection using surface-enhanced Raman scattering (SERS)," *Phys. Rev. Lett.*, vol. 78, pp. 1667-1670, MAR 3 1997, 1997.

[19] S. M. Nie and S. R. Emery, "Probing single molecules and single nanoparticles by surface-enhanced Raman scattering," *Science*, vol. 275, pp. 1102-1106, FEB 21 1997, 1997.

[20] C. A. Murray, D. L. Allara and M. Rhinewine, "Silver-Molecule Separation Dependence of Surface-Enhanced Raman-Scattering," *Phys. Rev. Lett.*, vol. 46, pp. 57-60, 1981, 1981.

[21] L. A. Dick, A. D. McFarland, C. L. Haynes and R. P. Van Duyne, "Metal film over nanosphere (MFON) electrodes for surface-enhanced Raman spectroscopy (SERS): Improvements in surface nanostructure stability and suppression of irreversible loss," *J Phys Chem B*, vol. 106, pp. 853-860, JAN 31 2002, 2002.

[22] T. Vodinh, "Sers Chemical Sensors and Biosensors - New Tools for Environmental and Biological Analysis," *Sensors and Actuators B-Chemical*, vol. 29, pp. 183-189, OCT 1995, 1995.

[23] (). . Available: http://www.rta.biz/Content/SERV_Vials.asp.

[24] S. Farquharson, A. Gift, P. Maksymiuk and F. Inscore, "Surface-enhanced Raman spectra of VX and its hydrolysis products," *Appl. Spectrosc.*, vol. 59, pp. 654-660, MAY 2005, 2005.

[25] M. C. Netti, S. Coyle, J. J. Baumberg, M. A. Ghanem, P. R. Birkin, P. N. Bartlett and D. M. Whittaker, "Confined surface plasmons in gold photonic nanocavities," *Adv Mater*, vol. 13, pp. 1368-1370, SEP 14 2001, 2001.

[26] S. Coyle, M. C. Netti, J. J. Baumberg, M. A. Ghanem, P. R. Birkin, P. N. Bartlett and D. M. Whittaker, "Confined plasmons in metallic nanocavities," *Phys. Rev. Lett.,* vol. 87, pp. 176801, OCT 22 2001, 2001.

[27] U. C. Fischer, J. Heimel, H. J. Maas, M. Hartig, S. Hoeppener and H. Fuchs, "Latex bead projection nanopatterns," *Surf. Interface Anal.,* vol. 33, pp. 75-80, FEB 2002, 2002.

[28] U. C. Fischer and H. P. Zingsheim, "Sub-Microscopic Pattern Replication with Visible-Light," *Journal of Vacuum Science & Technology,* vol. 19, pp. 881-885, 1981, 1981.

[29] C. L. Haynes and R. P. Van Duyne, "Nanosphere lithography: A versatile nanofabrication tool for studies of size-dependent nanoparticle optics," *J Phys Chem B,* vol. 105, pp. 5599-5611, JUN 21 2001, 2001.

[30] K. Kneipp, Y. Wang, H. Kneipp, I. Itzkan, R. R. Dasari and M. S. Feld, "Population pumping of excited vibrational states by spontaneous surface-enhanced Raman scattering," *Phys. Rev. Lett.,* vol. 76, pp. 2444-2447, APR 1 1996, 1996.

[31] S. R. Emory and S. M. Nie, "Near-field surface-enhanced Raman spectroscopy on single silver nanoparticles," *Anal. Chem.,* vol. 69, pp. 2631-2635, JUL 15 1997, 1997.

[32] C. Netti, J. Lincoln and G. Flinn, "Reliable Substrate Technology for Surface Enhanced Raman Spectroscopy," *Raman Technology for Today's Spectroscopists,* 2005.

[33] P. G. Etchegoin and E. C. Le Ru, "A perspective on single molecule SERS: current status and future challenges," *Physical Chemistry Chemical Physics,* vol. 10, pp. 6079-6089, 2008, 2008.

[34] M. Bora, B. J. Fasenfest, E. M. Behymer, A. S. -. Chang, H. T. Nguyen, J. A. Britten, C. C. Larson, J. W. Chan, R. R. Miles and T. C. Bond, "Plasmon Resonant Cavities in Vertical Nanowire Arrays," *Nano Letters,* vol. 10, pp. 2832-2837, AUG 2010, 2010.

[35] M. I. Stockman, "Nanofocusing of optical energy in tapered plasmonic waveguides," *Phys. Rev. Lett.,* vol. 93, pp. 137404, SEP 24 2004, 2004.

[36] D. K. Gramotnev, M. W. Vogel and M. I. Stockman, "Optimized nonadiabatic nanofocusing of plasmons by tapered metal rods," *J. Appl. Phys.,* vol. 104, pp. 034311, AUG 1 2008, 2008.

[37] J. Y. Gui, D. A. Stern, D. G. Frank, F. Lu, D. C. Zapien and A. T. Hubbard, "Adsorption and Surface Structural Chemistry of Thiophenol, Benzyl Mercaptan, and Alkyl Mercaptans - Comparative-Studies at Ag(111) and Pt(111) Electrodes by Means of Auger-Spectroscopy, Electron-Energy Loss Spectroscopy, Low-Energy Electron-Diffraction, and Electrochemistry," *Langmuir,* vol. 7, pp. 955-963, MAY 1991, 1991.

[38] H. Kang, T. Park, I. Choi, Y. Lee, E. Ito, M. Hara and J. Noh, "Formation of large ordered domains in benzenethiol self-assembled monolayers on Au(111) observed by scanning tunneling microscopy," *Ultramicroscopy,* vol. 109, pp. 1011-1014, JUL 2009, 2009.

[39] A. Fernandez, H. T. Nguyen, J. A. Britten, R. D. Boyd, M. D. Perry, D. R. Kania and A. M. Hawryluk, "Use of interference lithography to pattern arrays of submicron resist structures for field emission flat panel displays," *Journal of Vacuum Science & Technology B,* vol. 15, pp. 729-735, MAY-JUN 1997, 1997.

[40] R. L. Aggarwal, L. W. Farrar, E. D. Diebold and D. L. Polla, "Measurement of the absolute Raman scattering cross section of the 1584-cm(-1) band of benzenethiol and the surface-enhanced Raman scattering cross section enhancement factor for femtosecond laser-nanostructured substrates," *J. Raman Spectrosc.*, vol. 40, pp. 1331-1333, SEP 2009, 2009.

[41] T. H. Joo, M. S. Kim and K. Kim, "Surface-Enhanced Raman-Scattering of Benzenethiol in Silver Sol," *J. Raman Spectrosc.*, vol. 18, pp. 57-60, FEB 1987, 1987.

[42] D. Lin-Vien, N. B. Colthup, W. G. Fateley and J. G. Grasselli, *The Handbook of Infrared and Raman Characteristic Frequencies of Organic Molecules.* New York: Academic Press, 1991.

[43] G. Varsanyi, *Vibrational Spectra of Benzene Derivatives.* New York: Academic Press, 1969.

[44] L. J. Wan, M. Terashima, H. Noda and M. Osawa, "Molecular orientation and ordered structure of benzenethiol adsorbed on gold(111)," *J Phys Chem B,* vol. 104, pp. 3563-3569, APR 20 2000, 2000.

[45] K. T. Carron and L. G. Hurley, "Axial and Azimuthal Angle Determination with Surface-Enhanced Raman-Spectroscopy - Thiophenol on Copper, Silver, and Gold Metal-Surfaces," *J. Phys. Chem.*, vol. 95, pp. 9979-9984, NOV 28 1991, 1991.

[46] S. J. Lee and K. Kim, "Development of silver film via thermal decomposition of layered silver alkanecarboxylates for surface-enhanced Raman spectroscopy," *Chemical Communications,* pp. 212-213, 2003, 2003.

[47] S. Mathias, R. G. Cecchini and E. D. C. Filho, "Dipole Moments of Cyclohexanethiol, Alpha-Toluenethiol and Benzenethiol," *J. Phys. Chem.*, vol. 65, pp. 425-&, 1961, 1961.

CHAPTER 9

APPLICATION OF NANOPLASMONICS FOR LIVE CELL IMAGING

Introduction

Fluorescence cell imaging is one of the most powerful and ubiquitous methods in cell biology research due to its specificity and high sensitivity [178]. Besides the instrumentation, the limitations to the sensitivity of fluorescence cell imaging include the quantum yield and photostability of fluorophore, and the auto-fluorescence of the cells. Due to dynamic behavior exhibited by live cells, it is always desirable to look in to the cellular processes with a high spatial and temporal resolution, and preferably for an indefinite duration of time. In addition, due to the heterogenous nature of cell biology, often it is required to conduct the experiment at lower magnification, but with sufficient contrast to observe the cellular perturbation. Lower magnification generally results in lower collection efficiency and hence such studies are limited by the weakness of the fluorescence signal. The collection efficiency can be offset by using high numerical aperture (NA) lenses. Although this will improve the resolution (according to Rayleigh criterion, diffraction limited lateral resolution, $r_{lateral} = C\lambda/(n\sin\alpha) \approx 0.61\lambda/NA$; where C = constant = 0.61 (coherence), n = refractive index of medium between object and lens, α = semi angle and λ is the wavelength of incident light; The axial resolution, $r_{axial} \approx 2n\lambda/NA^2$), using higher *NA* lens will result in losing on the depth of field ($d = n\lambda/NA^2 + n\,r/(M \square NA)$) where M is the magnification) [179]. Increasing *NA* or magnification results in a decrease of the depth of field and hence one need to continuously focus up and down to probe the whole layer of a thick specimen [180]. This is a hindrance to automated high-throughput screening processes.

Although the weak fluorescence of traditional dyes (due to their comparatively low extinction coefficient) and low photostability of molecular fluorophore (mainly due to irreversible chemical reactions with oxygen free radicals commonly known as photobleaching) can be circumvented by using a new class of semiconductor nanocrystals probes commonly called quantum dots, the low biocompatibility and blinking of emission signal of quantum dots

restricts the application in live cell imaging. Traditionally glass or polymer based substrate are used for cellular imaging. Due to higher refractive index of the substrate as compared to air, most of the fluorescence of the fluorophore is emitted in to the substrate. Therefore, in experimental set up where the excitation and collection are performed at the same side (e.g. in epifluorescence microscope, scanning microarray devices), the collection efficiency of light is very low. In fact, one study showed that only 20% of the total emitted light is collectable on standard glass substrates [181]. In order to increase the collection efficiency and to increase the fluorescence signal, recently a new strategy has been deployed by using metal coated slides for cell imaging [182]. On a metal coated mirror slides the intensity of fluorescence signal can be increased by more than 4 folds as compared to glass slides. The fluorescence enhancement has been attributed to two mechanisms (1) mirror effect [183] and (2) surface plasmon resonance [126, 184-187]. The reflection of the excitation light on the mirror substrate induces an enhancement of the excitation field and also the emitted light is redirected by the mirror substrate, toward the objective lens, thus increasing the collection efficiency [180]. However, the flat surface morphology limits plasmonic coupling and fluorescence enhancement efficiency [188]. In fact, plasmons are not created when flat metal surfaces are illuminated with light as surface plasmons are induced only under special optical conditions (Otto configuration or Kretschmann configuration, where the thin metal film is required to be illuminated through a glass prism or high refractive index material and at a precise angle) [189].

One such configuration used for cell imaging is known as Total Internal Reflection Fluorescence Microscopy (TIRFM) [190]. In TIRFM a laser beam passes through a high numerical aperture (N.A.) objective and undergoes total internal reflection when reflected from a high-refractive index medium (e.g., glass) into a low-refractive index medium (e.g. cell/water). The electromagnetic evanescent wave thus produced penetrates the cell membrane adjacent to the coverglass and excites fluorophores within an ultra thin optical section of ~100 nm, thereby reducing background noise from out-of-focus fluorescence. However, because of a partial loss of light confinement due to light scattering in the cell, excited fluorophores in the inner part of the cell may contribute to background noise and compromise sensitivity. In addition, the above system requiring a large incident angle and complicated optical systems (prisms and glass with high refractive) for the SPR coupling, makes it unsuitable for imaging under commercial fluorescence microscopes or array readers. Another approach of enhancing fluorescence signal is

by coupling light to localized surface plasmons (LSPR) which rely on the coupling of fluorophore to random distributions of metallic nanoparticles [191]. However, in order to get considerable enhancement precise control over spatial position of the fluorophore relative to the nanoparticle is required which makes these methods unsuitable for applications in cell imaging applications. Surface plasmons can also be coupled by subwave-length metal-coated gratings using excitation light from the same side as the grating surface [80, 192, 193]. The advantages of grating coupled SPR as compared to prism-coupled SPR includes small resonance angle, higher coupling efficiency and simple optical setup [188].

We recently reported a highly ordered nanopillar array for uniform surface enhancement Raman scattering (SERS) applications [194]. As oppose to ordered array structure, which can only support few plasmonic modes, random array structures can support as well as localize large number of plasmonic modes [195]. In the present study, we have created a randomly distributed nanocone substrate on silicon and coated with silver for surface-plasmon-enhanced fluorescence detection and cell imaging. We observed three dimensional fluorescence enhancement on our substrate evidenced from the confocal fluorescence imaging of Chinese Hamster Ovary (CHO) cells grown on the substrate. Interestingly, the fluorescence intensity was amplified more than 100 fold as compared to glass substrate and the position of maximum intensity was more than 10 μm further away from the sample surface. The details of the fabrication, imaging and data analysis are presented in the following sections.

Cell culture

Chinese Hamster Ovary (CHO) cells are maintained in Ham's F12 medium containing 5% fetal bovine serum (FBS), 1% antibioticantimycotic solution (10 units/mL penicillin G sodium, 10 ug/mL streptomycin sulfate, 25 ug/mL amphotericin B, 0.85% saline; Invitrogen, Carlsbad, CA), and 1% glutamine and grown in 100 mm glass culture plates at 37 °C in a humidified atmosphere of 5% CO2. The cells exhibit normal morphology, express cell contact inhibition and grow as a monolayer without expression of neoplastic foci. CHO cells are transferred when the culture becomes confluent. For the experiment, the cells are re-suspended to

1e6 cells per mL. For the confocal imaging, the cells are seeded on the nanopillar plasmonic structure and incubated at 37 °C in a humidified atmosphere of 5% CO2 for at least 12 hours to allow attachment.

Cell labeling protocol

FM 1-43 FX (Cat # F35355, Invitrogen) dye is used to stain the cell membrane. A working staining solution of 5 ul/ml dye in ice-cold PBS solution is prepared. The ice-cold temperature is used as the dyes are quickly endocytosed. Finally, the nanocone substrate with the cells is washed with fresh PBS before immersing in the staining solution for about one minute. The substrate is immediately taken for the imaging after staining.

Fluo-4, AM (Invitrogen, Carlsbad, CA) dye is used to monitor the calcium (Ca2+) level of the cell and as a label for the viable cell cytoplasm. A working staining solution of 5 μl/ml dye in fresh PBS solution is prepared. The substrate with cells on top of it is washed with fresh media and then immerse in the staining solution. The substrate with the cells is incubated with the staining solution for 15 minutes at 37 °C in a humidified atmosphere of 5% CO2 before imaging.

The cell nucleus is stained with blue fluorescent Hoechst dyes (Invitrogen, Carlsbad, CA). The substrate with the cells is incubated in a 2 μl/ml staining solution for about 15 minutes at 37 °C and a humidified atmosphere of 5% CO2 before imaging.

Confocal imaging

The cell imaging is performed using Zeiss LSM 710 Confocal Microscope (Carl Zeiss, Wake forest, NC). The microscope system consists of a Zeiss 710 confocal scanner, Axio Observer Z1 microscope and a Spectraphysics Mai-Tai Ti-Sapphire laser. Three visible excitation lines (405 nm, 488 nm and 561 nm) are used for our experiment. The microscope is equipped with QUASAR 34 channel spectral detector (2 standard PMTs and a 32 channel PMT array) with spectral resolutions up to 3 nm. ZEN 2009 software is used for the hardware control and spectral un-mixing. The laser power used for the experiment is about 0.2% of the total available power (25 mW).

SEM fixation protocol for cells and SEM imaging

Initially, the cell media is replaced by a fixative solution (EM grade 2.0 % paraformaldehyde and 2.5% glutaraldehyde in 0.1 M Na-Cacodylate buffer, pH 7.4) and kept for 4 hours in a 4 °C refrigerator. Then the cells are rinsed with buffer solution (0.1 M Na-Cacodylate buffer, pH 7.4) for 10 minutes on a shaker table. After the buffer rinse, gradual dehydration (37% ethanol, 10 min; 67% ethanol, 10 min; 95% ethanol, 10 min; 100% ethanol, 3 x 10 min) is performed for the cells. Finally, all the ethanol in the sample is replaced by carbon dioxide by performing critical point drying (CPD) in a 100% ethanol environment. Prior to SEM imaging the sample was sputter-coated with 7-nm gold-palladium coating and the imaging is performed using Philips XL30 ESEM-FEG in Hi-Vac mode.

Results and Discussion

Figure 9.1a shows a schematic overview of the experimental set up. In the experiment living cells are situated on top of a nanocone substrate, which is composed of dense nanocone structures covered by a thin layer of silver. The silver-coated nanocone structures can support both propagating surface plasmon and localized plasmon at visible wavelength range. Additionally the silver coated nanocone structures are capable of "nano-focusing" or "concentrating" optical energy creating high electromagnetic field [196] that can be coupled to a cell. Figure 9.1b shows schematically a cell on a glass substrate and a cell on a nanocone plasmonic substrate respectively. A scanning electron micrograph of the tapered silicon nanocone structures before and after coated with 80 nm thick silver layer is shown in Fig. 9.1c and 9.1d, respectively. The cross-sectional SEM in Fig 9.1c shows non-periodic array of nanocones covering the substrate. Figure 9.1e and f show the scanning electron microscope images of spherical and elongated CHO cells on the nanocone structures.

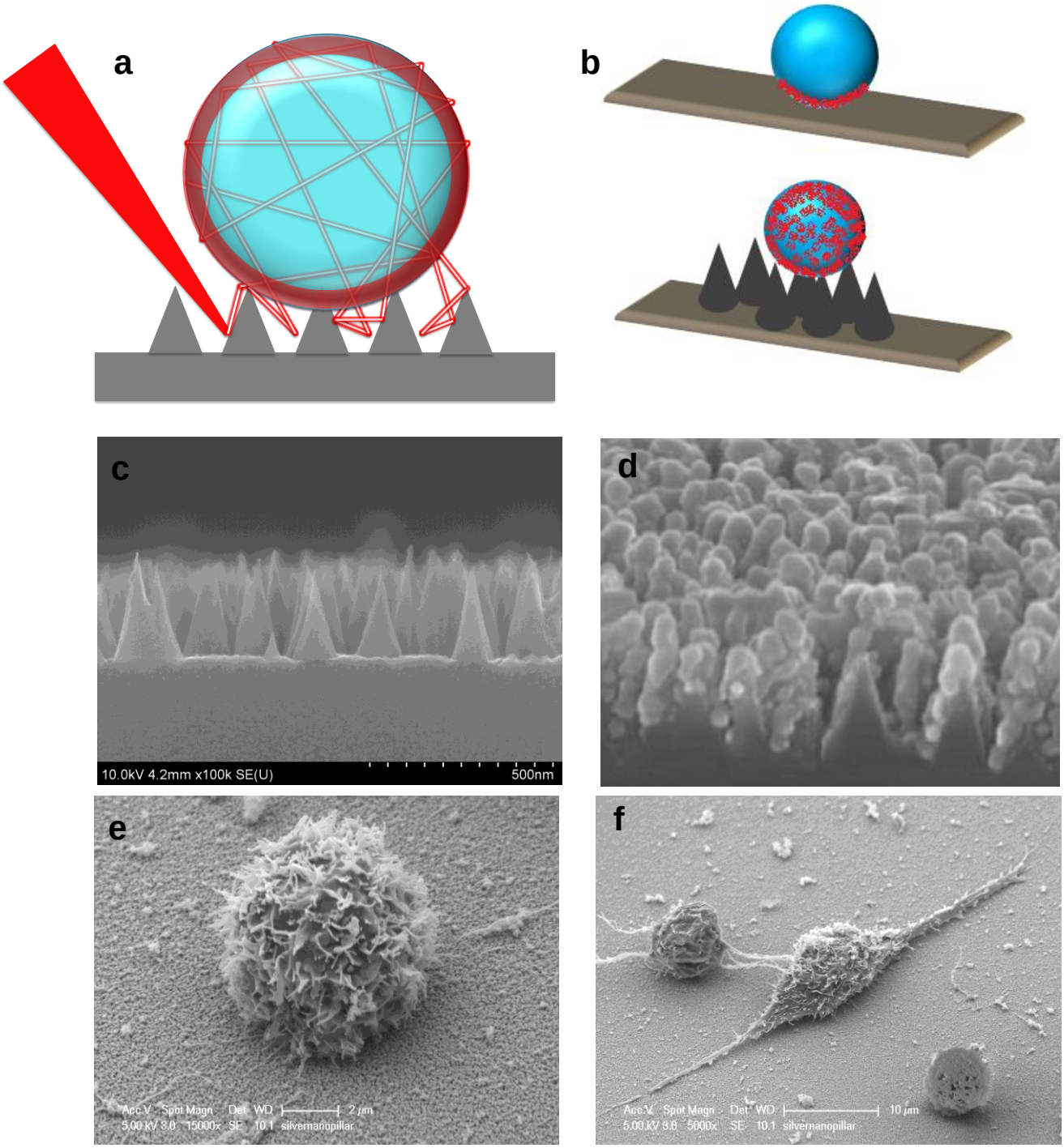

Figure 9.1: (a) Schematic illustration of coupling of light from the nanocone substrate in to the cell for enhanced fluorescence. (b) Schematic illustration of enhancement observed when cell is on a glass substrate and on a nanocone plasmonic substrate respectively. (c) Scanning electron micrograph (SEM) of the fabricated silicon nanocone structure (d) Nanocone structure after deposition of 80 nm silver (e) SEM of a spheroidal CHO cell and an elongated CHO cell on the nanocone substrate.

Cell imaging experiment

After confirming that the substrate can provide surface plasmon coupling, we grow Chinese Hamster Ovarian (CHO) cells on the nanocone substrate. The cell membrane and DNA of the live cell are stained with fluorescent dyes in one set of experiments. In another set of experiments, fluorescent labels are applied to calcium ions in the cytoplasm and the DNA of the live cell. The labeled CHO cells on the nanocone structure are imaged using a high-resolution laser scanning confocal microscope. The 405 nm, 488 nm and 561 spectral lines were used for the excitation of fluorophore dyes. The laser beam is illuminated on the nanocone substrate after focusing through the cell. We used an extremely low laser power and short imaging time; 0.2% of 25 mW laser power for green fluorescence excitation and 1.58 μs pixel dwell time.

Confocal imaging for fluorophore labeled to cell cytoplasm

A bright field image of CHO cells grown on the substrate is shown in Fig. 9.2a. For the comparison purpose, we intentionally patterned the substrate surface to make an array of square areas with silver nanocone plasmonic structure and the rest of substrate surface is covered with a smooth silver film. The cytoplasmic calcium fluorophore emission (label in green) in the cell grown on the nanocone substrate can be observed in 3D fluorescence imaging (Fig. 9.2b). In contrast, the cells on smooth silver surface express undetectable to extremely low fluorescence emission only except near the immediate surface of smooth silver film. The fluorescence intensity below and beyond cell span is due to the point spread function of the fluorescence emission. The vertical cross-sectional cell images (Fig. 9.2c) at various vertical positions show that the enhancement of the cytoplasm calcium fluorescence on the nanocone substrate extends up to the top position on the spheroidal cell, around 12 μm above the nanocone substrate. In comparison to that of the cytoplasm, the fluorescence enhancement for the nucleus fluorescence is modest. The viability of CHO cells in the imaging experiments is evident by the normal morphology expressed by the cells on the nanocone substrate after 12 hours of incubation. The fluorescent expression of fluo-4 inside the cell requires cleavage of fluo-4 AM by intracellular

esterase, demonstrating viable activity of enzymes in the cytoplasm and intact cell membrane [197].

Confocal imaging for fluorophore labeled to cell membrane

To extend the generality of our interpretation, we performed another set of experiment with cell membrane and nucleus labeled by red and blue emission fluorophores, respectively. The x-z plane cross-section image is shown (Fig. 9.2d). Due to overwhelmingly high fluorescence enhancement for the 3D cell membrane on the nanocone substrate, the other cell membrane on the smooth silver surface are not visible under such a high intensity contrast. However, the fluorescence intensity of the cell nucleus on the nanocone region and that of the nuclei of the cells on the smooth silver surface are comparable. It is well known that metal enhanced fluorescence is distance dependent and the fluorescence is enhanced only when the fluorophore is in the vicinity of metal nanostructure at an optimal distance of about 5-30 nm [187, 198]. The red fluorescence near the immediate surface of the substrate is due to fluorophore staining solution out of the culture medium. However, the red fluorophore, which labels the cell membrane, is not discernable at all, above the substrate surface, except for the cell sitting on nanocone structure. The fluorescence enhancement away from the surface is further elucidated from the 3-D z-stack images of number of cells on smooth as well as nanopillar substrate (Fig. 9.2f). Due to overwhelming fluorescence enhancement further away from substrate surface, the fluorescent-labeled cell membrane can be seen only for the cell on the top of nanocone structure (Fig. 9.2e). The vertical cross-sectional cell images (Fig. 9.2f) at various z-position again confirmed that the strong cell membrane fluorescence enhancement on the nanocone substrate is extending up to the top position on the spheroidal cell, around 15 μm above the nanocone substrate.

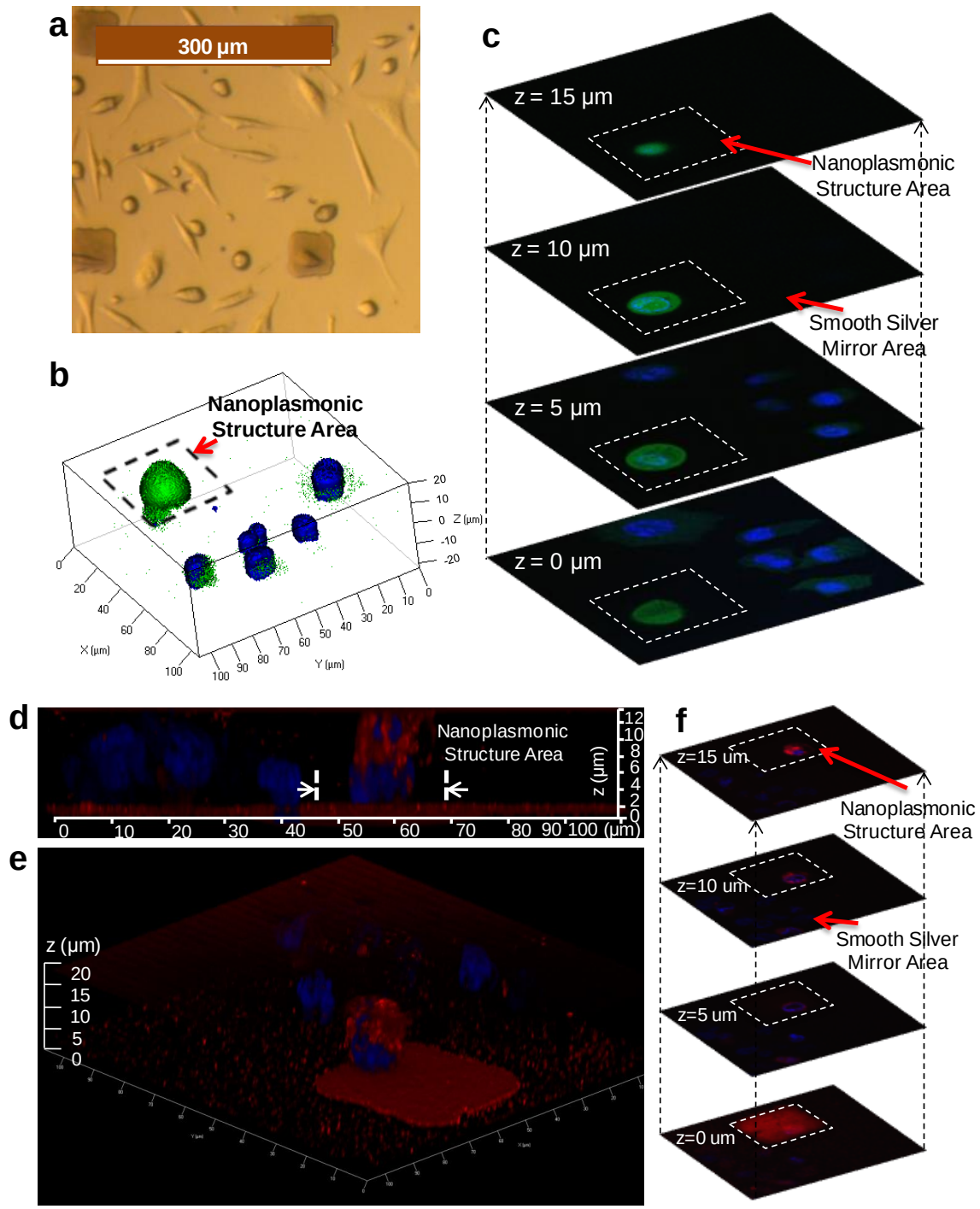

Figure 9.2: Confocal fluorescence microscopy imaging of live cells on the nanocone substrate (a) Bright field image of large number of cells grown on the substrate (b) 3-D confocal image of CHO cells on the nanocone plasmonic structure (c) Vertical cross-section of the cells at different z-position. z = 0 denotes on the surface of the substrate and z > 0 is away from the surface (d) Far-field fluorescence enhancement of the fluorophore labeled to the CHO cell membrane (e) 3-D confocal fluorescence image for the CHO cells when fluorophore is labeled to the cell membrane and nuclei of the cells (f) The vertical cross-section (z-stack) image for the cell showing that the cell membrane fluorescence enhancement.

Quantitative cell imaging analysis

The quantitative analysis for fluorescence enhancement factor is performed by comparing the average fluorescence intensity at each depth (z-coordinate) of the z-stack images taken by confocal fluorescence microscope. The average fluorescence intensities for the cell membrane, cytoplasm and nucleus are shown in Fig. 9.3. Increasing z distance denotes the imaging plane away from the substrate surface, that is, z = 0 is on the substrate. The actual height or thickness of the cell is around 12 μm or z = 12 μm. Since the membrane of the cells are about 7 nm thick [199], some of the fluorophore on the cell cytoskeletons that are attached to the nanocone substrate will experience the metal enhanced fluorescence (MEF). We observed 8 fold increases in fluorescence intensity of the membrane of the cell on the nanocone substrate as compared to silver-coated smooth surface (Fig. 9.3a). Interestingly, this is similar to the amount of enhancement measured by fluorescence spectroscopy experiment for a red fluorescing dye R6G [Chapter 4, Fig. 4.5d]. The enhancement factor was calculated as [186, 188, 200]

$$EF = \frac{I_M - I_{MB}}{I_G - I_{GB}}$$

Here, I_M and I_{MB} are the fluorescence intensities of cells measured on the nanocone/flat silver surfaces and the background intensity when cell is absent, respectively. I_G and I_{GB} are the fluorescence intensity of the cell on glass slide and background intensity, respectively. On the cell membrane at z = 6 μm, we observed a 23 fold fluorescence intensity increase on the nanocone substrate compared to that on the silver-coated smooth surface. Given that the silver-coated smooth surface can provide approximately 5-fold fluorescence enhancement (Fig. 4.5d), the total fluorescence enhancement factor for the cell membrane obtained by the fluorescence enhancing platform will be 115 folds with respect to a glass slide surface. The calculated enhancement factor is much higher than the conventional metal enhanced fluorescence in near field, that is, approximately 40 folds with respect to a glass slide surface according to our spectroscopic measurement (Fig. 4.5d). Even by comparing the maximum fluorescence intensity measured on the silver-coated smooth surface (at z = 0 μm) and that on the nanocone substrate (at z = 7 μm), there is still a 14-fold increase on the nanocone substrate. Most interestingly, the

maximum fluorescence enhancement on the silver-coated nanocone structure is found at an imaging plane far from the surface (z = 6~8 μm), which cannot be explained by conventional metal-enhanced fluorescence mechanisms. One of the reasons for the intensity peaking at the 6 μm position is due to the morphology of the cell (spherical) on the nanocone substrate as compared to elongated cells on the smooth surface. As we are calculating the average integrated intensity in each plane, the mid plane of the cell (around z = 6 μm) has more number of fluorophores and hence higher intensity as compared to the bottom of the cell. However, the overall higher intensity away from the surface of the nanocone substrate is still need to be explained.

Similar intensity enhancement is observed for fluorophores labeled to the cell cytoplasm on the nanopillar plasmonic structure as compared to the cells on the silver-coated smooth surface (Fig. 9.3c). The fluorescence enhancement observed is higher for fluorophore labeled on cell membrane (115 times), than when fluorophore labeled to cytoplasm calcium (approximately 70 folds). As shown in Fig. 9.3b and Fig. 9.3d, the peak fluorescence intensity for the nucleus of the cell near the smooth surface is slightly higher than that of the cell nucleus on the nanocone structure. However, the fluorescence intensity of the fluorophore labeled to the nucleus on the nanocone structure is higher than the cells on the smooth surface further away from substrate plane. To illustrate our point more clearly, cells on two control samples (glass and smooth silicon substrate) and nanocone structure are imaged using the same imaging parameters set up (laser power of 0.48 mW, pixel dwell time of 2.55 μs). As shown in Fig. 9.3e-g, the higher fluorescence intensity for the cells on nanocone structure can be clearly seen. In fact with this higher power and long integration time setting the cell image intensity on nanocone structure becomes saturated due to the extremely high enhancement. In order to exclude the possibility of cell fluorescence increase due to mechanical stimulation of nanocone structure, we carry out confocal image of CHO cell on silicon nanocone control sample without any silver coating. Figure 9.4b shows both the fluorophore channels: fluorophore labeled to the cytoplasm of the cell and fluorophore labeled to the nucleus of the cell. Clearly, the fluorescence intensity of the cells on uncoated nanocone substrate and on uncoated smooth surface is quite similar.

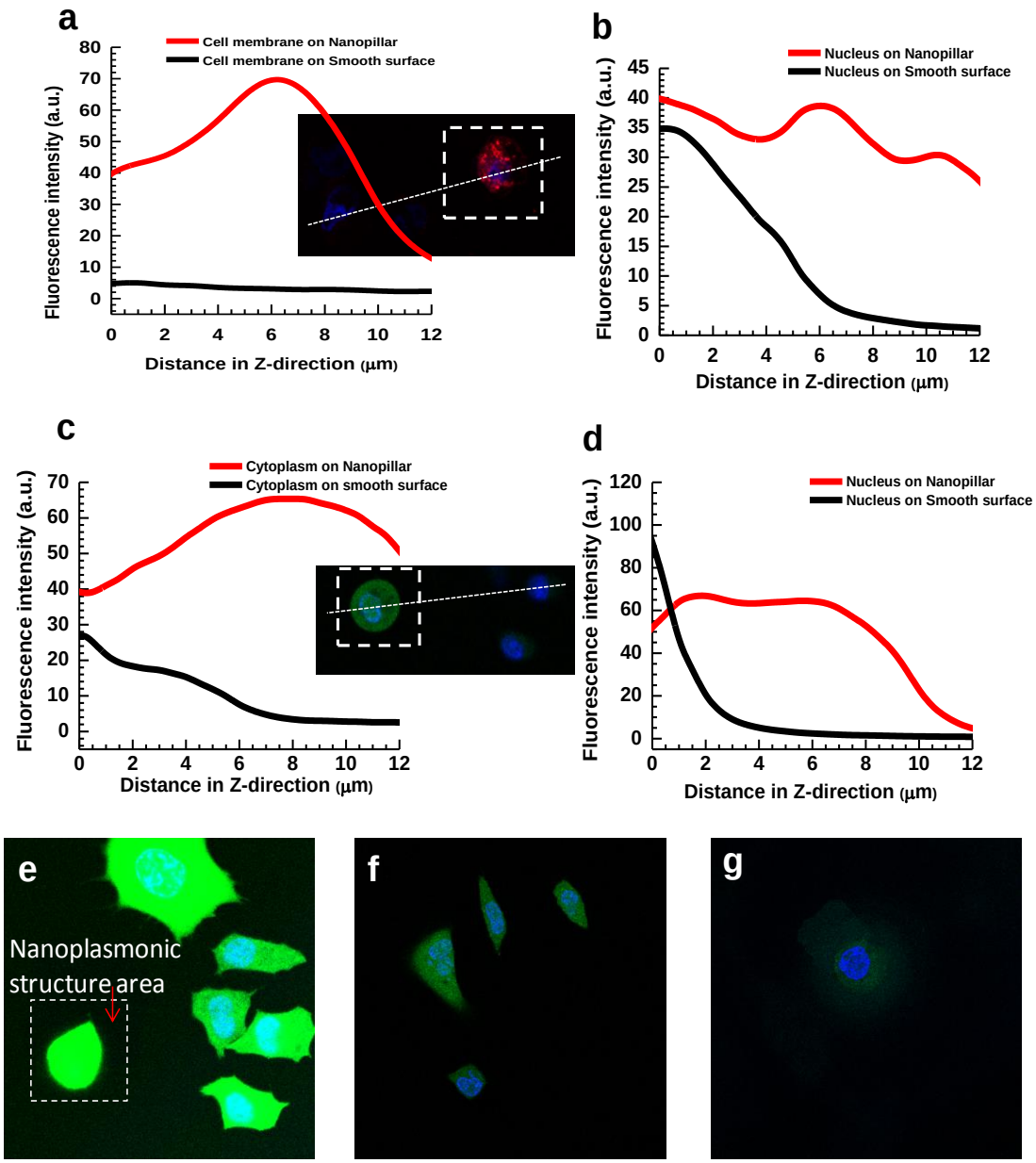

Figure 9.3: Quantitative analysis of fluorescence enhancement in confocal cell imaging (a) Comparison of the average fluorescence intensity of the membrane of the cells on the silver-coated nanocone structure and on the silver-coated smooth surface. (b) Comparison of average fluorescence intensity of the nucleus of the cells on the silver-coated nanocone structure and on the silver-coated smooth metal surface. (c) Comparison of average fluorescence intensity of the fluorophore attached to the cytoplasm of the cells when it is on the silver-coated nanocone structure and on the silver-coated smooth surface. (d) Comparison of average fluorescence intensity of the nucleus of the cells on the silver-coated nanocone structure and on the silver-coated smooth surface for the case when the cytoplasm of the cell is also labeled. Confocal cell imaging with identical laser power setting (0.48 mW) and pixel dwell time (2.55 μs) for cells on (e) silver-coated nanocone substrate (f) silver-coated smooth substrate and (g) glass substrate.

Mechanism for fluorescence enhancement

We believe light trapping is taking place inside the cell. In a device (cell) "light trapping" will happen if the optical path length is several times the actual device (cell) thickness. Here the optical path length of a device is defined as the distance that an unabsorbed photon may travel within the device before it escapes out of the device. Light trapping is usually achieved by changing the angle at which light travels in the cell making the light to enter the cell at critical angles. A textured surface will not only reduce reflection as previously described but will also couple light obliquely into the cell, thus giving a longer optical path length. Due to multiple random reflection, light can be trapped inside the cell and make multiple passes through the cell, thus allowing higher fluorescence intensity. Local variations in refractive index are the basic physical cause for light scattering in optical media. The average refractive index of living cells depends mostly on the protein concentration. A typical mammalian cell has an average protein content of 18 percent mass [201], corresponding to a refractive index of about 1.37. The main components of cell membranes are phospholipids, cholesterol and membrane-spanning proteins and usually have a higher refractive index than the proteins in the cytoplasm. The refractive index of membranes is about 1.48 [202]. This difference in refractive index between cytoplasm and membranes will have an impact on the light scattering properties inside the cells. Differences in refractive index influence the phase of the propagating light waves [203]. As shown in Figure 9.4a, c part of incident light (I_0) is reflected (I_r) and remainder is refracted/ transmitted (I_t) at the interface. As the transmitted light (I_t) encounter another interface, it will undergo partial reflection (I_{tr}) and partial transmission (I_{tt}) and so on. Since, these lights are components of the same wave, they will have the same frequency, but can have different phases [204]. Constructive interference of the reflected light wave can give rise to higher intensity. But how does the light enters the cell? The evanescent electric field is generated at the optical frequency due to propagating surface plasmon at the tip of the nanocone. The evanescent field penetrates the cell with an exponentially decaying intensity, that falls by a factor, (1/e), just 100 nm from the interface [205]. This light undergoes multiple reflections inside the cell due to difference in refractive index inside the cell. Cell membrane is having higher refractive index than outside buffer solution. There is also a possibility of total internal reflection inside the cell when light is

traveling from a high- to a low-refractive-index medium. For example, with membrane RI of 1.48 and PBS buffer RI of 1.334 [206], critical angle for total internal reflection to occur is 64.3363^{o}. Hence we argue that strong scattering occurs within nanostructured area (evidenced by strong SERS signal), and due to random reflection inside the cell resulted in the observed enhancement in fluorescence further away from the substrate surface.

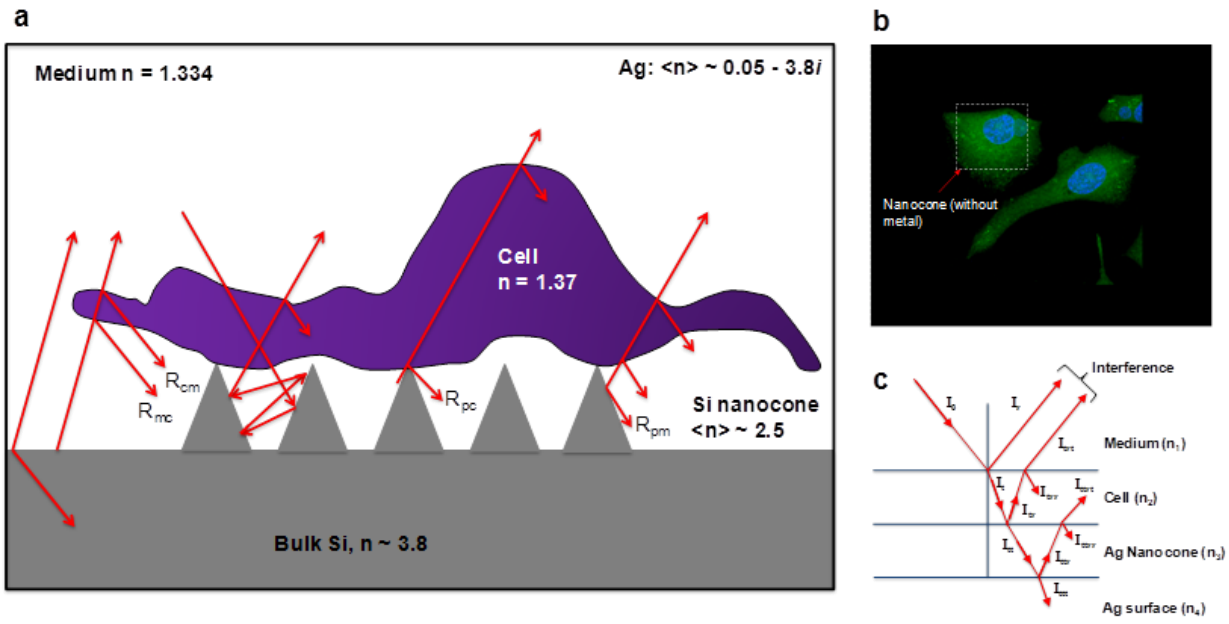

Figure 9.4: (a, c) Multiple reflections in a nanopillar-cell system. R_{cm}: reflection at cell-medium interface; R_{mc}: reflection at medium-cell interface; R_{pc}: reflection at pillar-cell interface; R_{pm}: reflection at pillar-medium interface; (b) Confocal image of CHO cells on uncoated nanocone substrate, showing similar levels of the fluorescence intensity of the cells on the nanocone region (boxed) and on smooth region.

Conclusions

Nanoplasmon surface composed of nanocone structures is a platform for three-dimensional fluorescence enhanced cell imaging with high sensitivity. We have demonstrated that the nanoplasmon surface can enhance the fluorescence signal from a cell membrane (FM 1-43 FX) by 115 folds and from a cell cytoplasm (Fluo-4, AM) by 70 folds. We anticipate that the nanocone surface can provide higher intensity for the dyes labeled to the cells and at the same

time less photobleaching on the dyes and hence will be an ideal candidate as microscopy substrates to observe very early stage protein expressions after transfection.

References

[1] J. W. Lichtman and J. A. Conchello, "Fluorescence microscopy," *Nat. Methods*, vol. 2, pp. 910-919, DEC, 2005.

[2] S. Inoue and R. Oldenbourg, "Microscopes," in *Handbook of Optics*, 2nd ed.Anonymous New York: McGraw-Hill, 1995, .

[3] E. Le Moal, E. Fort, S. Leveque-Fort, A. Janin, H. Murata, F. P. Cordelieres, M. Fontaine-Aupart and C. Ricolleau, "Mirror slides for high-sensitivity cell and tissue fluorescence imaging," *J. Biomed. Opt.*, vol. 12, pp. 024030, MAR-APR, 2007.

[4] E. Le Moal, S. Lévêque-Fort, E. Fort, J. P. Lacharme, M. P. Fontaine-Aupart and C. Ricolleau, "Active substrates improving sensitivity in biomedical fluorescence microscop," in *Confocal, Multiphoton, and Nonlinear Microscopic Imaging II, Proc. SPIE*, Munich, Germany, 2005, .

[5] E. Le Moal, E. Fort, S. Leveque-Fort, F. P. Cordelieres, M. -. Fontaine-Aupart and C. Ricolleau, "Enhanced fluorescence cell imaging with metal-coated slides," *Biophys. J.*, vol. 92, pp. 2150-2161, MAR 15, 2007.

[6] M. Moskovits, "Surface-Enhanced Spectroscopy," *Rev. Mod. Phys.*, vol. 57, pp. 783-826, 1985.

[7] C. D. Geddes and J. R. Lakowicz, "Metal-enhanced fluorescence," *J. Fluoresc.*, vol. 12, pp. 121-129, JUN, 2002.

[8] K. Aslan, I. Gryczynski, J. Malicka, E. Matveeva, J. R. Lakowicz and C. D. Geddes, "Metal-enhanced fluorescence: an emerging tool in biotechnology," *Curr. Opin. Biotechnol.*, vol. 16, pp. 55-62, 2, 2005.

[9] P. P. Pompa, L. Martiradonna, A. Della Torre, F. Della Sala, L. Manna, M. De Vittorio, F. Calabi, R. Cingolani and R. Rinaldi, "Metal-enhanced fluorescence of colloidal nanocrystals with nanoscale control," *Nature Nanotechnology*, vol. 1, pp. 126-130, NOV, 2006.

[10] X. Cui, K. Tawa, K. Kintaka and J. Nishii, "Enhanced Fluorescence Microscopic Imaging by Plasmonic Nanostructures: From a 1D Grating to a 2D Nanohole Array," *Advanced Functional Materials*, vol. 20, pp. 945-950, MAR 24, 2010.

[11] K. Lee, L. D. Hahn, W. W. Yuen, H. Vlamakis, R. Kolter and D. J. Moone, "Metal-Enhanced Fluorescence to Quantify Bacterial Adhesion," *Advanced Materials,* vol. 23, pp. 101, 2011.

[12] X. Cui, K. Tawa, H. Hori and J. Nishii, "Tailored Plasmonic Gratings for Enhanced Fluorescence Detection and Microscopic Imaging," *Advanced Functional Materials,* vol. 20, pp. 546-553, FEB 22, 2010.

[13] J. R. Lakowicz, "Radiative decay engineering 5: metal-enhanced fluorescence and plasmon emission," *Anal. Biochem.,* vol. 337, pp. 171-194, FEB 15, 2005.

[14] K. Balaa, E. Fort and Nikon Instruments, "Surface Plasmon Enhanced TIRF Imaging," *Imaging & Microscopy,* vol. 11, pp. 55-56, 2009.

[15] K. A. Willets and R. P. Van Duyne, "Localized surface plasmon resonance spectroscopy and sensing," *Annu. Rev. Phys. Chem.,* vol. 58, pp. 267-297, 2007.

[16] W. Knoll, "Interfaces and thin films as seen by bound electromagnetic waves," *Annu. Rev. Phys. Chem.,* vol. 49, pp. 569-638, 1998.

[17] H. Raether, "Surface-Plasmons on Smooth and Rough Surfaces and on Gratings," *Springer Tracts Mod. Phys.,* vol. 111, pp. 1-133, 1988.

[18] E. Popov, N. Bonod and S. Enoch, "Comparison of plasmon surface waves on shallow and deep metallic 1D and 2D gratings," *Optics Express,* vol. 15, pp. 4224-4237, APR 2, 2007.

[19] M. R. Gartia, Z. Xu, E. Behymer, H. Nguyen, J. A. Britten, C. Larson, R. Miles, M. Bora, A. S. Chang, T. C. Bond and G. L. Liu, "Rigorous surface enhanced Raman spectral characterization of large-area high-uniformity silver-coated tapered silica nanopillar arrays," *Nanotechnology,* vol. 21, pp. 395701, OCT 1, 2010.

[20] K. Arya, Z. B. Su and J. L. Birman, "Localization of the Surface-Plasmon Polariton Caused by Random Roughness and its Role in Surface-Enhanced Optical Phenomena," *Phys. Rev. Lett.,* vol. 54, pp. 1559-1562, 1985, 1985.

[21] M. I. Stockman, "Nanofocusing of optical energy in tapered plasmonic waveguides," *Phys. Rev. Lett.,* vol. 93, pp. 137404, SEP 24, 2004.

[22] K. R. Gee, K. A. Brown, W. N. U. Chen, J. Bishop-Stewart, D. Gray and I. Johnson, "Chemical and physiological characterization of fluo-4 Ca2+-indicator dyes," *Cell Calcium,* vol. 27, pp. 97-106, FEB 2000, 2000.

[23] H. Mertens, A. F. Koenderink and A. Polman, "Plasmon-enhanced luminescence near noble-metal nanospheres: Comparison of exact theory and an improved Gersten and Nitzan model," *Physical Review B,* vol. 76, pp. 115123, SEP, 2007.

[24] B. Alberts, A. Johnson, J. Lewis, M. Raff, K. Roberts and P. Walter, *Molecular Biology of the Cell*, 5th ed.Anonymous New York: Garland Science, 2007, .

[25] S. Guo, J. J. Heetderks, H. Kan and R. J. Phaneuf, "Enhanced fluorescence and near-field intensity for Ag nanowire/nanocolumn arrays: evidence for the role of surface plasmon standing waves," *Optics Express*, vol. 16, pp. 18417-18425, OCT 27, 2008.

[26] B. Alberts, D. Bray, J. Lewis, M. Raff, K. Roberts and J. D. Watson, "Macromolecules: Structure, shape, and information," in *Molecular Biology of the Cell*Anonymous New York: Garland Science, 1994, pp. 89-138.

[27] J. Beuthan, O. Minet, J. Helfmann, M. Herrig and G. Muller, "The spatial variation of the refractive index in biological cells," *Phys. Med. Biol.*, vol. 41, pp. 369-382, MAR, 1996.

[28] R. Michael, J. van Marle, G. F. J. M. Vrensen and T. J. T. P. van den Berg, "Changes in the refractive index of lens fibre membranes during maturation - impact on lens transparency," *Exp. Eye Res.*, vol. 77, pp. 93-99, JUL, 2003.

[29] I. Cornelesetenvelde, J. Bonnet, H. J. Tanke and J. S. Ploem, "Reflection Contrast Microscopy - Visualization of (Peroxidase-Generated) Diaminobenzidine Polymer Products and its Underlying Optical Phenomena," *Histochemistry*, vol. 89, pp. 141-150, 1988, 1988.

[30] G. I. Mashanov, D. Tacon, A. E. Knight, M. Peckham and J. E. Molloy, "Visualizing single molecules inside living cells using total internal reflection fluorescence microscopy," *Methods*, vol. 29, pp. 142-152, FEB, 2003.

[31] F. C. Chien and S. J. Chen, "Direct determination of the refractive index and thickness of a biolayer based on coupled waveguide-surface plasmon resonance mode," *Opt. Lett.*, vol. 31, pp. 187-189, JAN 15, 2006.

CHAPTER 10

COLORIMETRIC PLASMON RESONANCE IMAGING USING NANO LYCURGUS CUP ARRAYS

Introduction

Label-free techniques are important because they can provide direct information about molecular binding events due to addition or depletion of mass at the sensor surface, manifested in a change of bulk physical property. In spite of undisputed advantages over label- and reporter based technologies, label-free technologies have not gained entry in to everyday lab use mainly due to technical requirements, cost, low throughput, and need for high user expertise. In recent years, colorimetric based sensors have emerged as a leading tool to find it place from lab bench-top-to-home turf (such as simple pH strip to complex glucose and pregnancy immunoassay strips). Colorimetric techniques are mainly attractive because of their low cost, use of inexpensive equipment, use of fewer signal transduction hardware, and above all, providing simple-to-understand results. Colorimetric sensor can be used for both qualitative analyte identification as well as quantitative analysis. Here, in this chapter we present a colorimetric sensor based on nanohole plasmonic substrate, which we call "nano Lycurgus cup array" or in short "nanoLCA".

Background

Lycurgus cup [207] created by ancient Romans 2000 years ago can appear different colors depending on the direction of light illumination in which it is viewed due to metal nanoparticle optical scattering. It has inspired nanoplasmonics research over the past decade [208-217]. Here we present a nanoscale Lycurgus cup arrays (nanoLCA) device that has the property of appearing green when light is shone on to it and changing the color to red without direct light illumination (see supplementary movie). The above colorimetric device fabricated on

transparent plastic substrate consists of about one billion nano Lycurgus cups in an array with subwavelength opening and decorated with metal nanoparticles on side walls. Strikingly different from metallic nanohole arrays [218] or quasi-3D plasmonic crystals [85] with extraordinary optical transmission which usually give rise to multiple transmission spectral features, nanoLCA exhibits metal nanoparticle-like single transmission wavelength peak in the whole visible ranges. Electromagnetic simulation revealed the plasmon resonance scattering modes of the metal nanoparticles on the cup side walls and the corresponding single peak wavelength scattering light selectively transmitted by the nanoLCA. The huge transmission and reflection wavelength shifts upon binding of molecules on our flexible, high-throughput, large area nanoLCA device are up to 200 nm (with maximum sensitivity of 46000 nm per refractive-index unit (RIU) and figure of merit (FOM) of 1022), much greater than the typical nanoparticle plasmon resonance wavelength shift and large enough to detect the color differences directly by naked eyes and conventional bright field microscopes. This enables to eliminate the need for precision spectrometer or fluorescence labeling. We demonstrated the ultrasensitive label free colorimetric plasmon resonance imaging of different refractive indices solutions, single and double stranded oligonucleotides and antigen-antibody protein interactions on our nanoLCA device.

Existing technology

With the advancement of nanoscale fabrication, label-free sensors such as photonic crystal [219], whispering gallery mode (WGM) [220] and surface plasmon resonance (SPR) [214] based devices are increasingly being used for detecting DNA bases, recognizing antigen-antibody, probing protein interaction, immunoassays and identifying pathogen. Most of the above sensors work on the principle of shift in the resonance wavelength after conjugation of biomolecules to the surface of the sensor. However, the resonance peak wavelength shift (PWS) for most of the current sensors is of the order of few nanometers only [220, 221] (although SPR has much higher sensitivity of 2×10^6 nm per RIU [222] for bulk refractive index, the absolute change in wavelength is extremely minimal for commercial SPR sensor in Kretschmann configuration) [222, 223]. Hence, the identification of the unknown analyte (or concentration of a known analyte) requires specialized instrument such as high precision spectrometer,

multiplexer for sweeping the laser wavelengths, WGM trap, complex optical system to generate SPR (for example, prism, accurate angle tuning for the optical beam) etc. Localized surface plasmon resonance (LSPR) sensors [214], based on colloidal plasmonic particles (silver, gold), overcome some of the above limitations. However, the sensitivity of LSPR based sensors are at least an order of magnitude less compared to the gold standard prism coupled SPR sensors (Kretschmann configuration) [224]. In LSPR configuration, the scattering spectra of the plasmonic particles shift to a different wavelength (usually to a longer wavelength) after conjugation to specific analytes. However, the colloid particle sizes and positions are random and difficult to control over a large area. Thus, in the same sample area, different particles give rise to different scattering spectra and hence, for the same analyte the shifts in the wavelength are different [214]. In addition, a high precision spectrometer is required to record the spectra and then complex image analysis is required to extract usable data. Although related to the field of plasmonics, label free sensor such as surface enhanced Raman spectroscopy (SERS) based techniques are not discussed here.

Another method to get high sensitivity plasmonic resonance is to make sub-wavelength holes in optically thick metal surfaces. This is also commonly known as extraordinary optical transmission (EOT) substrates [218, 225]. The fabrication of such substrates relies on expensive, time consuming and low throughput electron beam lithography and focused ion beam milling. Also, due to presence of single layer of metal surface, usually the nonradiative Drude (ohmic) damping losses are high, leading to damping of resonance with analytes on the top of the metal surface [226]. In addition, EOT substrates generally show multiple transmission peaks in the visible range, making it difficult for true colorimetric sensing modalities [218]. Quasi 3-D plasmonic crystals [85] offer a way to increase the sensitivity by employing multiple layers of metal surfaces on nanohole surface. But mostly the resonance of such device has been demonstrated in near infrared and far infrared wavelength. Also, after adsorption of analyte, no shift (or minimal shift) in the resonance was observed. Most of the analyte detection or quantification was done from the change in the infrared transmission intensities.

In contrast, we employ a nanoimprint method to produce nanoLCA substrate on plastic substrate to reduce cost and simplify the fabrication process. Metal (Ag or Au) was deposited on the nanoLCA by electron beam evaporation, producing metal surface on the rim of the holes, on the bottom of the holes and also nanoparticles-like structure on the sidewalls of the holes. Due to selective transmission of the scattering spectra from the nanoparticles, our device is characterized by single transmission spectral peak in the entire visible wavelength, giving rise to the Lycurgus cup effects (see supplementary movie). Due to unprecedented high sensitivity (about 46000 nm per RIU), nanoLCA device is very sensitive in detecting small changes in refractive index of the analyte and gives rise to a huge shift in the resonance wavelength which is even detectable by naked eyes and normal bright field (BF) microscopy making it a true colorimetric sensor.

Details of the nanoLCA

The detailed fabrication steps of the nanoLCA device are given in Chapter 2. Figure 10.1 depicts the schematic of the nanoLCA structure. As shown in the inset, it consists of nanofunnel shaped cup structure decorated with multiple nanoparticles along the side walls. The master nanocone pattern is first fabricated on a glass substrate using laser interference lithography technique [36, 227] with a range of different heights (h = 250, 500 and 1000 nm). We successfully transferred the two-dimensional square lattice of nanoLCA (pitch, p = 350 nm) to a flexible and optically transparent polyethylene terephthalate (PET) film using nanoreplica molding process. In order to make the structure surface plasmon active, we deposited different thickness, t, of silver metal layer (t = 40, 60, 70, 80, 90, 100 and 120 nm). The detailed optical characterizations are presented in Chapter 4.

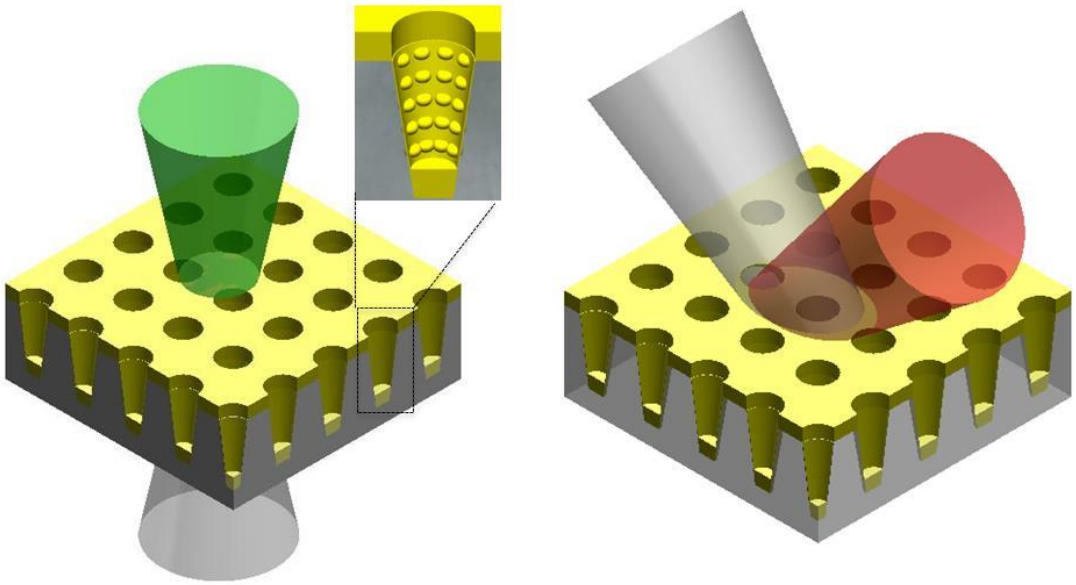

Figure 10.1: Schematic of the nanoLCA.

In order to demonstrate the apparent analogy to Lycurgus cup, Figure 10.2 shows optical image of the fabricated nanoLCA structure coated with metal (t = 90 nm) with (left) and without (right) direct illumination of white light, respectively.

Figure 10.2: The Lycurgus cup in British Museum dated back to fourth century AD. Due to scattering of nanoparticles on sidewall (5-60 nm in diameter), the cup appears green in reflected light and appears red in transmission light. Optical micrograph of nanoLCA taken using a camera under direct illumination (green) and without illumination (red) of Xenon lamp flashlight.

Chemical imaging on nanoLCA sensor

Due to strong interaction between surface plasmon and molecules near metal surface, surface plasmon based sensor has been widely used to exploit the plasmon-molecule interaction [228]. One of such modalities is the refractive index sensing using surface plasmon for molecules that have no (or minimal) optical absorption or that has electronic absorption energies far away from the surface plasmon resonances. To illustrate the point, we have demonstrated the refractive index sensing using fourteen different chemicals with varying refractive indices (n = 1.333 – 1.56).

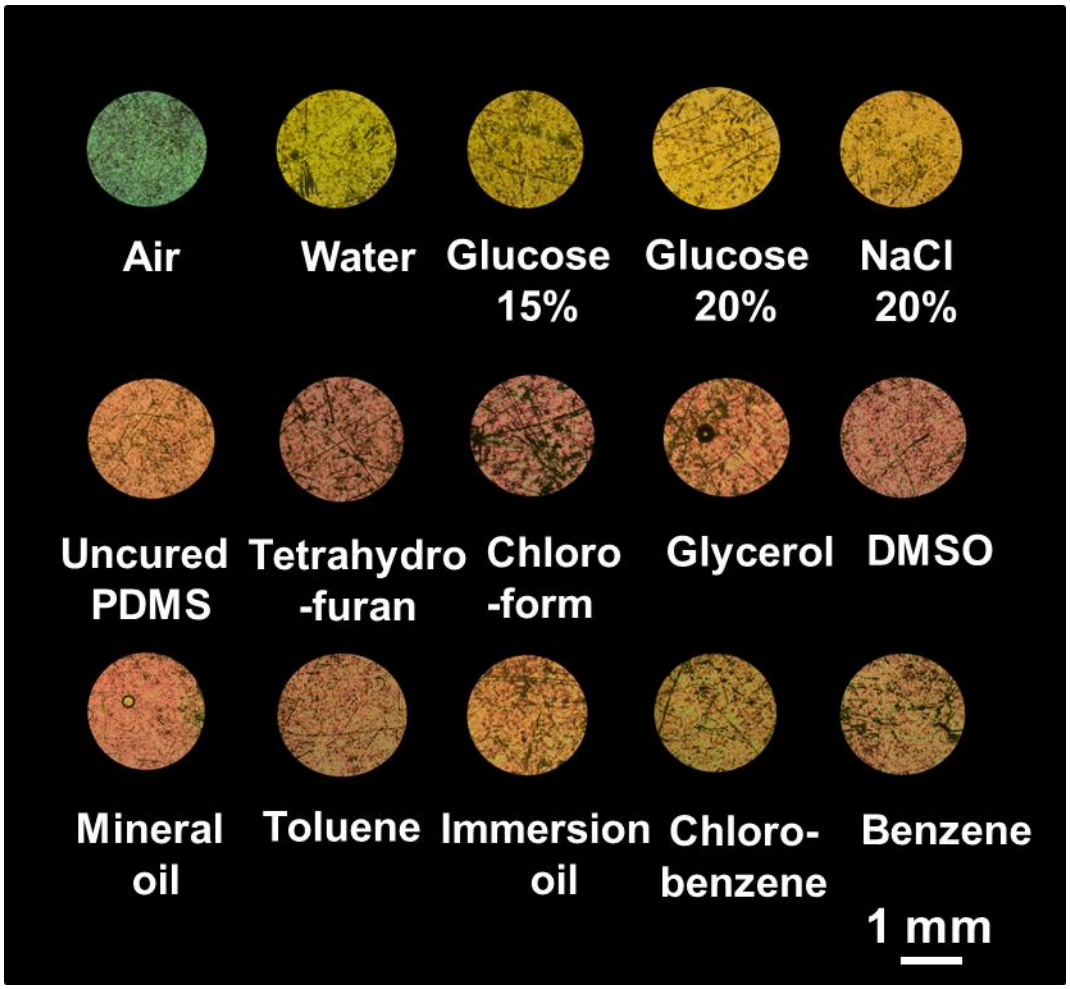

Figure 10.3: Transmission mode optical image of fourteen different chemicals with varying refractive indices on top of a nanoLCA device.

As shown in Figure 10.3 (transmission mode) and Figure 10.4 (reflection mode images), the transmitted light through the nanoLCA changed from light blue to green and to red with gradual increase in the refractive index. For example, the intensity of Red channel increased to 208 (Immersion oil, n =1.51) from 18 (Air, n=1). The reflection images also showed large shift in color (from red to light green) upon the gradual increase of refractive index. Since the surface plasmon resonance peak shift is large (~100 nm) after changing the refractive index environment of the superstrate, it is possible to distinguish the chemicals from the colorful transmission images.

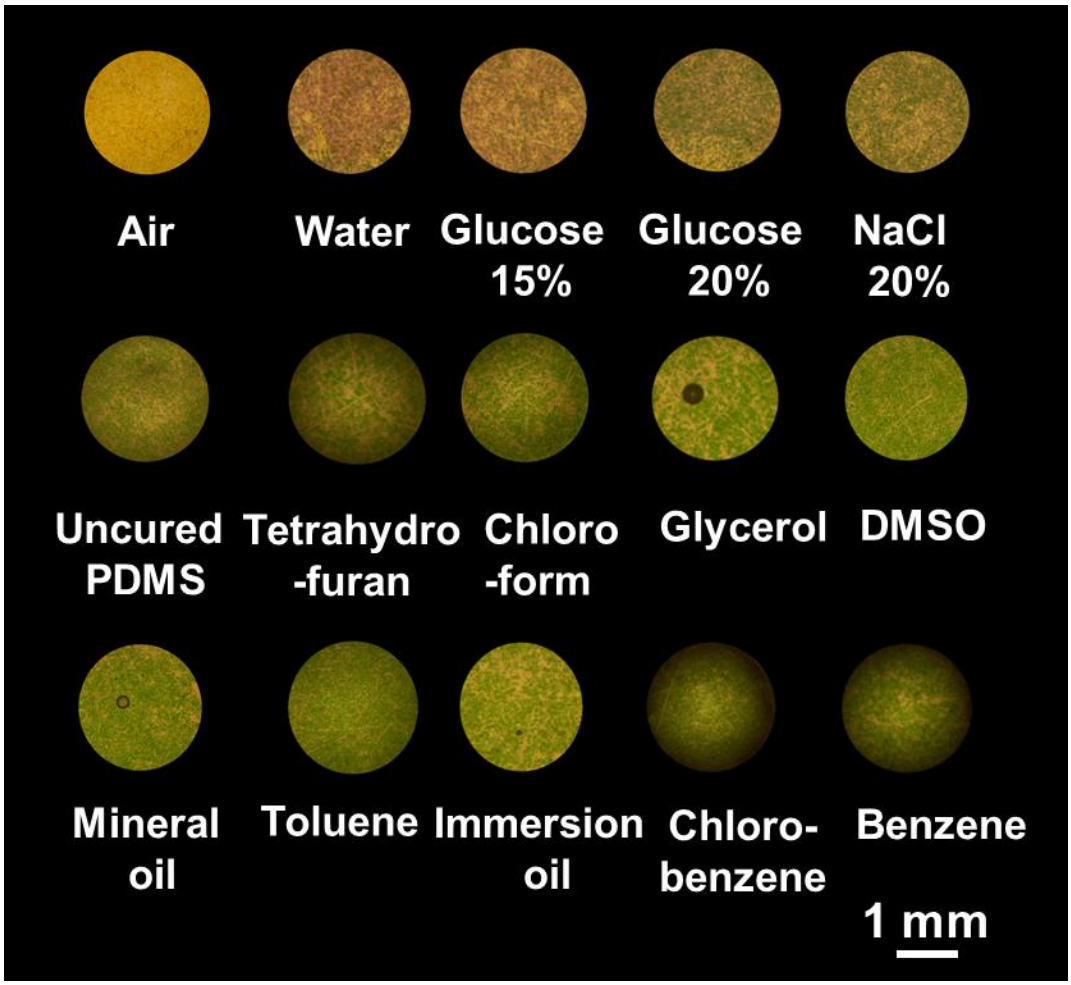

Figure 10.4: Reflection mode optical image of fourteen different chemicals with varying refractive indices on top of a nanoLCA device.

Chemical spectroscopy with nanoLCA sensor

NanoLCA transmission spectra were collected using Varian Cary 5G UV-Vis-NIR spectrophotometer (spectral bandwidth = 1 nm, data interval = 1 nm) with normal incidence transmission mode with different chemicals. Figure 10.5 shows the spectroscopic results of nanoLCA with h = 500 nm, p = 350 nm, and t = 90 nm. Transmission spectra obtained using

other height (h = 1000 nm) and chemicals (glycerol, glucose, NaCl) are reported in supplementary Fig. 10.6 – 10.9.

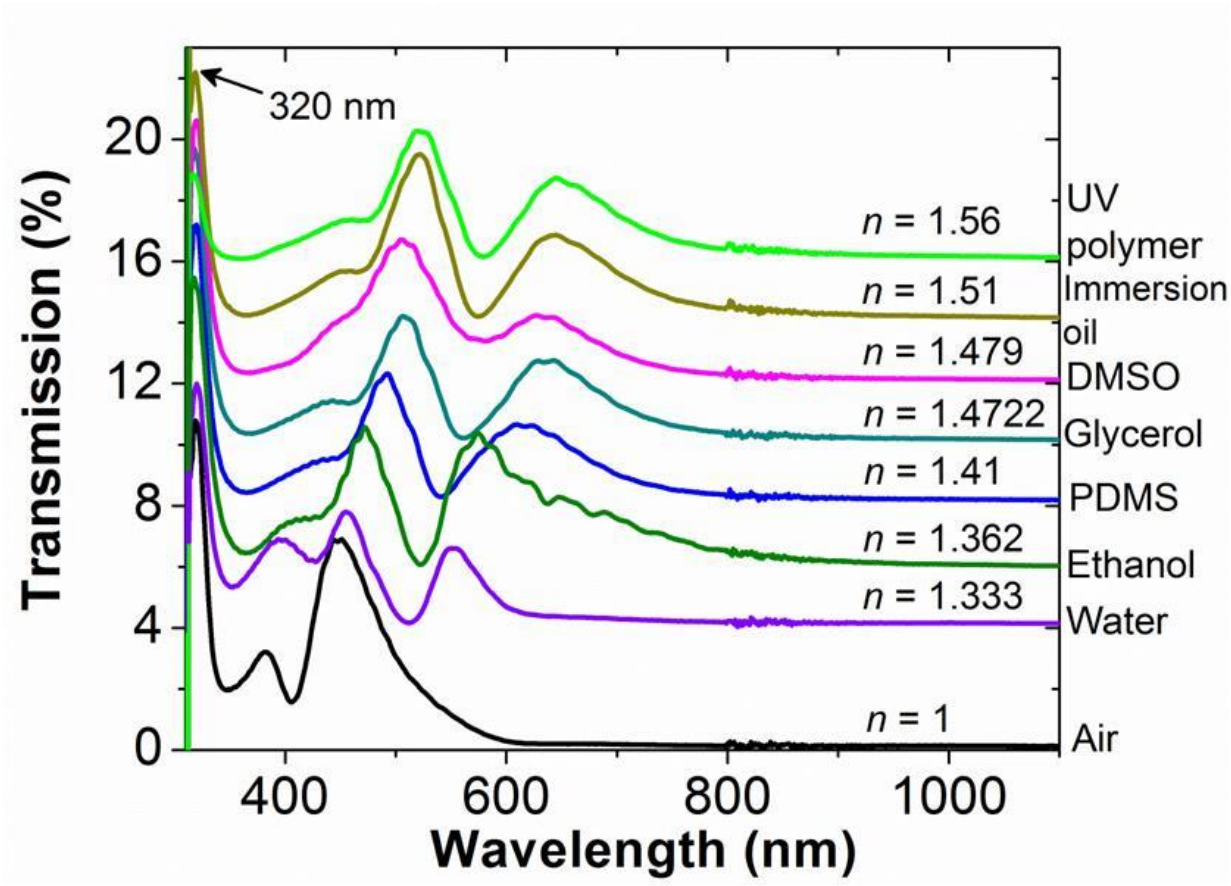

Figure 10.5: Transmission spectra of nanoLCA (h = 500 nm) with chemicals of varying refractive indices.

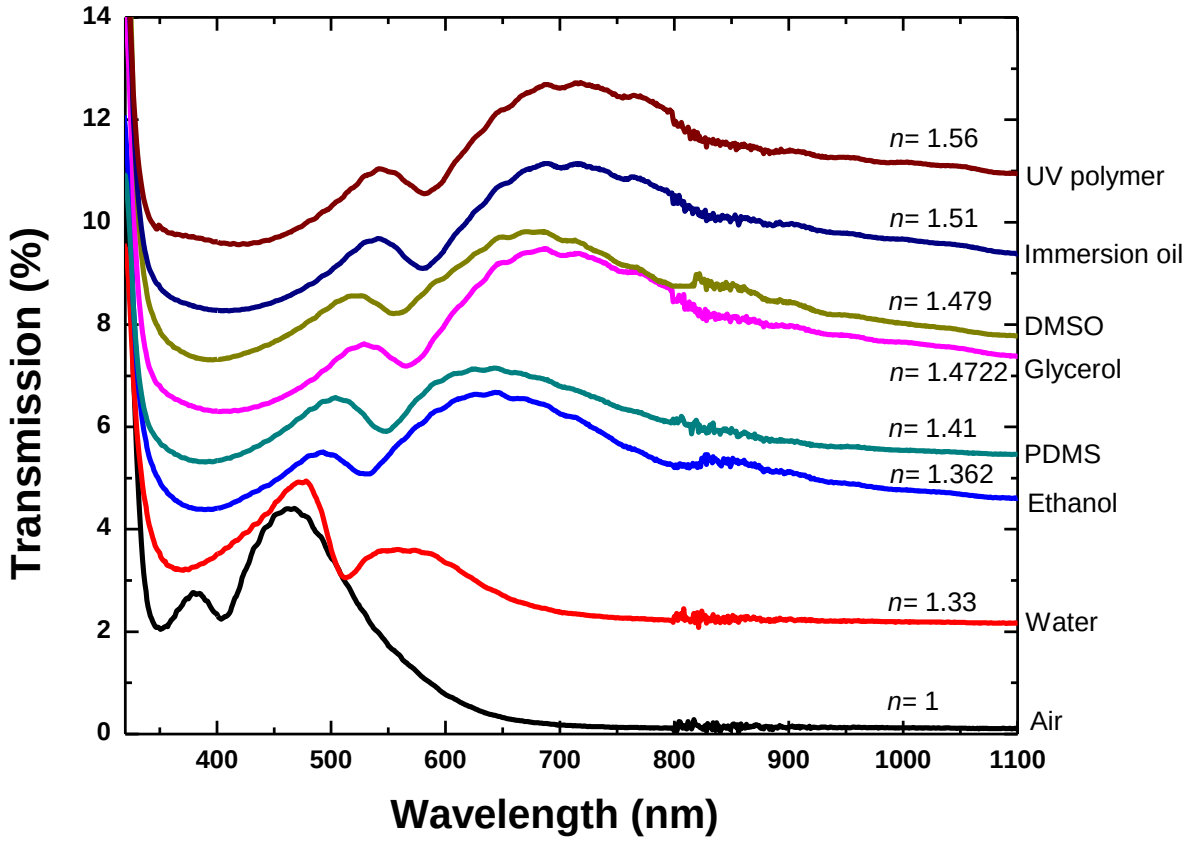

Figure 10.6: Transmission spectra of nanoLCA (h = 1000 nm) with chemicals of varying refractive indices.

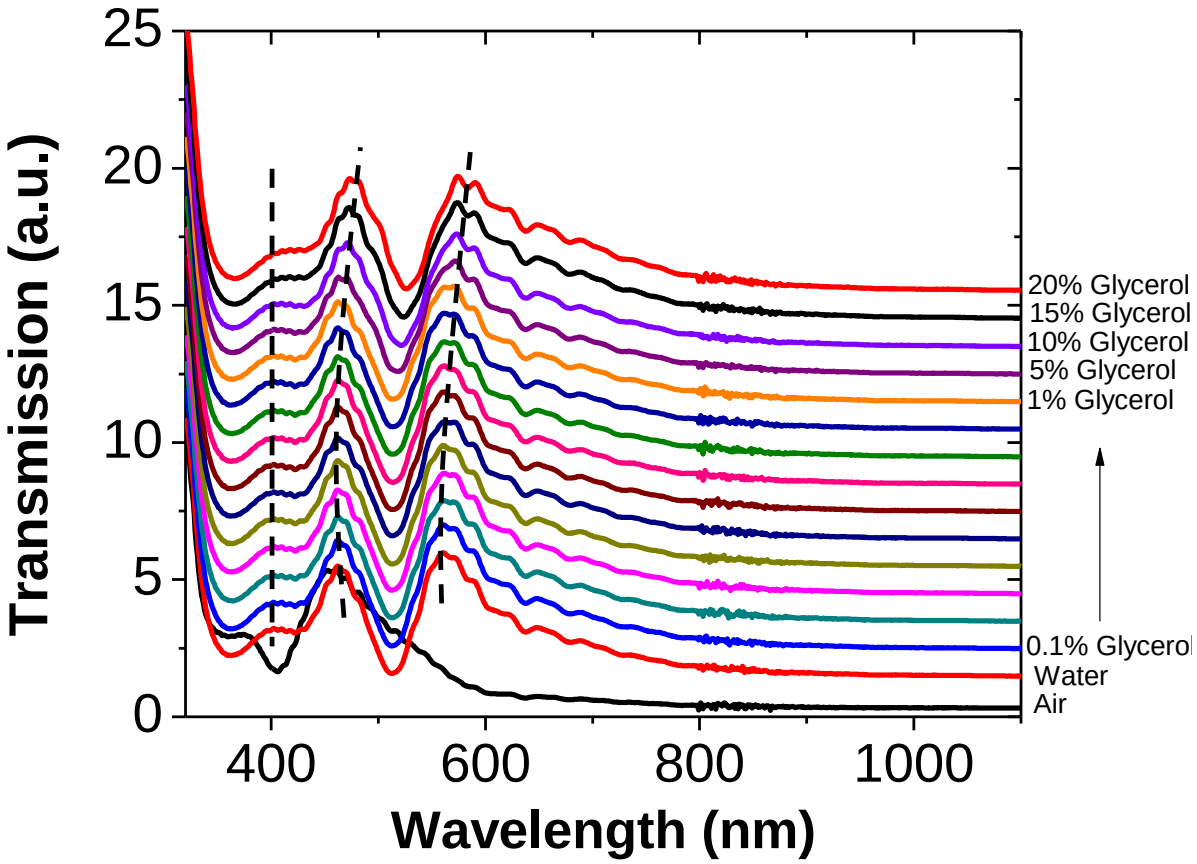

Figure 10.7: Transmission spectra of nanoLCA (*h* = 500 nm) with different concentration of Glycerol solution. The LSPR mode (~ λ = 560 nm) is red-shifted with increase of Glycerol concentration (0-20% by weight).

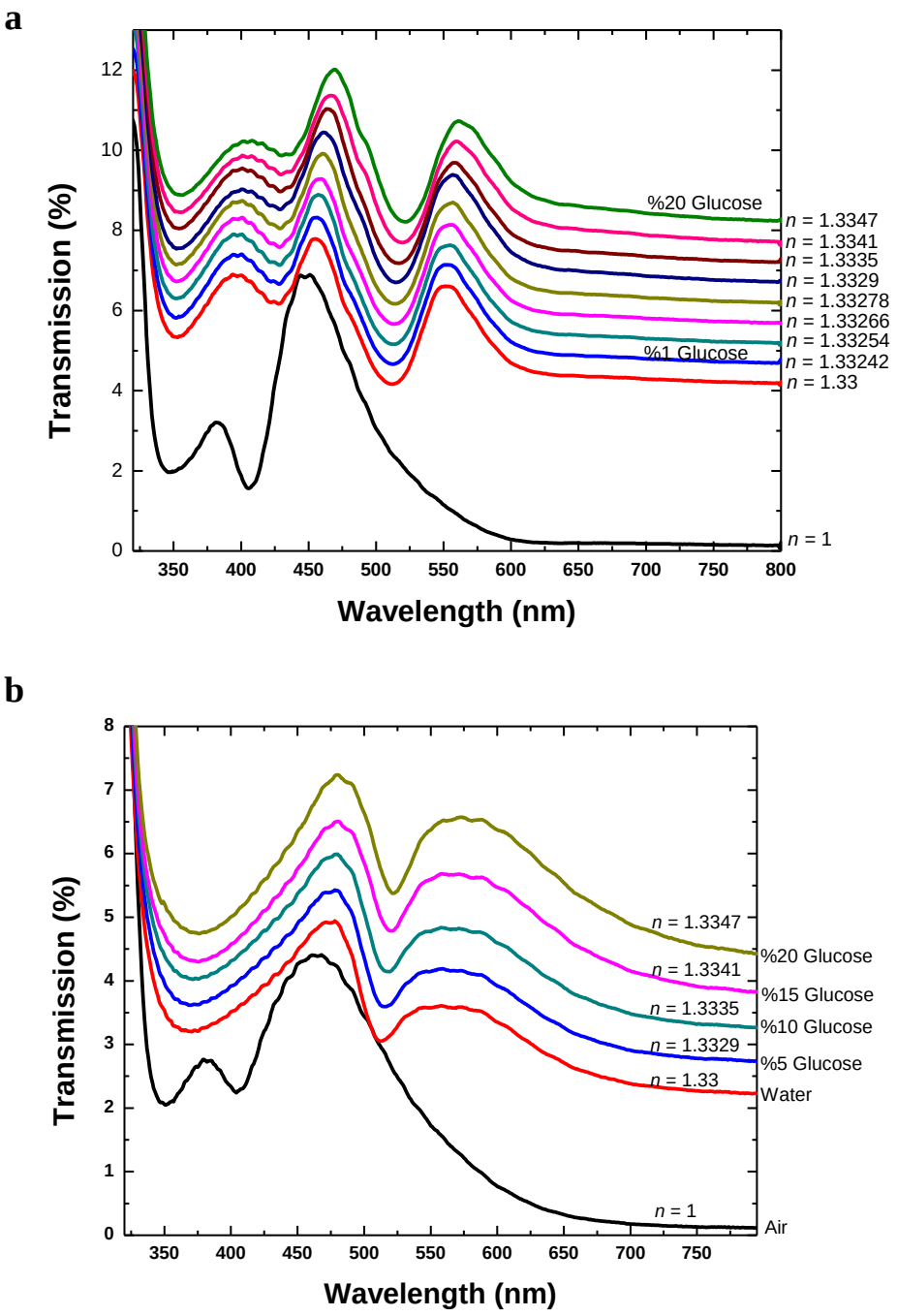

Figure 10.8: Transmission spectra of nanoLCA a. h = 500 nm b. h = 1000 nm with different concentration of Glucose solution. The corresponding refractive indices of Glucose solution is also shown.

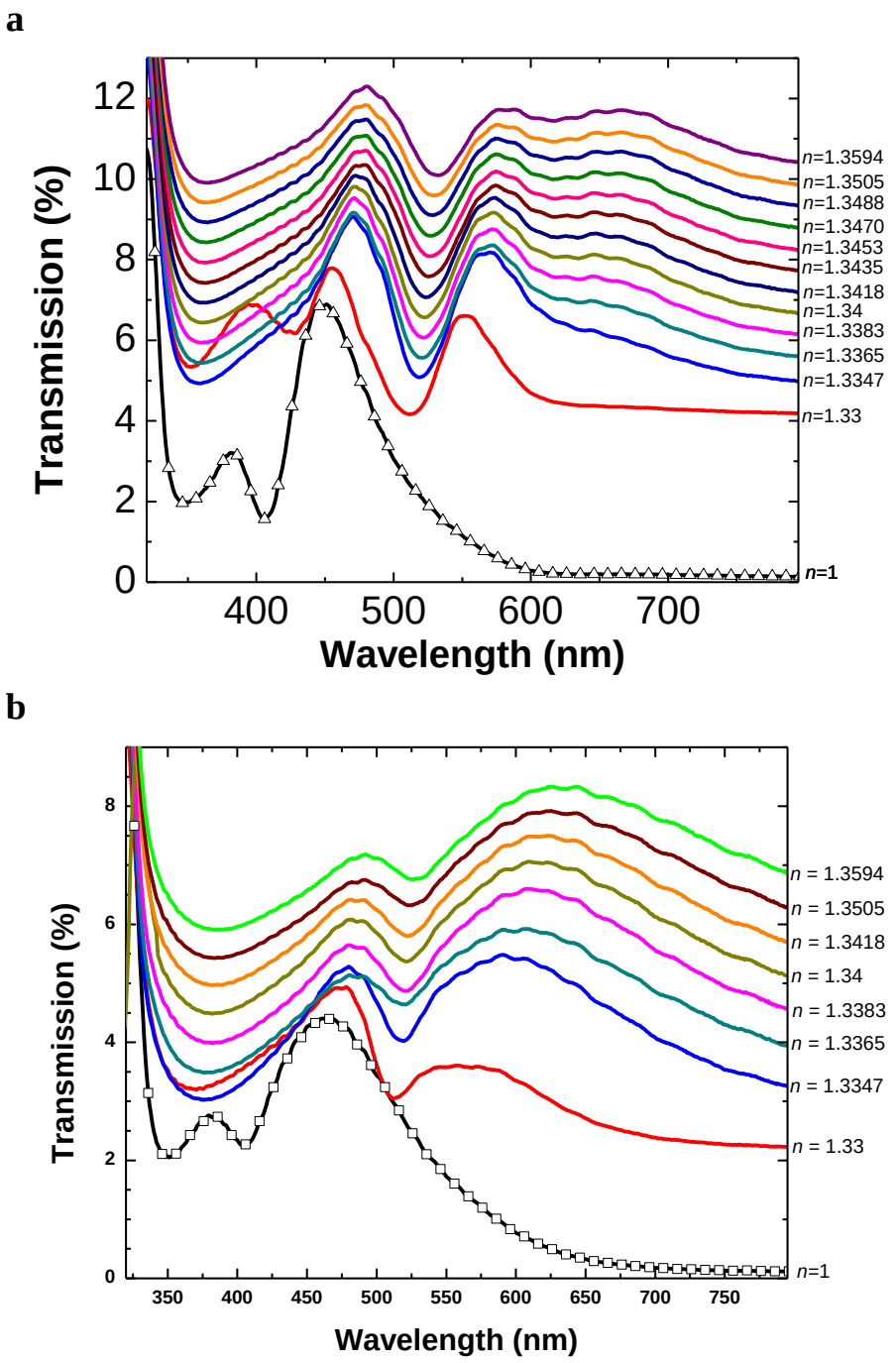

Figure 10.9: Transmission spectra of nanoLCA a. h = 500 nm b. h = 1000 nm with different concentration of NaCl solution.

Image analysis

The color images of the nanoLCA devices were captured using a transmission light microscope with 5x magnification (Olympus, Center Valley, PA, USA) with exposure time of 40 ms (gain=1; gamma=1). Each image is composed of three 8-bit channels of red, green, and blue, and therefore, each color image is 24-bit. For the calculation of mean intensity, an area of the 300 x 300 pixels (approximately 0.44 mm by 0.44 mm) was cropped from the original image to remove the boundary areas. The raw microscope images were splitted into three red, green, and blue (RGB) channels. The mean ($\mu = \sum_{i=1}^{N} x_i \Big/ N$), standard deviation ($\delta = \left(\frac{1}{N-1} \sum_{i=1}^{N} \left(x_i - \mu \right)^2 \right)^{1/2}$), and mode of the intensity of the cropped area for each component were determined by the built-in MATLAB R2011b functions (MathWorks, Natick, MA, USA).

Further, Earth's mover distance (EMD) algorithm was implemented to compute the flow that minimizes the overall ground distance between two signatures, S_A and S_B. Each signature, $S_x = \{(x_1, w_{x1}),...,(x_M, w_{xM})\}$, consists of m clusters with x_i, a cluster representative, and w_{xi}, the weight of the cluster. The distance, d_{ij}, is the vector norm (ground distance) between clusters a_i and b_j. For each RGB channel, the signature consists of the binned (N=100) intensity of the pixels in the cropped area and the weights of the bins, which were calculated as the number of pixels in the bin divided by the total number of pixels. In EMD calculation, the flow, f, between the clusters a_i and b_j, is calculated to minimize the overall work function:

$WORK\left(A, B, \mathbf{F}\right) = \sum_{i=1}^{M} \sum_{j=1}^{N} d_{ij} f_{ij}$. After the overall work function has been minimized, the EMD is calculated as: $EMD(A, B) = \sum_{i=1}^{M} \sum_{j=1}^{N} d_{ij} f_{ij} \Big/ \sum_{i=1}^{M} \sum_{j=1}^{N} f_{ij}$. In the EMD calculation of RGB images, the signature of DI water was compared to itself (as a negative control) and the signature of other dissimilar solutions.

Figure 10.10 shows the mean red channel intensity derived from the images shown in Fig. 10.3 and 10.4. We have also implemented the Earth Mover Distance (EMD) algorithm to compare how much the image with varying RI environment are different from that of image with

water environment. Figure 10.11 and 10.12 shows the variation of green and blue channel respectively.

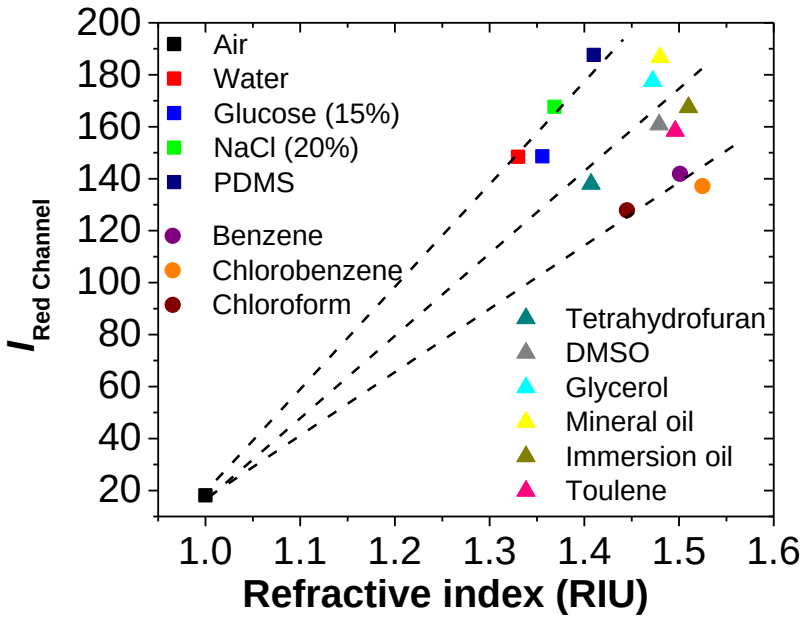

Figure 10.10: Variation of averaged red channel intensity with refractive-index.

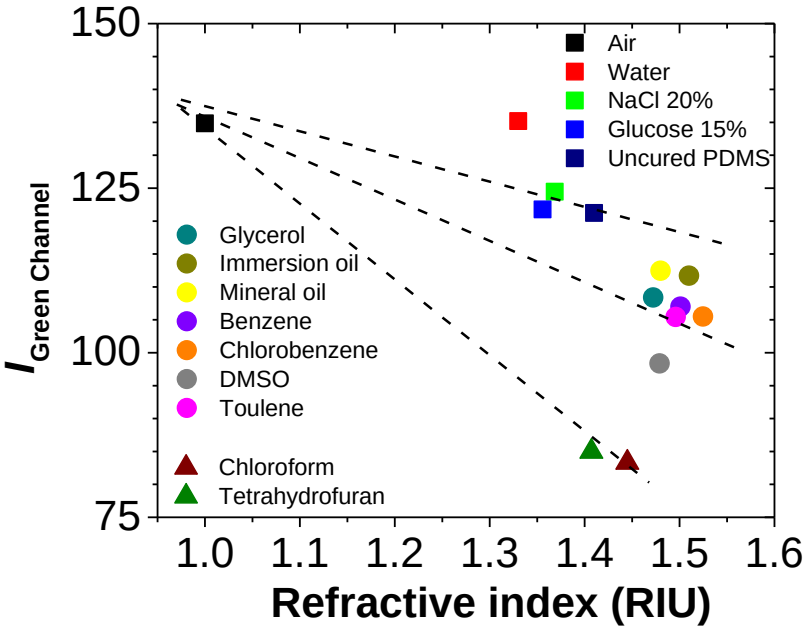

Figure 10.11: Variation of averaged green channel intensity with refractive-index.

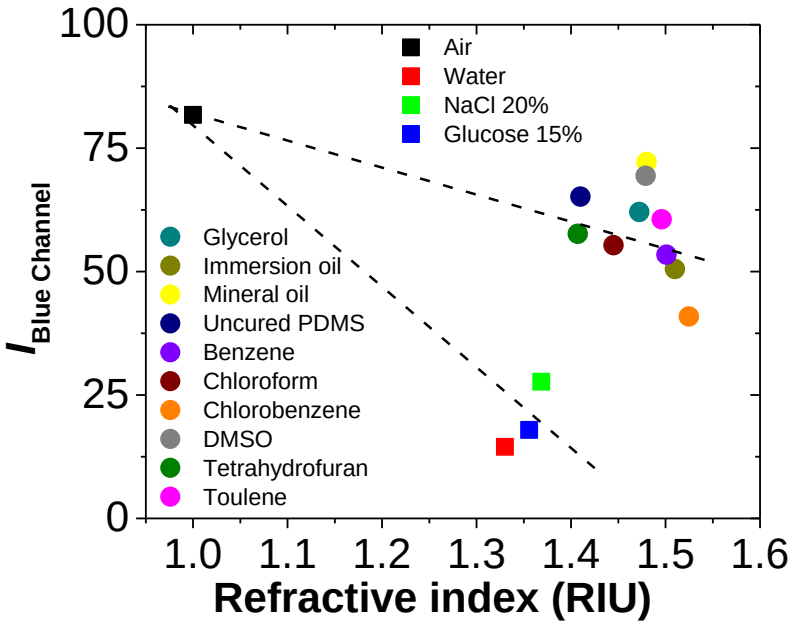

Figure 10.12: Variation of averaged blue channel intensity with refractive-index.

In view of large shift in the resonance wavelength due to higher sensitivity of our sensor, we can monitor the refractive index change from the BF transmission/reflection images using a simple optical microscope with a white light source. Figure 10.13 depicts structured illumination of nanoLCA using photo lithographically patterned "NANO" and "ILLINOIS" mask. White light is illuminated from below the mask, but only green light passes through the nanoLCA sensor and collected by the charge coupled device (CCD) detector of the microscope. After putting ethanol (refractive index, n = 1.362) on the "IL" part of the word "ILLINOIS", the color changes from light blue to yellow. Similarly, the transmitted color changed from light blue to green and red for water and immersion oil respectively. The vibrant color created after mixing of 15% NaCl (middle orange), immersion oil (red), and ethanol (yellow) on the nanoLCA device is also shown in Fig. 10.13.

Figure 10.13: Creation of vibrant colors in transmission mode image of nanoLCA with mixture of NaCl, immersion oil and ethanol. The word 'NANO' was printed on a transparency sheet and nanoLCA device was kept on top of it. Light was illuminated from the bottom of the transparency. An ethanol drop was placed on part of the letter 'N' which appears orange in the transmission image. The rest of the letter is green due to the transmission property of nanoLCA. To illustrate the high spatial control, a lithography mask in quartz with the word 'ILLINOIS' was made and light was transmitted from the bottom of the mask while the nanoLCA sitting on top of it. The color appears green with air interface but changes to orange, light green and red for ethanol, water and immersion oil interfaces respectively.

Sensitivity and figure-of-merit (FOM) of nanoLCA

In order to compare the sensitivity of nanoLCA, we measured the LSPR peak wavelength shift by precisely varying the concentration of NaCl solution. At low concentration (< 1mg mL^{-1}

or 0.1% NaCl), with a difference of RI by 2 x 10^{-4} RIU (refractive index unit) [84] we observed wavelength shift of LSPR mode to be ~ 9 nm (Fig. 10.14c), which corresponds to sensitivity of 46000 nm RIU^{-1}, exceeding all previously reported sensitivity by almost two order of magnitude. An average sensitivity of 8066 nm RIU^{-1} (R^2=0.987) was achieved for higher concentration (>1mg mL^{-1} or 0.1% NaCl) (Fig. 10.14d). In order to compare the sensitivity of different metallic plasmonic sensors, a metric called figure of merit (FOM), $\frac{\Delta\lambda}{\Delta n}\left(\frac{1}{\Delta w}\right)$, where $\Delta\lambda$ is the amount of shift for the resonance peak wavelength for Δn is the change in the RI, Δw is the full-width-half-maximum (FWHM) of the peak in consideration, is widely used. We calculate a maximum FOM of ~ 1022 and an average FOM ~ 179 which far exceeds all reported FOM of nanohole structures (including the theoretical upper limit of FOM ~108 for gold standard SPR sensors [84, 219, 229]; metallic naoparticles has FOM ~ 0.9-5.4 and SPP structure has FOM ~ 23). We assert that the high sensitivity is due to selective transmission of nanoparticle scattering light by the nanoLCA. There is also contribution from subradiant (long plasmon lifetime) SPP waves (at λ =381 nm) (with a narrow full width at half maximum of 18 nm). Due to longer plasmon lifetime, the plasmon energy can be transferred to the emissive superradiant LSPR mode (at λ=450 nm) (with FWHM of 48 nm) giving rise to further enhancement of local electric field. The corresponding bright-field image with different NaCl concentration is shown in Fig. 10.14a. Typical spectrum for low concentration of NaCl solution is reported in Fig. 10.14b.

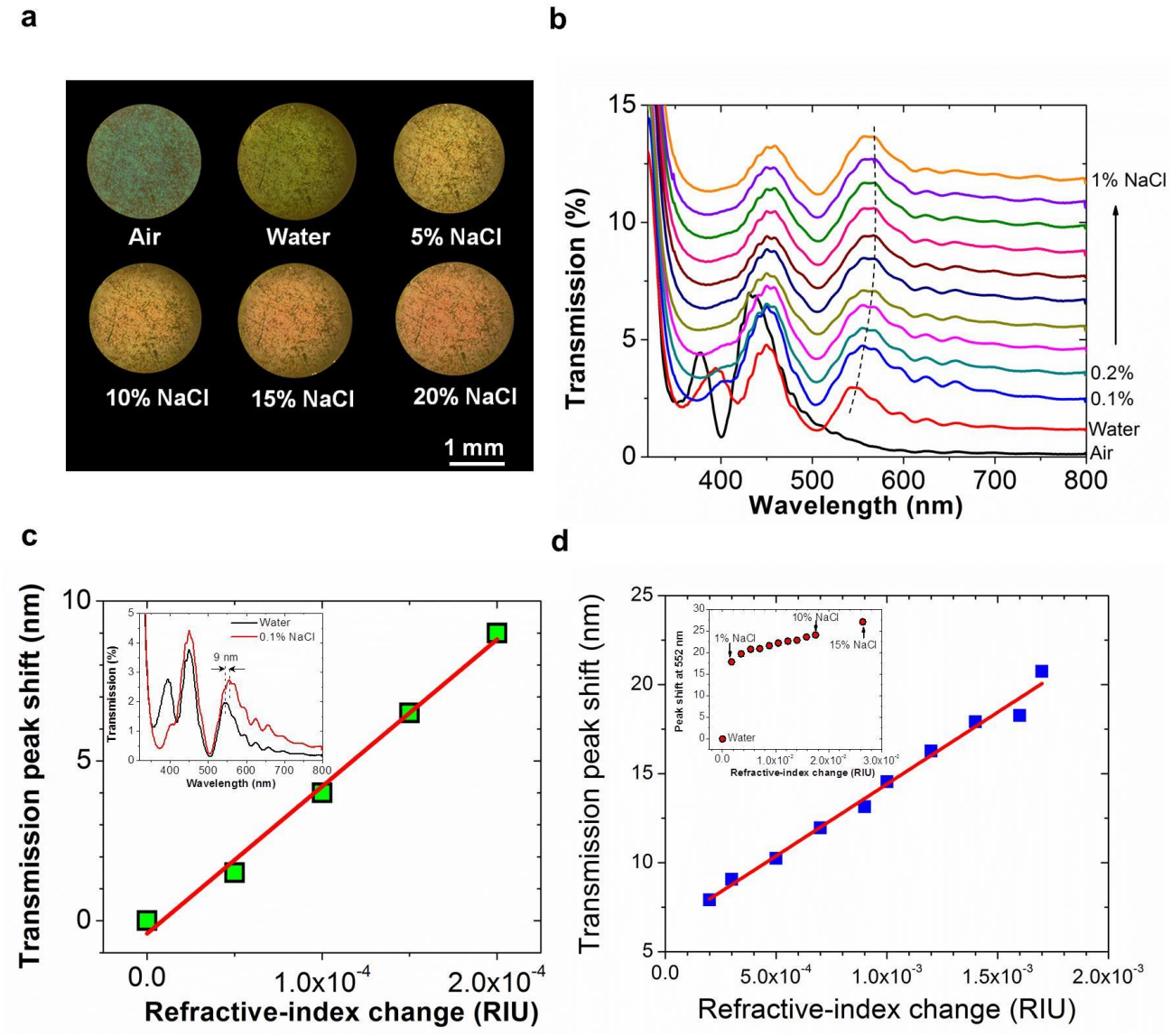

Figure 10.14: Refractive-index sensitivity and figure of merit of nanoLCA obtained using NaCl solution. (a) Optical micrograph of nanoLCA (h = 500 nm, t = 90 nm) with different concentration of NaCl solutions (0-20% by weight). (b) Transmission spectra of nanoLCA in presence of NaCl concentration of 0-1% with an increment of 0.1%. The LSPR resonance peak due to Mie scattering of nanoparticles along the sidewall (shown with dotted line) are red-shifted with change in NaCl concentration. (c) Sensitivity of nanoLCA calculated using a linear fitting scheme from the transmission spectra LSPR resonance peak shift obtained for NaCl concentration of 0-0.1% with an increment of 0.025%. The sensitivity was calculated to be 46,000 nm per RIU. (d) Sensitivity of nanoLCA calculated for Nal concentration range from 0-1%. The average sensitivity in high concentration range was calculated to be 8066 nm per RIU. The inset shows the LSPR resonance peak shift for nanoLCA for NaCl concentration range from 0-15%. The large peak shift at lower concentration clearly demonstrates that nanoLCA is more sensitive in lower concentration range.

Colorimetric DNA sensing using nanoLCA

To demonstrate the utility of nanoLCA for biosensing applications, we measured the hybridization of a short chain of probe oligonucleotides (5'-thiol-CAGCAAATGGGCTCCGAC-3') and its perfectly matched target oligonucleotide (3'-GTCGGAGCCCATTTGCTG-5'-HEX). The 5' end of the probe oligonucleotides was modified with a thiol group for ease of immobilizing on Ag surface. Our colorimetric SPR imaging technique does not require any label on the DNA, however, the target oligo was tagged with fluorophore HEX for independently verifying the hybridization in fluorescence mode. Figure 10.15 shows the detection of hybridization of oligonucleotides down to 100 pM through the BF imaging of nanoLCA. We are able to visualize the colorless DNA and able to differentiate the concentration of DNA based on the color change of the sensor device. The transmission spectrum showed a red-shift of ~ 32 nm after DNA hybridization for the nanoLCA with h = 1000 nm (Fig. 10.17).

As shown in Fig. 10.16, the hybridization of target oligonucleotide at 0.1 nM and 1 nM to the probe oligonucleotide resulted in approximately 1.9 and 2.1 times increase respectively in the intensity of the red channel compared to that of the negative control. Likewise, in the green channel, we observed approximately 3.3 and 4.3 times increase after the hybridization of the same concentrations of probe oligonucleotide. The difference in red channel intensity and EMD values are much more sensitive in lower concentration range compared to higher concentration, at which sensor is more likely saturating (confirming our earlier observation about RI-solution testing).

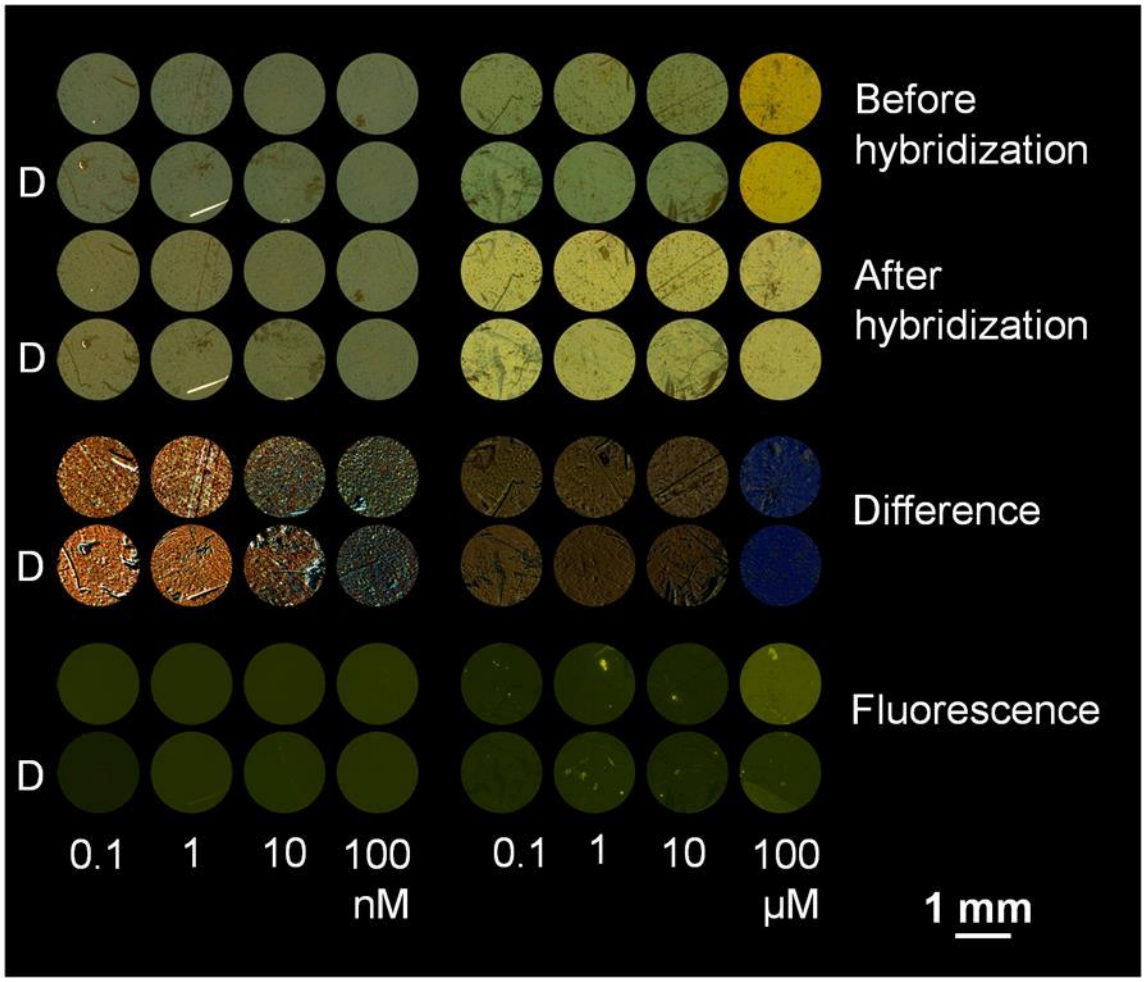

Figure 10.15: Detection of DNA hybridization on nanoLCA. (a) Bright field images of short chain oligonucleotides before and after hybridization. Here 'D' denotes duplicate experiments. The difference shows the direct subtraction of 'before hybridization' images from the 'after hybridization' images. Here, orange color (left) denotes higher count than blue color (right).

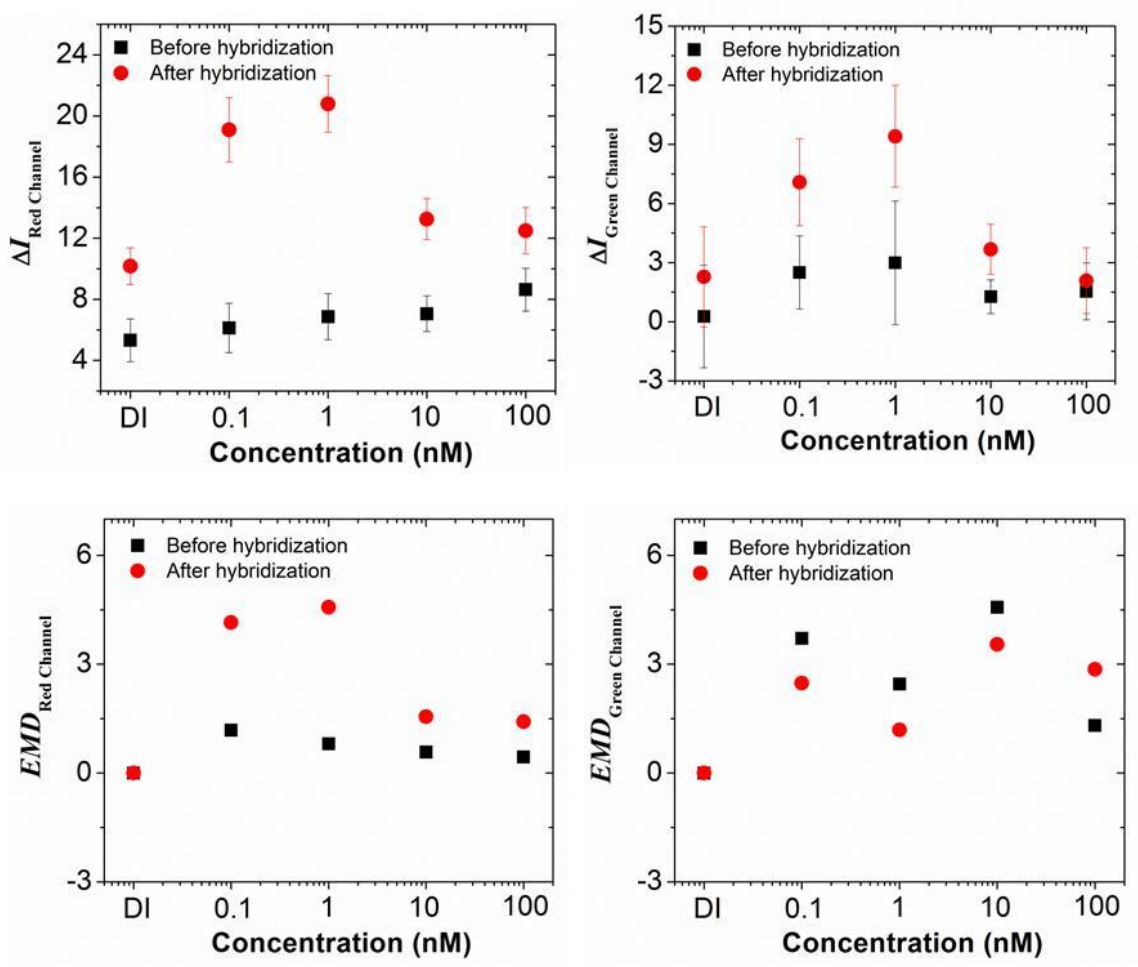

Figure 10.16: Variation of red and green channel intensity with different concentration of oligonucleotides before and after hybridization. The variation of EMD counts with concentration is also shown below for red and green channel respectively.

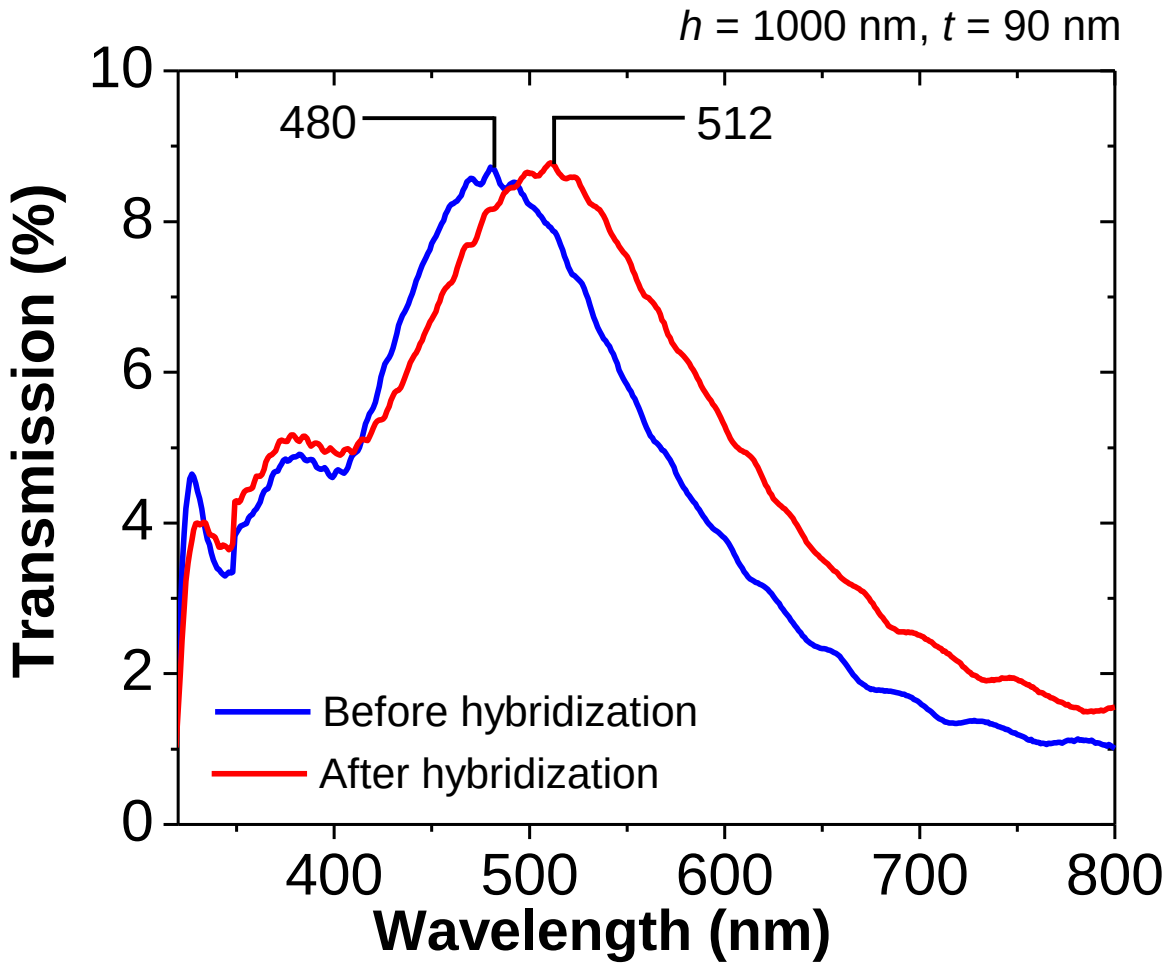

Figure 10.17: Transmission spectrum of nanoLCA (*h* = 1000 nm) before and after DNA hybridization. The concentration of DNA-1 solution was 100 μM (prepared in DI water) and the concentration of DNA-2 solution was 10 μM (prepared in 1x PBS).

Protein-protein binding experiments on nanoLCA

Furthermore, we performed a simple biomolecular protein-protein interaction experiment to demonstrate the therapeutic antibody screening functionality on nanoLCA. In order to make carboxylated monolayer and thiol linker on the surface, 3-Mercaptopropionic acid (MPA) (10 mM) and 6-Mercaptohexanoic acid (MHA) (1 mM) in anhydrous ethanol solution were used. Immobilization of protein (BSA) to the surface was achieved by linking one of the amine functional groups on protein to the carboxyl group through a peptide bond (amide linkage) in the presence of catalyst N-(3-Dimethylaminopropyl)-N′-ethylcarbodiimide hydrochloride (EDC) (50

mM) and N-Hydroxysuccinimide (NHS) (200 mM). Different concentrations of BSA solution (0.001 -1 mg/mL) were prepared in DI water. The concentration of anti-BSA solution prepared in 1x Phosphate Buffer Saline (PBS) was kept constant (0.01 mg/mL). Images were taken at each step (before addition of solution, after addition of solution and after washing and drying).

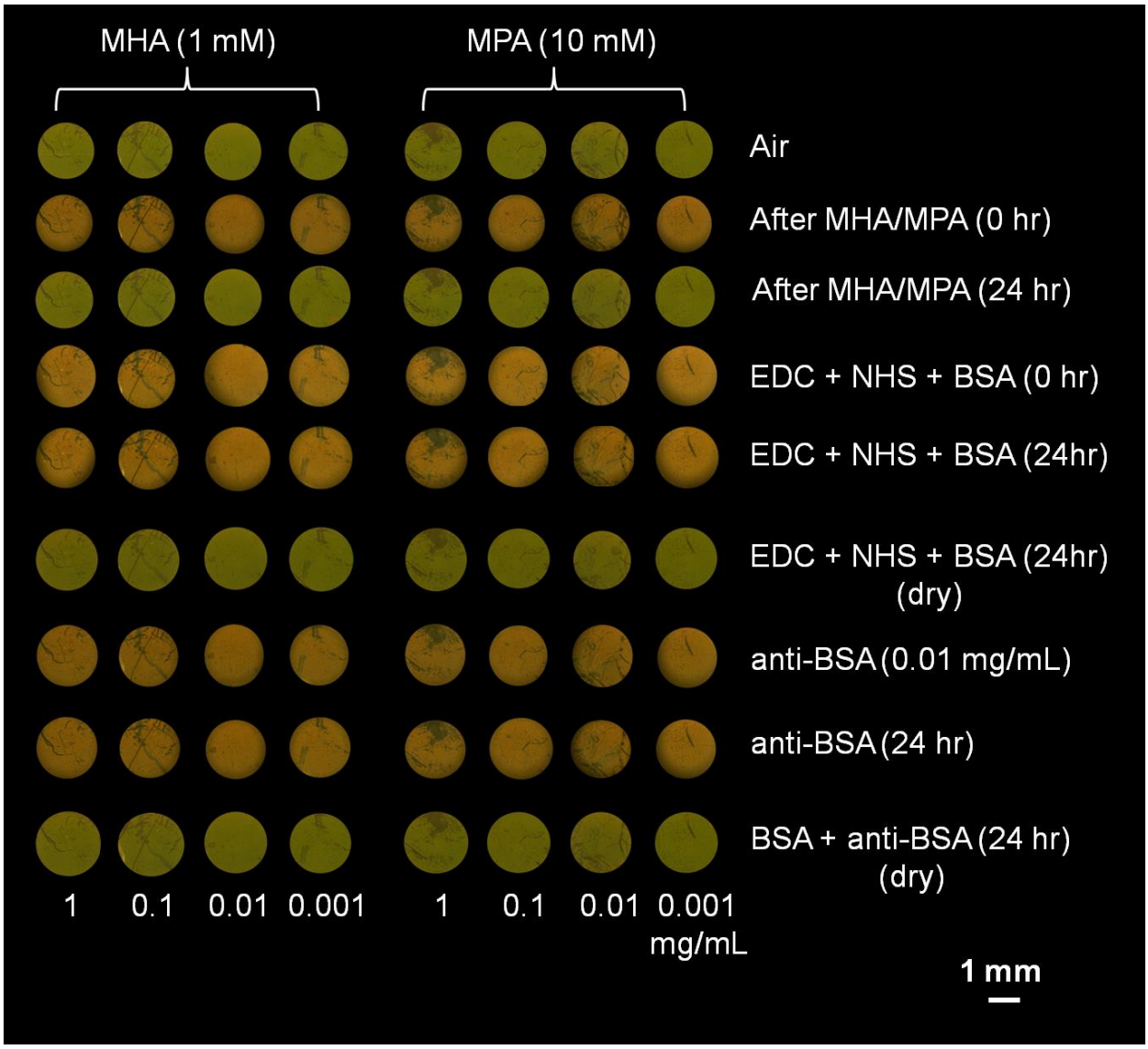

Figure 10.18: Bright field imaging of BSA and anti-BSA on nanoLCA. The surface was first carboxylated using ethanolic solution of 3-Mercaptopropionic acid (MPA) (10 mM) and 6-Mercaptohexanoic acid (MHA) (1 mM). The bright field images of nanoLCA after each step is presented.

We are able to observe the color changes on the sensor surface (raw images in Fig. 10.18) due to BSA/ anti-BSA immune complex formation which is also relevant to the studies related to

the receptor sites of red blood cells [230]. As shown in Fig. 10.19 (top is red channel intensity, bottom is for green channel intensity), we can clearly discern between before and after immune complex formation for different concentration of BSA/anti-BSA from the nanoLCA imaging data (Fig. 10.20). The spectral shift observed for the nanoLCA structure after BSA modification was ~ 42 nm (Fig. 10.20). For a similar experiment, resonant wavelength shift of ~ 5 nm was observed [83], which is 8.4 times lower than in the case of nanoLCA structure (even without optimization). In the colorimetric analysis, we observed a decrease in the intensity of the red and green channels following the BSA/anti-BSA complex formation. Further, in a previously reported experiment [226] using an EOT plasmonic structure, only reduction of transmitted intensities after antibody adsorption to the surface was observed (the color was changed from red (before protein incubation) to black (after protein incubation)). In contrast, nanoLCA leads to a change in color after protein adsorption due to the higher sensitivity of the device. The DNA and BSA experiments were performed in a 96-well microplate.

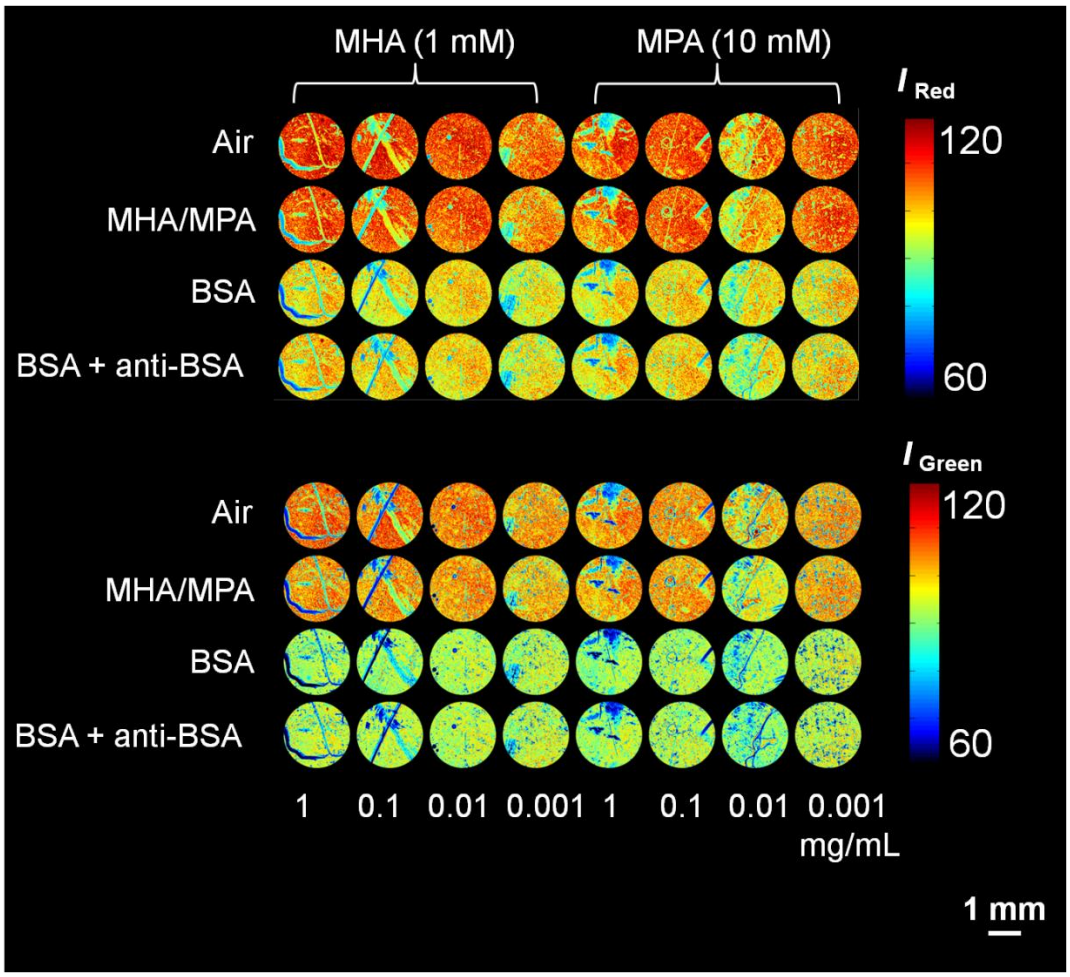

Figure 10.19: Biomolecular protein detection on nanoLCA. Variation of red channel (top) and green channel (bottom) intensity derived from the bright field images of nanoLCA coated with BSA (third and seventh row) and BSA+anti-BSA (fourth and eighth row). The images with air (first and fifth row) and MHA/MPA (second and sixth row) interfaces are also shown. The first four columns are for the cases when MHA (1 mM) is used for protein immobilization (0.001-1 mg/mL). The last four columns are the cases when MPA (10 mM) is used for protein immobilization (0.001-1 mg/mL) on nanoLCA surface.

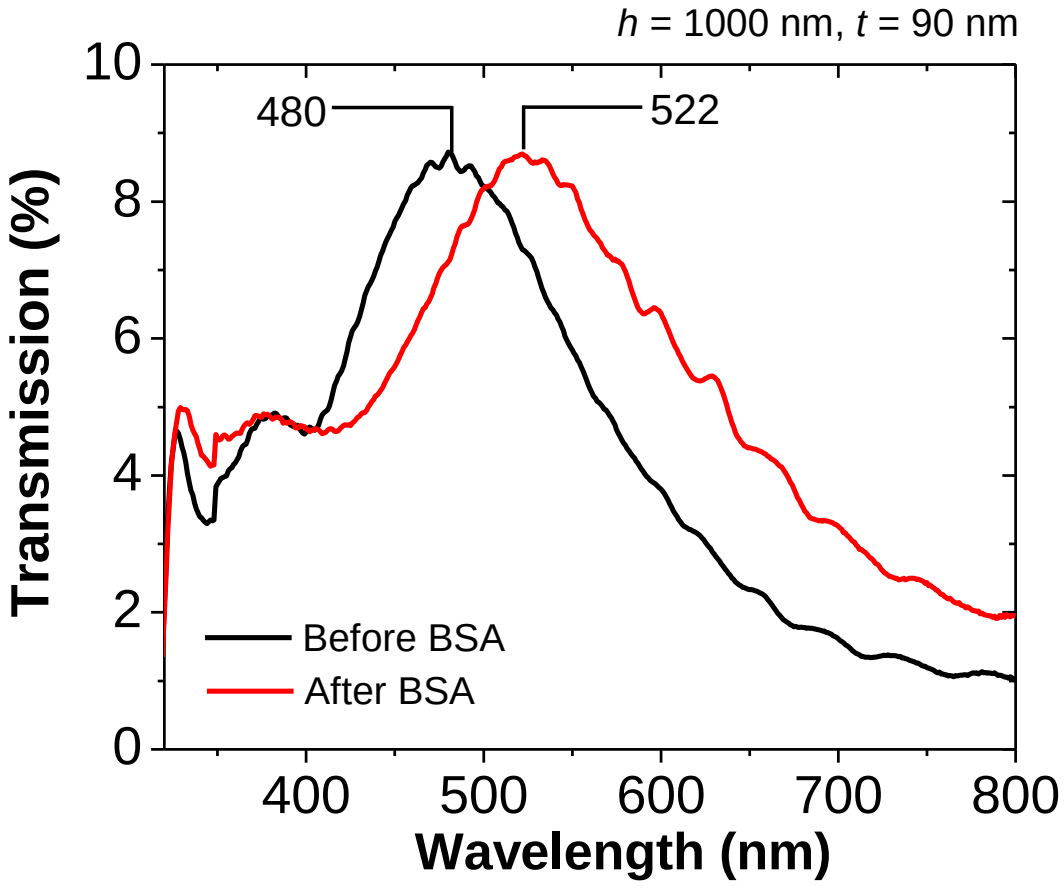

Figure 10.20: Transmission spectrum of nanoLCA (h = 1000 nm) before and after immobilizing BSA on the surface. The concentration of BSA solution was 10 μM.

Colorimetric microfluidics without colorant

We have also performed the experiment with microfluidics to show that nanoLCA can be integrated to a microfluidic device. Figure 10.21 shows the BF image of the nanoLCA sensor with a polydimethylsiloxane (PDMS) microfluidic on top of it. At the contact point of the PDMS to the surface of the nanoLCA sensor, a color change is observed (green is in contact with air, red is in contact with PDMS). An added advantage of nanoLCA is that the proper contact of the device to the microfluidic surface can be checked even before the actual experiments. Figure

10.21 also shows the mixing experiments with glycerol-water and DMSO-water solution to demonstrate the gradient change in color due to different concentration of solutions in a microfluidic-on-nanoLCA environment.

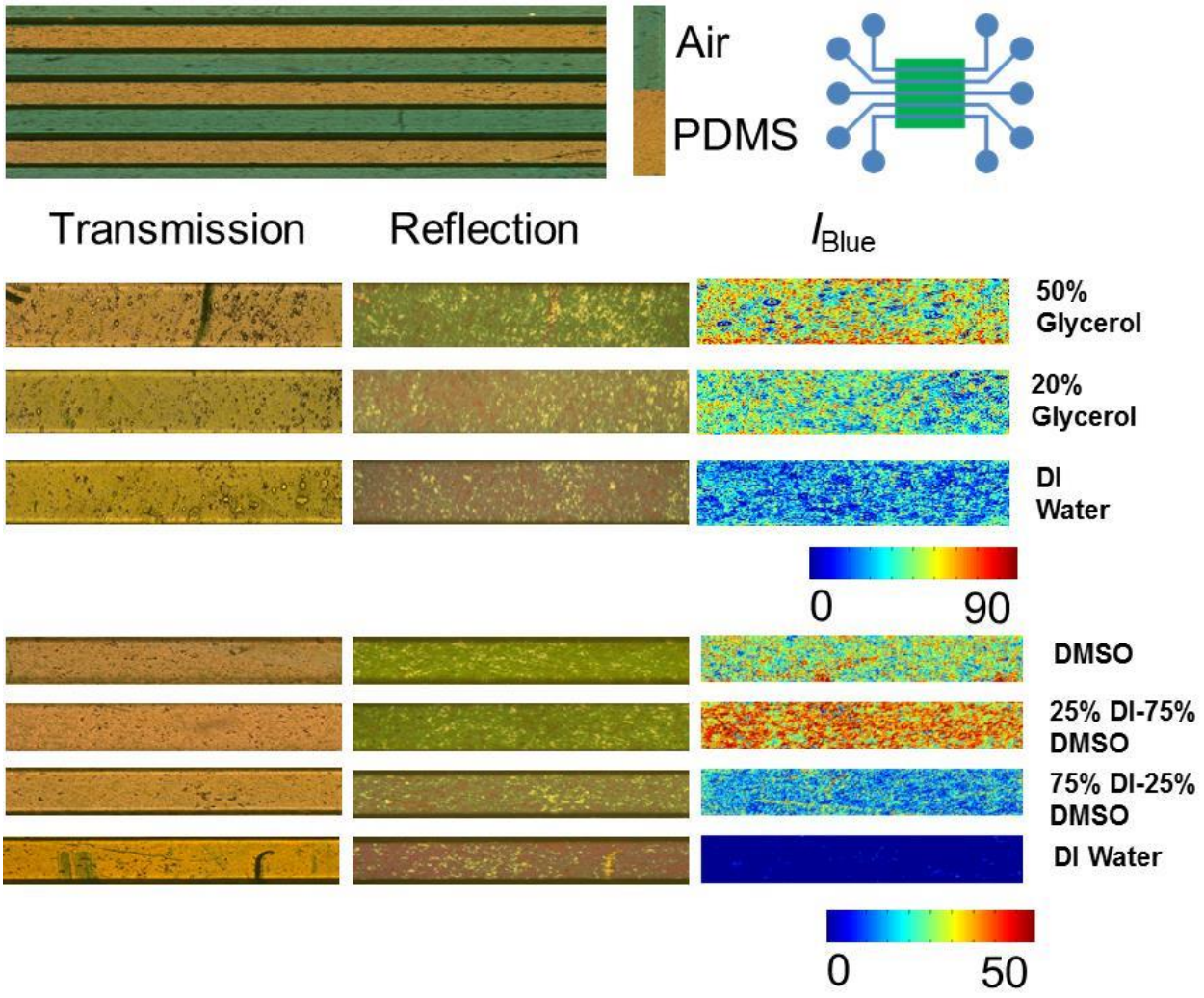

Figure 10.21: Bright field transmission image of nanoLCA with a PDMS microfluidic device (schematically shown to the right) on top of it. The orange color is bcause of the PDMS in contact with the nanoLCA. The green color is for the empty microfluidics channel. The images below show the bright field transmission (left), reflection (middle) and blue channel intensities (right) of mixing experiments on nanoLCA with DI water-Gycerol (middle) and DI water-DMSO (bottom).

Conclusions

In summary, we have developed a 'biochemical color camera' device mimicking Lycurgus cup effect to observe and perform quantitative biochemical sensing with unprecedented sensitivities. We have demonstrated the utility of the sensor for highly sensitive refractive-index sensing, DNA hybridization detection, protein-protein interaction and integration to portable microfluidics device for lab-on-chip applications. We envisage extensive use of the device for DNA microarrays, therapeutic antibody screening for drug discovery and pathogen detection in resource poor setting and a low cost, higher sensitive alternative to existing SPR/LSPR instruments.

References

[1] U. Leonhardt, "Optical metamaterials - Invisibility cup," *Nat. Photonics,* vol. 1, pp. 207-208, APR, 2007.

[2] W. A. Murray and W. ?. Barnes, "Plasmonic Materials," *Adv Mater,* vol. 19, pp. 3771-3782, 2007.

[3] M. E. Stewart, C. R. Anderton, L. B. Thompson, J. Maria, S. K. Gray, J. A. Rogers and R. G. Nuzzo, "Nanostructured plasmonic sensors," *Chem. Rev.,* vol. 108, pp. 494-521, FEB 2008, 2008.

[4] S. Lal, S. Link and N. J. Halas, "Nano-optics from sensing to waveguiding," *Nature Photonics,* vol. 1, pp. 641-648, NOV 2007, 2007.

[5] H. Chen, X. Kou, Z. Yang, W. Ni and J. Wang, "Shape- and size-dependent refractive index sensitivity of gold nanoparticles," *Langmuir,* vol. 24, pp. 5233-5237, MAY 20, 2008.

[6] D. P. Lyvers, J. Moon, A. V. Kildishev, V. M. Shalaev and A. Wei, "Gold Nanorod Arrays as Plasmonic Cavity Resonators," *Acs Nano,* vol. 2, pp. 2569-2576, DEC, 2008.

[7] S. Zhang, K. Bao, N. J. Halas, H. Xu and P. Nordlander, "Substrate-Induced Fano Resonances of a Plasmonic: Nanocube: A Route to Increased-Sensitivity Localized Surface Plasmon Resonance Sensors Revealed," *Nano Letters,* vol. 11, pp. 1657-1663, APR, 2011.

[8] J. N. Anker, W. P. Hall, O. Lyandres, N. C. Shah, J. Zhao and R. P. Van Duyne, "Biosensing with plasmonic nanosensors," *Nature Materials*, vol. 7, pp. 442-453, JUN 2008, 2008.

[9] N. Ahamad, A. Bottomley and A. Ianoul, "Optimizing Refractive Index Sensitivity of Supported Silver Nanocube Monolayers," *Journal of Physical Chemistry C*, vol. 116, pp. 185-192, JAN 12, 2012.

[10] S. J. Zalyubovskiy, M. Bogdanova, A. Deinega, Y. Lozovik, A. D. Pris, K. H. An, W. P. Hall and R. A. Potyrailo, "Theoretical limit of localized surface plasmon resonance sensitivity to local refractive index change and its comparison to conventional surface plasmon resonance sensor," *Journal of the Optical Society of America A-Optics Image Science and Vision*, vol. 29, pp. 994-1002, JUN, 2012.

[11] C. Qian, C. Ni, W. Yu, W. Wu, H. Mao, Y. Wang and J. Xu, "Highly-Ordered, 3D Petal-Like Array for Surface-Enhanced Raman Scattering," *Small*, vol. 7, pp. 1801-1806, JUL 4, 2011.

[12] T. W. Ebbesen, H. J. Lezec, H. F. Ghaemi, T. Thio and P. A. Wolff, "Extraordinary optical transmission through sub-wavelength hole arrays," *Nature*, vol. 391, pp. 667-669, FEB 12 1998, 1998.

[13] M. E. Stewart, N. H. Mack, V. Malyarchuk, J. A. N. T. Soares, T. Lee, S. K. Gray, R. G. Nuzzo and J. A. Rogers, "Quantitative multispectral biosensing and 1D imaging using quasi-3D plasmonic crystals," *Proc. Natl. Acad. Sci. U. S. A.*, vol. 103, pp. 17143-17148, NOV 14 2006, 2006.

[14] N. Ganesh, W. Zhang, P. C. Mathias, E. Chow, J. A. N. T. Soares, V. Malyarchuk, A. D. Smith and B. T. Cunningham, "Enhanced fluorescence emission from quantum dots on a photonic crystal surface," *Nature Nanotechnology*, vol. 2, pp. 515-520, AUG 2007, 2007.

[15] F. Vollmer and S. Arnold, "Whispering-gallery-mode biosensing: label-free detection down to single molecules," *Nature Methods*, vol. 5, pp. 591-596, JUL 2008, 2008.

[16] I. D. Block, L. L. Chan and B. T. Cunningham, "Photonic crystal optical biosensor incorporating structured low-index porous dielectric," *Sensors and Actuators B-Chemical*, vol. 120, pp. 187-193, DEC 14 2006, 2006.

[17] A. J. Haes and R. P. Van Duyne, "A unified view of propagating and localized surface plasmon resonance biosensors," *Analytical and Bioanalytical Chemistry*, vol. 379, pp. 920-930, AUG 2004, 2004.

[18] S. Roh, T. Chung and B. Lee, "Overview of the Characteristics of Micro- and Nano-Structured Surface Plasmon Resonance Sensors," *Sensors*, vol. 11, pp. 1565-1588, FEB 2011, 2011.

[19] A. V. Kabashin, P. Evans, S. Pastkovsky, W. Hendren, G. A. Wurtz, R. Atkinson, R. Pollard, V. A. Podolskiy and A. V. Zayats, "Plasmonic nanorod metamaterials for biosensing," *Nature Materials,* vol. 8, pp. 867-871, NOV 2009, 2009.

[20] C. Genet and T. W. Ebbesen, "Light in tiny holes," *Nature,* vol. 445, pp. 39-46, JAN 4 2007, 2007.

[21] A. A. Yanik, A. E. Cetin, M. Huang, A. Artar, S. H. Mousavi, A. Khanikaev, J. H. Connor, G. Shvets and H. Altug, "Seeing protein monolayers with naked eye through plasmonic Fano resonances," *Proc. Natl. Acad. Sci. U. S. A.,* vol. 108, pp. 11784-11789, JUL 19 2011, 2011.

[22] M. R. Gartia, Z. Xu, E. Behymer, H. Nguyen, J. A. Britten, C. Larson, R. Miles, M. Bora, A. S. -. Chang, T. C. Bond and G. L. Liu, "Rigorous surface enhanced Raman spectral characterization of large-area high-uniformity silver-coated tapered silica nanopillar arrays," *Nanotechnology,* vol. 21, pp. 395701, OCT 1 2010, 2010.

[23] A. Fernandez, H. T. Nguyen, J. A. Britten, R. D. Boyd, M. D. Perry, D. R. Kania and A. M. Hawryluk, "Use of interference lithography to pattern arrays of submicron resist structures for field emission flat panel displays," *Journal of Vacuum Science & Technology B,* vol. 15, pp. 729-735, MAY-JUN 1997, 1997.

[24] H. Chen, T. Ming, L. Zhao, F. Wang, L. Sun, J. Wang and C. Yan, "Plasmon-molecule interactions," *Nano Today,* vol. 5, pp. 494-505, 2010, 2010.

[25] J. M. McMahon, J. Henzie, T. W. Odom, G. C. Schatz and S. K. Gray, "Tailoring the sensing capabilities of nanohole arrays in gold films with Rayleigh anomaly-surface plasmon polaritons," *Optics Express,* vol. 15, pp. 18119-18129, DEC 24 2007, 2007.

[26] J. Henzie, M. H. Lee and T. W. Odom, "Multiscale patterning of plasmonic metamaterials," *Nature Nanotechnology,* vol. 2, pp. 549-554, SEP 2007, 2007.

[27] L. Varga, E. Thiry and G. Fust, "Bsa Anti-Bsa Immune-Complexes Formed in the Presence of Human-Complement do Not Bind to Autologous Red Blood-Cells," *Immunology,* vol. 64, pp. 381-384, JUL 1988, 1988.

[28] A. G. Brolo, R. Gordon, B. Leathem and K. L. Kavanagh, "Surface plasmon sensor based on the enhanced light transmission through arrays of nanoholes in gold films," *Langmuir,* vol. 20, pp. 4813-4815, JUN 8 2004, 2004.

CHAPTER 11

DIPOLE-PHOTONIC-PLASMONIC RESONANCE ENERGY TRANSFER (DIP-PRET) FOR INJECTION SEEDED AMPLIFICATION

Introduction

Previously described energy transfer processes such as FRET [231, 232], PRET [233], DET [234] and radiative energy transfer [235] are short-ranged and the energy transfer efficiency decreases exponentially with distance. Using Whispering Gallery Mode (WGM) coupling, long range energy transfer has been achieved [236-240]. However, the energy transfer efficiency in such processes is low [240, 241]. In addition, large linewidth of fluorescence dyes limits the number of coding, sensitivity and specificity in multiplexed immunoassay screening. Here, we demonstrate experimentally, a new energy transport route through the coupling of dipole – photonic - plasmonic resonance energy transfer (DiP-PRET) for achieving injection seeded amplification. With this design, we have achieved substantially narrowed laser-like emission spectrum along with energy transfer efficiency of over 90% and fluorescence signal enhancement up to a factor of > 1200x, two orders of magnitude higher than reported previously [240, 242-245]. The DiP-PRET system can be optimized for biomolecular sensing, cytometry, and sandwiched immunofluorescence assays detection with high sensitivity, and specificity.

Background

Broadly, energy transfer between donor-acceptor can be either radiative or non-radiative process. Radiative energy transfer generally does not involve any interaction between emitter

and source molecule to trigger the energy transfer (simple emission and absorption of a photon). On the other hand, non-radiative energy transfer such as Förster Resonance Energy Transfer (FRET), Dexter Energy Transfer (DET), and Plasmon Resonance Energy Transfer (PRET) require certain type of interaction mechanism to initiate the energy transfer. FRET is based on near field dipole-dipole coulombic interaction [231], DET involves electron exchange requiring overlap of wavefunction of donor-acceptor molecules [234], and PRET is due to the dipole-dipole interaction between plasmon dipole and the molecular dipole [233]. The energy transfer processes are short ranged and the transfer efficiency decreases exponentially with distance. For example, if r is the donor-acceptor distance, DET has the lowest range of energy transfer with an exponential distance dependence, exp $(-2r/L)$, where L is the sum of the Van der Waals radii of the donor and the acceptor. The energy transfer range of DET process is ~ 1 nm [235]. In FRET, the energy transfer process is proportional to $R_0^6/\left(R_0^6 + r^6\right)$, where R_0 is the Förster distance. The energy transfer is limited by r ~ 10 nm [235]. Similarly PRET is proportional to $1/r^n$ [246], where n is determined by the quantized dimensionality of the system. The energy transfer follows r^{-6} dependence for a point dipole (e.g. quantum dots), r^{-5} scaling for 1D system such as line dipole (e.g. nanowires), r^{-4} dependence for 2D arrays of dipole, and r^{-3} dependence for point dipole interacting with bulk dipoles (e.g. colloid nanoparticles). The energy transfer in PRET is efficient up to r ~ 100 nm. In contrast to these non-radiative energy transfers, radiative energy transfer has the largest energy transfer range, with coupling efficiency following $1/r^2$. However, the long range coupling efficiency in radiative energy transfer process is very low. For example, emitter and source situating 10 μm apart, the efficiency of emitter absorbing a photon radiated by the source is only about 8×10^{-12}, assuming an absorption cross-section of 10^{-16} cm^2.

Using optical elements such as lenses and waveguides one can possibly concentrate and store energy to increase long range coupling efficiency between donor and acceptor [235, 247]. However, due to short interaction duration (as each photon flies by the acceptor once) [247], small mode volume and longer storage time is required [248] to achieve high coupling efficiency. In this context, cavity, e.g. whispering gallery mode resonator (WGR), assisted energy transfer scheme has been proposed to increase the long range coupling efficiency by first coupling the donor emission into cavity modes, circulating the photon for a long time, and finally absorbing by the acceptor for enhanced emission. Since the photons are circulated in the cavity for longer time, the interaction duration can be improved as well. WGRs, however, show weak field enhancement [248, 249] and large mode volumes in spite of the high Q-factor [250]. In contrast, plasmonic cavity can provide strong field enhancement and ultrasmall mode volume, but has low Q-factor [248, 251]. Here, by combining plasmonic and a WGR cavity in the DiP-PRET system, we report long range energy transfer with high efficiency, strong field enhancement and high Q-factor (> 3000).

According to Fermi's golden rule, the spontaneous emission process is proportional to the local density of optical states (LDOS) available to the gain medium [252]. Further, LDOS can be increased by a factor known as Purcell factor ($F = \frac{3}{4\pi^2}\left(\frac{Q}{V_{mode}}\right)\left(\frac{\lambda}{2n}\right)^3$, where Q is the cavity quality factor, V_{mode} is the mode volume, λ is the resonant wavelength and n is the refractive index of the medium) by placing the gain medium near a cavity [251, 253]. It is reported that plasmonic cavity with small mode volume can increase the LDOS by a factor of 1000 [251, 253, 254]. The higher energy transfer efficiency realized by the DiP-PRET system is due to the modification of radiative and non-radiative decay rates of the dipole (gain medium) by providing

additional LDOS from both the plasmonic substrate and the WGM of the photonic structure. The DiP-PRET system is also advantageous compared to isolated LSPR or SPR systems, because LSPR and SPR have short interaction length (5-50 nm) [255], are highly radiative in nature, and hence, they dissipates the energy quickly leading to quick dephasing [256] and loss in resonance. On the other hand, the WGR structure in DiP-PRET system allows it to have a longer photon circulation time resulting in a sharper line width of the radiative modes (as line width is inversely proportional to the dephasing time) [248, 256].

Localized surface plasmon resonance (LSPR) has been used to achieve enhanced spontaneous emission [257, 258], stimulated emission [251], higher harmonic generation [259], enhanced Raman scattering [260], and nanoscale lasers [261]. Generally combining propagating surface plasmon polariton (SPP) (thin metal layer covering) to high Q-resonator leads to degradation of quality factor due to scattering and absorption losses in metals [237, 262, 263]. However, LSPR coupling (e.g. using metal nanoparticles) to high Q-factor resonator has been shown not to affect the Q-factor [264, 265]. In fact, WGR-plasmonic based system has been used to enhance Raman scattering [266-268], on-chip nanoparticle detector [265, 269], protein detection [270] and single virus detection [271]. All the previous studies deal with modification of the polarizability of metal nanoparticle through the evanescent field of WGM. So, it's a one-way energy transfer from WGR to metal nanoparticle and no feedback in to the WGR-plasmonic system. Here, we explore the feedback loop system involving WGR-plasmonic-gain medium for achieving seed injection amplification.

Fabrication of plasmonic device

Photolithography and reactive ion etching process is used to make the plasmonic substrate on 4-inch wafer. First, the area where nanopillar structures are to be etched is patterned by photolithography. Secondly, by using a mixture of HBr and O_2 gases, the silicon substrate is etched by HBr and oxidized by O_2 simultaneously [272]. The nanopillar structures are synthesized by taking advantage of high etching selectivity of HBr for silicon to oxide (200: 1). Finally, a thin layer of silver coating is applied to provide plasmonic property to the substrate.

DiP-PRET system

The DiP-PRET system consist of protein (NeutrAvidin) conjugated dye molecules (DyLight 650) coated on biotinylated polystyrene microspheres (10.14 µm, 2 µm) and drop casted on a plasmonic nanopillar substrate.

Conjugation protocol for the dye/ protein

The biotinylated polystyrene microspheres (MS) are obtained from Bangs Laboratories Inc. The dye (NeutrAvidin Dylight 650 (NA-Dy), 1mg/mL) was purchased from Thermo Scientific. NA-Dy solution (100 µg/mL) was prepared for 500 µL using PBS buffer. 50 µL of MS was mixed with NA-Dy solution (1:10). The mixture was incubated on a shaker for 30 minutes (or 0.5 – 2 hrs depending on the concentration) covered by aluminum foil. Then the solution was centrifuged at 3000 rpm for 2 min and re-suspended with the buffer using a vortex mixer. The procedure was repeated 4 times. Finally, 1 µL drop from the solution was casted on the glass/plasmonic substrate for further experimentation.

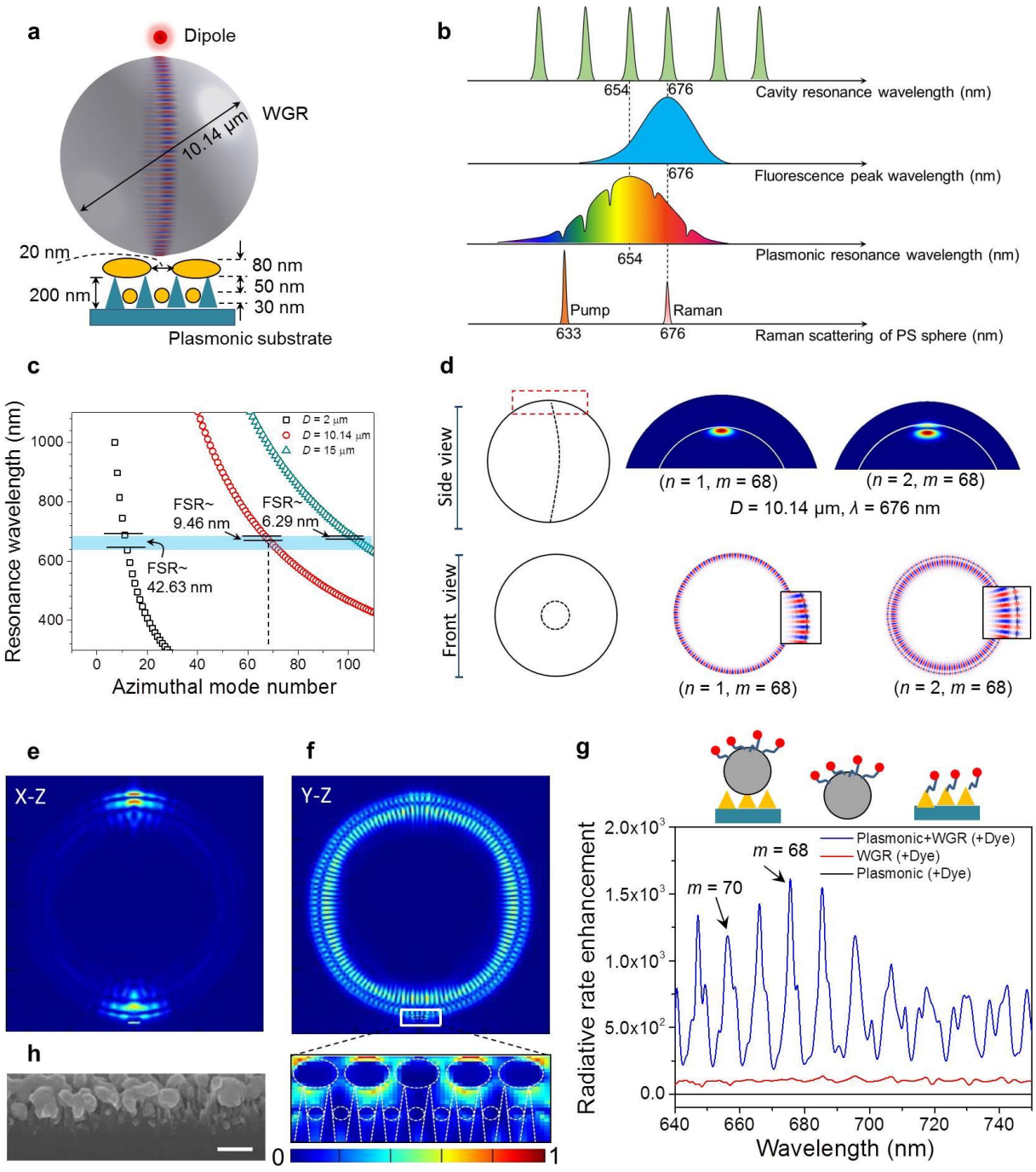

Figure 11.1: Experimental set-up and numerical simulation for DiP-PRET system. **a,** A schematic of the DiP-PRET system comprising dye molecule (dipole), a polystyrene microsphere (whispering gallery resonator, WGR) and a plasmonic substrate. Diameter of the sphere, D = 10.14 μm, dielectric constant, n_d = 1.58, silicon pillar height, h = 200 nm, thickness of metal, t = 80 nm, gap between pillar, g_p = 60 nm, gap between top metal particle, g_m = 20 nm, dipole is oriented in y-direction. **b,** DiP-PRET mechanism for seed injection amplification and stimulated Raman scattering. The pump light excites the fluorescence

emission from dye (DyLight 650) at 676 nm. The pump light also excites the polystyrene WGR into its natural vibrational frequency and the pump photons are scattered to a lower optical frequency (Raman-Stokes wavelength) at 676 nm. If the WGR cavity is designed in such a way that the scattered photons and the fluorescence emitted photons coincides with the WGR cavity's resonance wavelength, seed injection amplification will happen at Raman-Stokes wavelength. Further, if the fluorescence emitted photons coincides with the WGR cavity and plasmonic cavity's resonance wavelength, seed injection amplification will occur. **c,** Cavity mode dispersion curves calculated for the polystyrene dielectric microsphere at diameter D = 2, 10.14 and 15 μm. The calculated free spectral range, FSR, is also noted in the figure. **d,** Calculated first and second-order radial and azimuthal optical eigen mode of D = 10.14 μm sphere at λ=676 nm (m=68). The colors represent electric field of the optical modes. **e,** Calculated field intensity distribution in x-z and **f,** y-z planes. The inset shows the enhancement in between metal particles. **g,** Comparison of calculated radiative rate enhancement of dipole over the free space as a function of wavelength on DiP-PRET (Plasmonic + WGR + Dye), WGR + Dye, and Plasmonic + Dye value at the same position (between two metal particles). **h,** Cross-sectional scanning electron micrograph (SEM) image of plasmonic structure. The scale bar is 200 nm.

Figure 11.1a shows the schematic of the DiP-PRET system. A 633 nm HeNe CW laser (with beam width 1.12 μm) was used to excite the fluorescence from the dye electronic dipole in a photoluminescence (PL) microscopy (50x objective, NA= 0.45) set-up. When pumped at an appropriate wavelength, the fluorescent dye molecule will undergo spontaneous emission. Here there are four possibilities of light emission – (i) the spontaneous emission of dye molecules will propagate in free space (and partially detected by the detector), (ii) emission of dye couples to the LSPR mode of the plasmonic substrate, (iii) emission of dye couples to WGR and the WGR resonance will be emitted by the system, and (iv) spontaneous emission of dye transfer to LSPR mode through cascaded coupling of WGR and final emission from the surface plasmon.

In order to address all the four possibilities, we first calculated the photonic modes available for the WGR. A full vectorial finite element analysis was performed for the 2, 10.14 and 15 μm WGR.

Numerical simulation

The whispering gallery mode inside the spherical microresonator is simulated using COMSOL. The details of simulations are described in Appendix B. As the geometry is axisymmetric, 2D model is used. The air surrounding the resonator is also modeled to simulate the location of where the optical mode occurs. Oxborrow lists the system of differential equations for simulating the whispering gallery mode [273]. Comsol generates mesh and solves for the resonant frequency of the optical mode near the specified mode number.

In order to calculate the power enhancement, the three dimensional finite-difference time-domain (3D-FDTD) method was implemented with the software from Lumerical Solutions, Inc. An electric dipole source was placed at 100nm apart from the top of the 10.14 nm polystyrene sphere with the polarization in y-direction to demonstrate the dye molecule emitting fluorescence at the wavelength of 676 nm with 70 nm of width. The perfectly matched layers in x-, y-, and z-direction surrounded the whole structure including the sphere and the five-by-five periodic array of plasmonic structure. The electric field distribution over the structures was plotted with the mesh size of 1 nm.

Figure 11.1b schematically shows DiP-PRET amplification mechanism for seed injection amplification and stimulated Raman scattering, which we will describe in details later. Briefly, the pump light excites the fluorescence emission from dye (DyLight 650) at 676 nm. The pump light also excites the polystyrene WGR into its natural vibrational frequency and the pump photons are scattered to a lower optical frequency (Raman-Stokes wavelength) at 676 nm. If the WGR cavity is designed in such a way that the scattered photons and the fluorescence emitted photons coincides with the WGR cavity's resonance wavelength, seed injection amplification (or stimulated Raman scattering if no fluorescence dye is present) will happen at Raman-Stokes

wavelength. Further, if the fluorescence emitted photons coincides with the WGR cavity and plasmonic cavity's resonance wavelength, also seed injection amplification will occur. Figure 11.1c shows the resonance wavelength of the eigen mode of the WGM cavity as a function of azimuthal mode number, *m*, for different diameter of WGR. The calculated free spectral ranges (FSR) of 2, 10.14 and 15 μm WGR are 42.63 nm, 9.46 nm and 6.29 nm, respectively. Figure 11.1d shows the calculated first and second-order radial and azimuthal optical eigen mode of D = 10.14 μm sphere at λ=676 nm (m=68). The dye (DyLight 650) was chosen for the overlap of its absorption and emission spectrum with eigen modes of WGR and LSPR mode of the plasmonic substrate. The model system is composed of a dipole (dye) on top of a polystyrene sphere which sits on a nanopillar silicon substrate deposited with 80 nm of silver (plasmonic substrate) (Fig. 11.1h). Figure 11.1e shows the electric field intensity distribution in the x-z and y-z planes simulated by FDTD method. The WGM resonance in the WGR is observable, and the highest electric field intensity is at the contact area with the plasmonic substrate, especially between the metal coated pillars, as shown in the inset (Fig. 11.1f). Figure 11.1g shows the comparison of calculated radiative rate enhancement for the dipole on the plasmonic substrate, on the WGR and on the DiP-PRET system. The dipole radiative rate enhancement is calculated by taking the ratio of integrated power outflow (see Methods) of the dipole-plasmonic, dipole-WGR and DiP-PRET system to that of dipole on a glass surface. The simulated DiP-PRET system exhibits enhancement of the order of 10^3 times of the dipole radiative rate along with narrowing of the emission spectrum with full-width-half-maximum (FWHM) = 2.19 nm on DiP-PRET system compared to FWHM = 45 nm on glass substrate.

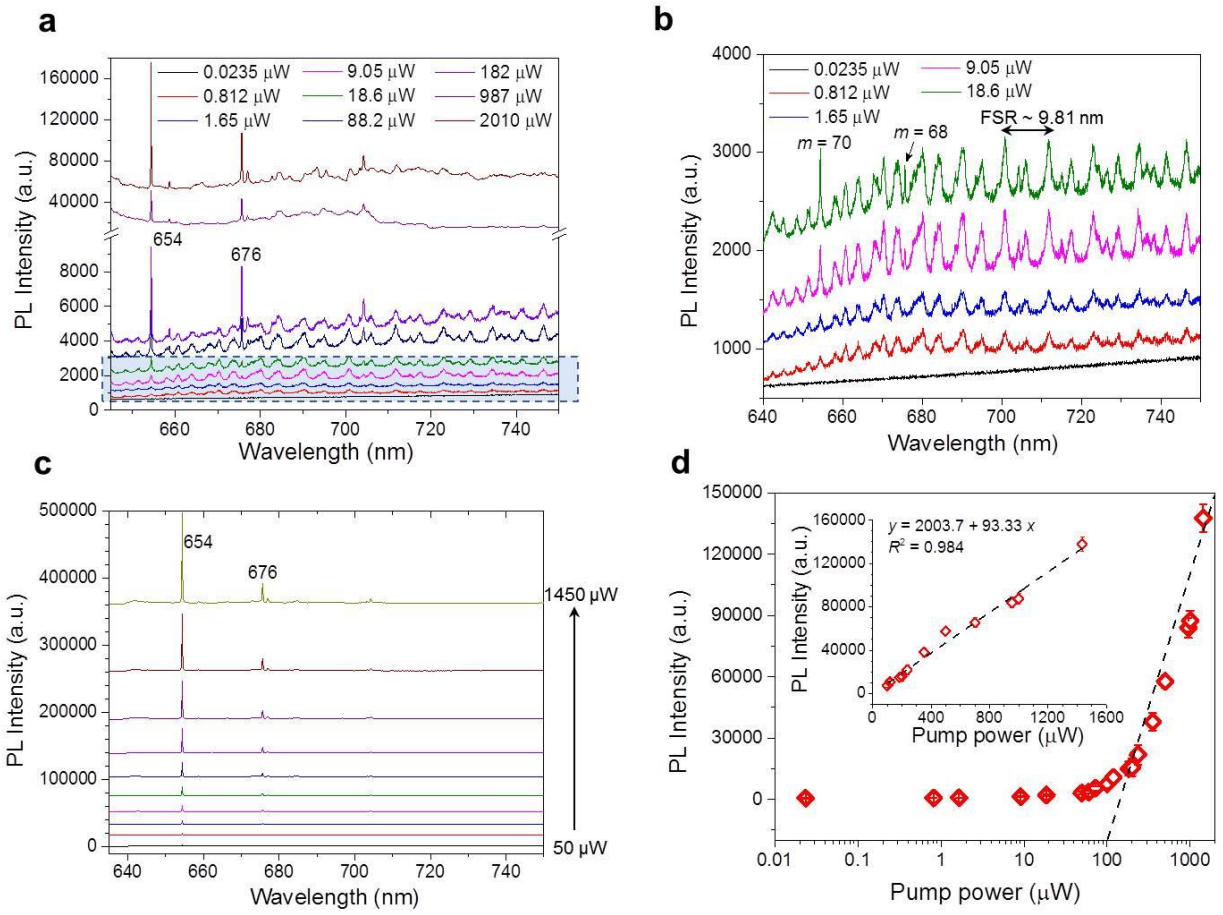

Figure 11.2: Seed injection amplification on a DiP-PRET system. **a,** The photoluminescence (PL) emission from a single bead (D=10.14 μm) on a DiP-PRET system as a function of input laser power. **b,** Enlarged view of part of the PL spectra shown as shaded region in **a. c,** PL spectra with careful variation of input laser power by using neutral density filters. **d,** The peak PL intensity dependence on the excitation pump power at λ=654 nm. The inset shows the linear fit to data above threshold of 100 μW. The error bars represent PL intensity variation at the same power and corresponds to $\pm$1 standard deviation.

Figure 11.2a shows the PL spectra for a single DiP-PRET system (single bead) at room temperature. The PL intensity increases with increasing pump power of the incident laser. Figure 11.2b (zoomed in for the shaded region in Fig. 11.2a) clearly shows the WGM resonance like behavior of the PL spectra at low incident power. The experimental FSR~ 9.81 nm matches well with the simulation results. Above a threshold power of 100 μW (with incident intensity, 8

kW/cm^2), the output PL intensity at λ=654 and 676 nm rose exponentially with increasing pump energy. The emission spectra are substantially narrowed (FWHM, 0.19 nm at λ=654 nm, FWHM, 0.22 nm at λ=676 nm) compared to free space spontaneous emission spectrum of the dye (FWHM, 43 nm) with emission maximum at λ=676 nm. The WGR has modes (*m*=68, *m*=70) at λ=676 nm and λ=654 nm, respectively. To identify the threshold, the PL spectra are obtained as a function of incident power with small intervals (Figure 11.2c). The variation of integrated PL intensity at 654 nm (Figure 11.2d) shows non-linear characteristics with a clear threshold at 100 μW. The output PL intensity data above the threshold can be fit with a linear line (Figure 11.2d, inset).

Out of the four possibilities mentioned earlier we rule out the first two- spontaneous emission of dye and coupling of dye to plasmonic substrate- as they do not explain the behavior obtained in Figure 11.2a and b. As shown in Fig. 11.6 and 11.7, the spontaneous emission of dye and coupling of dye to plasmonic substrate has broad emission spectra. Even though dye coupled to WGR on glass substrate (without the plasmonic substrate) reveals narrow emission spectrum (at 654 nm and 676 nm), the intensity of these peaks is two order of magnitude smaller compared to DiP-PRET system. Figure 11.3a shows a comparison of PL intensity with incident laser power for DiP-PRET system, with and without dye, to that of dye on glass, plasmonic substrate and WGR at λ=654 nm. The DiP-PRET system with dye showed order of magnitude higher PL intensity compared to other cases.

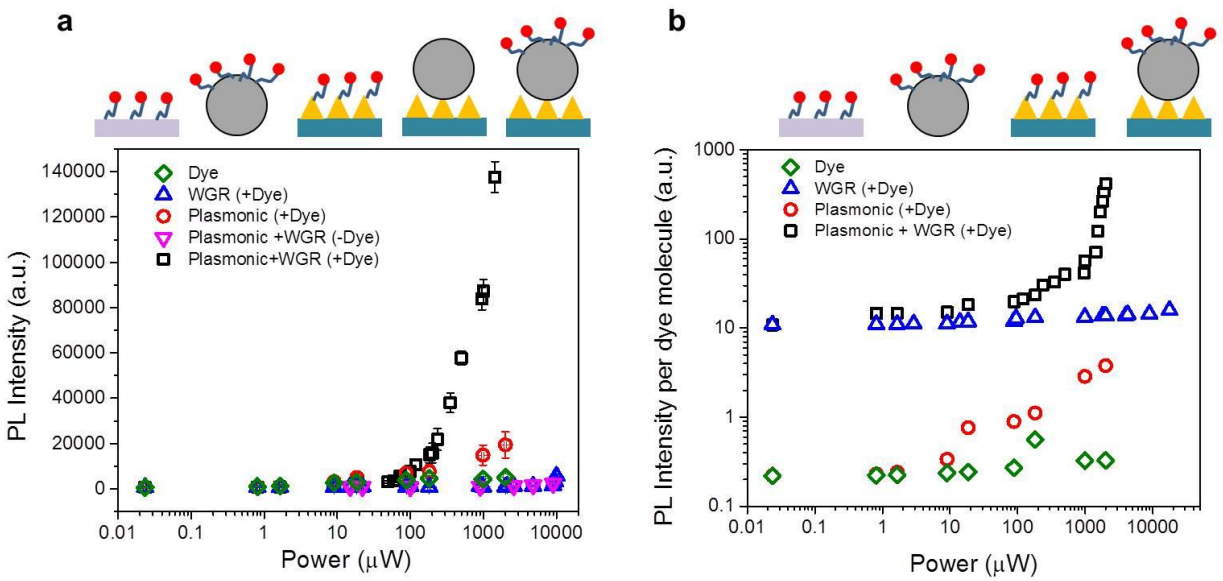

Figure 11.3: Photoluminescence enhancement on a DiP-PRET system. **a,** Comparison of PL intensity at λ=654 nm of WGR, with and without dye on a glass/ plasmonic substrate, and dye alone on glass/ plasmonic substrate. The schematics of each case are shown above the plot. The data points are collected from PL spectrum obtained at each power for individual cases. The error bars for WGR indicates sphere-to-sphere variation. The error bars for dye, plasmonic + dye indicates spot-to-spot variation. All error bars correspond to ±1 standard deviation. **b,** Comparison of average PL intensity per dye molecule at λ=676 nm for WGR, plasmonic and plasmonic + WGR. The dye used is DyLight 650.

Due to the narrowing spectrum features and enhanced intensity, we argue that the observed behavior in Figure 3a is due to the energy transfer from dipole of the dye molecules to surface plasmon mode by means of the WGM of the dielectric resonator as predicted in Fig. 1d. As we show later, the stimulated Raman process can be ruled out as an alternative explanation for our observation. Figure 11.3b shows a comparison of average PL intensity per dye molecule on a WGR, plasmonic substrate and DiP-PRET system corresponding to resonance peak at λ=676 nm. With a hydrodynamic diameter of 11.1±0.1 nm [274] for avidin-biotin complex and average 1.9 dye molecules per NeutrAvidin, the average number of dye molecules per 10.14 μm microsphere at saturation is ~ 1.6 x 10^6. The average number of dye molecules per microsphere on a laser spot size of 1.25 μm^2 is calculated to be 4750. Similar number of molecules on glass (4722) within

equal laser spot size can be obtained by spreading 1 µL of 100 nM dye solution on 12.56 mm^2 area. By comparing the PL counts per dye molecule on DiP-PRET system and on glass, we obtained a fluorescence signal enhancement of about 1278 fold at λ=676 nm.

Calculation of number of dye molecules conjugated to microspheres

The concentration of protein (NA) in the sample was measured using a NanoDrop ND-1000 spectrophotometer (Nano Drop Technologies, Rockland, Delaware, USA) by using the absorbance value at A_{280} and A_{650}. The protein concentration was measured as, Protein concentration $(\mathrm{M}) = \left[A_{280} - CF \times (A_{650})\right] \times \text{dilution factor} / \varepsilon$, where ε is the molar extinction coefficient of the protein and *CF* is the correction factor for the dye's contribution to A_{280}. The degree of labeling, DOL, (moles dye per mole protein) was calculated as, DOL $= A_{650} \times \text{dilution factor} / (\varepsilon' \times \text{protein concentration (M)})$, where ε' is the molar extinction coefficient of the fluorescent dye.

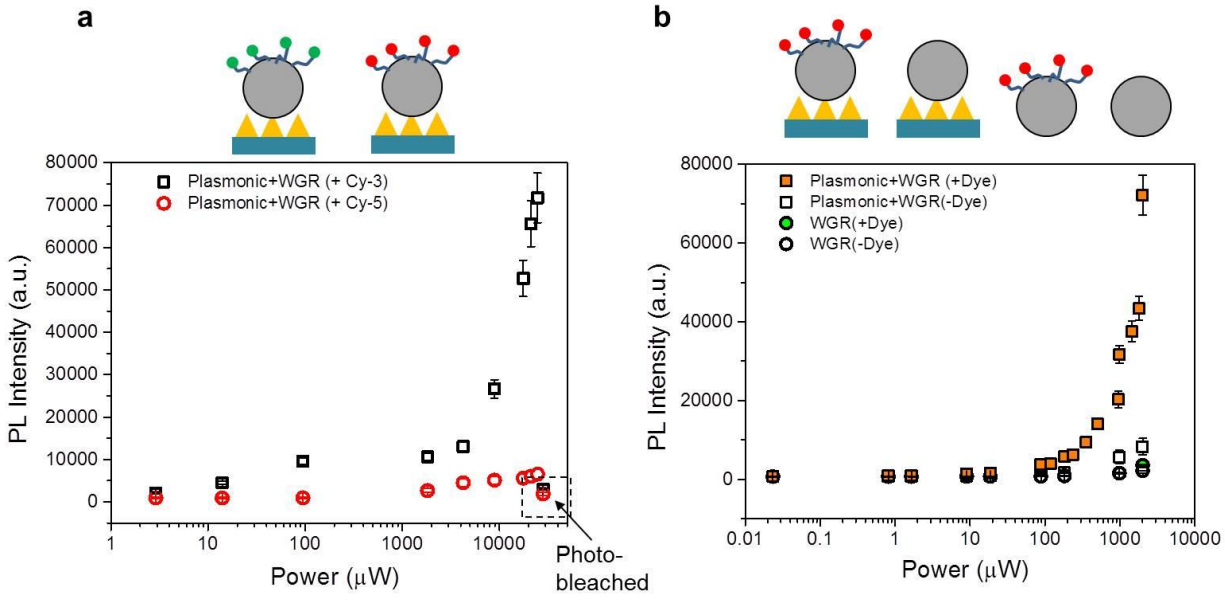

Figure 11.4: Necessity of gain medium and plasmonic substrate for DiP-PRET system to obtain seed injection amplification. **a,** Comparison of PL intensity at λ=563 nm for DiP-PRET system with Cy-3 and Cy-5 dye. The excitation laser wavelength is λ=532 nm. The PL spectra are obtained in the wavelength

range of λ=540-620 nm. **b,** Comparison of PL intensity at λ=676 nm with different power for WGR with and without dye on glass/ plasmonic substrate. The excitation laser wavelength is λ=633 nm. The dye used is DyLight 650. The PL spectra are collected in the range of λ=635-750 nm. All error bars represent ±1 standard deviation.

In order to verify the necessity of gain medium in the DiP-PRET process two samples were prepared: one microsphere conjugated with Cy-3 dye, and the other microsphere conjugated with Cy-5 dye. We used a 532 nm laser to excite the dye and measure the PL spectra from λ=540-620 nm range. Since Cy-3 has emission peak at 563 nm and Cy-5 has emission peak at 676 nm, only the microsphere with the Cy-3 dye will have the gain medium in the detection range. Figure 11.4a shows the comparison of PL intensity for Cy-3 and Cy-5 with power. Cy-3 has much higher PL intensity compared to Cy-5. This proves that DiP-PRET is a seed injection process and gain medium is a necessity for efficient DiP-PRET system. In order to rule out the stimulated Raman scattering process at 654 nm we took the Raman spectra of polystyrene sphere with 532 nm and 633 nm excitation. We did not find any Raman peak at 654 nm (Fig. 11.8) but we found a peak at stokes shift of 1002 cm^{-1} (corresponding to 676 nm for 633 nm excitation, and 563 nm for 532 nm excitation). Figure 11.4b compares the PL intensity with and without the dye on microsphere for a DiP-PRET and glass system. Since the stimulated Raman scattering process in less efficient compared to fluorescence the contribution from stimulated scattering at λ= 676 nm can be ruled out. The so called optoplasmonic scheme also showed ~100 times less amplification than DiP-PRET system (Fig. 11.9), consistent with the recently reported result [240].

All the ingredients required for seed injection amplification- gain medium, stimulated emission, population inversion- are present in the DiP-PRET system. With absorption cross-section of 9.5 x 10^{-16} cm^2 and fluorescence quantum yield of 24%, DyLight 650 dye can act as a

gain medium. The stimulated excitation of the dye is provided by the WGR and surface plasmon substrate. The population inversion could be explained through a quasi-four-level system (Figure 11.5a). After the absorption of an incident pump photon, the dye molecule will undergo a transition from the ground state, $|0\rangle$ to a higher electronic state $|3\rangle$. Both ground state and excited state are composed of numerous vibrational states typically responsible for the observed broad absorption and emission spectra [275]. Once in the excited state, the dye will quickly relax (~ ps) into its lowest vibrational state, $|2\rangle$, through a non-radiative transfer process. From level $|2\rangle$ to level $|1\rangle$, the transition can occur through either spontaneous emission process or stimulated emission process [275]. Since, the relaxation of molecules in vibrational levels is fast, population inversion is feasible if population at level $|2\rangle$ is higher than that of level $|1\rangle$ ($N_2 > N_1$). One of the possibilities in achieving it is by increasing the effective lifetime at level $|2\rangle$.

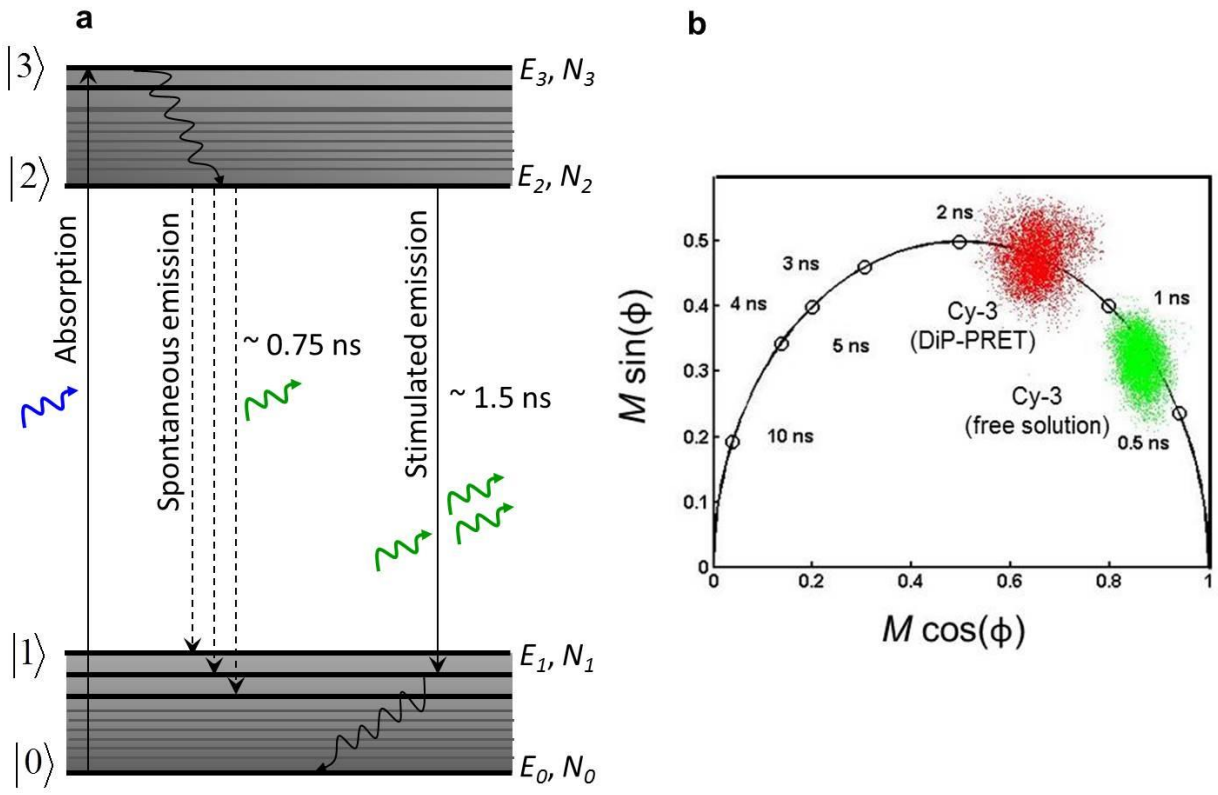

Figure 11.5: Scheme to obtain seed injection amplification. **a,** Energy diagram of quasi-four-level system for a model DiP-PRET system with Cy-3. **b,** Experimental polar plot representation of fluorescence lifetime for Cy-3 in free solution (Petri Dish) and on a DiP-PRET system. Here, *M* is the modulation ratio associated with lifetime and ϕ is phase corresponding to lifetime component which can be represented as [22], $M = \frac{1}{\sqrt{1+(\omega\tau)^2}}, \phi = \tan^{-1}(\omega\tau)$. ω is the circular frequency of modulation and τ is the fluorescence lifetime of the dye.

We measured the lifetime of Cy-3 in free solution and on a DiP-PRET system using frequency-domain fluorescence lifetime imaging microscopy (FLIM) system [252]. In free solution, the lifetime of Cy-3 is measured to be 0.75 ns, whereas on the DiP-PRET system the lifetime is increased by 2 times to 1.5 ns (Fig. 11.5b) pointing to the feasibility of population inversion. Hence, a net gain for the dye can be achieved with DiP-PRET system.

We also calculate the energy transfer efficiency [235], η, in the DiP-PRET system as $\eta = I_{DiP-PRET} / (I_{DiP-PRET} + I_{D-Ph} + f_1 * I_{D-Pl} + f_2 * I_D)$, where $I_{DiP\text{-}PRET}$, $I_{D\text{-}Ph}$, $I_{D\text{-}Pl}$, I_D are the integrated PL intensities in the wavelength range of λ= 650-720 nm (covering the spectral spread of gain medium) for the DiP-PRET, dipole-Photonic, dipole-Plasmonic and dipole-glass system respectively; f_1 and f_2 are the correction factors to account for the variation in PL intensity due to number of molecules present on plasmonic and glass substrate compared to microspheres (WGR). To get a better signal-to-noise ratio, a higher concentration of dye (1 µM) was used on plasmonic and glass substrate (Fig. 11.6-11.7). By averaging the PL intensities obtained from more than 100 microspheres over an area of 2 mm^2, we calculated an efficiency of ~ 90.5 %.

Fluorescence fluorescence intensity comparison with different concentration

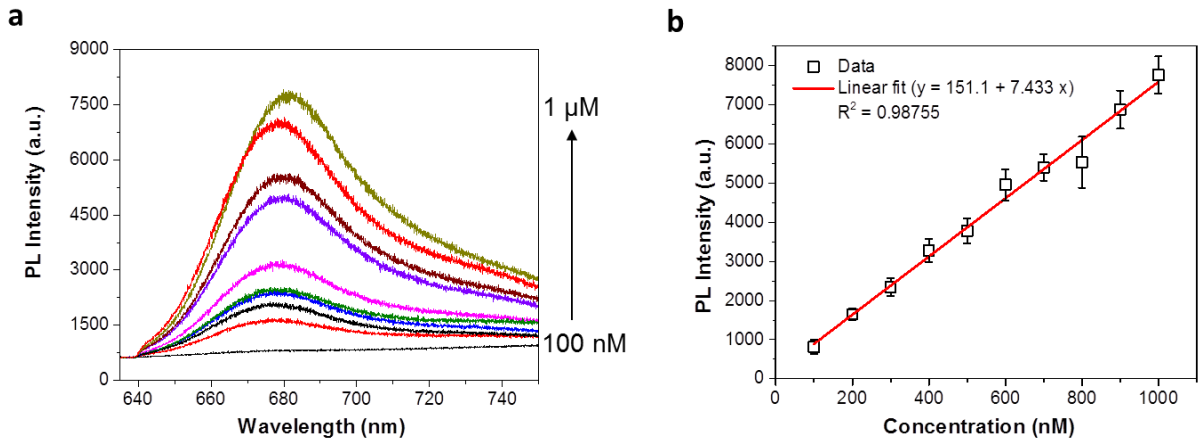

Figure 11.6: (a) Variation of PL intensities with increasing concentration of NA-DyLight 650 from 100 nM to 1 µM. The objective used was 50x, accumulation time of 10s, incident power of 9.05 µW, and excitation wavelength of 632.8 nm. (b) The peak PL intensities in (a) can be fit to a linear curve with R^2 = 0.98755. The slope of the curve gives intensity of 7.433 counts/ nM concentration. This value is used in calculating the PL intensity counts per dye molecule in Fig. 11.3b.

PL intensity of dye (DyLight 650) at different power on Glass and on Nanopillar

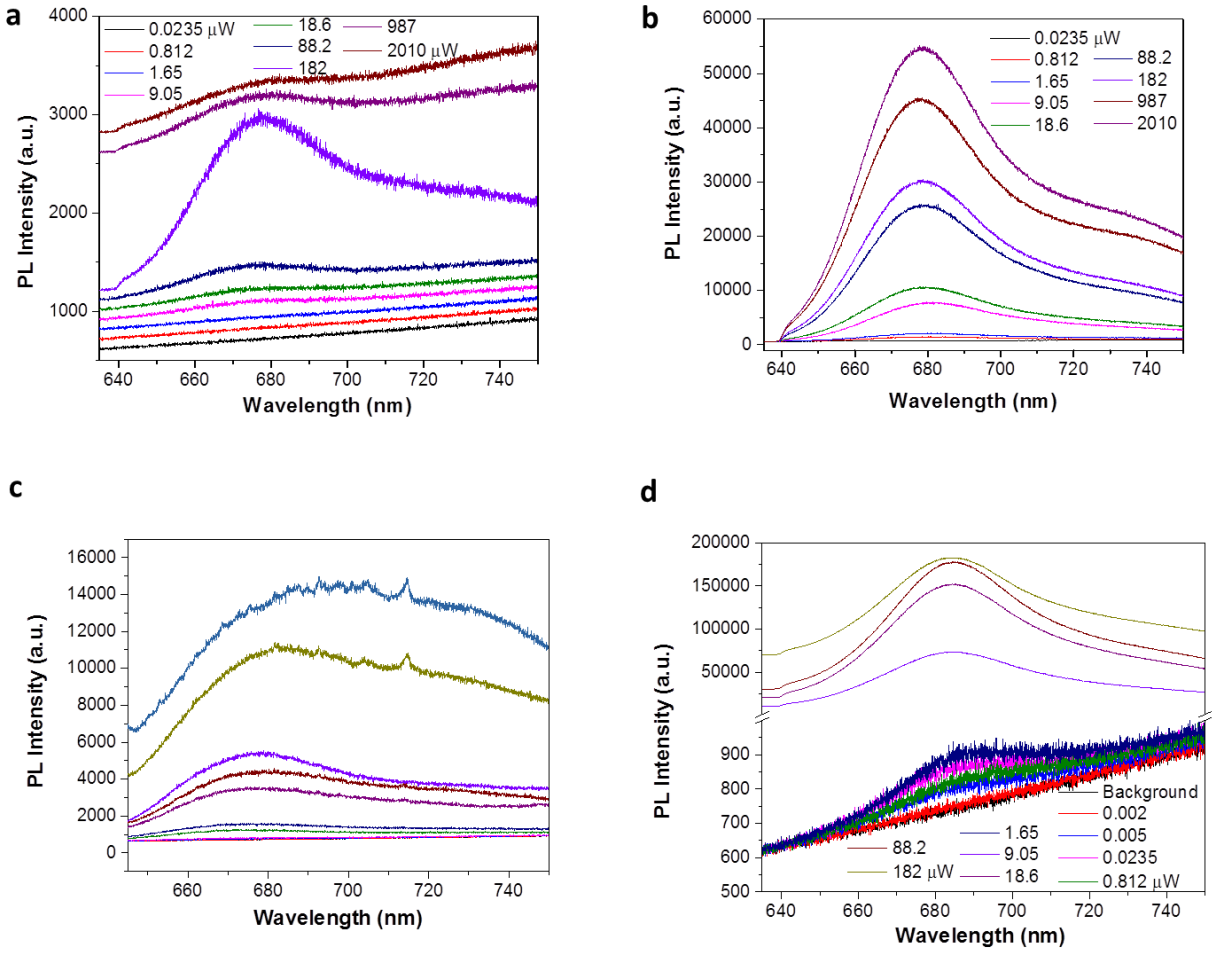

Figure 11.7: (a) PL intensity of NA-DyLight 650 (concentration = 100 nM) on glass at different incident power. (b) PL intensity of NA-DyLight 650 (concentration = 1 µM) on glass at different incident power. (c) PL intensity of NA-DyLight 650 (concentration = 100 nM) on nanopillar plasmonic substrate at different incident power. (d) PL intensity of NA-DyLight 650 (concentration = 1 µM) on nanopillar plasmonic substrate at different incident power. For all the spectra, the incident wavelength is 632.8 nm, accumulation time is 10s and objective used is 50x. The correction factors used to calculate the energy transfer efficiency (f_1, f_2) is derived from these spectra.

Raman spectra of 10.14 µm microsphere without dye

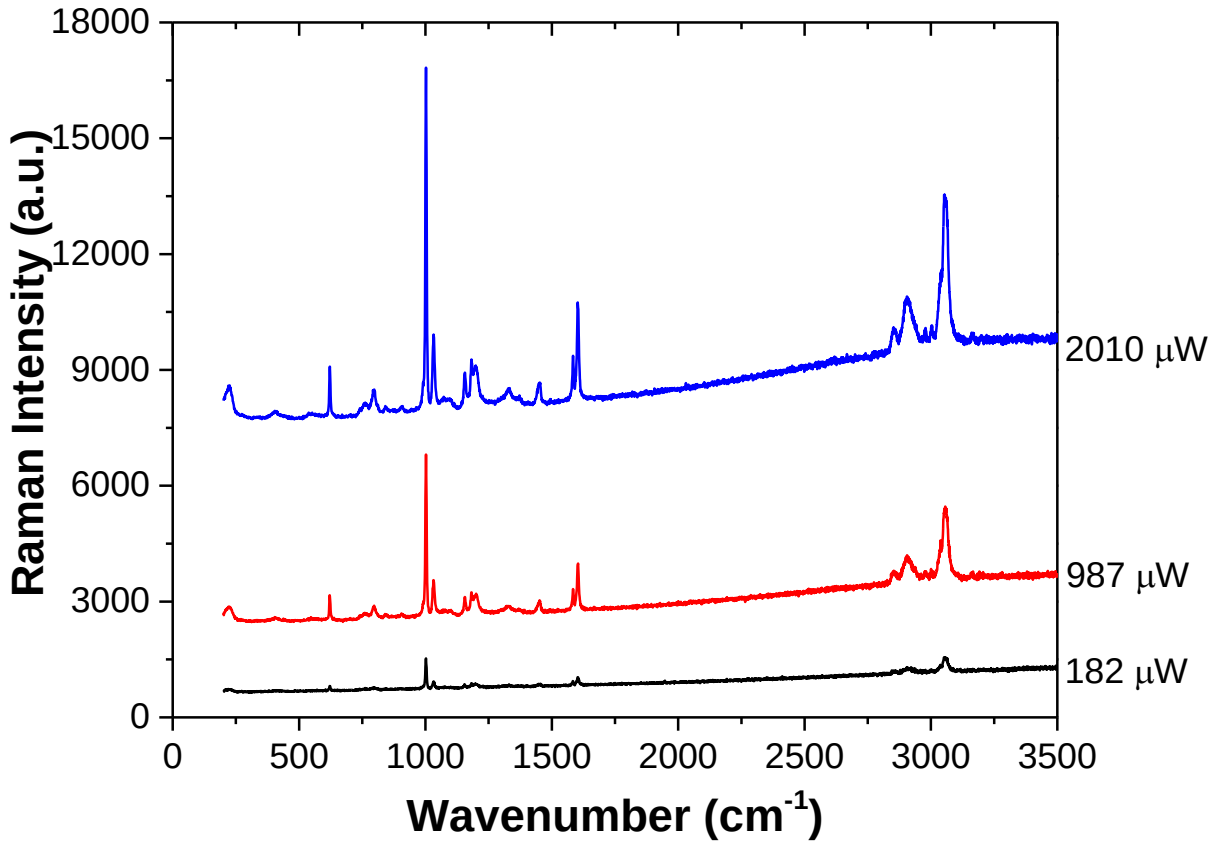

Figure 11.8: Raman spectra of 10 µm microsphere without dye at different dye. The excitation wavelength is 632.8 nm, objective used is 50x and accumulation time to get one spectrum is 10s. The strong peak at 1002 cm^{-1} corresponds to a stokes shifted wavelength of λ=676 nm. It is important to notice that there is no stokes shifted Raman peak at λ=654 nm, which is strongly enhanced in our DiP-PRET system. This again confirms that the peak enhanced observed at λ=654 nm is not due to stimulated scattering processes.

Results for Optoplasmonic scheme

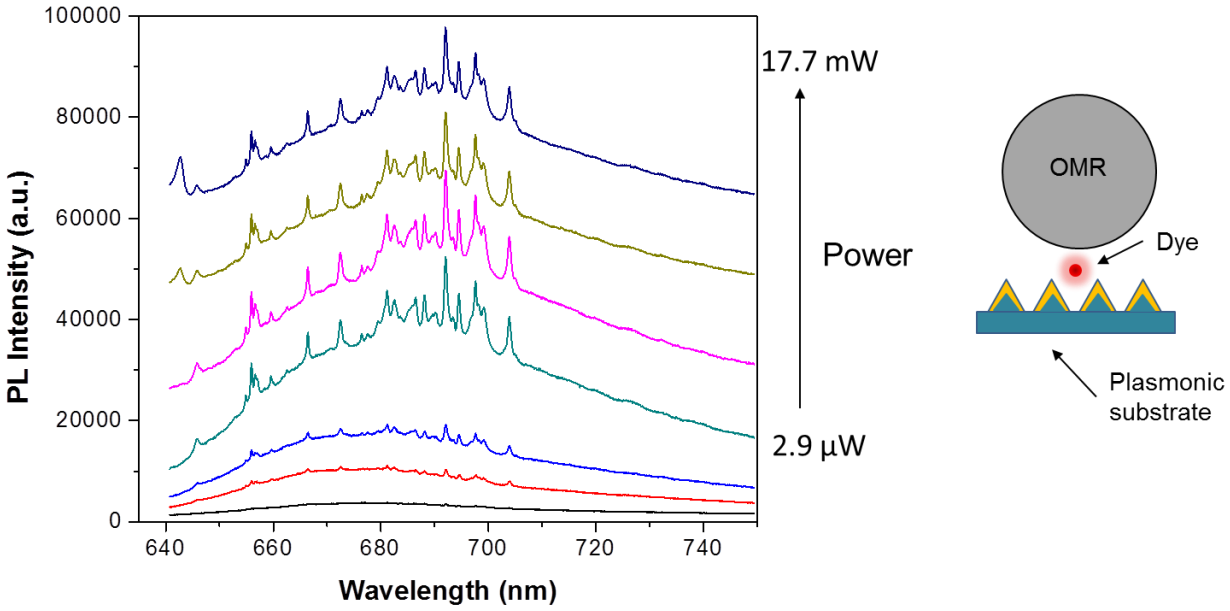

Figure 11.9: The PL spectra obtained at different power for an Optoplasmonic (plasmonic-dipole-photonic) scheme. In this case the dye (Cy-5) is first attached to the plasmonic substrate and then the 10.14 µm microsphere without any dye conjugated to it, was drop casted on it. The broad fluorescence background (with a peak at ~ 680 nm) for all the spectra is evident. Many narrow Raman scattered peaks and WGM related peaks are also superimposed on the broad fluorescence background. It is important to notice that the spectral features are quite different than DiP-PRET system (where enhancement of specific peaks occurs with suppression of fluorescence background). Also, quantitatively, the peak enhancement at λ= 654 and 676 nm are much smaller (~ 100 times smaller) compared to DiP-PRET system. The schematic of the Optoplasmonic system is sketched to the right. For all the spectra, the incident wavelength is 632.8 nm, accumulation time is 10s and objective used is 50x.

Conclusions

In summary, using the DiP-PRET system we achieved seed injection amplification with over 90% energy transfer efficiency and 1278-fold fluorescence enhancement. Emission spectral peak with linewidth as narrow as 0.19 nm was realized at room temperature, paving the way for highly sensitive and selective detection of low concentration and even single biomolecules. We envision that the results of this work can be adapted to a wide variety of microbead based assay

including biomolecular sensing, cytometry and sandwiched assays (miRNA, DNA, ELISA) with enhanced sensitivity and selectivity. The laser-like emission demonstrated in the DiP-PRET system also suggests a new design of continuous wave pumped laser with integrated WGR and nanoplasmonic structures.

References

[1] T. Forster, "Transfer mechanisms of electronic excitation energy," *Bioenergetics Radiation Res*, vol. Suppl. 2, pp. 326-339, 1960, 1960.

[2] M. Berggren, A. Dodabalapur, R. E. Slusher and Z. Bao, "Light amplification in organic thin films using cascade energy transfer," *Nature*, vol. 389, pp. 466-469, OCT 2 1997, 1997.

[3] G. L. Liu, Y. Long, Y. Choi, T. Kang and L. P. Lee, "Quantized plasmon quenching dips nanospectroscopy via plasmon resonance energy transfer," *Nature Methods*, vol. 4, pp. 1015-1017, DEC 2007, 2007.

[4] D. L. Dexter, "A Theory of Sensitized Luminescence in Solids," *J. Chem. Phys.*, vol. 21, pp. 836-850, 1953, 1953.

[5] P. Andrew and W. L. Barnes, "Energy transfer across a metal film mediated by surface plasmon polaritons," *Science*, vol. 306, pp. 1002-1005, NOV 5 2004, 2004.

[6] F. Vollmer and S. Arnold, "Whispering-gallery-mode biosensing: label-free detection down to single molecules," *Nature Methods*, vol. 5, pp. 591-596, JUL 2008, 2008.

[7] B. Min, E. Ostby, V. Sorger, E. Ulin-Avila, L. Yang, X. Zhang and K. Vahala, "High-Q surface-plasmon-polariton whispering-gallery microcavity," *Nature*, vol. 457, pp. 455-U3, JAN 22 2009, 2009.

[8] Y. Sun, S. I. Shopova, C. Wu, S. Arnold and X. Fan, "Bioinspired optofluidic FRET lasers via DNA scaffolds," *Proc. Natl. Acad. Sci. U. S. A.*, vol. 107, pp. 16039-16042, SEP 14 2010, 2010.

[9] S. V. Boriskina and B. M. Reinhard, "Spectrally and spatially configurable superlenses for optoplasmonic nanocircuits," *Proc. Natl. Acad. Sci. U. S. A.*, vol. 108, pp. 3147-3151, FEB 22 2011, 2011.

[10] W. Ahn, Y. Hong, S. V. Boriskina and et al., "Demonstration of efficient on-chip photon transfer in self-assembled optoplasmonic networks," *ACS Nano*, vol. 7, pp. 4470-4478, 2013.

[11] W. Ahn, S. V. Boriskina, Y. Hong and B. M. Reinhard, "Photonic-Plasmonic Mode Coupling in On-Chip Integrated Optoplasmonic Molecules," *Acs Nano*, vol. 6, pp. 951-960, JAN 2012, 2012.

[12] D. Gerard, J. Wenger, A. Devilez, D. Gachet, B. Stout, N. Bonod, E. Popov and H. Rigneault, "Strong electromagnetic confinement near dielectric microspheres to enhance single-molecule fluorescence," *Optics Express*, vol. 16, pp. 15297-15303, SEP 15, 2008.

[13] B. Krajnik, M. Gajda-Raczka, D. Piatkowski, P. Nyga, B. Jankiewicz, E. Hofmann and S. Mackowski, "Silica nanoparticles as a tool for fluorescence collection efficiency enhancement," *Nanoscale Research Letters*, vol. 8, pp. 146, MAR 28, 2013.

[14] J. J. Schwartz, S. Stavrakis and S. R. Quake, "Colloidal lenses allow high-temperature single-molecule imaging and improve fluorophore photostability," *Nature Nanotechnology*, vol. 5, pp. 127-132, FEB, 2010.

[15] D. Gerard, A. Devilez, H. Aouani, B. Stout, N. Bonod, J. Wenger, E. Popov and H. Rigneault, "Efficient excitation and collection of single-molecule fluorescence close to a dielectric microsphere," *Journal of the Optical Society of America B-Optical Physics*, vol. 26, pp. 1473-1478, JUL, 2009.

[16] W. L. Barnes, "Fluorescence near interfaces: the role of photonic mode density," *Journal of Modern Optics*, vol. 45, pp. 661-699, APR 1998, 1998.

[17] S. Gotzinger, L. D. Menezes, A. Mazzei, S. Kuhn, V. Sandoghdar and O. Benson, "Controlled photon transfer between two individual nanoemitters via shared high-Q modes of a microsphere resonator," *Nano Letters*, vol. 6, pp. 1151-1154, JUN 2006, 2006.

[18] V. J. Sorger, R. F. Oulton, J. Yao, G. Bartal and X. Zhang, "Plasmonic Fabry-Perot Nanocavity," *Nano Letters*, vol. 9, pp. 3489-3493, OCT, 2009.

[19] L. K. Ausman and G. C. Schatz, "Whispering-gallery mode resonators: Surface enhanced Raman scattering without plasmons," *J. Chem. Phys.*, vol. 129, pp. 054704, AUG 7, 2008.

[20] K. Vahala, "Optical microcavities," *Nature*, vol. 424, pp. 839-846, AUG 14, 2003.

[21] W. Zhou, M. Dridi, J. Y. Suh, C. H. Kim, D. T. Co, M. R. Wasielewski, G. C. Schatz and T. W. Odom, "Lasing action in strongly coupled plasmonic nanocavity arrays," *Nature Nanotechnology*, vol. 8, pp. 506-511, 2013.

[22] M. R. Gartia, J. P. Eichorst, R. M. Clegg and G. L. Liu, "Lifetime imaging of radiative and non-radiative fluorescence decays on nanoplasmonic surface," *Appl. Phys. Lett.*, vol. 101, pp. 023118, JUL 9, 2012.

[23] A. F. Koenderink, "On the use of Purcell factors for plasmon antennas," *Opt. Lett.*, vol. 35, pp. 4208-4210, DEC 15, 2010.

[24] M. I. Stockman, "The spaser as a nanoscale quantum generator and ultrafast amplifier," *Journal of Optics*, vol. 12, pp. 024004, FEB, 2010.

[25] M. R. Gartia, A. Hsiao, A. Pokhriyal, S. Seo, G. Kulsharova, B. T. Cunningham, T. C. Bond and G. L. Liu, "Colorimetric Plasmon Resonance Imaging Using Nano Lycurgus Cup Arrays," *Advanced Optical Materials*, vol. 1, pp. 68-76, 2013.

[26] S. V. Boriskina and B. M. Reinhard, "Adaptive on-chip control of nano-optical fields with optoplasmonic vortex nanogates," *Optics Express*, vol. 19, pp. 22305-22315, OCT 24 2011, 2011.

[27] A. Kinkhabwala, Z. Yu, S. Fan, Y. Avlasevich, K. Muellen and W. E. Moerner, "Large single-molecule fluorescence enhancements produced by a bowtie nanoantenna," *Nature Photonics*, vol. 3, pp. 654-657, NOV, 2009.

[28] D. Punj, M. Mivelle, S. B. Moparthi, T. S. van Zanten, H. Rigneault, N. F. van Hulst, M. F. Garcia-Parajo and J. Wenger, "A plasmonic 'antenna-in-box' platform for enhanced single-molecule analysis at micromolar concentrations," *Nature Nanotechnology*, vol. 8, pp. 512-516, 2013.

[29] S. Kim, J. Jin, Y. Kim, I. Park, Y. Kim and S. Kim, "High-harmonic generation by resonant plasmon field enhancement," *Nature*, vol. 453, pp. 757-760, JUN 5, 2008.

[30] S. Nie and S. Emery, "Probing single molecules and single nanoparticles by surface-enhanced Raman scattering," *Science*, vol. 275, pp. 1102-1106, FEB 21, 1997.

[31] R. F. Oulton, V. J. Sorger, T. Zentgraf, R. Ma, C. Gladden, L. Dai, G. Bartal and X. Zhang, "Plasmon lasers at deep subwavelength scale," *Nature*, vol. 461, pp. 629-632, OCT 1, 2009.

[32] A. Kaplan, M. Tomes, T. Carmon, M. Kozlov, O. Chen, G. Bartal and H. G. L. Schwefel, "Finite element simulation of a perturbed axialsymmetric whispering-gallery mode and its use for intensity enhancement with a nanoparticle coupled to a microtoroid," *Optics Express*, vol. 21, pp. 14169-14180, 2013.

[33] Y. Xiao, Y. Liu, B. Li, Y. Chen, Y. Li and Q. Gong, "Strongly enhanced light-matter interaction in a hybrid photonic-plasmonic resonator," *Physical Review A*, vol. 85, pp. 031805, MAR 27, 2012.

[34] J. D. Swaim, J. Knittel and W. P. Bowen, "Detection limits in whispering gallery biosensors with plasmonic enhancement," *Appl. Phys. Lett.*, vol. 99, pp. 243109, DEC 12, 2011.

[35] J. Zhu, S. K. Ozdemir, Y. Xiao, L. Li, L. He, D. Chen and L. Yang, "On-chip single nanoparticle detection and sizing by mode splitting in an ultrahigh-Q microresonator," *Nature Photonics,* vol. 4, pp. 46-49, JAN 10, 2010.

[36] W. Kim, V. Safonov, V. Shalaev and R. Armstrong, "Fractals in microcavities: Giant coupled, multiplicative enhancement of optical responses," *Phys. Rev. Lett.,* vol. 82, pp. 4811-4814, JUN 14, 1999.

[37] K. A. Fuller and D. D. Smith, "Cascaded photoenhancement from coupled nanoparticle and microcavity resonance effects," *Optics Express,* vol. 15, pp. 3575-3580, MAR 19, 2007.

[38] I. White, H. Oveys and X. Fan, "Increasing the enhancement of SERS with dielectric microsphere resonators," *Spectroscopy,* vol. 21, pp. 36-+, APR, 2006.

[39] S. I. Shopova, R. Rajmangal, S. Holler and S. Arnold, "Plasmonic enhancement of a whispering-gallery-mode biosensor for single nanoparticle detection," *Appl. Phys. Lett.,* vol. 98, pp. 243104, JUN 13, 2011.

[40] M. A. Santiago-Cordoba, S. V. Boriskina, F. Vollmer and M. C. Demirel, "Nanoparticle-based protein detection by optical shift of a resonant microcavity," *Appl. Phys. Lett.,* vol. 99, pp. 073701, AUG 15, 2011.

[41] V. R. Dantham, S. Holler, V. Kolchenko, Z. Wan and S. Arnold, "Taking whispering gallery-mode single virus detection and sizing to the limit," *Appl. Phys. Lett.,* vol. 101, pp. 043704, JUL 23, 2012.

[42] Y. Chen, Z. Xu, M. R. Gartia, D. Whitlock, Y. Lian and G. L. Liu, "Ultrahigh Throughput Silicon Nanomanufacturing by Simultaneous Reactive Ion Synthesis and Etching," *Acs Nano,* vol. 5, pp. 8002-8012, OCT, 2011.

[43] M. Oxborrow, "Traceable 2D finite-element simulation of the whispering-gallery modes of axisymmetric electromagnetic resonators," *IEEE Trans. Microw. Theory Tech.,* vol. 55, pp. 1209-1218, 2007.

[44] C. S. Neish, I. L. Martin, R. M. Henderson and J. M. Edwardson, "Direct visualization of ligand-protein interactions using atomic force microscopy," *Br. J. Pharmacol.,* vol. 135, pp. 1943-1950, APR 2002, 2002.

[45] M. C. Gather and S. H. Yun, "Single-cell biological lasers," *Nature Photonics,* vol. 5, pp. 406-410, JUL, 2011.

CHAPTER 12

PERSPECTIVE AND FUTURE DIRECTIONS ON PLASMONICS

Plasmonics has become a field of its own. Plasmonics offers new fundamental science as well as practical real world applications. We have made tremendous progress miniaturizing things starting from the telegraph in 1820's to today's computer chip (Figure 12.1). But we are hitting "the wall" in terms of achieving operating speed of the device. Figure 12.2 shows the operating speed and device sizes of semiconductors (electronics), insulators (photonics), and metals (plasmonics). The physical limitations of different technologies are shown by the dashed line. For example, heat generation and interconnect delay time limits the speed achievable in semiconductor electronics to about 10 GHz. Similarly, the fundamental laws of diffraction limit the size of dielectric photonics [276]. Fundamentally, plasmonics has the potential to break these limits and possibly link photonics and nanoelectronics. Besides, due to the high sensitivity of plasmonics based sensors, plasmonics has already found real world applications, particularly refractive-index-based sensors for drug, pharma industry and biology laboratory in general. In fact, the focus of my thesis was mainly concerned with the biosensing application of plasmonics.

Plasmonics is at its best providing nanoscale confinement and high spatial localization of electromagnetic field. Nanoscale confinement leads to small mode volume, further decreasing the feature size of the devices. The high spatial localization leads to increase in effective electric field and change in local density of photonic states (LDOS). In turn, this affects the excitation and emission properties of nearby molecules or emitters. The high Purcell factor provided by plasmonics has already been used for fluorescence enhancement [257, 258], surface enhanced Raman spectroscopy [260], and even lasing [251].

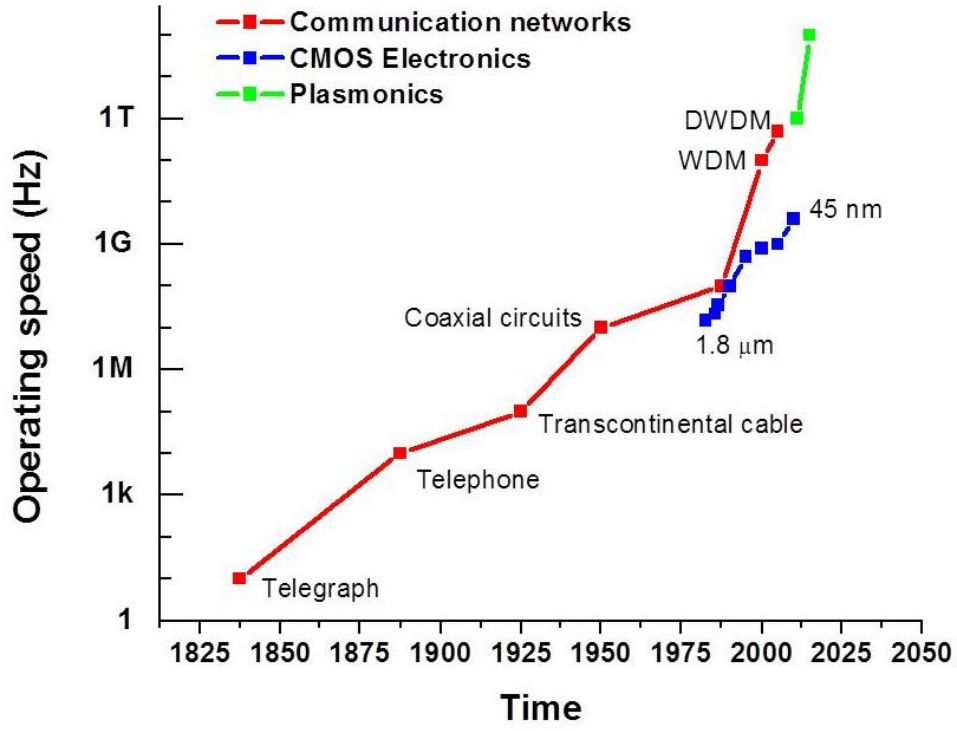

Figure 12.1: Progress made in past century and outlook for the future.

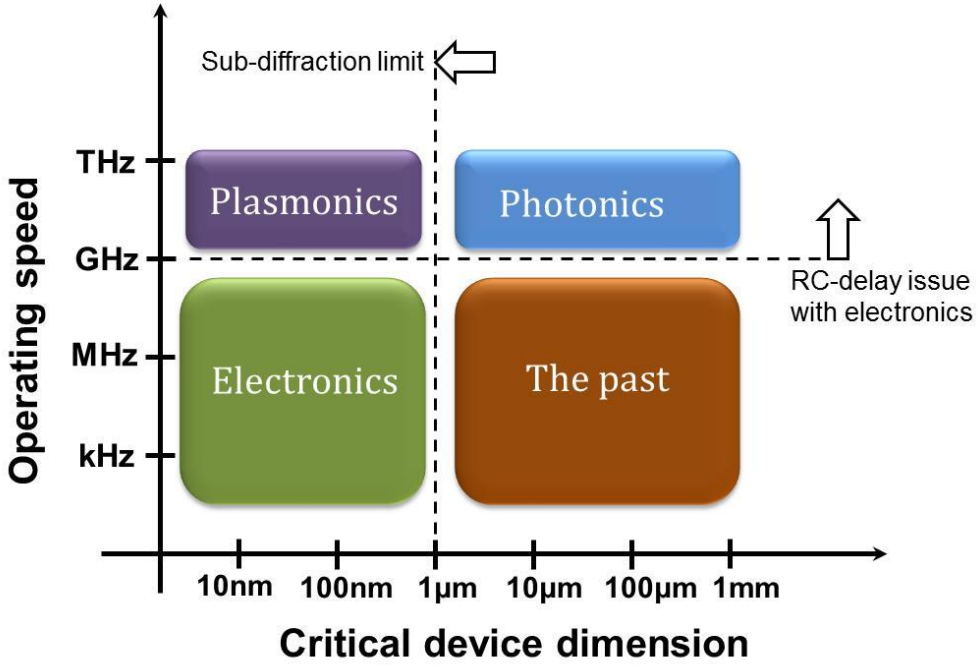

Figure 12.2: Operating speed achieved by different devices. Image adapted from [276].

Nonlinear plasmonics

The thesis mainly deals with linear spectroscopy and linear behavior of plasmonics. Nonlinear optical behaviors are predominantly weak as they are governed by photon-photon interactions [277]. Plasmonics can offer interesting nonlinear behavior as it can increase the local electromagnetic field by multiple orders of magnitude facilitating strong optical nonlinearity. Recently, plasmonics has been utilized for second harmonic generation [278, 279], higher harmonic generation [280], plasmonic waveguide for extreme-ultraviolet (EUV) light generation [281].

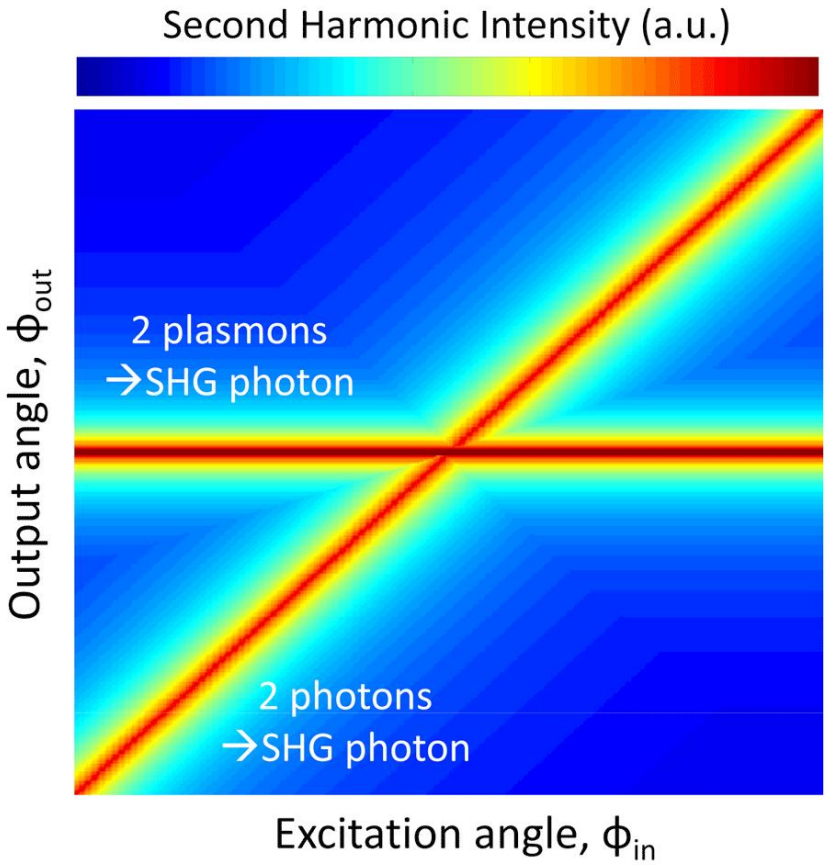

Figure 12.3: Second harmonic generation (SHG) on plasmonic structures [278].

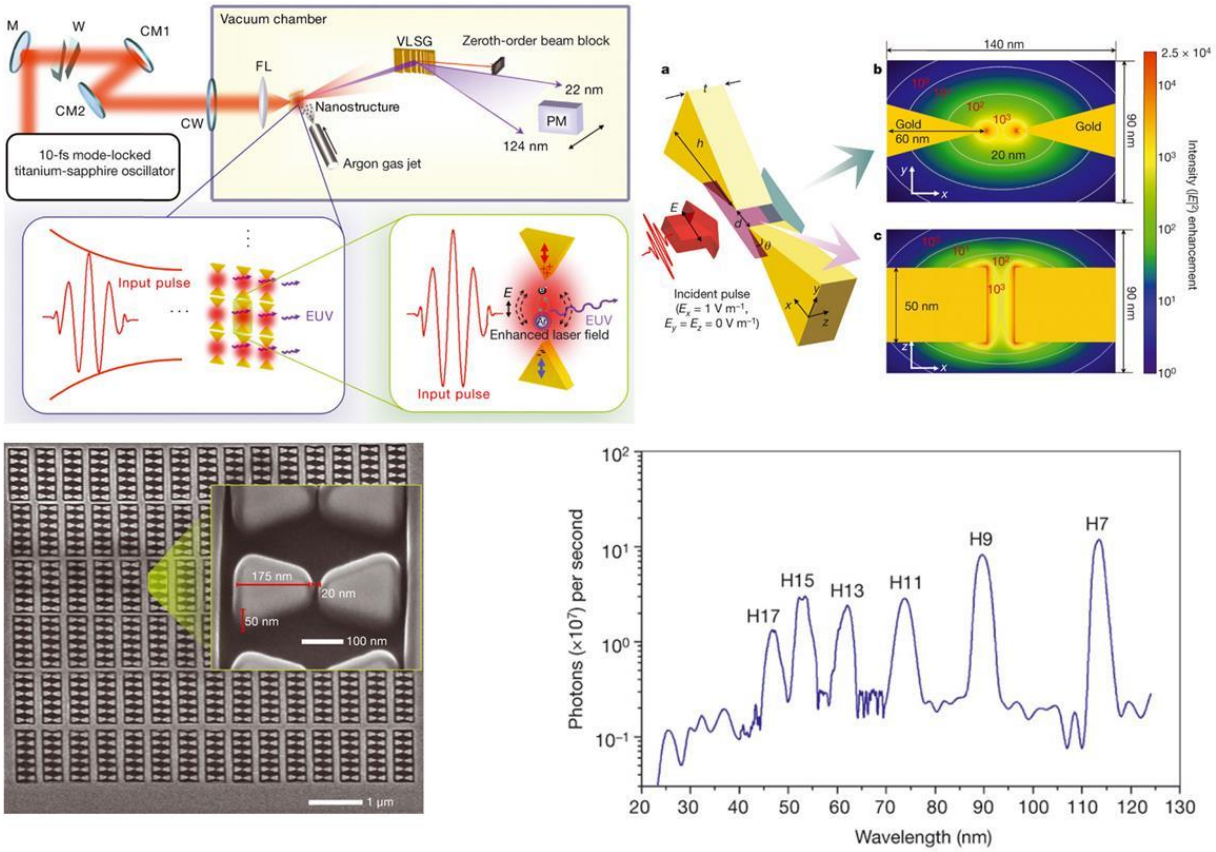

Figure 12.4: Higher harmonic generation from bow-tie plasmonic structures. Image adapted from [280].

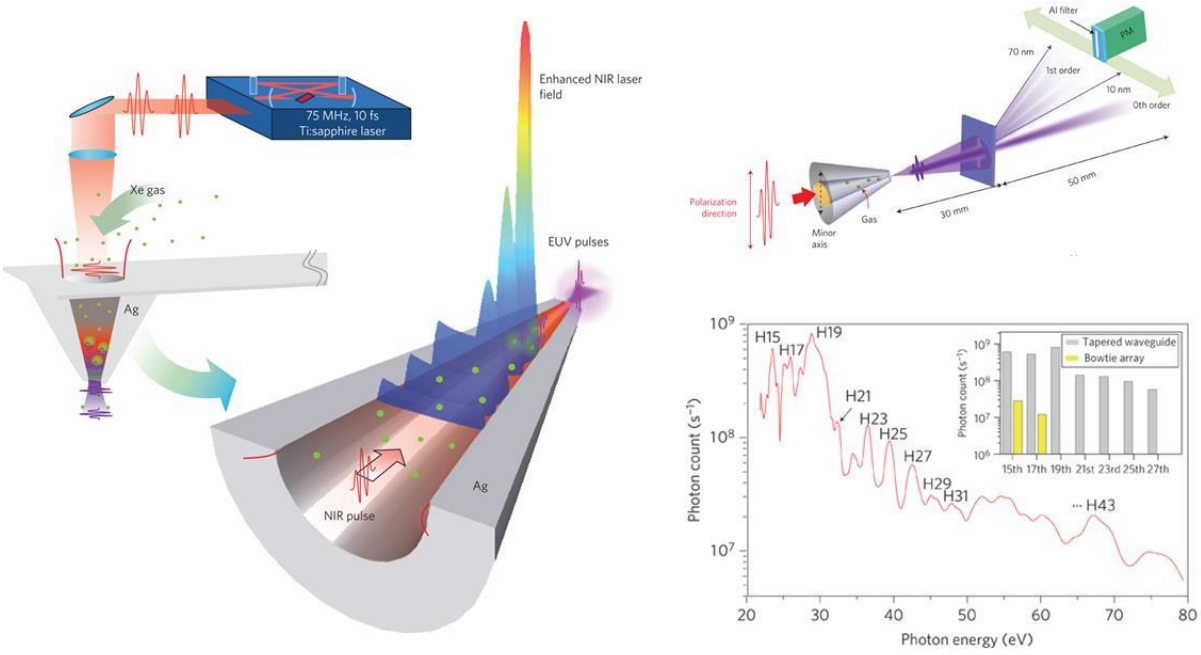

Figure 12.5: EUV light generation using plasmonic waveguide. Image adapted from [281].

Label free colorimetric DNA/protein microarray technologies

Important transcription factor controlling important gene expression are often encoded by low abundance proteins, mRNA and DNA. Detection of such proteins and DNA in microarray is limited by the quantum yield and photostability of fluorophore, giving rise to low signal-to-noise ratio. Traditionally glass or polymer based substrate are used for DNA microarrays. Due to higher refractive index of the substrate as compared to air, most of the fluorescence of the fluorophore is emitted in to the substrate. Therefore, in experimental set up where the excitation and collection are performed at the same side (e.g. in scanning microarray devices), the collection efficiency of the emitted light is very low. In fact, one study showed that only 20% of the total emitted light is collectable on standard glass substrates. In order to increase the collection efficiency and to increase the fluorescence signal, the proposed 3D plasmonic substrate can be used for microarrays.

The de-facto method of fluorescence-based detection in current DNA microarrays technology requires expensive, bulky microarrays readers to detect the signals. Subsequently it requires complex image analysis to interpret the results, which clearly prohibits the implementation of this method for readily on-field homeland defense chemical-biological warfare agent detection. In this regard, label-free colorimetric based detection of hybridization on 3D plasmonic substrate is an attractive alternative approach for detecting DNA sequences. In fact recently, small scale protein array has been demonstrated using plasmonic substrates [282].

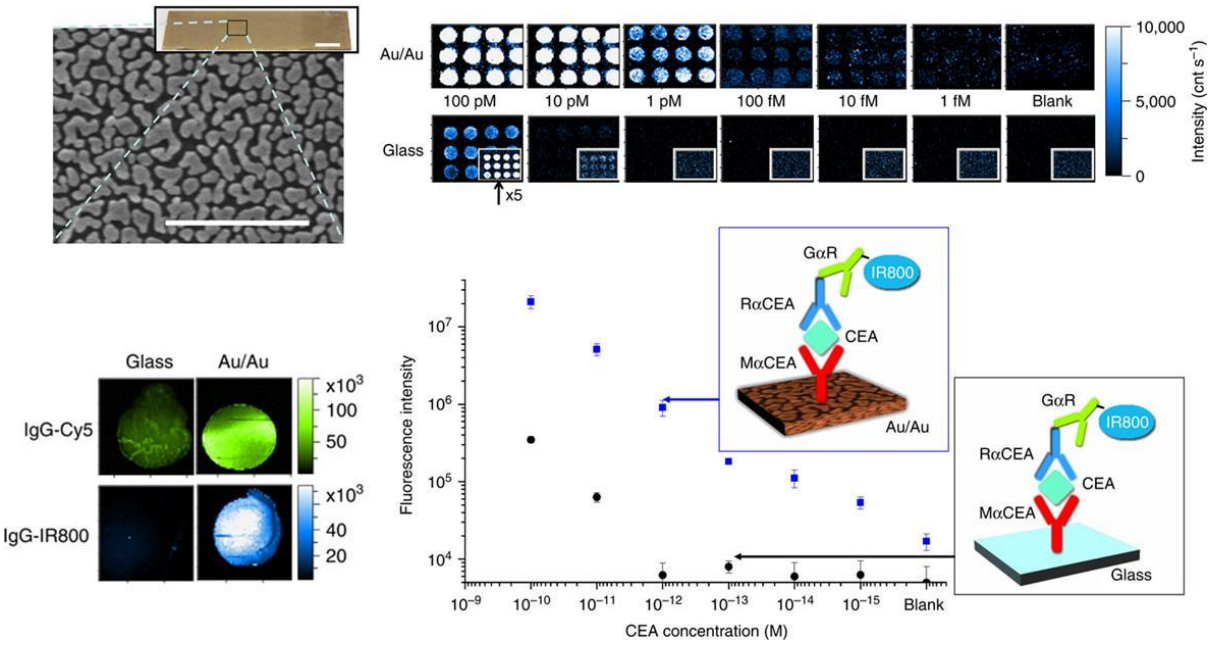

Figure 12.6: Protein microarray on plasmonic substrate. Image adapted from [282].

Plasmonic nanolithography for high density microarray printing

Diffraction limited photodeprotection techniques (for example, Affymetrix uses a mask based photodeprotection and NimbleGen uses a maskless digital micromirror projection based deprotection technique to synthesize the microarray) limit the number of spot that can be printed on a given substrate. In this context, the proposed 3D surface plasmon based substrate can provide suitable platform to print DNA microarrays beyond the diffraction limit at a lower cost. The basic principle behind surface plasmon nanolithography is based on the idea that, illuminated light can couple with surface plasmon to generate high field intensity. The coupled light can be engineered to emit at a much shorter wavelength compared to that of illumination light by designing the metal layer of the 3D plasmonic substrate. In addition, the interference of surface plasmon polariton wave from the subwavelength nanohole structures can locally cause increased exposure of a thin layer of resist (or layer to be deprotected) directly below the metal mask enabling sub diffraction limited microarray spot.

Graphene plasmonics

Graphene, a two dimensional material, has unique mechanical, electrical and thermal properties. The optical properties of graphene have been less investigated. Combining grapheme with plasmonics will allow modulation of optical transmission in visible spectrum [283]. Hybrid graphene-plasmonic structures have already been utilized for better surface enhanced Raman spectroscopy [284], and photodetectors [285, 286].

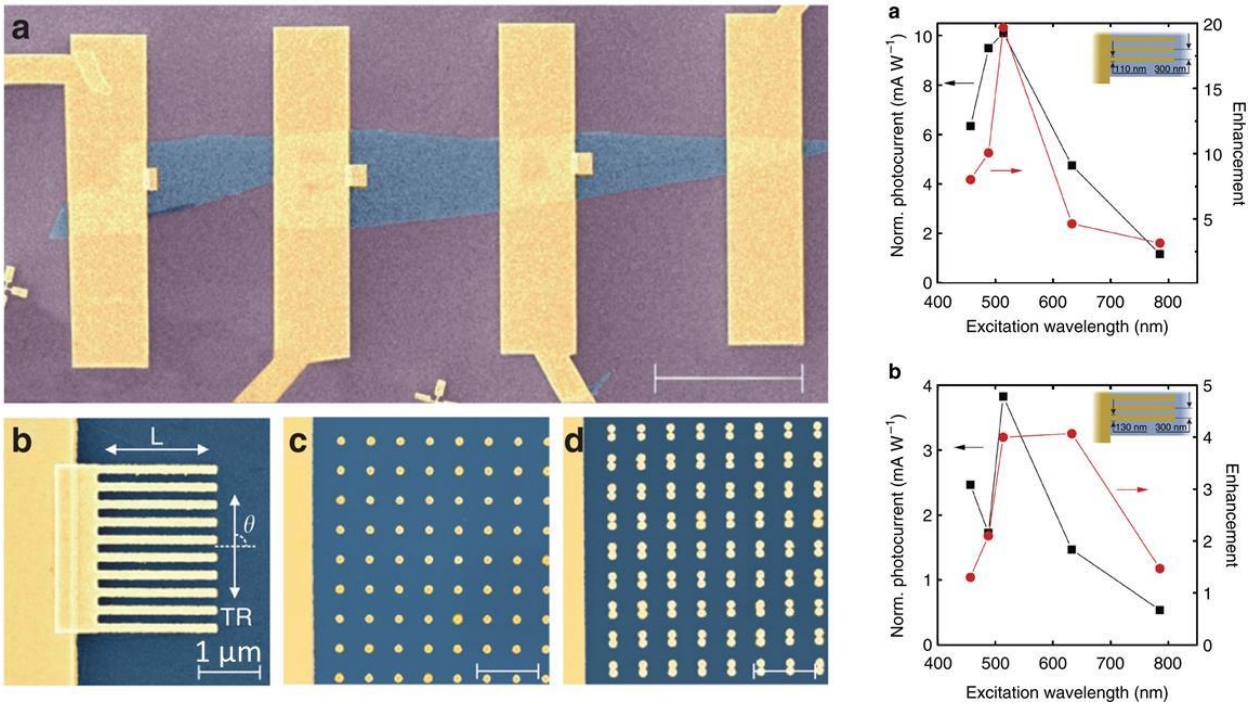

Figure 12.7: Hybrid grapheme-plasmonic structures for generation of photovoltage. Image adapted from [285].

Plasmonic light trapping for solar cell applications

Conventionally, solar cell thickness is typically 180–300 μm. Thin film solar cell has thickness of ~ 2 μm. Because of limitation in thickness, most of the solar spectrum (particularly in the intense 600–1,100 nm spectral range) is transmitted rather absorbed by the materials [287]. Light trapping can be achieved by using plasmonics materials. For example, using strong scattering and absorption properties of plasmonic metal nanoparticles embedded in the thin-film solar cells, more light can be trapped by increasing the effectively path length of the light.

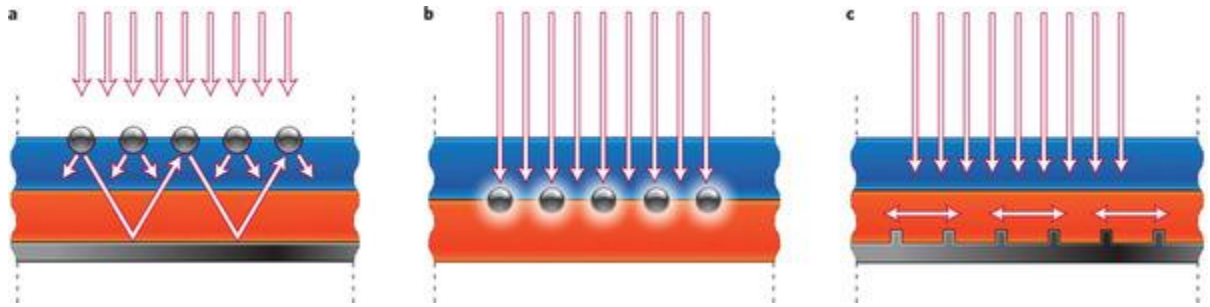

Figure 12.8: Light trapping using plasmonic materials. Image adapted from [287].

Plasmonic photodetector

In general, semiconductor based photodiodes are devices which convert light into a current of electrons. Recently, metal based plasmonics has been utilized to convert photon in to electron. The device works in the following way: "Photons coupled into a metallic nanoantenna excite resonant plasmons, which decay into energetic, "hot" electrons injected over a potential barrier at the nanoantenna-semiconductor interface, resulting in a photocurrent" [288].

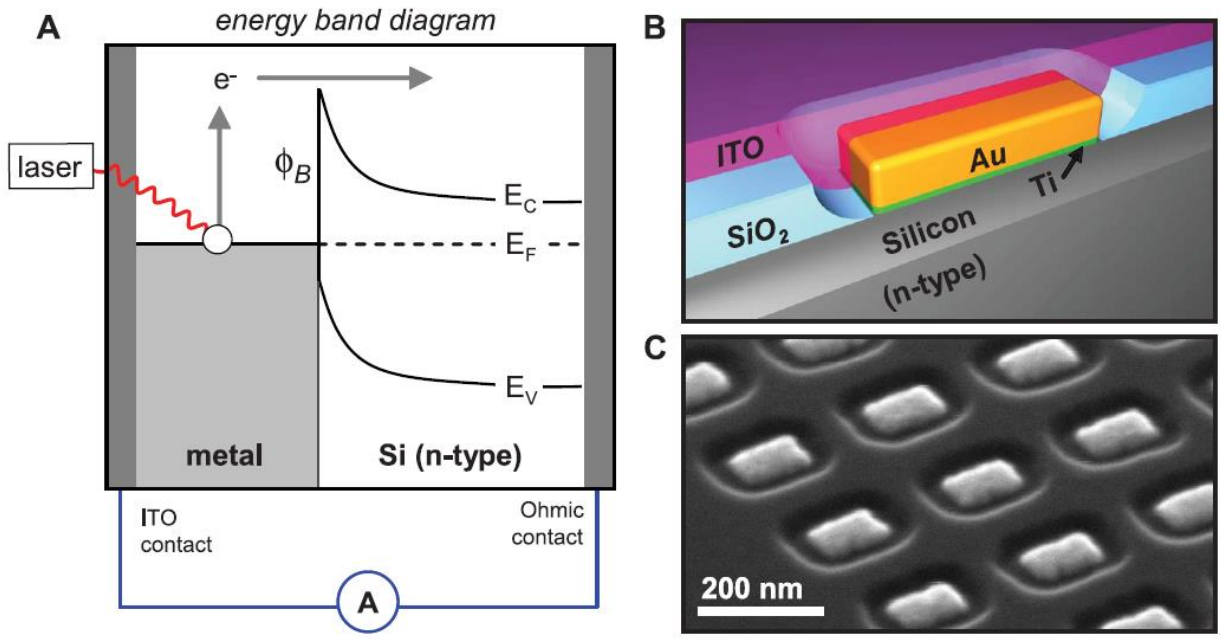

Figure 12.9: Plasmonic photodetector. Image adapted from [288].

Plasmonic color filters

Currently, dielectric interference layers need to be deposited on individual diodes for existing color or polarization sensitive diode arrays. This makes the processing steps complicated. Plasmonic nanohole array or plasmonic nanoresonators can be an alternative way to achieve the color filtering [289, 290].

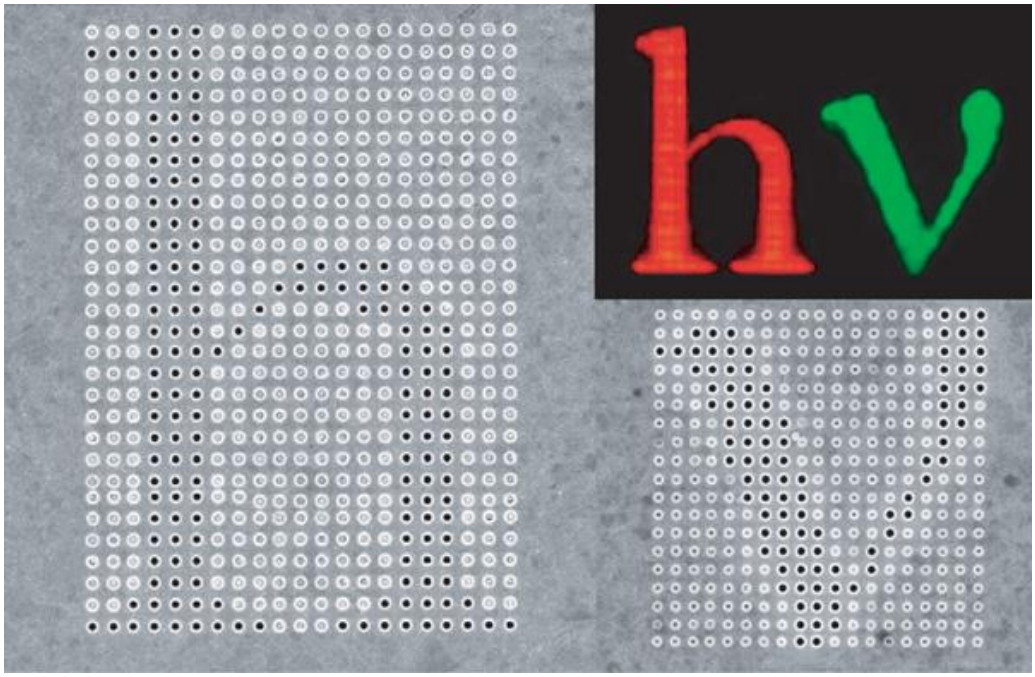

Figure 12.10: Array of holes made in Ag film using FIB milling. When illuminated with white light, the transmitted color shows red and green colors for the periods 550 and 450 nm respectively. Image adapted from [289].

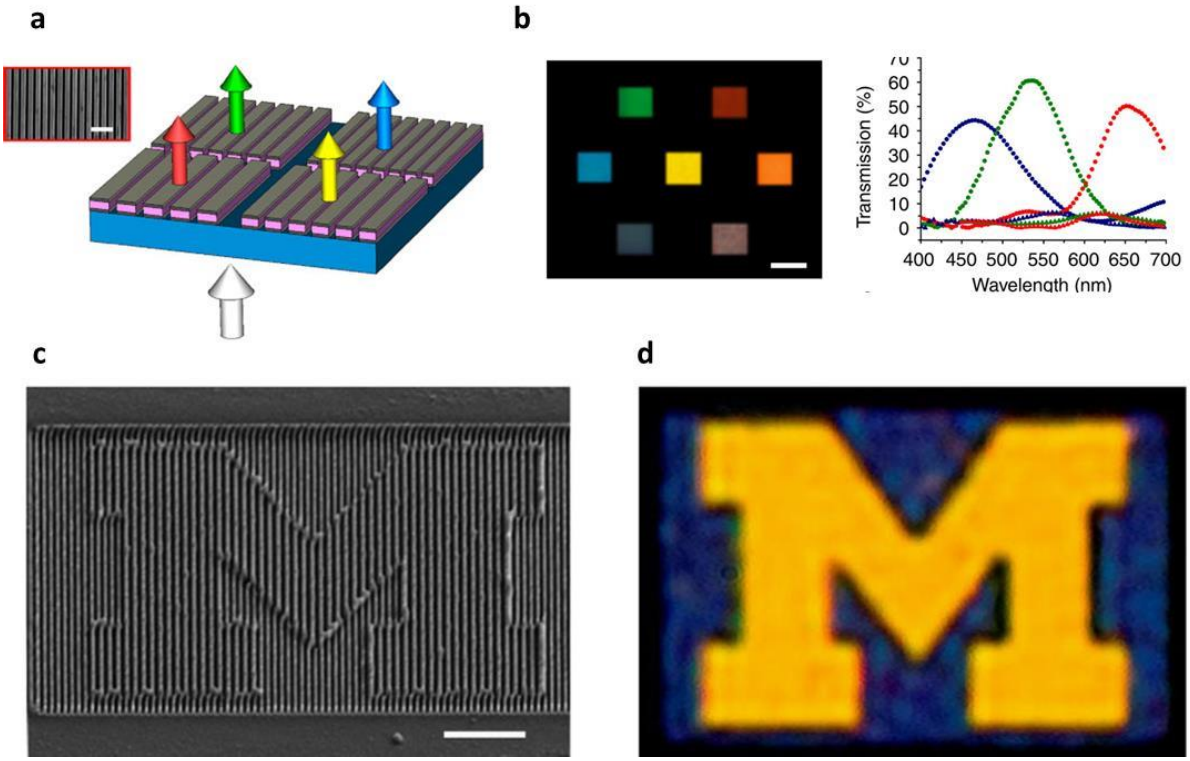

Figure 12.11: Plasmonic color filtering. Image adapted from [290].

Thermoplasmonics and catalysis

Because of strong absorption of visible and near infra-red wavelength regime and also being a metal, plasmonic materials have very good thermal properties. In fact, the thermal properties have been exploited for photothermal treatment of cancer cells [291] and catalysis for growth of nanowires and nanocrystals [292].

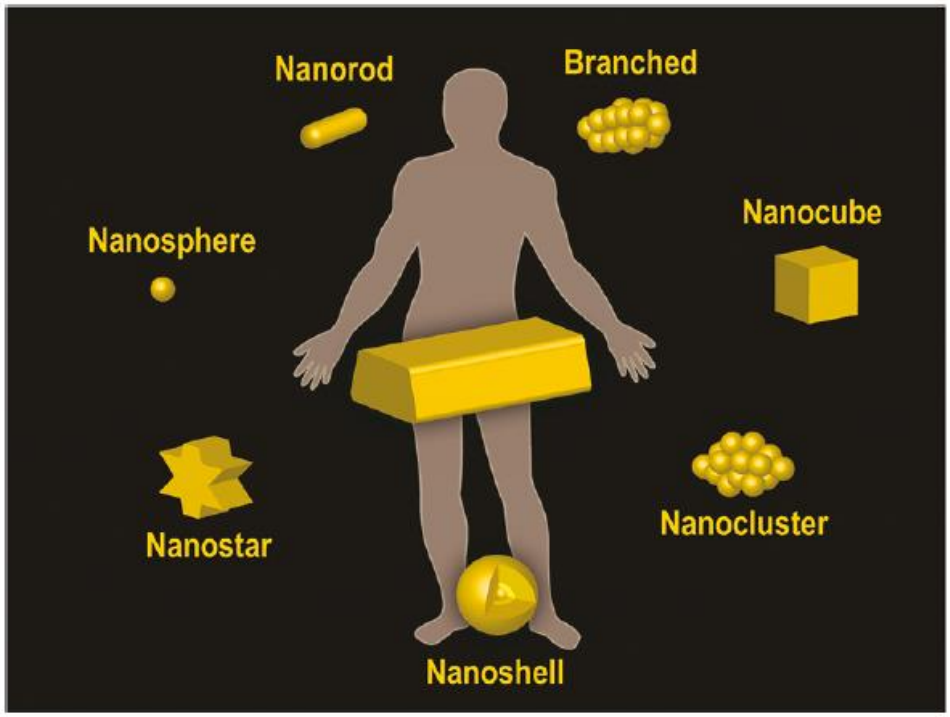

Figure 12.12: Plasmonics used in clinical practice. Image adapted from [293].

Challenges

Although, there are many advantages of plasmonics, there are few challenges to overcome too. For example, the surface geometry, topology and grain boundaries are difficult to control during metal deposition. This leads to unwanted absorption and scattering losses. This also limits the use of plasmonics for photonics applications such as lasers and wave guiding. Another important limitation is the surface chemistry which is essential in biosensing applications. Each metal surfaces and metal structures require individual surface chemistry optimization. Hence, it makes it challenging to adapt to wide variety of biological applications.

Conclusions

In spite of above challenges, “sky is the limit” when it comes to possible applications of plasmonics. Many practical applications utilizing plasmonics have already been implemented and many more to come in near futures. I hope this thesis will be a humble addition to the giant field of plasmonics.

References

[1] M. L. Brongersma and V. M. Shalaev, "APPLIED PHYSICS The Case for Plasmonics," *Science,* vol. 328, pp. 440-441, APR 23, 2010.

[2] A. Kinkhabwala, Z. Yu, S. Fan, Y. Avlasevich, K. Muellen and W. E. Moerner, "Large single-molecule fluorescence enhancements produced by a bowtie nanoantenna," *Nature Photonics,* vol. 3, pp. 654-657, NOV, 2009.

[3] D. Punj, M. Mivelle, S. B. Moparthi, T. S. van Zanten, H. Rigneault, N. F. van Hulst, M. F. Garcia-Parajo and J. Wenger, "A plasmonic 'antenna-in-box' platform for enhanced single-molecule analysis at micromolar concentrations," *Nature Nanotechnology,* vol. 8, pp. 512-516, 2013.

[4] S. Nie and S. Emery, "Probing single molecules and single nanoparticles by surface-enhanced Raman scattering," *Science,* vol. 275, pp. 1102-1106, FEB 21, 1997.

[5] W. Zhou, M. Dridi, J. Y. Suh, C. H. Kim, D. T. Co, M. R. Wasielewski, G. C. Schatz and T. W. Odom, "Lasing action in strongly coupled plasmonic nanocavity arrays," *Nature Nanotechnology,* vol. 8, pp. 506-511, 2013.

[6] M. Kauranen and A. V. Zayats, "Nonlinear plasmonics," *Nature Photonics,* vol. 6, pp. 737-748, NOV, 2012.

[7] J. A. Dionne, "Mirror, Mirror," *Physics,* vol. 5, pp. 38, 2012.

[8] N. B. Grosse, J. Heckmann and U. Woggon, "Nonlinear Plasmon-Photon Interaction Resolved by k-Space Spectroscopy," *Phys. Rev. Lett.,* vol. 108, pp. 136802, MAR 26, 2012.

[9] S. Kim, J. Jin, Y. Kim, I. Park, Y. Kim and S. Kim, "High-harmonic generation by resonant plasmon field enhancement," *Nature,* vol. 453, pp. 757-760, JUN 5, 2008.

[10] I. Park, S. Kim, J. Choi, D. Lee, Y. Kim, M. F. Kling, M. I. Stockman and S. Kim, "Plasmonic generation of ultrashort extreme-ultraviolet light pulses," *Nature Photonics,* vol. 5, pp. 678-682, NOV, 2011.

[11] S. M. Tabakman, L. Lau, J. T. Robinson, J. Price, S. P. Sherlock, H. Wang, B. Zhang, Z. Chen, S. Tangsombatvisit, J. A. Jarrell, P. J. Utz and H. Dai, "Plasmonic substrates for multiplexed protein microarrays with femtomolar sensitivity and broad dynamic range," *Nature Communications,* vol. 2, pp. 466, SEP, 2011.

[12] A. N. Grigorenko, M. Polini and K. S. Novoselov, "Graphene plasmonics," *Nature Photonics*, vol. 6, pp. 749-758, NOV, 2012.

[13] X. Ling, L. Xie, Y. Fang, H. Xu, H. Zhang, J. Kong, M. S. Dresselhaus, J. Zhang and Z. Liu, "Can Graphene be used as a Substrate for Raman Enhancement?" *Nano Letters*, vol. 10, pp. 553-561, FEB, 2010.

[14] T. J. Echtermeyer, L. Britnell, P. K. Jasnos, A. Lombardo, R. V. Gorbachev, A. N. Grigorenko, A. K. Geim, A. C. Ferrari and K. S. Novoselov, "Strong plasmonic enhancement of photovoltage in graphene," *Nature Communications*, vol. 2, pp. 458, AUG, 2011.

[15] Y. Liu, R. Cheng, L. Liao, H. Zhou, J. Bai, G. Liu, L. Liu, Y. Huang and X. Duan, "Plasmon resonance enhanced multicolour photodetection by graphene," *Nature Communications*, vol. 2, pp. 579, DEC, 2011.

[16] H. A. Atwater and A. Polman, "Plasmonics for improved photovoltaic devices," *Nature Materials*, vol. 9, pp. 205-213, MAR, 2010.

[17] M. W. Knight, H. Sobhani, P. Nordlander and N. J. Halas, "Photodetection with Active Optical Antennas," *Science*, vol. 332, pp. 702-704, MAY 6, 2011.

[18] C. Genet and T. W. Ebbesen, "Light in tiny holes," *Nature*, vol. 445, pp. 39-46, JAN 4, 2007.

[19] T. Xu, Y. Wu, X. Luo and L. J. Guo, "Plasmonic nanoresonators for high-resolution colour filtering and spectral imaging," *Nature Communications*, vol. 1, pp. 59, AUG, 2010.

[20] L. Hirsch, R. Stafford, J. Bankson, S. Sershen, B. Rivera, R. Price, J. Hazle, N. Halas and J. West, "Nanoshell-mediated near-infrared thermal therapy of tumors under magnetic resonance guidance," *Proc. Natl. Acad. Sci. U. S. A.*, vol. 100, pp. 13549-13554, NOV 11, 2003.

[21] L. Cao, D. N. Barsic, A. R. Guichard and M. L. Brongersma, "Plasmon-assisted local temperature control to pattern individual semiconductor nanowires and carbon nanotubes," *Nano Letters*, vol. 7, pp. 3523-3527, NOV, 2007.

[22] A. S. Thakor, J. Jokerst, C. Zavaleta, T. F. Massoud and S. S. Gambhir, "Gold Nanoparticles: A Revival in Precious Metal Administration to Patients," *Nano Letters*, vol. 11, pp. 4029-4036, OCT, 2011.

APPENDIX A

Details of FDTD simulation for nanoLycurgus cup array (nanoLCA) device

Geometry

The geometry of the device was first made using the graphical user interface (GUI) of the FDTD software (Lumerical Inc.). The dimensions are shown in Fig. A1. The side wall particles are modeled as rings. The distance between each rings were 20 nm and the height of each ring was 55 nm.

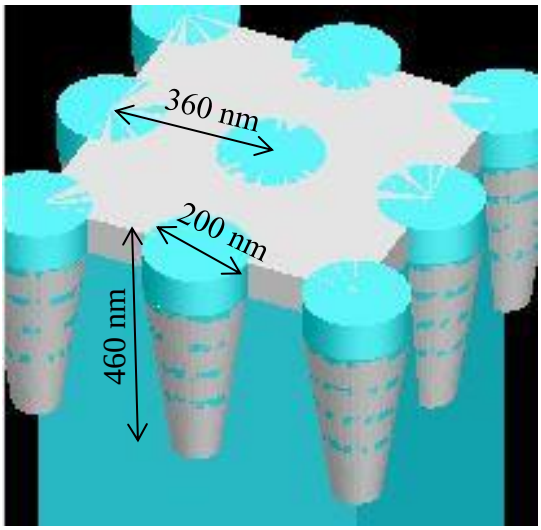

Figure A.1: Schematic showing the simulated dimensions of nanoLCA.

Boundary conditions and simulation region

Periodic boundaries were used for the periodic directions (x and y). The simulation span corresponds to 1 unit cell of the device. For directions that are not periodic (z), perfectly matched layer, PML (absorbing) boundaries were used as shown in Fig. A2.

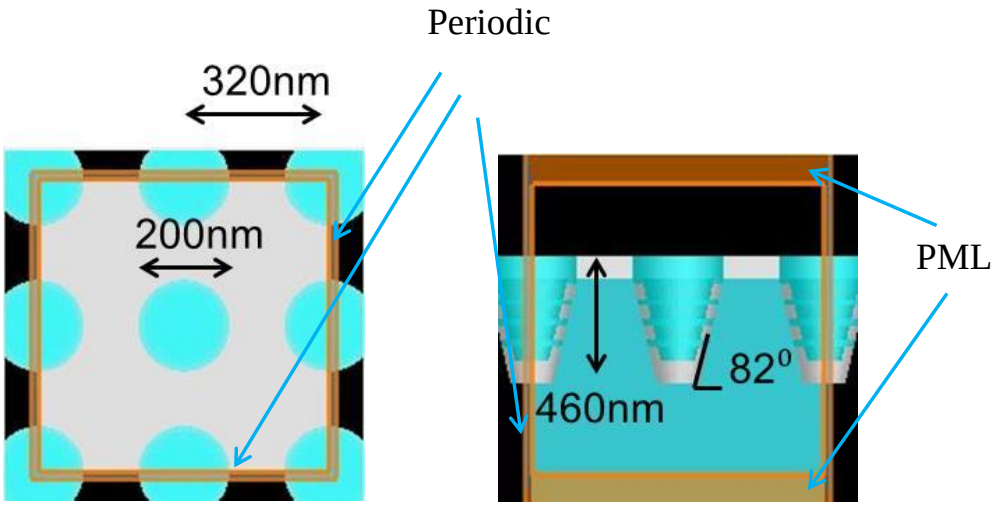

Figure A.2: Schematic showing the boundary conditions and simulation regions.

Source

Plane wave sources propagating in positive *y* direction (bottom of the cup towards top side) was used for the simulations. The source was kept 30 nm below the bottom silver layer of the nano cup as shown in Fig. A3.

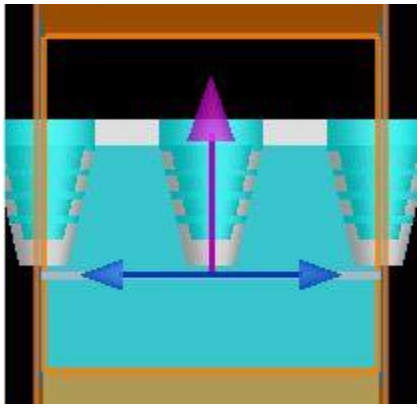

Figure A.3: Schematic showing the light source.

Meshing (also described in http://docs.lumerical.com/en/fdtd/knowledge_base.html**)**

In Lumerical FDTD, a non-uniform mesh is automatically generated based on the mesh accuracy slider bar. The "mesh accuracy" parameter ranges from integer value of 1-8, where 1 is low accuracy (coarse mesh), and 8 is high accuracy (smaller mesh). The mesh accuracy of 1

corresponds to λ/dx=6, where dx= mesh size and λ= wavelength, whereas a mesh accuracy of 6 corresponds to λ/dx =26. As computation time within FDTD varies with inversely with the mesh size to the fourth power (1/dx)4 using a coarser mesh can result in significantly faster simulation times. While coarser mesh can effect the accuracy of the results. Hence, generally a grid independence test is performed before every simulation to choose the appropriate mesh size to get accurate results while optimizing the simulation time.

Another consideration in choosing the proper mesh size is the number of mesh points per wavelength (ppw. For example, accuracy 1 corresponds to a target of 6 ppw. Acc 2 ->10 ppw, Acc 3 ->14ppw (taken from http://docs.lumerical.com/en/fdtd/knowledge_base.html), and so on, in increments of 4 ppw per point on the slider bar. It is important to remember that wavelength is inversely proportional to the refractive index. In high index materials, the effective wavelength is smaller, meaning that the meshing algorithm will use a smaller mesh in high index materials. We used overall mesh order of 4 and local mesh size of 1.5 nm in this work.

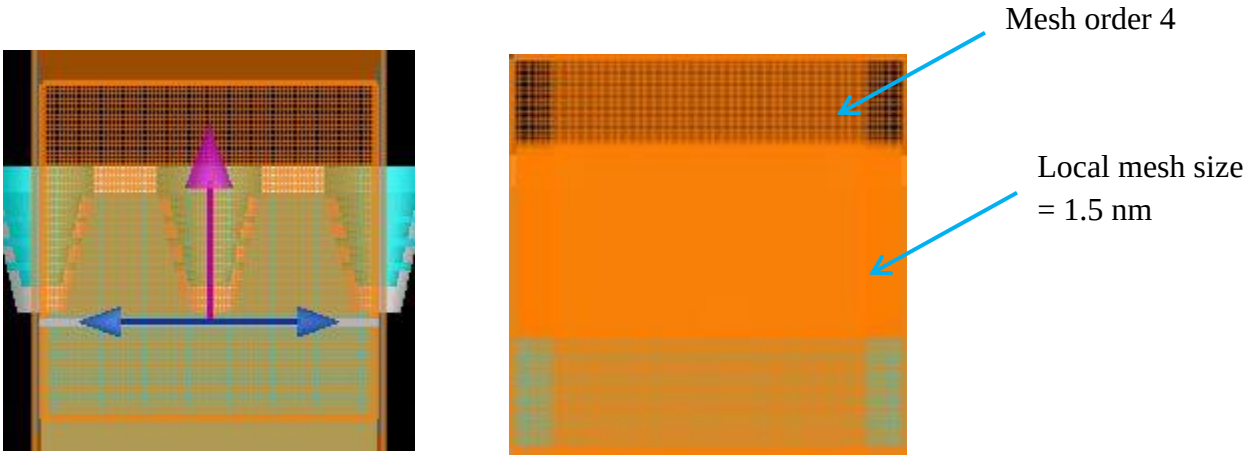

Figure A.4: Schematic of meshing used for the simulation.

Monitors and analysis

Near field and far field

In order to visualize the near field results (such as electric field), we have placed profile monitors in the near field region of the structure. In order to obtain the far field scattering pattern we used

monitor located above or below the structure (depending on whether we want scattering in the forward or backwards direction). Note that the monitor plane should always be placed in a homogeneous region in the near field. It is also possible to use the projection functions to calculate the far field distribution of finite sized periodic arrays (even if the simulation is infinitely periodic).

Transmission/Reflection

In many cases, we are only interested the total transmission/reflection of the device. This can be easily calculated by placing power monitors above and below the structure, and then plotting the transmission results. Note that power flowing towards the -x/-y/-z directions will carry a negative sign.

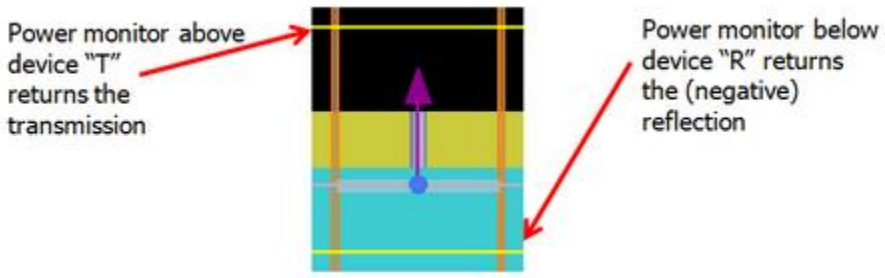

Figure A.5: Example of transmission and reflection monitors [adapted from http://docs.lumerical.com/en/fdtd/sp_periodic_structures.html.]

For structures that support multiple grating orders, one may want to look at the transmission/reflection into particular orders. FDTD Solutions has built-in grating projection calculations that can be used to calculate the direction and intensity of light reflected or transmitted through a periodic structure. The Object Library also provides a "grating_transmission" analysis group  which can be used to find the transmission into any order. For a list of examples, see the gratings section of the applications library at http://docs.lumerical.com/en/fdtd/sp_periodic_structures.html.

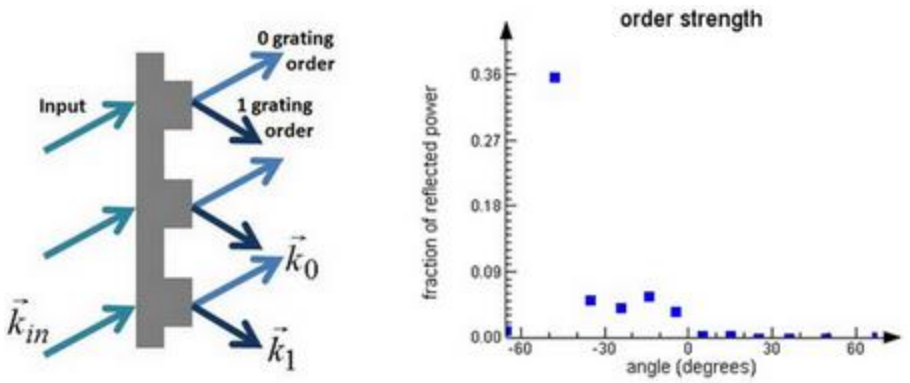

Figure A.6: Example of diffraction grating order [adapted from http://docs.lumerical.com/en/fdtd/sp_periodic_structures.html.]

Material properties

In order to calculate the electromagnetic fields in the plasmonic structure, Palik's data was used to fit the dispersion relation of metals (real and imaginary part).

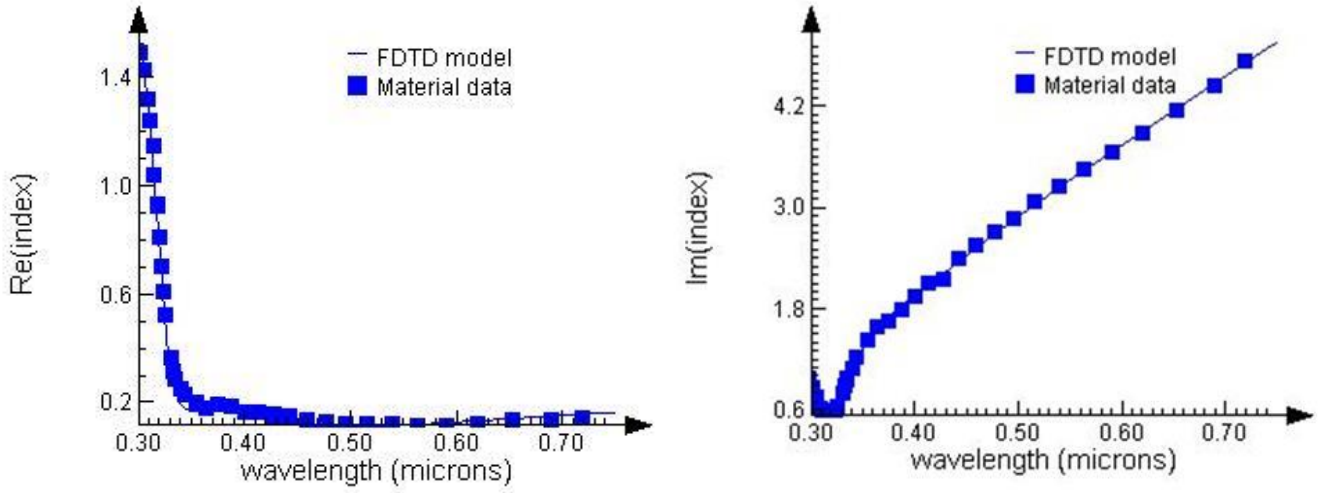

Figure A.7: Dispersion relation used in FDTD simulation for Ag (using Palik's data).

APPENDIX B

Details of FEM simulation to calculate the whispering gallery mode (WGM) in a microresonator

The different steps to be followed are:

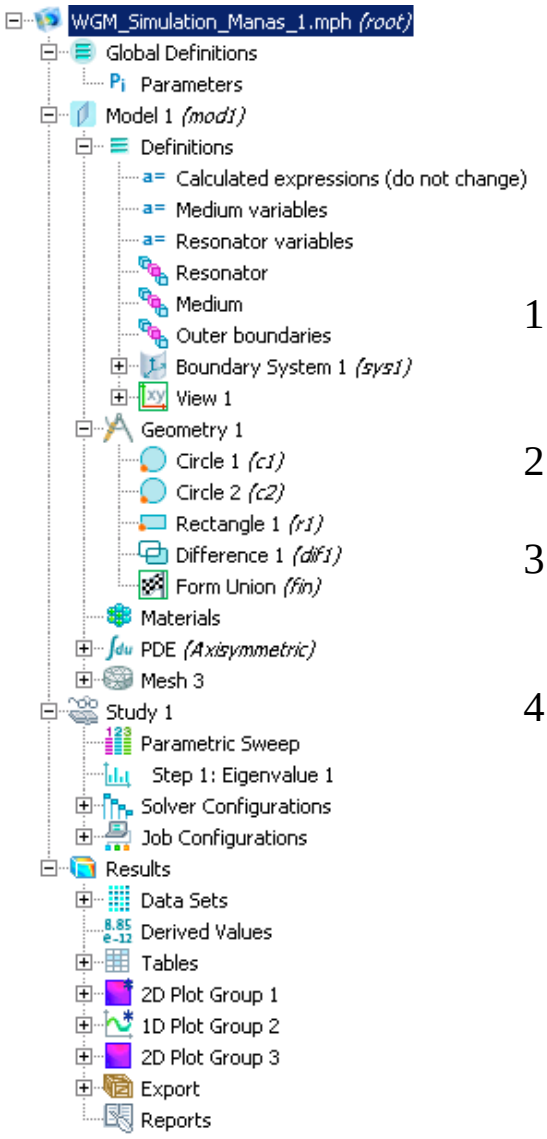

1. Parameters
   - Defines M number, material refractive index
2. Geometry
   - Define resonator geometry
3. Definitions of materials
   - Define selected geometry to resonator and surrounding
4. Mesh
   - Can define finer/coarser mesh

1. Parameters

Key parameters

- M number = (Perimeter)/(Wavelength)

  M number is an integer value

- Refractive Index, N_medium

  Of the resonator material
- For the spherical resonator, resonator radius/diameter can be defined here as well

Parameters

Name	Expression	Value	Description
c	299792458	2.9979E8	speed of light (exact!)
k	2*pi/c	2.0958E-8	
fc	k^2	4.3926E-16	constant used internally --do not modify
alpha	1.0	1.0000	penalty coefficient on Div H
M	round(2*pi*r_1/(lamda/n_medium))-4	11.000	azimuthal mode order
delta_e	0.0	0	fractional increment (for determining filling factors)
e1	n_medium^2*(1+delta_e)	2.5137	relative permittivity of isotropic_dielectric_1
e2	1.0	1.0000	ditto for isotropic_dielectric_2
delta_eperp1	0*1e-3	0	fractional increment (for determining filling factors)
eperp1	9.2725*(1+delta_eperp1)	9.2725	relative permittivity of uniaxial_dielectric_1 perpendicular to cylindrical axis
delta_epara1	0*1e-3	0	fractional increment (for determining filling factors)
epara1	11.3486*(1+delta_epara1)	11.349	relative permittivity of uniaxial_dielectric_1 parallel to cylindrical axis
eperp2	1.0	1.0000	relative permittivity of uniaxial_dielectric_2 perpendicular to cylindrical axis
epara2	1.0	1.0000	ditto but parallel to cylindrical axis
e_293K_alumina	9.8	9.8000	relative permittivity of alumina at room temperature
eperp_4K_sapph_UWA	9.2725	9.2725	UWA values for cryogenic HEMEX sapphire

2. Geometry

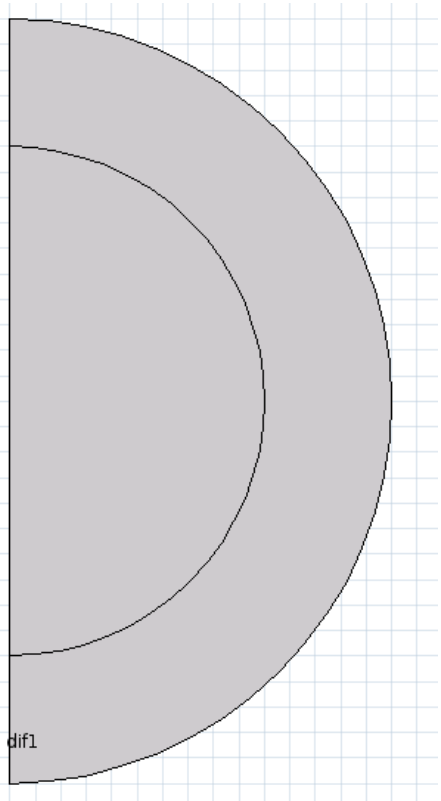

Figure B.1: The 2D geometry of the microresonator.

First, the geometry may be defined by drawing 2 concentric circles. Since this is axisymmetric model, the axis of rotation must be at x=0 and only half of the circle must be defined. The other half of the circle may be deleted by drawing a geometry that covers half of the circle and perform Boolean difference operation.

3. Defining materials of the resonator

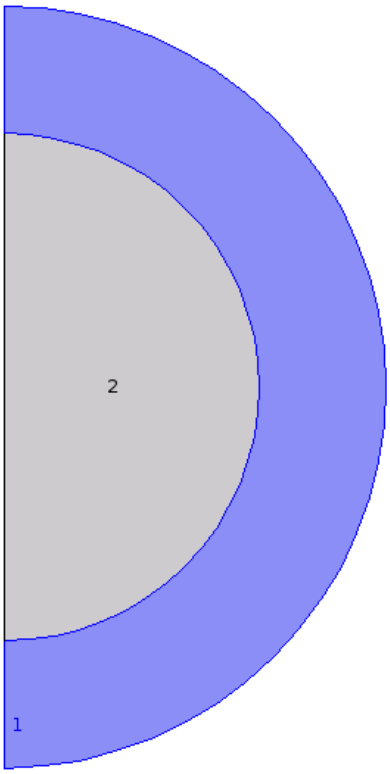

- Click 1 and add to Medium variables (surrounding)
- Click 2 and add to Resonator variables (resonator)

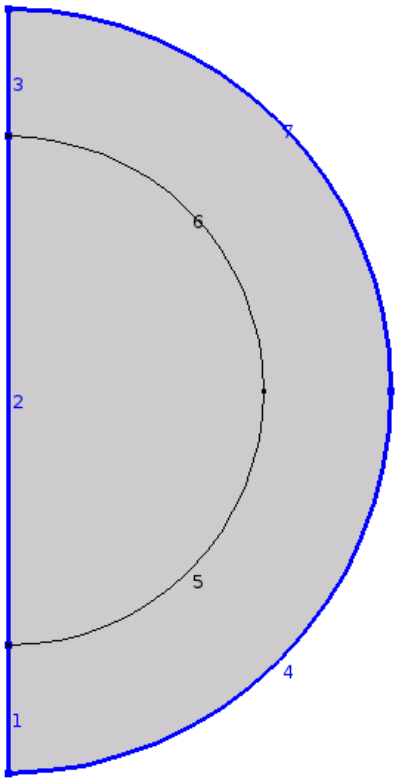

Outer boundaries

- Click all outside boundaries of the simulating regions

Figure B.2: To define the materials of resonator and surrounding area.

4. Meshing

COMSOL generates mesh automatically. User may choose to make the mesh finer/coarser as necessary.

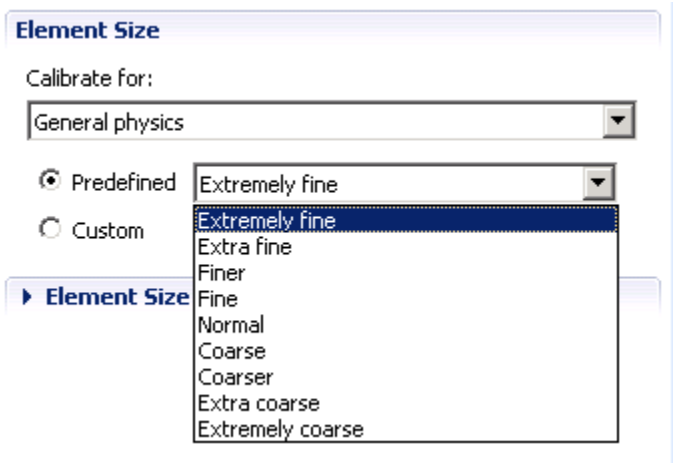

Figure B.3: Screen shot showing the meshing option in COMSOL.

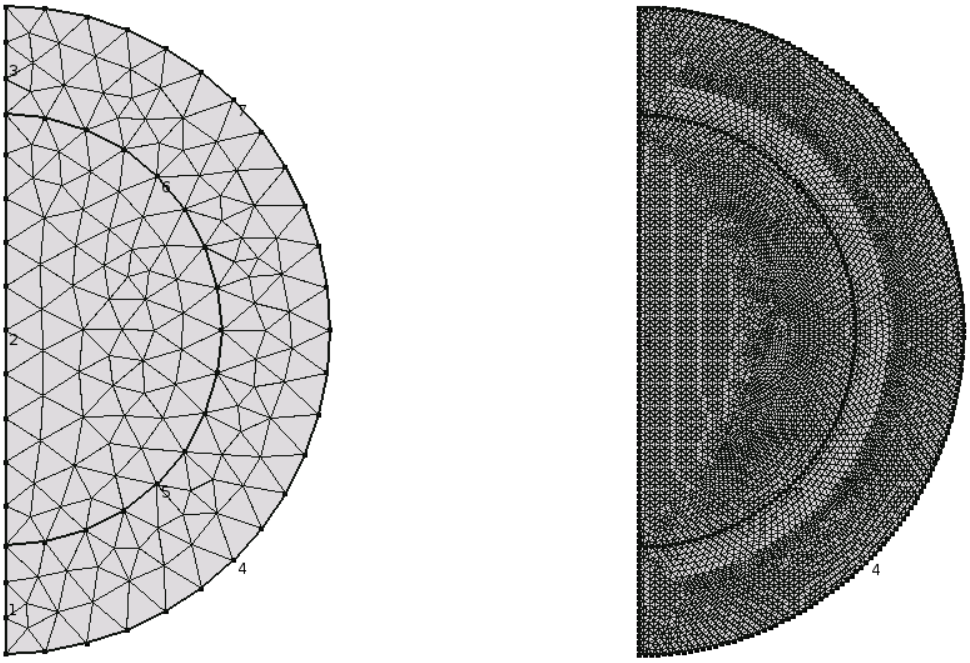

Figure B.4: Examples of coarse meshing and fine meshing in COMSOL.

Parametric study

For repeating simulation continuously, parametric sweep menu can be used. In order to parametrically sweep resonator radius, radius must be defined in Parameters section (Fig. B5).

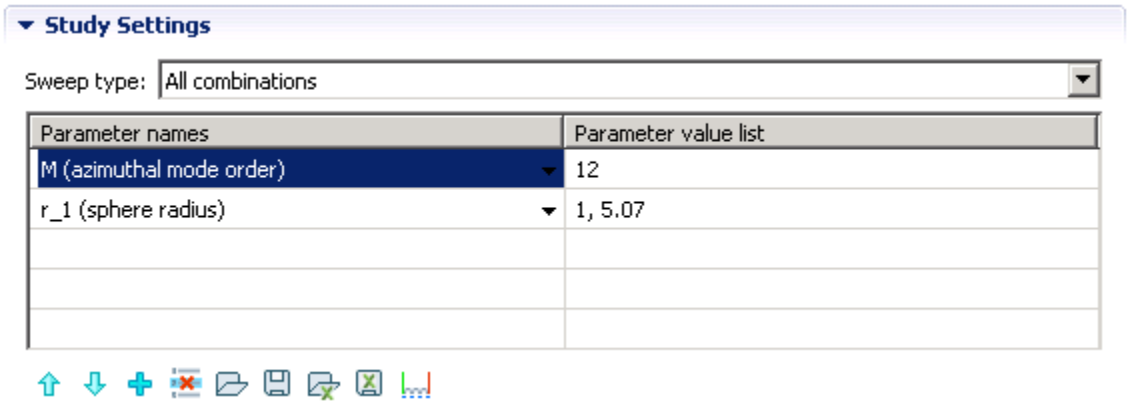

Figure B.5: Examples of parametric sweep option in COMSOL.

Results

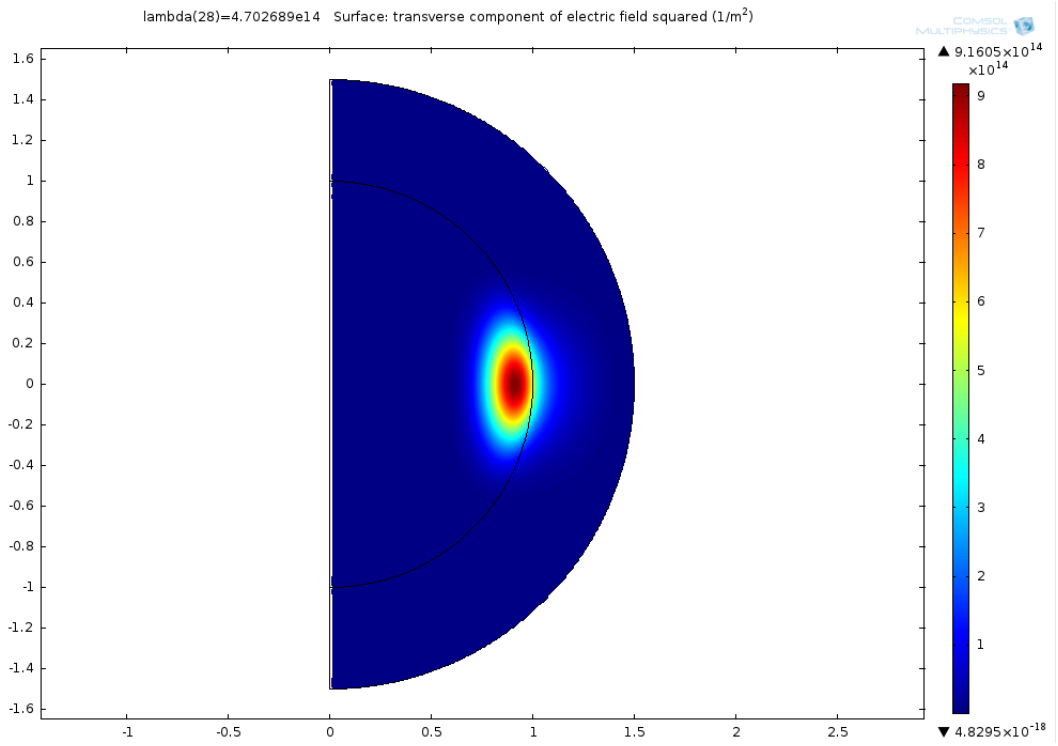

Figure B.6: Examples of first order mode (radial electric field).